The Physical Mechanism of Blood-Brain Barrier Opening Using Focused Ultrasound and Microbubbles

Yao-Sheng Tung

Submitted in partial fulfillment of the
requirements for the degree
of Doctor of Philosophy
in the Graduate School of Arts and Sciences

COLUMBIA UNIVERSITY
2012

ABSTRACT

The Physical Mechanism of Blood-Brain Barrier Opening Using Focused Ultrasound and Microbubbles

Yao-Sheng Tung

The key to effective treatment of neurological diseases resides in the safe opening of the blood-brain barrier (BBB), a specialized structure that impedes the delivery of therapeutic agents to the parenchyma. Despite the fact that several approaches have been successful in overcoming the BBB impermeability, none of them can induce localized BBB opening noninvasively except for focused ultrasound (FUS) in conjunction with microbubbles. The physical mechanism behind the opening, however, has not been identified. Insight into the mechanism can be critical for delineating the safety profile for in both small and large animals alike. Therefore the purpose of this dissertation is to first determine the physical mechanism of FUS-induced BBB opening in mice and then translate this approach to non-human primates.

To accomplish this goal, an *in vivo* transcranial cavitation detection system was developed and tested, built in phantoms and *in vivo*, to monitor the behavior of the microbubbles in the FUS bean, and to determine the type of cavitation, i.e., the activation of bubbles in an acoustic field, during BBB opening. We showed that the inertial cavitation (IC), a collapse of a bubble, which can vary from a fragmentation of the bubble to shock wave and liquid jets depending on the pressure, thereby damaging the endothelial cells of the brain capillaries, was not required to induce BBB opening in mice. With this system, the role of microbubble properties, including the diameter and shell components, in the BBB opening were determined. When the BBB opens with stable cavitation (SC), i.e., relatively moderate amplitude changes in the bubble size, the bubble diameter is similar to the capillary diameter (i.e., at 4-5, 6-8 μm) while with inertial cavitation it is not (i.e., at 1-2 μm). The bubble may thus have to be in closer proximity to the capillary wall to induce BBB opening without IC. The BBB opening properties, such as volume and permeability, however, were not affected by the shell component of the microbubbles in mice. The connection between the physical and physiological mechanism was then investigated to identify the lowest peak rarefactional pressure BBB opening threshold at 1.5 MHz (0.18 MPa). A sufficiently long pulse (pulse length = 0.5 ms) was required for the SC to induce BBB opening at the lowest pressure. However, the tight junctions, the main formation of the BBB, were found not to be disrupted after sonication at both low (0.18 MPa) and high (0.45 MPa) pressures. Therefore, the transcellular pathway may be the main route of the FUS-induced BBB opening. Finally, the cavitation-guided BBB opening system was used to induce reversible BBB opening in non-human primates. This is a major step towards clinical feasibility. In conclusion, a transcranial cavitation detection system was developed, in order to characterize the physical mechanism, the role of the microbubbles, and the corresponding physiological response of the FUS-induced BBB opening.

Table of Contents

Table of Contents i

List of Tables v

List of Figures vi

Glossary xix

Acknowledgments xx

Chapter 1 Introduction 1

- 1.1 Motivation 2
- 1.2 Overview and significance 3

Chapter 2 Noninvasive and Localized Blood-Brain Barrier Opening Using Focused Ultrasound and Microbubbles 6

- 2.1 Introduction 7
- 2.2 The Blood-Brain Barrier 7
- 2.3 FUS-induced BBB opening 10
  - 2.3.1 Focused ultrasound 10
  - 2.3.2 Microbubbles 11
  - 2.3.3 BBB opening using FUS and microbubbles 13
    - 2.3.3.1 Animal models for BBB opening 13
    - 2.3.3.2 Investigation of experimental conditions 14
    - 2.3.3.3 Delivery of large compounds through the opened BBB 18
    - 2.3.3.4 Safety assessment 20
- 2.4 Possible mechanism of FUS-induced BBB opening 22
  - 2.4.1 Physiological mechanism 22
  - 2.4.2 Physical mechanism – acoustic cavitation 24

Chapter 3 Development of a Transcranial Cavitation Detection System 27

3.1 Introduction 28
3.2 Materials and Methods 29
  3.2.1 Phantom validation of the skull effect 29
    3.2.1.1 Experimental Setup 29
    3.2.1.2 Skull preparation and targeting procedure 32
    3.2.1.3 microbubble preparation and sonication 34
    3.2.1.4 Acoustic emission signal acquisition and analysis 35
  3.2.2 *In vivo* transcranial cavitation detection in mice 36
    3.2.2.1 Experimental Setup 36
    3.2.2.2 Magnetic resonance imaging 39
    3.2.2.3 Histological analysis 40
    3.2.2.4 Acoustic emission signal acquisition and analysis 41
3.3 Results 42
  3.3.1 Phantom validation of the skull effect 42
  3.3.2 *In vivo* transcranial cavitation detection in mice 50
3.4 Discussion 55
  3.4.1 Phantom validation of the skull effect 55
  3.4.2 *In vivo* transcranial cavitation detection in mice 59
3.5 Conclusion 63

Chapter 4 Microbubble-Dependent Mechanism of Blood-Brain Barrier Opening Using Focused Ultrasound and Microbubbles 64
4.1 Introduction 65
4.2 Theoretical models for microbubble oscillation 68
  4.2.1 Oscillation of a free air and a shelled microbubble 69
  4.2.2 Oscillation of a lipid-shelled microbubble 71
4.3 Materials and Methods 72
  4.3.1 Mono-dispersed microbubbles 72
    4.3.1.1 Microbubble size distribution 72
    4.3.1.2 Microbubble shell materials 74
  4.3.2 Sonication protocol 75

4.3.2.1 *In vivo* study for BBB opening properties assessment 75
4.3.2.2 Phantom validation for IC threshold determination 76
4.3.3 MRI protocol 77
4.3.4 Acoustic emission signal processing 78
4.4 Results 79
4.4.1 Bubble size dependent BBB opening properties 79
4.4.1.1 *In vivo* BBB opening investigation 79
4.4.1.2 IC threshold determination of mono-dispersed microbubbles 88
4.4.2 Shell effect on bubble behavior during BBB opening 92
4.5 Discussion 97
4.5.1 Bubble size dependent BBB opening properties 97
4.5.1.1 *In vivo* BBB opening investigation 97
4.5.1.2 IC threshold of lipid-shelled mono-dispersed microbubble 103
4.5.2 Shell effect on bubble behavior during BBB opening 105
4.6 Conclusion 109

Chapter 5 The Cavitation-Dependent Tight-Junction Integrity of Blood-Brain Barrier Opening Using Focused Ultrasound and Microbubbles 111
5.1 Introduction 112
5.2 Materials and Methods 113
5.2.1 Sonication protocol 113
5.2.2 BBB opening confirmation 115
5.2.3 Immunofluorescence Staining 115
5.3 Results 116
5.3.1 SC- and IC-induced BBB opening 116
5.3.2 Fluorescence imaging and Tight Junction integrity 118
5.4 Discussion 121
5.4.1 Cavitation-dependent mechanism of BBB opening 122
5.4.2 Safe BBB opening using low mechanical index 126
5.5 Conclusion 127

Chapter 6 Translation of the Focused Ultrasound Induced Blood-Brain Barrier Opening System to Non-Human Primates 128
6.1 Introduction 129
6.2 Materials and Methods 130
6.2.1 Sonication protocol 130
6.2.2 MRI and acoustic emission detection 134
6.3 Results 135
6.3.1 BBB opening and corresponding cavitation response 135
6.3.2 Closing timeline and accuracy 142
6.4 Discussion 144
6.5 Conclusion 149

Chapter 7 Conclusion and future directions 151
7.1 Conclusion 152
7.2 Future directions 154

List of Publications Related to the Thesis 156

Reference 158

Appendix A Kinetic model for permeability map 177

Appendix B Transcranial focusing quality quantification 181

List of Tables

Table 2.1 Techniques shown to induce BBB opening and their advantages 9

Table 2.2 Three main microbubbles used in BBB opening. The data of Optison and Definity is obtained from the package insert. The data of Sonovue is from Molecular Imaging and Contrast Agent Database (MIDAC) 12

Table 2.3 Animal models used in FUS-induced BBB opening 14

Table 2.4 Investigations on the experimental parameters 16

Table 2.5 Molecules used in the FUS-induced BBB opening 19

Table 3.1 Number of mice with BBB opening / number of mice studied at each pressure.38

Table 4.1 Abbreviations, molecular weight, viscosity, and gel-liquid transition temperature of each acyl-chain length...74

Table 4.2 Number of mice studied at each pressure and each bubble size...........................75

Table 4.3 Number of mice studied at each pressure and each acyl-chain length.................75

Table 4.4 Expansion ratio (R_{max}/R_0) for each diameter and each theoretical model............89

Table 4.5 Safety assessment (damaged / BBB-opened mice) at each pressure and each acyl-chain length...92

Table 5.1 Acoustic parameters for SC-induced BBB opening 114

Table 6.1 Acoustic parameters and corresponding targeting region # denotes the number of sonications. N is the number of monkeys. VC: Visual Cortex. HC: Hippocampus Ca: Caudate Pu: Putamen...131

Table 6.2 The axial focal shift, BBB opening volume, and MRI contrast enhancement of two opening regions. The focal shift is as our expectation shown in *Appendix B.* 143

Table B.1 Targeting coverage for the different anatomical aims through NHP and human skulls. 190

List of Figures

Figure 2.1 – A schematic diagram of the major differences between (a) general capillaries and (b) brain capillaries. The endothelium of brain capillaries has the tight junction between the cells, as well as lacks intercellular clefts, fenestrations, and pinocytosis. This figure is modified from Churchland et al.[27] 8

Figure 2.2 – Illustration of the focused ultrasound. The rarefactional pressure map shown in the XY-plane and XZ-plane demonstrates the ellipsoidal focus of the FUS transducer used for BBB opening in this dissertation. 10

Figure 2.3 – Illustration of a microbubble composition, modified from Sirsi et. al.[34] 11

Figure 2.4 – Physiological transport across the BBB[95]. The main routes for molecular traffic across the BBB are (a) paracellular aqueous pathway, but restricted by the tight junction which is mainly established by the transmembrane proteins (claudins and occludin), linked to cytoskeletal actin through ZO-1; (b) the lipid membranes of the endothelium offers an effective diffusive route for lipid-soluble agents; (c) transport proteins for glucose, amino acids, purine bases, nucleosides, and choline; (d,e) receptor- or adsorptive-mediated endocytosis. Modified from Abbott et al.[95] and Chou et. al.[101] 23

Figure 2.5 – Schematic diagram illustrating the microbubble behavior and cavitation types. A microbubble decreases in size during the compressional phase, and expands during the rarefactional phase. Low-intensity ultrasound induces a stable oscillation of a microbubble in the capillaries, named as stable cavitation where the harmonics (red arrows) and ultra-harmonics (black arrows) are generated. However, at higher intensities, the microbubble grows rapidly for a few cycles. Very soon, the inertial energy of the fluid surrounding the microbubble during the compression forcibly collapses the microbubble, generating fluid jet or shock waves, along with broadband response (red curve). 26

Figure 3.1 – Block diagrams of the experimental setup. The PCD was positioned at a (a) 60^o and (b) 90^o relative to the longitudinal axis of the FUS beam. The space between

latex membrane and phantom was degassed water, and the big water tank was not shown on this figure. The overlap between the focal region of PCD and FUS was also illustrated in the insets. The cylindrical region was the focal region of PCD and the cigar-shaped region was the focal region of FUS. The water tank, in which the phantom was immersed, is not shown for clarity purposes......................................31

Figure 3.2 – The channel phantom below the *ex vivo* mouse skull was localized using raster scan with the pulse-echo transducer as shown. (a) The first raster scan was used to find the position of the vessel while (b) the second raster scan of the RF signal amplitude was used to find the position of the left parietal bone, where in previous studies was the acoustic window through which to sonicate to target the left-hippocampus region (cross symbol). The white bar indicates the grid which was yellow shown in (b). [Image of the mouse skull available at http://www.digimorph.org.] 33

Figure 3.3 – Block diagram of the experimental setup. The PCD was positioned at a (a) 60^o and (b) 90^o relative to the longitudinal axis of the FUS beam. The space between latex membrane and phantom was degassed water, and the big water tank was not shown on this figure. The overlap between the focal region of PCD and FUS was also illustrated in the insets. The cylindrical region was the focal region of PCD and the cigar-shaped region was the focal region of FUS. The water tank, in which the phantom was immersed, is not shown for clarity purposes......................................37

Figure 3.4 – Illustration of the inertial cavitation dose (ICD) calculation of the *in vivo* experiments. (a) The spectrogram of the first pulse from 0.02 to 0.15 ms after a 4 MHz high-pass filter (chebshev type 1) at 0.60 MPa. The harmonics and the broadband response could be observed in this figure. The corresponding V_{RMS} was depicted in (b) and the ICD was obtained using the integral of V_{RMS} curve between two dash lines. 42

Figure 3.5 – Frequency response of the first pulse (a,c) through no skull and (b,d) through an *ex vivo* skull at 5 distinct acoustic pressures. Acoustic emissions were collected with a PCD positioned at (a,b) 60º and (c,d) 90º from the longitudinal axis of the

FUS beam. Broadband acoustic emissions were detected at and higher than 0.45 MPa. 44

Figure 3.6 – Spectrogram of the first pulse in the phantom study without and with the microbubbles at 5 distinct acoustic pressures. Acoustic emissions were acquired with a PCD positioned at 60º and 90º from the longitudinal axis of the FUS beam. No broadband acoustic emissions were detected without the microbubbles while with the microbubbles the broadband acoustic emissions were detected at pressure at or higher than 0.45 MPa. At 0.30 MPa, the ultra-harmonics were detected at the 90º-PCD but not the 60º-PCD. 45

Figure 3.7 – The spectrogram (a,c) without the skull and (b,d) through an *ex vivo* skull at five distinct acoustic pressures. The duration of each sonication was 2 s, i.e., 20 pulses. Please note that the broadband acoustic emissions could only be detected at the first two pulses at 0.45 MPa in (b) and their amplitudes were much lower than at higher pressures. 46

Figure 3.8 – (a) Root mean square (V_{RMS}) and (b) ICD at 5 distinct acoustic pressures are indicated here. In order to emphasize the difference between 5 distinct acoustic pressures, the limit of the y-axis is from 0 to 0.5 at 60º-PCD, with the presence of skull. ICD was quantified as the area below V_{RMS} curve, at each pressure. Twenty pulses were applied for each sonication set. The ICD at 0.45 MPa was significantly larger than 0.30 MPa (*:$P < 0.05$, indicates the threshold of inertial cavitation).....47

Figure 3.9 – B-mode imaging provided a means of determining whether the microbubbles were present following sonication. Images were acquired after 2 seconds of sonication at 5 distinct acoustic pressures in skull and non-skull experiments........48

Figure 3.10 – (a) The illustration of ROI and (b) the correlation between ICD and the intensity decrease ratio of B-mode imaging at 5 distinct acoustic pressures (0.30, 0.45, 0.60, 0.75 and 0.90 MPa). The intensity decrease ratio at 0.45 MPa was significantly larger than 0.30 MPa (*: $P < 0.05$) 49

Figure 3.11 – BBB opening using confirmed by 3D-MRI images, using (a) System-A and (c) System-B. The corresponding spectrograms of the first pulse using (b) System-

A and (d) System-B showed that the broadband acoustic emissions were detected at 0.45 MPa and 0.60 MPa but not at 0.15 MPa and 0.30 MPa. The 3D-MR images confirmed that the BBB could open at 0.30 MPa, i.e., without inertial cavitation...51

Figure 3.12 – The inertial cavitation dose (ICD) at 4 distinct acoustic pressures (a) using the System-A and (b) using the System-B. ICD was quantified as the area under the V_{RMS} curve from 0.095 ms to 0.145 ms, at each pressure. The signal used for quantification was from a focused hydrophone. For the System-A, the ICD at 0.45 MPa and 0.60 MPa was significantly higher than 0.15 MPa and 0.30 MPa (*: $P <$ 0.05). For the System-B, the ICD at 0.60 MPa was significantly higher than at 0.30 MPa and 0.15 MPa. The ICD at 0.45 MPa was also significantly higher than 0.15 MPa (*: $P < 0.05$). 52

Figure 3.13 – 2D-MRI images and H&E-stained horizontal sections of the BBB-opened hippocampi at (a-c) 0.15 MPa, (d-f) 0.30 MPa, (g-i) 0.45 MPa, and (j-l) 0.60 MPa using the System-A with microbubbles administration. Sonicated brains at 0.15 MPa, 0.30 MPa and 0.45 MPa showed no histological damage. Brain samples sonicated at 0.60 MPa (j-l) showed higher incidence of microscopic damage at multiple distinct damaged sites. Black arrows point to the RBC extravasations. Black boxes in the left and middle column indicate the enlarged regions shown in the middle column and right column, respectively. Magnifications and scale bars in (a,d, g, j) were 40x and 200 μm, in (b, e, h, k) 100x and 100 μm, and in (c, f, I, l) 200x and 50 μm, respectively. 53

Figure 3.14 – 2D-MR images and H&E-stained horizontal sections of the BBB-opened hippocampi at (a-c) 0.15 MPa, (d-f) 0.30 MPa, (g-i) 0.45 MPa, and (j-l) 0.60 MPa using the System-B with microbubbles administration. Sonicated brains at 0.15 MPa, 0.30 MPa and 0.45 MPa showed no histological damage. Minor microscopic damage was noticeable in one location of the right hippocampus sonicated 0.60 MPa, constituting one distinct damaged site (g-i). Black arrows point to RBC extravasations. Black boxes inside the left and middle column showed enlarged regions in the middle and right columns, respectively. Magnifications and scale bars

in (a,d, g, j) were 40x and 200 μm, in (b, e, h, k) 100x and 100 μm, and in (c, f, I, l) 200x and 50 μm, respectively. 54

Figure 3.15 – Comparison between (a) water and (b) bubble experiments without skull for spectrogram from 90º-PCD at 0.90 MPa. Broadband acoustic emissions and the amplitude of the 3rd to 6th harmonics were not obtained in the water experiments..57

Figure 4.1 – The graphical user interface of bubblesim used to specify bubble, pulse and calculation parameters. 70

Figure 4.2 – The illustration of dynamic surface tension of a lipid-coated bubble as presented by Marmottant et al.[139] 72

Figure 4.3 – The size distribution of the Definity® microbubbles (a) according to the number concentration and (b) volume fraction was characterized. This indicated that the size distribution of Definity® microbubbles was not well centralized.........73

Figure 4.4 – Size distributions of 3 mono-dispersed microbubbles are depicted as number-weighted percent of the total concentration of bubbles and volume-weighted percent of the total volume of bubbles. Before *in vivo* experiment, the distribution is centralized at 1-2 μm, 4-5 μm, and 6-8 μm (solid black). Distribution analysis is performed again at the same day, after *in vivo* experiments (dashed red), depicting small decrease at the peaks..74

Figure 4.5 – Experimental timeline for each study in this chapter......................................76

Figure 4.6 – The BBB opening with 3 bubble diameters confirmed by 3D-MRI images with coronal (top left), sagittal (top right), and horizontal (middle left) views. The corresponding spectrogram (middle right) of the first pulse from 95 to 135 μs with microbubbles administration shows the acoustic response from microbubbles. The corresponding H&E sections (40x magnifications, bottom left) and permeability maps (bottom right) are also provided. In the case of 1-2 μm bubbles, the broadband acoustic emissions are detected at 0.45 and 0.60 MPa but not at 0.15 and 0.3 MPa. The 3D-MR images confirmed that the BBB is opened at 0.45 and 0.60 MPa, with inertial cavitation. In the case of 4-5 and 6-8 μm bubbles, the broadband acoustic emissions are detected at 0.45 and 0.60 MPa but not at 0.15 and 0.3 MPa.

The 3D-MR images confirmed that the BBB is opened at 0.30 MPa without inertial cavitation or 0.45 MPa and 0.60 MPa with inertial cavitation. In each H&E image, its center indicated the focus as viewed on the MRI. No damage was detected in any of these cases (see Fig. 4.11 for cases with damage). 81

Figure 4.7 – Statistical analysis of the stable cavitation dose (SCD) at the ultra-harmonics 3.75 MHz (2.5f), 5.25 MHz (3.5f), 6.75 MHz (4.5f), 8.25 MHz (5.5f), 9.75 MHz (6.5f), and 11.25 MHz (7.5f) against three distinct pressures at three microbubble diameters. The SCD at the 6-8-μm diameter was significantly higher than at the 1-2-μm diameter (*: $P < 0.05$, compared to 1-2-μm diameter) in most cases, and at the 4-5-μm diameter in two cases (#: $P < 0.05$, compared to 4-5-μm diameter). At 0.30 MPa, i.e., no inertial cavitation occurrence, the SCD at the 4-5-μm or 6-8-μm diameter was significantly higher than at the 1-2-μm diameter in 7 cases, which provides the evidence that the BBB is opened via the stable cavitation..................82

Figure 4.8 – The quantification of (a) the inertial cavitation dose (ICD), (b) BBB opening volume and (c) the correlation in between. Statistical analysis indicates that the ICDs and BBB opening volume are both pressure and bubble-size dependent. [*: $P < 0.05$, compared to 1-2-μm diameter, #: $P < 0.05$, compared to 4-5-μm diameter]. Regression analysis shows a linear correlation between the ICD and the BBB opening volume with three bubble diameters. It also shows that inertial cavitation is necessary for 1-2 μm bubbles to induce BBB opening. The intercept indicates that the BBB can be opened without inertial cavitation in the case of 4-5 and 6-8-μm diameter bubbles...83

Figure 4.9 – Mean quantitative K_{trans} measurements. The results are presented in two different ways in order to demonstrate the dependence of the BBB opening K_{trans} on both the acoustic pressure and the microbubble size. The mean K_{trans} in the epicranial muscle (no barrier) is also presented for comparison. One asterisk (*) refers to a statistical significance of $P < 0.05$ and two asterisks (**) refer to a statistical significance of $P<0.01$. 85

Figure 4.10 – Histology at the BBB opening threshold. The mouse was sacrificed either 3 hrs or 7 days after sonication. In both cases, no red blood cell extravasations and

dark neurons were found with H&E staining, which means that safe BBB opening can be achieved at adequate pressure with all bubble diameters. 85

Figure 4.11 – Permeability and histological findings of the only three mice that exhibited neuronal damage and cell loss. (a) T1 image, (b) corresponding permeability map and (c-h) H&E sections of the first mouse, sonicated at 0.45 MPa using 4-5 μm bubbles. (i) T1 image, (j) corresponding permeability map and (k-p) H&E sections of the second mouse, sonicated at 0.60 MPa using 4-5 μm bubbles. (q) T1 image, (r) corresponding permeability map and (s-x) H&E sections of the third mouse, sonicated at 0.60 MPa using 6-8 μm bubbles. The black boxes in (c, f, k, n, s, v) refer to the regions of interest depicted in (d, g, l, o, t, w), respectively. The black boxes in (d, g, l, o, t, w) refer to the regions of interest depicted in (e, h, m, p, u, x), respectively. 87

Figure 4.12 – Transverse T2 images of the brain from each mouse cohort. Dark areas in the sonicated regions (indicated by white arrows) were detected at higher pressures for the larger bubbles as a result of susceptibility artifacts from the excessive Gd-DTPA presence in the extravascular extracellular space. 88

Figure 4.13 – The frequency spectrum and ICD of the 1-2-μm diameter bubbles. The IC threshold is determined to lie between 0.30 and 0.35 MPa (***: *$P < 0.001$)*. The SC does not occur between 0.15 and 0.35 MPa. 90

Figure 4.14 – The frequency spectrum and ICD of the 4-5-μm diameter bubbles. The IC threshold is determined to lie between 0.30 and 0.35 MPa (**: *$P<0.01$*), but the SC occurs at 0.30 MPa. 90

Figure 4.15 – The frequency spectrum and ICD of the 6-8-μm diameter bubbles. The IC threshold is determined to lie between 0.35 and 0.40 MPa (***: *$P<0.001$*), but the SC occurs at 0.30 MPa. 91

Figure 4.16 – Simulation of the oscillation of a 1.5 μm diameter bubble at 0.20 MPa PRP using Bubblesim (unshelled, shelled), and Marmottant model. The "compress-only" behavior of a lipid shelled microbubble is observed here. 91

Figure 4.17 – The 2D horizontal T1-weighted MR image (top left), corresponding spectrogram of the first pulse (top right), 2D horizontal permeability map (bottom left), and H&E sections of the hippocampus (bottom right) in each table entry at 3 bubble diameters and 3 peak-rarefactional pressures. Few histological damage cases were noted and shown here (black arrow: dark neuron, red arrow: red blood cell extravasations) were observed with inertial cavitation occurrence (see Table 3 for summary of damage cases). 93

Figure 4.18 – Transverse T2 images of the brain from each mouse cohort. Dark areas in the sonicated regions (indicated by white arrows) were detected at all pressures for the C24 bubbles, which indicated that C24 may not be an appropriate shell material for BBB opening application. 94

Figure 4.19 – Statistical analysis of the stable cavitation dose (SCD) at the ultra-harmonics 3.75 MHz (2.5f), 5.25 MHz (3.5f), 6.75 MHz (4.5f), 8.25 MHz (5.5f), 9.75 MHz (6.5f), and 11.25 MHz (7.5f) with three acyl-chain lengths at three distinct pressures. No significant difference was observed across the different acyl-chain lengths in most cases. However, at 9.75 MHz and 11.25 MHz, the SCD of the C16 microbubbles was significantly higher than the C24 microbubbles (*: $P < 0.05$). Since the center frequency of the PCD is 10 MHz, the sensitivity may be higher when the ultra-harmonic is close the 10 MHz. At 0.30 MPa, i.e., no inertial cavitation occurrence, the SCD was statistically higher than the background noise, which indicated that the BBB was opened through stable cavitation. 95

Figure 4.20 – Statistical analysis of the (a) inertial cavitation dose (ICD), (b) BBB opening volume, and (c) permeability between three acyl-chain lengths at three distinct pressures. The ICD of C24 microbubbles was significantly lower than the C16 and C18 microbubbles at 0.60 MPa (*: $P < 0.05$). In the rest cases, however, no statistically difference was observed. 96

Figure 4.21 – Comparison between (a) sagittal section of 3D-T1-MR images and (b) -6dB focal region of the FUS transducer in the case of 6-8 μm bubbles at 0.30 MPa. The consistence between the contrast enhancement region and focal region of the FUS transducer indicates that IC is not necessary to induce BBB opening. 98

Figure 5.1 – The 2D T1-weighted MR image of each acoustic parameter set shown in Table 1. At 5-Hz PRF, sonications were (a-d) at PLs of 0.1, 0.5, 2, and 5 ms at 300-s duration, or (e) at 20-ms PL and 30-s duration. In addition, identical duty cycle as set (c), sonication was at (f) 0.1-ms PL and 100-Hz PRF. The BBB was not opened in protocol (a) and (f), but was opened in protocol (b-e). Histological analysis (g-i) showed that no red blood cell extravasations were observed in protocol (d), i.e., the longest exposure time. The magnification in (g), (h), and (i) are 40x, 100x, and 200x, respectively. 117

Figure 5.2 – Statistical analysis of the BBB opening volume and normalized MR intensity on the effects of (a) 4 different PLs, and (b) exposure time. 118

Figure 5.3 – The 2D T1-weighted MR image of IC-induced BBB opening sonicated at PRFs of (a) 5 kHz, (b) 25 kHz, and (c) 100 kHz. The BBB opening volume, normalized MRI contrast enhancement, and inertial cavitation dose of 3 PRFs were measured (d). No significant difference was observed between all cases in terms of volume and intensity. The ICD of 100 kHz was significantly higher than the other cases. 119

Figure 5.4 – Fluorescence images and the corresponding frequency spectrum in the case of (a,b,e,f) SC- and (c,d,g,h) IC-induced BBB opening. The right hippocampus (b,d,f,h) was sonicated in the presence of microbubbles and fluorescently tagged 3-kDa dextran, whereas the left side was the control (a,c,e,g). The dextran molecules were restricted in the vessel in the case of SC-induced BBB opening (b), together with the occurrence of harmonics, while they were diffused to the hippocampus in the case of IC-induced BBB opening (d), together with the broadband response. The scale bar depicts 1 mm. 120

Figure 5.5 – Immunofluorescence staining in the cases of (a-d) SC- and (e-h) IC-induced BBB opening. The ZO-1 expression was indicated in green. No significant difference can be observed between the left (a,c,e,g) and the right (b,d,f,h) hippocampus, in both SC- and IC-induced BBB opening. 121

Figure 5.6 – Simulation of the oscillation of a 4.5-μm-diameter bubble at PRPs of 0.18 MPa and 0.15 MPa using Bubblesim. The shell viscosity was 0.19 Pa.s and the shear modulus was 32 MPa. The maximum diameter lies in 8-10 μm at 0.18 MPa, but in 5-7 μm at 0.15 MPa. 124

Figure 6.1 – Experimental setup for *in vivo* FUS-induced BBB opening in the operating room. (a) A single-element, circular focused ultrasound transducer with a hole in the center was driven by a function generator (Agilent Technologies, Palo Alto, CA, USA) through a 50-dB power amplifier (ENI Inc., Rochester, NY, USA). The center frequency, focal depth, outer radius and inner radius of FUS were 500 kHz, 90 mm, 30 mm and 11.2 mm, respectively. (b) *In vivo* of the transducer mounted on the stereotactic frame with a manipulator allowing precise positioning of the transducer in the stereotactic referential. (c) Monkey placed in the stereotactic frame. The monkey is shaved and a degassed echographic gel container is placed on the top of its head to insure maximal acoustic transmission. 131

Figure 6.2 – Targeting procedure for *in vivo* FUS-induced BBB opening. (a) A positioning rod (black arrow), indicating the position of the focus (5 cm away from the edge of the transducer), was used to target. (b) This positioning rod was mounted on the manipulator in order to locate the origin of the stereotactic coordinates. (c) The origin of the stereotactic coordinates indicated by the engraved cross on the metal piece between the ear-bars is targeted with the tip of the positioning rod............. 132

Figure 6.3 – Targeting region and corresponding view from three dimensional views, adapted from a web-based brain atlas[168]. 132

Figure 6.4 – Experimental timeline of *in vivo* BBB opening in NHPs. Two targets at 0.30 MPa (purple circle) and 0.45 MPa (orange circle) are also illustrated. 133

Figure 6.5 – (a) The spectrogram without microbubbles administration show that all the harmonics and broadband response are from microbubbles. Spectrograms during FUS sonication with monkey 2 at (b) 0.20 MPa, (c) 0.25 MPa, (d) 0.30 MPa, and MR images with (e) coronal and (f) sagittal planes show that the broadband response occur with all pressures, but no BBB opening is induced (dashed circle).136

Figure 6.6 – (a) The spectrogram without microbubbles administration show that all the harmonics and broadband response are from microbubbles. The spectrogram during FUS sonication with monkey (b) 0.45 MPa shows that the broadband response takes place. The MR image with (c) sagittal plane, however, shows that no BBB opening is induced (dashed circle). 136

Figure 6.7 – The BBB opening confirmed by 3D-MRI images. No higher harmonics and broadband response are present at 0.30 MPa in (a) the spectrogram without microbubbles administration. The corresponding spectrogram of the first pulse with microbubbles administration shows that the broadband acoustic emissions are detected at (b) 0.30 MPa and (c) 0.45 MPa. The 3D-MR images confirm that the BBB is opened at (d, e, g) 0.30 MPa and (f, h) 0.45 MPa with inertial cavitation. The yellow box in the sagittal plane in (d) defines a region of interest from which images in (e) and (f) were acquired. The coronal plane with BBB opening is provided at (g) 0.30 MPa and (h) 0.45 MPa. The white arrow in (c) indicates that the time-point of occurrence of the second harmonic coincides with the travel distance to the skull. 137

Figure 6.8 – Damage assessment. (a,c,d) 3D T2-weighted sequence. Edemas should appear brighter in these images. (b,e,f) 3D Susceptibility-Weighted Image (SWI) sequence was applied. Hemorrhages, as well as large vessels should appear in black in these images. (a,b) Same reconstructed coronal slice as shown in Fig. 6.7. The two opening sites are circled with the corresponding colors. There is no difference between the two hemispheres. (c,d,e,f) Corresponding reconstructed sagittal slices for the two opening sites. No edemas or hemorrhages are visible in the sonicated regions (dashed contour). 138

Figure 6.9 – BBB opening experiment targeting hippocampus using Definity® microbubbles and applying 0.6 MPa (yellow dashed line shows region of interest). 3D Spoiled Gradient-Echo (SPGR) T1-weighted sequence was applied after intravenous (IV) injection of gadodiamide 1 h after sonication. No damage was detected using Definity® microbubbles from T2-weighted sequence. 139

Figure 6.10 – BBB opening experiment targeting hippocampus using custimized microbubbles and applying 0.6 MPa (yellow dashed line shows region of interest). 3D Spoiled Gradient-Echo (SPGR) T1-weighted sequence was applied after intravenous (IV) injection of gadodiamide 1 h after sonication. An edema was visible using Definity® microbubbles from T2-weighted sequence. 140

Figure 6.11 – The correlation between the ICD and the BBB opening volume at 0.30 and 0.45 MPa at 4-5-μm diameter bubbles (a total of 11 openings). The volume at 0.60 MPa is not shown because only one big opening is induced by 4 sonications (Fig. 6.10). 141

Figure 6.12 – The region dependent SCD at 0.30 and 0.45 MPa. The amplitude level is putamen > caudate > visual cortex at 0.30 MPa, as well as visual cortex > caudate > hippocampus at 0.45 MPa. 141

Figure 6.13 – An example of BBB closing in the NHP caudate using 0.30 MPa and 4-5-μm microbubbles. The blue region indicates the opening region and it is no longer visible in day 4. The corresponding quantification of BBB opening volume indicates that the BBB is nearly closed on day 2. The error bar denotes the stander deviation of the MR intensity of the BBB opening area. 142

Figure 6.14 – The discrepancy between focal region (yellow area) and BBB opening region (blue area) at the caudate at 0.30 MPa. Corresponding spectrogram shows the cavitation response along 2 min duration. 143

Figure 6.15 – The discrepancy between the focal region (yellow area) and the BBB opening region (blue area) at the visual cortex at 0.45 MPa. Corresponding spectrogram shows the cavitation response along 2 min duration.........................144

Figure 6.16 – Three spectrograms of the cavitation response. (a) The spectrogram of all pulses provides the information about the microbubble persistence and the duration for them to reach the brain after the IV-injection. (b) The spectrogram of one pulse (red line in (a)) indicates the duration of inertial cavitation. (c) The actual location of the focus may be determined by the first 0.4 ms of one pulse, i.e., the red square in (b). 148

Figure 7.1 – Safety windows in terms of peak rarefactional pressure and microbubble types in mice. The safest window (green rectangular), in the absence of inertial cavitation (IC) and damage, lies between 0.15 and 0.30 MPa using 4-5- or 6-8-μm diameter bubbles, as well as between 0.30 and 0.45 MPa using Definity®. Another safety window, in the absence of damage with the IC occurrence (orange rectangular), lies between 0.30 and 0.45 MPa using 1-2-μm diameter bubbles or Definity®. However, the pressure threshold of the damage occurrence at 1-2-μm diameter bubbles has not been determined. 152

Figure A.1 – The arterial input function, averaged from a population of all 40 mice, by measuring the Gd-DTPA concentration in the internal carotid artery on the dynamic images. 180

Figure B.1 – Targeting images for monkey and human skulls based on combined reflectivity and time-of-flight measurements. Anatomical landmarks are clearly identified such as the occipital protuberance or lambda. 184

Figure B.2 – Examples of -6 dB pressure profiles obtained through a NHP skull for the four different orientations. Blue dashed lines represent the contour of the target (as indicated in the depicted plane. 187

Figure B.3 – Examples of -6 dB pressure profiles obtained through a human skull for the four different orientations. Blue dashed lines represent the contour of the target as indicated in the depicted plane. 188

Figure B.4 – Focusing performance assessment through human and NHP skulls. Attenuation represents the energy loss crossing the skull interface compared to that of the water. Tilt represents the angle between the axial dimension of the focus and the geometric axis of propagation. Lateral resolution and axial resolution represents the dimension of the focus (-6 dB cutoff). Lateral and axial shift represents the displacement of the center of the focus. 190

Glossary

AD	Alzheimer's disease
BBB	Blood-brain barrier
BDNF	Brain-derived neurotrophic factor
BRF	Burst repetition frequency
CNS	Central nervous system
DCE-MRI	Dynamic contrast enhanced-MRI
EB	Evans blue
FUS	Focused ultrasound
HIFU	High-intensity focused ultrasound
IC	Inertial cavitation
ICD	Inertial cavitation dose
IP	Intraperitoneal
IV	Intravenous
MI	Mechanical index
NHP	Non-human primates
P/E	Pulse Echo
PCD	Passive cavitation detector
PEG	Polyethylene glycol
PL	Pulse length
PRF	Pulse repetition frequency
PRP	Peak rarefacional pressure
RBC	Red blood cell
RMS	Root mean square
SC	Stable cavitation
SCD	Stable cavitation dose
SWI	Susceptibility-weighted imaging
TJ	Tight junction

Acknowledgments

It has been ten years since I started entering the field of therapeutic ultrasound. It was very tough for a person who has a background in “Business Administration” to pursuit his doctoral degree in Biomedical Engineering. Finally, this fantastic journey is close to its destination, combined with sweet memories. At this moment, I must express my deep gratitude to many people because I could not finish this dissertation without their contribution.

Of course, the most important one is my advisor, Dr. Elisa E. Konofagou, a smart, humor, energetic, and optimistic person. In the last five years, I had a really unforgettable experience with her. Her guidance keeps me on the correct track for my degree. Having a discussion with her makes me have full of energy to be productive for my research. Thanks for her encouragement, people in our lab are able to attend conferences annually and publish journal papers regularly. I really appreciate her guidance in different aspects, including inspiration, education, and communication, etc… Most importantly, I could not have a wonderful life in New York without her founding support!

Thanks to my dissertation committee, Dr. Mark Borden, Dr. Truman Brown, Dr. Barclay Morrison, III, and Dr. Paul Sajda, for their knowledge and wisdom for my dissertation. Especially thanks Dr. Mark Borden and his student Jameel Feshitan for their support on the mono-dispersed microbubbles which contribute on my studies about the role of microbubbles and cavitation dependent tight-junction integrity. Moreover, their microbubbles enable us to induce BBB opening in monkeys with 100% probability!

It is my pleasure to be able to join this BBB group in Ultrasound and Elasticity Imaging Laboratory (UEIL). We have many excellent scientists, including Dr. James Choi, Dr. Shougang Wang, Dr. Thomas Deffieux, Dr. Fotios Vlachos, Dr. Fabrice Marquet, Dr. Cherry Chen, Dr. Shoutao Wang, Babak Baseri, Kirsten Selert, Oluyemi Olumolade, Gesthimani Samiotaki, Matthew Downs, and Shih-Ying Wu. Several interns also contributed to this dissertation and the BBB group: Julio Herrera Estrada, Jennifer Hui and Jennifer Hui. I would also like to thank the rest of the UEIL for their comments on my presentation for the conference: Dr. Jianwen Luo, Dr. Jonathan Vappou, Dr.Sacha Nadlall, Dr. Danial Shahmirzadi, Dr. Jiangang Chen, Dr. Julien Grondin, Jean Provost, Gary Hou, Stanley Okrasinski, Ronny Li, Ethan Bunting, and Alexandre Costet.

Special thanks for our collaborators, Vincent Ferrara and Tobias Teicher,. in the Department of Neuroscience. The BBB opening in monkeys would not be achieved without their contribution! I would also like to thank Kenneh Hess, Fan Hua, Stephen Dashnaw, and Dr. Shashank Sirsi for assistance and training with experimental instruments. My work would not have been finished without their help.

I owe this accomplishment to Dr. Wen-Shiang Chen form the National Taiwan University. I would not have the chance to be here, Columbia University, without his guidance. As a Taiwanese, I really appreciated Wei-Ning Lee’s help for her kindness in guiding me in this lab. I was grateful to have support from: Chien-Huan Lai, Chen-Bang Chen, Chih-Chien Su, Chih-Chao Chen, Wei-Hsuan Dai, Andy Lin, Lo Kuan, Chin-Han Chiang, and Chang-Chih Lin.

Finally, I would love to thank my family for their endless love and selfless support, especially to my Dad in the heaven.

Chapter 1

Introduction

1.1 Motivation

Most neurological disorders and neurodegenerative diseases, such as Alzheimer's disease (AD), Parkinson's disease (PD), multiple sclerosis (MS) and amyotrophic lateral sclerosis (ALS), remain difficult to treat. To date, only 5% of the more than 7000 small-molecule drugs available can currently treat Central Nervous System (CNS) diseases because of the impermeability of the blood-brain barrier (BBB)[1]. The BBB is a specialized structure found between the capillary lumen and the brain parenchyma that only allows passive diffusion of lipid-soluble molecules with a molecular weight smaller than 400 Da[2]. Distinct from the general capillaries, the BBB consists of the tight junctions (TJs) between endothelial cells in CNS capillaries that restrict the passage of solutes. As a result, pharmacological agents cannot reach their desired targets, thus rendering therapeutically potent drugs clinically ineffective. Mechanical stress induced by the activation of microbubbles in an acoustic field is currently the only noninvasive approach to temporarily induce localized BBB opening, without damaging the surrounding tissues[3]. Since 2001 when the first microbubble-enhanced BBB opening using focused ultrasound (FUS) was reported, numerous reports have been published on the methodology and application. Our group has also recently achieved the delivery of therapeutic compounds, i.e., the Brain-Derived Neurotrophic Factor (BDNF) and neurturin (NTN), to the murine hippocampus[4]. The physical mechanism behind this approach, however, is still not entirely known.

In order to achieve the goal of developing a FUS technique that will allow pharmacological agents to cross the BBB under well controlled and safe conditions, it is necessary to have a very clear understanding of the mechanisms and determination of the endpoints in order to identify a safety window for FUS brain drug delivery. Although there are many indications as to the various mechanisms involved such as the dilation of vessels, temporary ischemia, mechanically induced opening of the tight junctions, and the activation of various transport mechanisms have been reported[5-7], the trigger cause induced by the microbubbles, however, is unclear. Therefore, the primary objective of this dissertation is to reveal the physical mechanism (i.e., bubble behavior of trigger cause) of BBB opening using a novel device in phantoms and *in vivo*. Meanwhile, theoretical models are applied to predict the type of oscillation of the acoustically-driven microbubbles. Once the physical mechanism is identified, a secondary objective entails the translation of the BBB opening system to non-human primates to verify the feasibility and mechanism in large animals.

1.2 Overview and significance

Acoustic cavitation, which refers to acoustically driven bubble activity, is considered to be the main cause of BBB opening since it does not occur without injecting preformed microbubbles at a given acoustic setting. At low acoustic pressures, acoustically driven bubble oscillations were shown to increase the permeability of surrounding cell membranes[8]. At high acoustic pressures, inertial cavitation, i.e., the collapse of bubbles, releases high energy and may generate high temperatures, high pressures, and high velocity jets that may damage the surrounding structures[9]. Therefore, knowing the pressure threshold for inducing inertial cavitation is important for controlling the potential side-effects. As of now, possible physical mechanisms for BBB opening via FUS and microbubbles include inertial cavitation, which may induce pores on the membrane of endothelial cells in the brain[9,10], and stable cavitation, bubble oscillation and microstreaming surrounding the microbubbles that may induce shear stress or repeated stretch affecting the tight junctions or the permeability of the endothelial cells[11].

Until recently the interaction among the microbubbles, the FUS beam, and the brain capillaries have not been thoroughly investigated. Imaging techniques, such as magnetic resonance imaging (MRI) and fluorescence imaging, have been used to confirm the FUS-induced BBB opening. In order to study the physical effects responsible for BBB opening, a passive cavitation detector (PCD) can be used to acquire the acoustic response stemming from the microbubble and tissue, thereby monitoring the bubble behavior during BBB opening. In addition, assessing the bubble behavior is necessary for establishing a well-controlled safety window during BBB opening. Since inertial cavitation may cause damage to the vessel structure surrounding the microbubbles, it should be prevented for FUS-induced BBB opening. Therefore, in order to determine the cavitation type during BBB opening, an *in vivo* transcranial PCD system was designed and built. The PCD system provides an alternative way to monitor the target and estimate the volume of BBB opening. Since the BBB opening is dependent on the microbubble size and the acoustic parameters[12], we hypothesize that the physical effect responsible for BBB opening can be unveiled by changing the microbubble properties and acoustic parameters based on our *in vivo* transcranial PCD system. The optimal parameters can thereby be determined for a safe and efficient BBB opening. The feasibility of BBB opening in non-human primates is also investigated for the future clinical treatment of neurodegenerative diseases with the proposed technology.

Furthermore, cavitation effects have been reported in several therapeutic ultrasound applications, including sonoporation[13], sonothrombolysis[14], gene transfection[15], high-intensity focused ultrasound (HIFU)[16], histotripsy[17], and lithotripsy[18], etc.. Since the bubble oscillation cannot be observed *in vivo*, an *in vivo* cavitation detection system may prove pivotal in determining the role of cavitation in different fields. As a result, the development of an *in vivo* cavitation detection system will have high medical significance.

This dissertation is structured as follows. First, the basics of the blood-brain barrier physiology and current brain drug delivery methods are summarized. Second, the basics behind FUS and microbubbles, as well as previous studies on the FUS-induced BBB opening including optimization, delivery of therapeutic compounds, safety assessment and the possible mechanism, will be described in *Chapter 2*. In order to reveal the physical mechanism of the FUS-induced BBB opening, the method of a transcranial PCD system during BBB opening is described (*Chapter 3*). This system offers the possibility to study the physical mechanism by adjusting the microbubble design and carefully selecting the acoustic parameters. The permeability measurement and safety inspection will be implemented in order to study the mechanism associated with distinct microbubble diameters and shell materials (*Chapter 4*). The theoretical model of bubble behavior will also be implemented with a vessel phantom validation (*Chapter 4*). After describing the role of microbubbles in the BBB opening mechanism, the connection between the physical and physiological mechanisms will be investigated to provide insight into the physiological response to the microbubble activity during BBB opening (*Chapter 5*). Finally, an *in vivo* transcranial cavitation system in monkeys will be described in order to achieve real-time cavitation-guided BBB opening in non-human primates (*Chapter 6*). The main conclusions are finally summarized and future work is discussed (*Chapter 7*).

Chapter 2

Noninvasive and Localized Blood-Brain Barrier Opening Using Focused Ultrasound and Microbubbles

2.1 Introduction

Identification of the physical mechanism of FUS-induced BBB opening requires a full understanding of the BBB physiology, focused ultrasound, and microbubbles. In this chapter, we will first provide basic concepts of the BBB physiology and summarize current brain drug delivery methods (section 2.2). The FUS, microbubbles, and previous reports on FUS-induced BBB opening will then be provided in detail in section 2.3. Finally, the different types of physiological and physical mechanisms will be introduced in section 2.4. In terms of physical mechanism, the types of cavitation and cavitation detection will also be summarized.

2.2 The Blood-Brain Barrier

The main limiting factor towards the development of novel treatments of neurological and neurodegenerative diseases is the blood-brain barrier (BBB): more than 98% of small-molecule drugs and nearly all large-molecule drugs do not cross this anatomic barrier[1,19]. The BBB is a complex regulatory system within the neurovascular unit, which controls the flow of nutrients and chemicals into and out of the brain parenchyma maintaining the brain homeostasis necessary for proper neuronal firing[20]. The BBB hinders the effective systemic delivery of neurological agents and biomarkers to the brain through a combination of passive, transport and metabolic barriers. Determining factors for the passage of molecules across the BBB are lipid solubility, charge and molecular size (threshold range spans between 50 Da and 400 Da)[2]. Therefore, potential therapeutic agents, such as growth factors[21,22], adenoviral gene therapy[23,24], inhibitors (100-1,000 Da) and proteins (30-3,000 kDa)[25,26], do not efficiently cross the BBB when administered systemically. Such delivery and efficacy are critical in inducing therapeutic effects and triggering biological pathways.

The difference between the general capillaries and the brain capillaries is depicted in Fig. 2.1. Most molecular traffic, which occurs via intercellular transport and pinocytosis in the general capillaries, is forced to take an intercellular route across the BBB through the tight junctions. Therefore, the BBB acts as a physical barrier impeding paracellular transfer through the junctions.

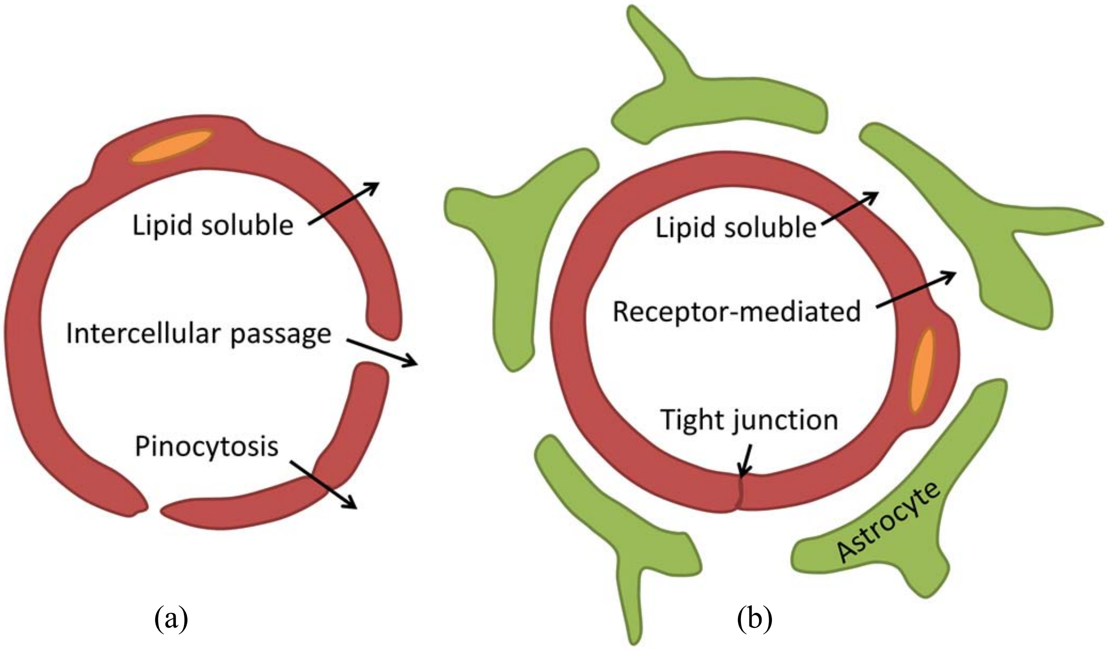

(a) (b)

Figure 2.1 – A schematic diagram of the major differences between (a) general capillaries and (b) brain capillaries. The endothelium of brain capillaries has the tight junction between the cells, as well as lacks intercellular clefts, fenestrations, and pinocytosis. This figure is modified from Churchland et al.[27]

Several techniques exist to circumvent the BBB, such as intracranial injections, mixing or attaching agents to BBB-modifying chemicals, and the chemical alteration of agents to be delivered through endogenous transport systems[1,20]. However, these techniques are either invasive, drug-specific or are plagued by very poor spatial specificity. Even the latest advances in brain gene therapy[28] provide cell specific drug delivery but not region specific. Global breaching of the BBB can be a risky process, as it increases influx of all molecules and therapeutic agents in untargeted areas of the brain[29] even if this approach has been proven to be successful for some applications such as metastatic lung cancer[30]. A controlled and safe opening of the BBB would enable the passage of pharmacological agents across the interstitial space that could enhance the neuronal activity in the aforementioned brain diseases, without causing permanent physiologic or anatomical damage. An ideal method would ensure drug-independent, reversible, localized and noninvasive delivery through the BBB to minimize potential hazards. Several methods currently available for opening the BBB are listed in Table 2.1. Except FUS, none of them can induce localized BBB opening noninvasively.

Table 2.1 Techniques shown to induce BBB opening and their advantages

Method	Noninvasive	Localized
Direct injection (e.g., intracerebral, intracerebroventricular)	☒	☑
Hyperosmotic solutions (e.g., mannitol)	☑	☒
Chemical modification of molecules (e.g., lipidization, endogenous transport systems)	☑	☒
Focused ultrasound and microbubbles	☑	☑

2.3 FUS-induced BBB opening

2.3.1 Focused ultrasound

"Ultrasound" defines the acoustic wave, with a frequency higher than the human audible frequency (> 20 kHz), generated from a transducer which converts the electrical stimulus into mechanical vibrations. Distinct from the conventional diagnostic ultrasound, a curved-shaped transducer is driven at frequencies between 200 kHz and 5 MHz to generate a high energy, compared with the intensity near the surface of the transducer, at the focus. The concept of FUS is illustrated in Fig. 2.2. Therefore, FUS can be used in the therapeutic applications which require localized and noninvasive treatment. Since the temperature at the focus can reach over 70°C, which leads to protein denaturation, at high acoustic pressures, this technique has been widely used in ablation of tumors[31-33]. This is most widely known as high-intensity focused ultrasound (HIFU). Compared with HIFU, however, the FUS in conjunction with microbubbles can induce BBB opening at relative low pressures (< 1 MPa). This approach is introduced in detail in section 2.3.3.

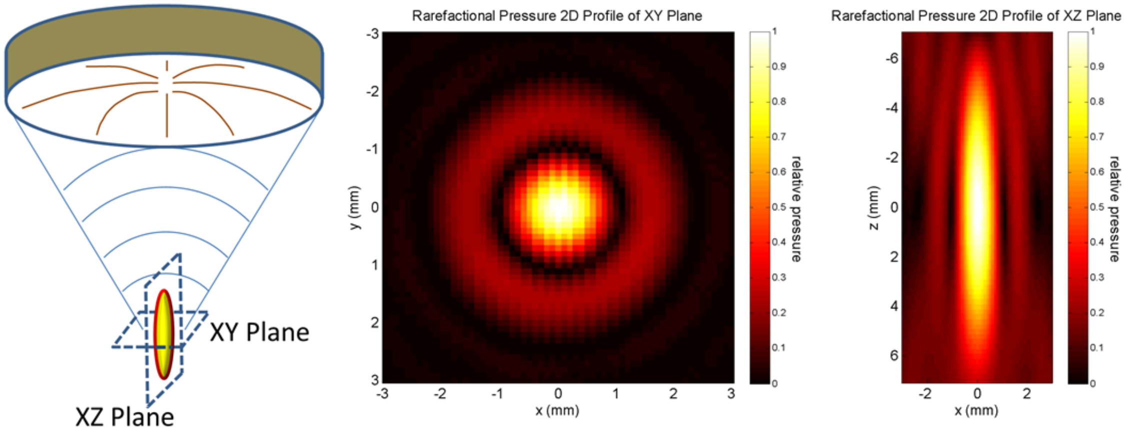

Figure 2.2 – Illustration of the focused ultrasound. The rarefactional pressure map shown in the XY-plane and XZ-plane demonstrates the ellipsoidal focus of the FUS transducer used for BBB opening in this dissertation.

2.3.2 Microbubbles

Microbubbles, also known as ultrasound contrast agents (UCA), are gas-filled bubbles. They are prevented from dissolving by a stabilizing shell. They are used in the clinic to help improve the ultrasound image contrast of blood vessels and blood cavities. In general, microbubbles have a typical size distribution centered around 3 to 4 μm in diameter. They are stabilized against dissolution by a coating that consists of a lipid, protein (albumin), or polymer shell. The basic illustration of a microbubble is depicted in Fig. 2.3. In general, the shell thickness of the lipid, protein, and polymer shell is around 3 nm, 15-20 nm, and 100-200 nm, respectively.

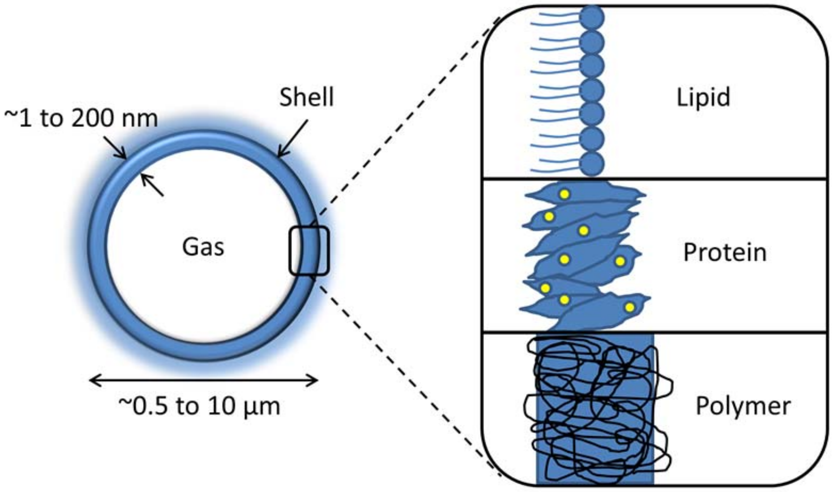

Figure 2.3 – Illustration of a microbubble composition, modified from Sirsi et. al.[34]

Besides initially used merely as the contrast agent for ultrasonic imaging, microbubbles have recently been shown critical in therapeutic ultrasound applications, such as HIFU[16], sonothrombolysis[35], and BBB opening[3,36]. The interaction between microbubbles and ultrasound can significantly enhance the effect of FUS. In HIFU, the effect of microbubble concentrations on the lesion volume and focal shift has been investigated. It has been shown that the lesion volume can be enhanced to 12 times higher than the one without microbubble administration, but with an acceptable shift of focus[16]. Previous research found that microbubbles could not only enhance the effectiveness of the thrombolytic agents in the presence of ultrasound, but microbubbles also had the potential to reduce the dose of the thrombolytic agents in the treatment of vascular thrombotic disease, and reduce the side effects of the thrombolytic therapy[37]. Unlike HIFU, in FUS-induced BBB opening, the BBB is not opened in the absence of the microbubble administration. The description of three mainly commercial microbubbles, including Definity®, Optison®, and Sonovue®, used in the BBB opening are listed in Table 2.2.

Table 2.2 Three main microbubbles used in BBB opening. The data of Optison and Definity is obtained from the package insert. The data of Sonovue is from Molecular Imaging and Contrast Agent Database (MIDAC)

Microbubble	Shell	Gas	Concentration (numbers / mL)	Mean Diameter (μm)
Definity®	Lipid	Perfluoropropane	1.2×10^{10}	1.1 - 3.3
Optison®	Albumin	Perfluoropropane	$5\text{-}8 \times 10^{8}$	3.0 - 4.5
Sonovue®	Lipid	Perfluorobutane	2.0×10^{8}	3

2.3.3 BBB opening using FUS and microbubbles

FUS-induced BBB opening was first observed using HIFU, accompanied with lesion formation[38]. It was also reported that abnormal permeability of the human blood-brain barrier can be induced by 300 kHz insonation, used for somothrombolysis, in one patient with severe cerebral small vessel disease[39]. A remarkable side effect was observed in this patient undergoing perfusion-MRI. Although the patient with cerebral small vessel disease may already have an impaired BBB (vascular leakage), it has to be tentatively regarded as a negative effect of this technique on the cerebral endothelium[39]. In 2001, with intravenous administration of microbubbles, the BBB was opened *in vivo* at acoustic pressures and duty cycles low enough that significant thermal effects may be avoided[3,40]. To date, several different aspects of this technique have been investigated, including different animal models, the optimization of experimental conditions, varied-sized compound delivery, safety assessment, physiological mechanism, and physical mechanism, which will be summarized in the following sections.

2.3.3.1 Animal models for BBB opening

The first BBB opening using FUS and microbubbles was implemented in rabbits with craniotomy[3]. Following this study, BBB opening has been achieved in additional species, such as, mice[41], rats[42], and pigs[43]. Since the craniotomy is invasive and time-consuming, the reversible BBB opening using transcranial FUS was then achieved in rats and rabbits[44,45]. Our group has also shown that the BBB can be reproducibly opened using transcranial FUS in a specific subcortical region associated with neurodegenerative disease, i.e., the hippocampus in mice[40,41]. Transgenic mice are being developed, in an attempt to generate models of human Alzheimer's disease to allow a better understanding of the mechanisms leading to initiation and progression of the disease, which would identify potential therapeutic targets and permit testing of drugs of real clinical potential[46]. Thus, the Alzheimer's-model mouse (AD mouse) is an appropriate model for FUS induced BBB opening[47]. Furthermore, in order to have clinical translation of this technique, the feasibility of FUS-induced BBB opening in non-human primates (NHP) has been accomplished by our group and will be described in most detail in *Chapter 6*[36,48]. The summary of all animal models and main contribution are listed in Table 2.3.

Table 2.3 Animal models used in FUS-induced BBB opening

Animal	Microbubble	Main contribution
Mice[40,41]	Optison®	Reproducible opening located at hippocampus
AD mice[47]	Optison®/Definity®	Successful opening in AD mice
Rats[42]	Optison®	Transcranial BBB opening in rats
Rabbits[3]	Optison®	BBB opening with/without craniotomy
Pigs[43]	In-house	First BBB opening in large animals
Monkeys[36,48]	In-house	First BBB opening and Cavitation-guided BBB opening in NHPs

2.3.3.2 Investigation of experimental conditions

After successfully opening the BBB in different models, the efficacy, efficiency, and the corresponding experimental conditions have been widely investigated. First, different acoustic parameters, such as frequency, peak rarefactional pressure (PRP), pulse length (PL), pulse repetition frequencies (PRF), and sonication duration, have been studied.

Several frequencies, e.g., 28 kHz[49], 260 kHz[45], 500 kHz[48], 690 kHz[44], 1 MHz[50], 1.5 MHz[41], 1.63 MHz[3], and 2.64 MHz[51], have been applied for opening the BBB. The PRP threshold for BBB opening was shown to increase with the applied sonication frequency. The threshold, however, remained constant when compared to the mechanical index (MI)[51]. The PRP threshold was also shown to decrease with PL while the PRF did not affect the threshold[52]. In addition, our group has demonstrated feasibility of BBB opening using a pulse length of 3 cycles (2 μs) at 1.5 MHz PL-based pulse, and capable of delivering a high dose of dextran homogenously throughout the targeted region[53]. Furthermore, a sonication duration lower than 180 s in duration is associated with a low probability of irreversible damage to the brain tissue at a PRP of 0.38 MPa[54].

Second, distinct microbubble concentration and types have been investigated in several studies. The microbubble concentration has shown no effect on the contrast enhancement of dextran or MRI images within the range among 50, 100, and 250 μL/kg at 0.5 MPa[12,52], but was shown to affect the Evans Blue (EB) delivery at 1.2 MPa[55]. In terms of microbubble properties, our group has shown that the PRP threshold for the smaller (1-2 μm in diameter) microbubbles is higher than that of the larger ones (4-5 and 6-8 μm)[56,57]. Larger microbubbles were observed having bigger opening volume, but having higher chance of inducing damage[57].

Third, because MRI was used in most studies for BBB opening confirmation, distinct parameters were applied in terms of optimization. A susceptibility-weighted MRI was first used to detect hemorrhage during BBB opening[42]. Both gradient echo and spin echo sequences were deemed reliable in indicating the degree of BBB opening[58]. The timing of contrast-enhanced MRI that best indicates blood–brain barrier (BBB) disruption has also been obtained. The spin-echo T1W images at 10 minutes post–contrast enhancement showed the best correlation with EB staining in both quantity of EB extravasation and spatial distribution[59]. In addition, MRI signal intensity change not only could be used to detect BBB opening during sonication, but could also be used to estimate the concentration of EB in the target tissue over the whole duration of BBB disruption after sonication[60].

Reversibility, i.e., the duration of BBB opening, has also been reported in several studies. In general, using commercial microbubbles, such as Optison®, Sonovue®, and Definity®, the opened BBB will close in 24 hours if the PRP is lower than 1 MPa. In our recent findings, however, the duration of BBB opening can be controlled between 1 and 5 days by selecting corresponding pressures (0.30 - 0.60 MPa), pulse length (100 - 10,000 cycles) and microbubble diameters (1-2, 4-5, and 6-8 μm)[61]. In addition, repeated BBB openings are being implemented to investigate the effect of the second BBB opening. With the 40 min interval, the MR contrast enhancement and histological examination of the second sonication was shown different from a single sonication[50]. The investigations in different experimental parameters were summarized in Table 2.4.

Table 2.4 Investigations on the experimental parameters

Parameter	1st author, year	Main contribution
PL	McDannold, 2008[52]	The PRP threshold was lower with 10 ms PL, compared with 0.1 and 1 ms PL.
	Choi, 2010[12]	The PLs of 0.033, 0.1, 0.2, 1.0, 2.0, 10, 20, and 30 ms at 0.46 MPa were evaluated.
	Choi, 2011[53]	The 3 cycles PL was capable of inducing homogenous BBB opening.
	O'Reilly, 2012[62]	The BBB has been disrupted using closely-timed 3-ms pulses, at repetitions rates as slow as 1 Hz
Duration	Chopra, 2010[54]	Longer duration may increase the probability of increasing irreversible damage.

PRF	McDannold, 2008[52]	No significant difference, in terms of MRI contrast enhancement, was observed among 0.5, 1, 2, and 5 Hz.
	Choi, 2010[12]	The BBB was not opened at 0.1-Hz PRF. No difference was observed among 5, 10, and 25-Hz PRF.
	Choi, 2012[53]	The fluorescence with a 100-kHz PRF and a 5-Hz BRF was significantly greater than other acoustic parameters
Microbubble properties	McDannold, 2007[63]	Optison® produced a larger effect than Definity® for the same acoustic pressure amplitude.
	Choi, 2010[56]	PRP threshold of the 1-2-μm diameter bubbles was higher than the 4-5-μm diameter bubbles.
	Tung, 2011[57]	The physical mechanism is bubble-size dependent.
	Vlachos, 2011[64]	The permeability is bubble-size dependent
Microbubble dose	Yang, 2007[55]	(Sonovue®) The amount of EB was significantly greater with 60 or 90 uL/kg than with 0 or 30 uL/kg at 1.2 MPa
	McDannold, 2008[52]	(Optison®) No difference was observed among 50, 100, and 250 uL/kg at 0.50 MPa.
	Yang, 2009[65]	(Sonovue®) A dose of 300 and 450 uL/kg induced greater EBs amount and longer opening duration than a 150 uL/kg.
	Choi, 2010[12]	Fluorescence intensity was not significantly different among 10, 50, and 250 uL/kg with Definity® at 0.46 MPa.
MRI	Liu, 2008[42]	susceptibility–weighted imaging is more sensitive than standard T2-weighted and contrast-enhanced T1-weighted MRI techniques in detecting hemorrhages
	Vlachos, 2010[66]	Comparison of two permeability models for BBB opening
	Yang, 2010[60]	MRI signal intensity change could be used to estimate the concentration of EB.
	Weng, 2010[59]	The spin-echo T1W images at 10 minutes post–contrast enhancement showed the better correlation with EB staining than the gradient-echo T1W images.
	Weng, 2011[58]	Both gradient echo and spin echo sequences were all reliable in indicating the degree of BBB opening.
	Howles, 2010[67]	This technique enables *in vivo* functional mapping of the mouse barrel field cortex with manganese-enhanced MRI
Reversibility	Hynynen, 2005[44]	(Optison®), the opened BBB is closed in 5 hrs at 0.40 MPa and at 260 kHz in rabbits.
	Wang, 2009[68]	(Sonovue®), the opened BBB is closed in 8 hrs at 0.80 MPa and at 1.1 MHz in rabbits.
	Xie, 2008[43]	(In-house MBs), the opened BBB is closed in 3 hrs at 0.25 MPa and at 1 MHz in pigs.
	Samiotaki, 2012	(Mono-dispersed in-house MBs), the opened BBB is closed from 1 to 5 days at 0.30–0.60 MPa and at 1.5 MHz in mice.

2.3.3.3 Delivery of large compounds through the opened BBB

The aim of optimization for experimental conditions was to successfully delivery drugs into the brain parenchyma. To date, except for the agents used for BBB opening confirmation, such as Ominiscan[40], Magnevist[69], Superparamagnetic iron oxide[70], 99mTc-DTPA[71], Evans Blue (EB)[72], Trypan Blue[73], Congo Red[73], fluorescence tagged dextran[74], and horseradish peroxidase[6], different agents have been shown across the BBB via the interaction between FUS and microbubbles.

FUS-induced BBB opening has been used for the delivery of various therapeutic agents. The deposition of doxorubicin (DOX), named as a strong candidate for chemotherapy of the central nervous system, has been increased due to the FUS-induced BBB opening[75,76]. BCNU, used in the treatment of several types of brain cancer, has also been successfully delivered to the brain tumors of rats[77-79]. Higher PRP (> 1 MPa) was usually applied for tumor treatment. For neurodegenerative disease treatment, however, successful delivery is more difficult because lower PRP is usually used to prevent the occurrence of ablation. Our group has achieved the delivery of brain-derived neurotrophic factor (BDNF) which can encourage the growth and differentiation of new neurons[4]. In addition, the delivery of neuron stem cells from the blood to targeted brain structures was also demonstrated[80]. This provided an alternative to cell therapy.

Antibody-based anticancer agents are promising chemotherapeutic agents. Among these agents, Herceptin (trastuzumab), a humanized anti-human epidermal growth factor receptor 2 (HER2c-erbB2) monoclonal antibody, was successfully delivered into the murine brain[81]. In addition, anti-Aβ antibodies, used to reduce the Aβ plaque involved with neuron degeneration, have also been delivered into the brain of AD (TgCRND8) mice[82]. A rabbit anti-human dopamine D4 receptor antibody, which recognizes the 3rd extracellular domain (Ac-176-185) of the human dopamine D4 receptor, has also been delivered in the murine brain[83]. Furthermore, the expressions of exogenous gene pBDNF-EGFP were observed in the cytoplasm of some neurons, and BDNF expressions were markedly enhanced by the combination of ultrasound and pBDNF-EGFP-loaded microbubbles[84]. The large agents and corresponding size were summerized in Table 2.5.

Table 2.5 Molecules used in the FUS-induced BBB opening

Compound	Name	Size
MRI or SPECT contrast agent	Omniscan[40]	573 Da
	Magnevist[69]	938 Da
	Superparamagnetic iron oxide (SPIO)[70]	50 nm
	99mTc-DTPA[71]	492 Da
Dye and fluorescence agent	Evans Blue[72]	960 Da
	Trypan Blue[73]	916 Da
	Congo Red[73]	697 Da
	Dextran[74]	3 kDa, 7 kDa, 2 MDa
	Horseradish peroxidase[6]	40 kDa
Therapeutic compounds	Doxorubicin[75,76]	544 Da
	BCNU[77-79]	214 Da
	BDNF[4]	27 kDa
	Neuron Stem cell[80]	--
Antibody	Herceptin[81]	148 kDa
	Anti Aβ[82]	--
	D4 rabbit receptor-targeting[83]	42 kDa
Gene delivery	exogenous gene pBDNF-EGFP[84]	--
Nano particle	Magnetic nanoparticles[85]	74-83 nm
	Gold nanoparticles[86]	50 nm

2.3.3.4 Safety assessment

In order to prevent the permanent damage on the healthy brain tissue, safety assessment is necessary. Most studies mainly concentrated on hematoxylin and eosin (H&E) analysis, which provided the information of red blood cell (RBC) extravasations and damaged neurons identified based on characteristics of dark neurons in the sections. These neurons had shrunken and triangulated cell bodies, eosinophilic peri-karyal cytoplasm and pyknotic basophilic nuclei. TUNEL is also a common method for detecting DNA fragmentation that results from apoptotic signaling cascades[87]. In addition, vanadium acid fuchsin (VAF)-toluidine blue staining is used to visualize ischemic neurons in the parenchyma in the sonicated areas[88]. Based on these histological analyses after FUS-induced BBB opening, the PRP threshold for vascular wall damage, hemorrhage, and eventually necrosis was 6.3 MPa. No ischemia or apoptosis was observed even if the PRP was 12.7 MPa, which induced 1.7 °C temperature rise[89].

Besides the histological analysis, MRI can be used as the damage identification. The susceptibility–weighted imaging (MR-SWI) has been shown more sensitive for possible tissue hemorrhage associated with BBB opening in a rat model. Also, temperature changes were measured with MRI by exploiting the temperature-dependence of the proton resonant frequency (PRF). Changes in the PRF were estimated with phase-difference images using a fast spoiled gradient echo (FSPGR) sequence[90]. Therefore, MRI is able to identify thermal effect during BBB opening, but no significant thermal effect has been observed so far. Permeability assessment can also provide the dynamic information of the molecular diffusion. Our group has investigated the permeability after FUS-induced BBB opening using dynamic contrast enhanced (DCE-MR) imaging, together with the effect of the diameter of microbubbles. The permeability after BBB opening was found to increase by at least a 100-fold[64,66]. Further details will be provided in *Chapter 4.*

The safety assessment of the short term (immediately after sonication up to a few hours) and long term (few days to several weeks) have been investigated by our group and McDonnald et. al[91,92]. For short survival time periods (30 min and 5 h), it was only the lower-pressure amplitudes that showed the least amount of short-term effects (0.3 to 0.46 MPa at 1.5 MHz)[91]. No lesions containing ischemic or apoptotic neurons were observed to 4 weeks after sonication at 0.7 or 1.0 MPa. Thus, using FUS in conjunction with microbubbles for targeted BBB opening does not appear to result in widespread damage to the neurons (either directly or through ischemia or apoptosis) or delayed effects up to one month after sonication[92].

Using the SPIO, it has been shown that the infiltration of phagocytes, i.e. the inflammatory response, does not occur using lower PRP (1.1 MPa, compared with 2.45 MPa)[93]. Furthermore, during the BBB opening experiments, the effect of anesthesia methods was investigated. Over the range of exposure levels tested, MRI contrast enhancement was significantly higher for animals anesthetized with ketamine/xylazine. Furthermore, the threshold for extensive erythrocyte extravasations was lower with ketamine/xylazine[94].

2.4 Possible mechanism of FUS-induced BBB opening

Understanding the mechanism of FUS-induced BBB opening is believed useful for optimization and the design of therapeutic agents. Here, we will first summarize the physiological response to the stimulus of microbubbles activated in the acoustic filed. The possible physical mechanism behind the physiological response will then be introduced.

2.4.1 Physiological mechanism

Figure 2.4 shows the general pathways for molecules across the BBB. Prior to the FUS-induced BBB opening, the tight junction (TJ) restricts the paracellular route, thus only small (<400 Da) and lipid soluble molecular can transport across the BBB through the lipophilic pathway, transport proteins, and endocytosis[95]. The cellular mechanism of FUS-induced BBB opening has been first reported in 2004. The data revealed that several mechanisms of transcapillary passage are possible after such sonications: 1. transcytosis; 2. endothelial cell cytoplasmic openings - fenestration and channel formation; 3. opening of a part of tight junctions; and 4. free passage through the injured endothelium[7]. As shown in Fig. 2.4, TJ-related protein includes occluding, claudin-1, claudin-5, and ZO-1. More specific, the TJ molecular structure was shown disassembled at 1.1 MPa peak rarefactional pressure (PRP) using a 1.5-MHz FUS and Optison® microbubbles, as well as the occludin, claudin-1 and ZO-1 was affected up to 4 hours after the sonication[6,7]. This TJ disruption may induce the activation of Akt signaling pathway, which plays a role in regulating neuronal cell survival during pathological alteration, in neuronal cells surrounding the opened BBB[96].

The gap junctions, which allow transfer of information between adjacent cells and are responsible for tissue homeostasis, was observed having reorganization instead of destruction or loss of gap-junctional plaques after BBB opening[97]. In addition, regarding the protein about the transcellular route, the expression of caveolin-1 has been shown to be increased after FUS-induced BBB opening, which is relevant to the receptor-mediated mechanism[98]. In addition, optical imaging used to observe the response of the brain vasculature has shown 1) the activation of vesicular transport was shown more expressed in the brain arterioles than in the capillaries[5]; 2) vasoconstriction[99] and 3) different types of leakage correlated to distinct PRP during BBB opening, from 0.3 to 0.8 MPa[100]. However, the physical mechanism on the microbubble interaction with ultrasound during BBB opening remains to be established.

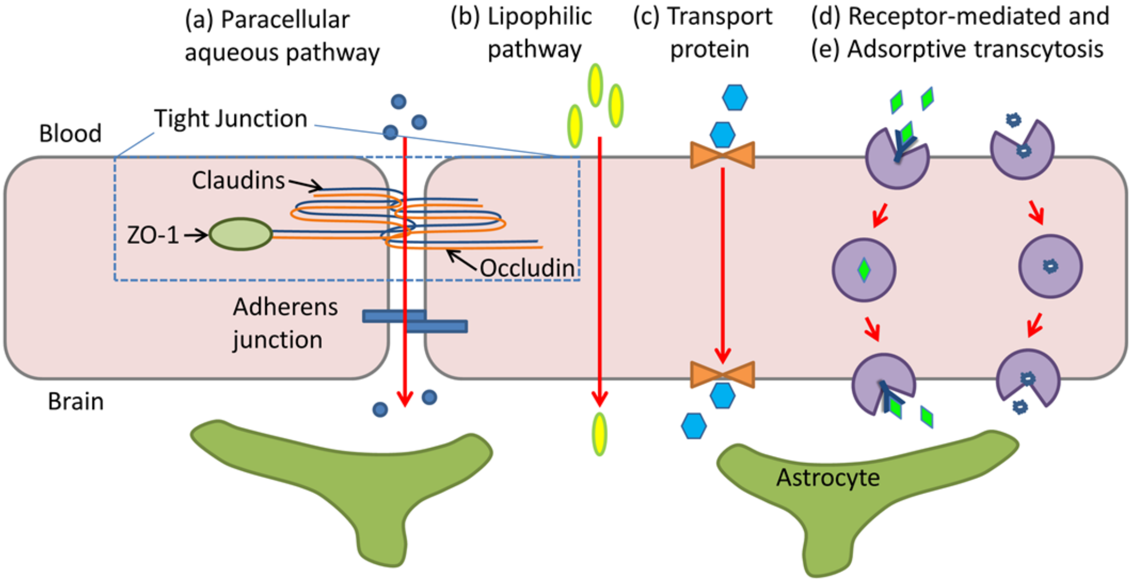

Figure 2.4 – Physiological transport across the BBB[95]. The main routes for molecular traffic across the BBB are (a) paracellular aqueous pathway, but restricted by the tight junction which is mainly established by the transmembrane proteins (claudins and occludin), linked to cytoskeletal actin through ZO-1; (b) the lipid membranes of the endothelium offers an effective diffusive route for lipid-soluble agents; (c) transport proteins for glucose, amino acids, purine bases, nucleosides, and choline; (d,e) receptor- or adsorptive-mediated endocytosis. Modified from Abbott et al.[95] and Chou et. al.[101]

2.4.2 Physical mechanism – acoustic cavitation

Cavitation is defined as any stimulated bubble activity. The stimulation may be due to flow, decompression, acoustic waves, sudden deposition of electromagnetic or ionizing radiation, or heat[102]. The activity can refer to bubble inception or dynamics. Acoustic cavitation refers to the generation, growth and interaction of small gas bubbles in a sound field. When exposed to an acoustic field in a fluid, the gas cavity or bubble can either oscillate gently at low pressure levels, or oscillate violently, resulting in large growth and rapid collapse at higher pressures. Traditionally, we call the former the stable cavitation (SC), and the latter the transient or inertial cavitation (IC)[102].

Apfel and Holland calculated the pressure threshold of inertial cavitation in water and showed that it increased with frequency[103]. Most studies on the threshold of cavitation effects with microbubbles were based on the assumption of a free bubble[104-109]. However, containment of a bubble within a vessel alters its behavior. Qin and Ferrara simulated the interaction between acoustically driven microbubbles in compliant microvessels and found that the threshold of bubble fragmentation was higher within more rigid vessels when compared to compliant vessels[110].

Rigid bubble motion as a result of the radiation force as well as visualization of radial oscillations have been proposed to explain why microbubbles within smaller tubes have a higher fragmentation threshold and greater persistence[111]. The relationship between the threshold of fragmentation for ultrasonic contrast agents and the acoustic parameters used has also been investigated[105]. However, cellulose tubes, which have been used in most vessel phantom studies, do not have the same properties as physiologic vessels. The observation of microbubble interaction with the microvessel wall of the *ex vivo* cecum has been investigated to demonstrate the process of bubble collapse into the endothelium and repeated expansion of the microbubble within the blood vessels[112]. It has been shown that the inertial cavitation can be correlated with cell damage in rabbit ear vessels[113,114]. The interaction between ultrasound and microbubbles has been shown to increase the permeability of the endothelial layer without any cell detachment or damage *in vitro*[115].

Since optical imaging can only be used to observe the superficial vasculature with the craniotomy, a better method has to be implemented in order to identify the type of microbubble behavior during BBB opening in the deep regions in absence of the craniotomy. In order to study the physical effects responsible for BBB opening, a passive cavitation detector (PCD) can be used to acquire the acoustic response stemming from the microbubble and tissue during BBB opening[116]. The frequency response can be classified into two categories. The first response is generated by SC, i.e., at harmonic, sub-harmonic and ultra-harmonic frequencies. The second response is generated by IC, which will produce broadband acoustic emission due to the collapse of microbubbles. In general, stable cavitation dose (SCD) and inertial cavitation dose (ICD) are generated by the integration of the amplitude at ultra-harmonics and broadband response, respectively, with the sonication duration[117,118]. In this dissertation, we will qualitatively demonstrate the frequency and quantitatively calculate the SCD and ICD in order to determine the cavitation type which dominate BBB opening.

The possible physical mechanism for BBB opening and corresponding frequency response can hence be depicted in Fig. 2.5. In SC, the stable expansion and contraction may be able to change the permeability of endothelial cells. The corresponding frequency spectrum and spectrogram clearly show the peaks at harmonics and ultra-harmonics without the broadband response. In IC, the collapse of microbubbles induces broadband response and the fluid jet may damage surrounding endothelial cells. Our group has achieved the *in vivo* transcranial cavitation detection in mice and provided evidence that the BBB opening could be induced at the absence of inertial cavitation, at 0.30 MPa[119,120]. We have also shown that the murine skull does not completely influence the detection of inertial cavitation[119], which is further described in *Chapter 3*.

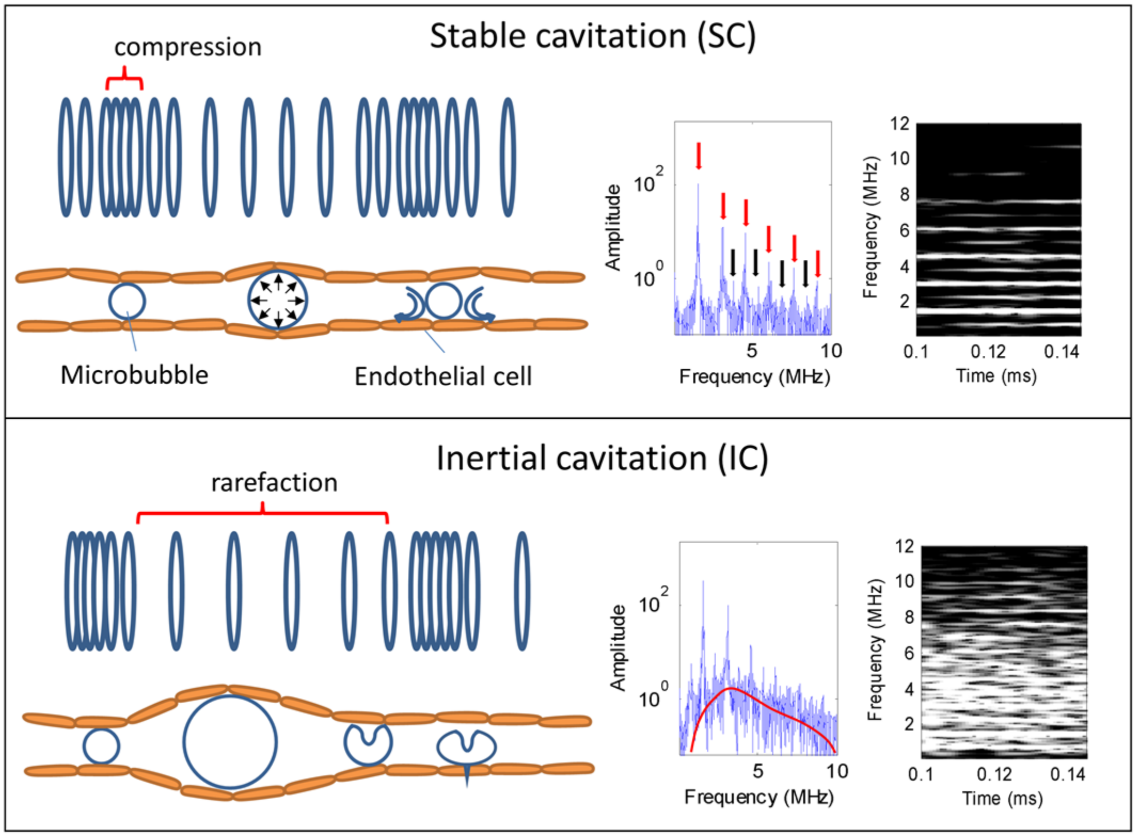

Figure 2.5 – Schematic diagram illustrating the microbubble behavior and cavitation types. A microbubble decreases in size during the compressional phase, and expands during the rarefactional phase. Low-intensity ultrasound induces a stable oscillation of a microbubble in the capillaries, named as stable cavitation where the harmonics (red arrows) and ultra-harmonics (black arrows) are generated. However, at higher intensities, the microbubble grows rapidly for a few cycles. Very soon, the inertial energy of the fluid surrounding the microbubble during the compression forcibly collapses the microbubble, generating fluid jet or shock waves, along with broadband response (red curve).

Chapter 3

Development of a Transcranial Cavitation Detection System

3.1 Introduction

A comprehensive assessment of the physical mechanism is warranted in order to establish a safety window of BBB opening. Till now, the physical mechanism of FUS-induced BBB opening remains largely uncovered. Not only is the interaction between the acoustically driven bubble and brain capillaries unknown but also the effect of the skull on the BBB opening threshold has not been thoroughly described. Several studies investigating BBB opening require craniotomy[3,52,63,92,121]. However, craniotomy is a difficult and time-consuming process that is associated with brain exposure, morbidity and occasional mortality. As a result, Hynynen et al. used low frequency (260 kHz), which resulted in lower phase aberration through the skull when opening the BBB transcranially[44,45]. Our group has characterized the FUS beam through the murine skull in simulations and *ex vivo* skull experiments in order to understand the effects of aberration and attenuation through the skull corresponding to the hippocampus[41]. Since Alzheimer's disease occurs in hippocampus, localized transcranial BBB opening in the murine hippocampus has been reported[40].

In order to study the bubble behavior during BBB opening, the relationship between acoustic cavitation and BBB disruption was previously investigated using a PCD, which suggested that inertial cavitation might not be necessary for BBB opening[121]. The peak-rarefactional pressure (PRP) threshold of BBB opening and inertial cavitation at 260 kHz was 0.29 MPa and 0.40 MPa, respectively, which suggested that inertial cavitation might not be necessary for BBB opening. However, that study was performed following craniotomy and ignored any effects that the skull may introduce such as a change in the threshold of inertial cavitation. As a result, *in vivo* transcranial cavitation detection during

BBB opening is necessary for studying the actual mechanism of BBB opening induced by FUS and microbubbles without craniotomy.

The objective of this chapter is to establish a novel system to detect bubble response transcranially and to identify the cavitation type during BBB opening in mice *in vivo*. First, a phantom study was carried out to separately assess the effect of the skull, the angle dependence, sensitivity and reliability of the PCD setup. The occurrence of inertial cavitation during BBB opening in mice *in vivo* was then investigated using two PCD setups to determine the optimal configuration. The spectrogram and inertial cavitation dose (ICD), the integration of the spectrum amplitude with time curve, were used to identify the threshold of inertial cavitation. MRI and histology were used to determine the BBB opening occurrence and macroscopic damage, respectively.

3.2 Materials and Methods

3.2.1 Phantom validation of the skull effect

3.2.1.1 Experimental Setup

The experimental setup of the phantom validation is shown in Fig. 3.1. A single-element circular focused ultrasound transducer (Riverside Research Institute, New York, USA) was driven by a function generator (Agilent Technologies, Palo Alto, CA, USA) through a 50-dB power amplifier (ENI Inc., Rochester, NY, USA). The center frequency, focal depth, outer radius and inner radius of the FUS transducer were 1.525 MHz, 90 mm, 30 mm and 11.2 mm, respectively. A single-element diagnostic transducer (center frequency: 7.5 MHz, focal length: 60 mm), which was driven by a pulser-receiver

(Panametrics, Waltham, MA, USA), was positioned through the opening of the FUS transducer. These two transducers were confocally aligned. A cone filled with degassed and distilled water was attached to the transducer system. The transducer was then mounted on a computer-controlled positioner (Velmex Inc., Bloomfield, NY). The dimensions of the focal region were measured and a lateral and axial full-width at half maximum (FWHM) intensity were of approximately 1.32 and 13.0 mm, respectively.

A 5-cm broadband, cylindrically focused hydrophone (Sonic Concepts, Bothell, WA, USA) with a cylindrical focal region (height 19 mm, diameter 3.64 mm) was placed at 60º (60º-PCD, Fig. 3.1(a)) or 90º (90º-PCD, Fig. 3.1(b)) from the longitudinal axis of the FUS beam. The hydrophone holder was adjusted to confocally align the hydrophone and the FUS transducer. The acoustic emissions from the microbubbles were acquired by the hydrophone followed by a 20-dB amplification (model 5800, Olympus NDT, Waltham, MA, USA) and collected using a digitizer (model 14200, Gage Applied Technologies, Inc., Lachine, QC, Canada).

Each sonication set included a pulse length of 100 cycles (67 μs) and a pulse repetition frequency (PRF) of 10 Hz. The total sonication duration of a sonication set was 2 s, i.e., 20 pulses. Acoustic signals emitted from microbubbles were acquired for each pulse. The peak-rarefactional pressure amplitude ranged between 0.30 and 0.90 MPa at a 0.15 MPa step size as calibrated in our previous studies[40].

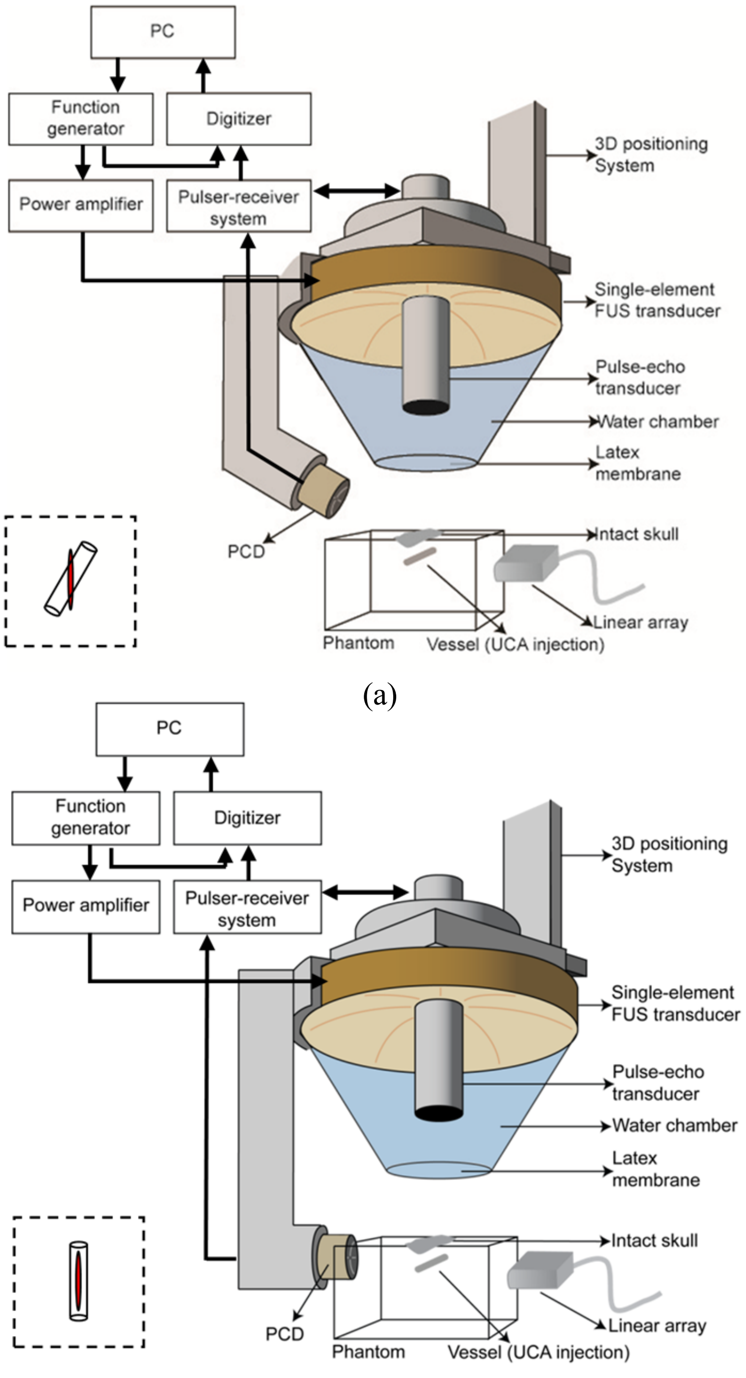

(a)

(b)

Figure 3.1 – Block diagrams of the experimental setup. The PCD was positioned at a (a) 60° and (b) 90° relative to the longitudinal axis of the FUS beam. The space between latex membrane and phantom was degassed water, and the big water tank was not shown on this figure. The overlap between the focal region of PCD and FUS was also illustrated in the insets. The cylindrical region was the focal region of PCD and the cigar-shaped region was the focal region of FUS. The water tank, in which the phantom was immersed, is not shown for clarity purposes.

The vessel phantom was constructed using acrylamide according to Takegami et al.[122] without the egg protein. The vessel was formed by inserting a polyethylene tube (model PE10, Becton Dickinson and Company, Sparks, MD, USA) before the phantom solidified and removing it immediately after. The phantom was immersed in a tank filled with degassed water (Fig. 3.1). The vessel was positioned 3 mm below the surface of the phantom to simulate the location of the vessel targeted in the *in vivo* application[40,41]. A linear-array transducer (center frequency 7.5 MHz, model 10L5, Terason Ultrasound, Burlington, MA) was placed perpendicular to the longitudinal axis of the FUS transducer (Fig. 3.1) and was used to map the spatial distribution of microbubbles after sonication.

3.2.1.2 Skull preparation and targeting procedure

Three brown mice (strain: C57BL/6, sex: male, mass: 20-25g) were euthanized, their skulls were extracted and then immersed into a formalin solution. All procedures used on the mice were approved by the Columbia University Institutional Animal Care and Use Committee. The thickness of the parietal bone was 0.18, 0.20 and 0.23 mm, respectively. The intact skull was degassed before each experiment in order to prevent any cavitation effects at the skull level that may affect the beam propagation. Based on previous experiments, the skull attenuates the pressure amplitude by approximately 18.1% at 1.525 MHz[40]. Therefore, the FUS transducer was driven at different voltages to ensure that the pressure values were of the same magnitude, with or without skull in place.

Figure 3.2 illustrates the targeting method through the skull that is also used to open the BBB in a subcortical structure such as the hippocampus *in vivo*[40]. Since the thickness and attenuation of the skull vary across its volume, a precise targeting method was required in order to propagate through the thinnest region. A grid-positioning method was used to ensure that the focal spot overlapped with the equivalent hippocampus location, which is the target in our *in vivo* studies[40,41]. First, a raster scan (Fig. 3.2(a)) was performed to ensure that the center of the FUS focal spot was placed in the middle of the vessel. Second, the FUS transducer was positioned above the skull. A second raster scan was performed to locate the region equivalent to the hippocampus location *in vivo*, i.e., 3 mm below the skull as indicated in Fig. 3.2(b).

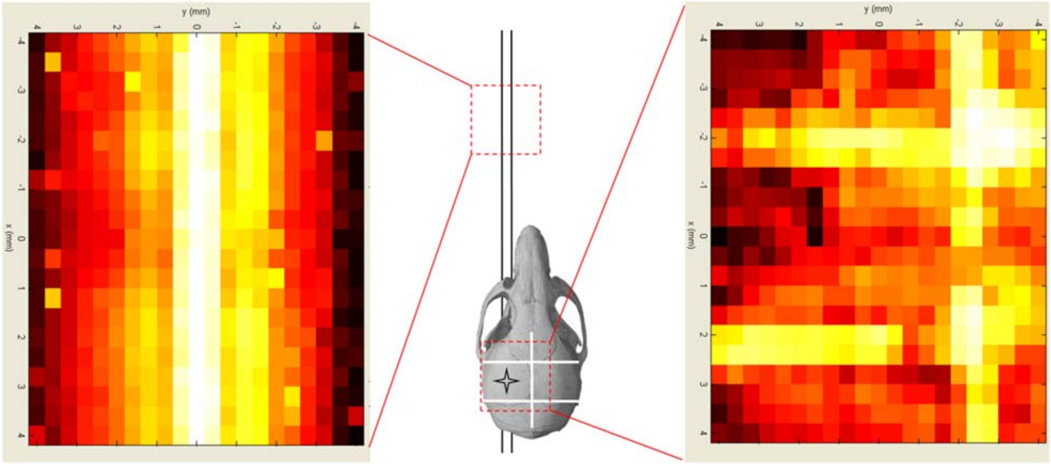

(a) (b)

Figure 3.2 – The channel phantom below the *ex vivo* mouse skull was localized using raster scan with the pulse-echo transducer as shown. (a) The first raster scan was used to find the position of the vessel while (b) the second raster scan of the RF signal amplitude was used to find the position of the left parietal bone, where in previous studies was the acoustic window through which to sonicate to target the left-hippocampus region (cross symbol). The white bar indicates the grid which was yellow shown in (b). [Image of the mouse skull available at http://www.digimorph.org.]

3.2.1.3 microbubble preparation and sonication

Definity® microbubbles (Bristol-Myers Squibb Medical Imaging, N. Billerica, MA, USA.), which constitute perflutren-filled, lipid-shelled microspheres, were used in our experiments. These microbubbles had a mean diameter of about 1.1 to 3.3 μm (Table 2.2), with 98% having a diameter lower than 10 μm, and a concentration of around 1.2×10^{10} bubbles/mL. In this study, the concentration was diluted in degassed phosphate buffered saline (PBS) to 2.5×10^{7} (number of bubbles/mL), which approximated what was used in *in vivo* studies[40,41]. The concentration (number of bubbles/mL) of microbubbles was measured by an automatic particle sizer (Accusizer 780A, NICOMP Particle Sizing Systems, Santa Barbara, CA), which used a laser light obscuration and scattering technique. In order to ensure that the concentration of the microbubbles did not change over time, e.g., caused by a decay of microbubbles, a new batch of diluted bubble suspension was used every 10 minutes. The same diluted bubble suspension was used for 10 independent sonication sets. At each pressure amplitude and PCD angle, five sonication sets were performed in the presence, and five in the absence, of the skull. A new phantom was used with each different skull, each for 15 – 20 sonication sets. Prior to each sonication set, new microbubbles were slowly injected into the vessel formed in order to avoid any change in the microbubble size distribution and concentration that may be introduced with a fast bubble injection[123]. Following each sonication set, degassed water was used to remove any remaining microbubbles inside the vessel.

3.2.1.4 Acoustic emission signal acquisition and analysis

The acoustic emissions acquired by the PCD were sampled at 80 MHz and processed using MATLAB® (2007b, Mathworks, Natick, MA). The resulting signals were analyzed using four independent methods: the frequency response of the first pulse of each sonication was obtained using a 4096-point FFT (Fig. 3.5), a spectrogram of the first pulse (Fig. 3.6), and the spectrogram depicted as the frequency response of the signal versus the 20 sonication pulses applied (Fig. 3.7), the root mean square (RMS) of the PCD's recorded voltage amplitude (V_{RMS}) for each pulse (Fig. 3.8(a)), and the average across all pulses (Fig. 3.8(b)).

In the calculation of the V_{RMS} and ICD, a highpass filter with a cut-off of 4 MHz was first applied to the acquired PCD signal. A comb filter was then used to exclude the ± 150 kHz range at the transducer's harmonic (nf, n = 1, 2, …,6), subharmonic (f/2) and ultraharmonic (nf/2, n = 3, 5, 7, 9) frequencies[124]. The ICD was defined as the integral of the area under the V_{RMS} curve over the entire sonication duration (2 s in this study). In order to reduce the noise in the ICD calculation, the V_{RMS} of water at each pressure amplitude was also calculated and was subtracted from the results of the bubble experiment to obtain the net bubble response.

Radiofrequency (RF) data from the linear array was acquired using the Terason system and processed using MATLAB®. B-mode imaging was then performed using the Hilbert function on the acquired RF data. The change in the B-mode imaging contrast due to microbubbles was calculated as the intensity ratio:

$$Intensityratio = \frac{I_{pre} - I_{post}}{I_{pre}} \tag{3.1}$$

where I_{pre} is the intensity of the region of interest (ROI) at the FUS focal region before sonication and I_{post} is the intensity of the ROI after sonication. The dimensions of the ROI were equal to 9.0×7.2 mm^2.

A Student's *t*-test was used to determine whether the ICD dose or intensity ratio was different between the two different pressures. A P-value of $P < 0.05$ was considered to represent a significant difference in all comparisons.

3.2.2 *In vivo* transcranial cavitation detection in mice

3.2.2.1 Experimental Setup

The experimental setup of *in vivo* transcranial cavitation detection is shown in Fig. 3.3. All procedures used on the mice were approved by the Columbia University Institutional Animal Care and Use Committee. Twenty-six (n=26) adult male mice (strain: C57BL/6, weight: 26.1±1.7g, Harlan Sprague Dawley, Indianapolis, IN, USA) were sonicated. The number of nice studied in each pressure were showed in Table 3.1. The animals were anesthetized with a mixture of oxygen (0.8 L/min at 1.0 Bar, 21℃) and 1.5-2.0% vaporized isoflurane (Aerrane, Baxter Healthcare Corporation, Deerfield, IL) using an anesthesia vaporizer (SurgiVet, Inc. Waukesha, WI). In this study, a grid system which could localize the sutures of the murine skull was used for the targeting procedure[41]. The right hippocampus was targeted and the PCD was placed on the right-hand side. The focal point was placed 3 mm beneath the skull so that the focal region overlapped with the right hippocampus and a small portion of the thalamus of the murine brain.

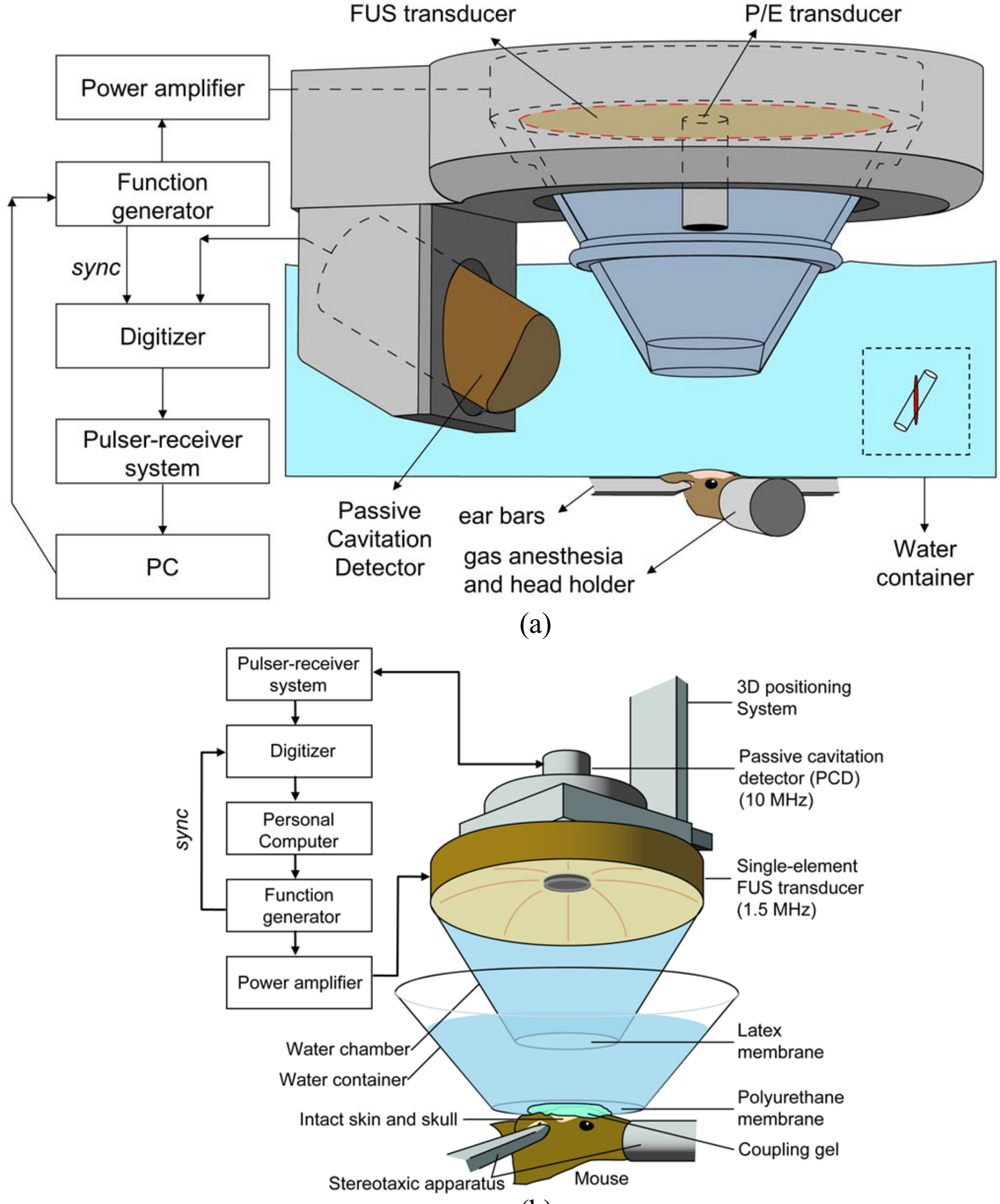

(a)

(b)

Figure 3.3 – Block diagram of the experimental setup. The PCD was positioned at a (a) 60° and (b) 90° relative to the longitudinal axis of the FUS beam. The space between latex membrane and phantom was degassed water, and the big water tank was not shown on this figure. The overlap between the focal region of PCD and FUS was also illustrated in the insets. The cylindrical region was the focal region of PCD and the cigar-shaped region was the focal region of FUS. The water tank, in which the phantom was immersed, is not shown for clarity purposes.

Table 3.1 Number of mice with BBB opening / number of mice studied at each pressure

	Pressure				
System/PCD	**0.15 MPa**	**0.30 MPa**	**0.45 MPa**	**0.60 MPa**	**Total**
A / Hydrophone	0/2	3/3	3/3	3/3	11
B / Hydrophone	0/2	3/3	3/3	3/3	11
B / 10- MHz P-E	0/1	1/1	1/1	1/1	4

In order to maintain the stability of the microbubbles, a new vial of Definity® microbubbles was activated each time using the manufacturer's instructions and only used for the experiments within 24 h after activation. Following activation, a 1:20 dilution solution was prepared using 1x phosphate-buffered saline (PBS) and slowly injected into the tail vein (1 μl per gram of mouse body weight). Two different FUS transducers were used in this study in order to confirm that FUS-induced BBB opening was transducer independent. The first FUS transducer (System-A, center frequency: 1.525 MHz; focal depth: 90 mm; outer radius: 30 mm; inner radius 11.2 mm, Riverside Research Institute, New York, NY, USA) was the same as in the phantom study and the targeted right hippocampus was sonicated one minute after bubble injection. The second FUS transducer (System-B, center frequency: 1.5 MHz; focal depth: 60 mm; outer radius: 30 mm; inner radius 11.2 mm, model: cdc7411-3, Imasonic, Besançon, France) was used to perform sonication immediately following bubble administration with the same acoustic parameters as System-A. A single-element pulse-echo (P/E) diagnostic transducer (center frequency: 10 MHz, Olympus NDT, Waltham, MA, USA) with a focal length of 60 mm was positioned through the center hole of the FUS transducer so that the foci of the two transducers could be properly aligned.

Both transducers used pulsed-wave FUS (burst rate: 10 Hz; burst duration: 20 ms; duty cycle: 20%) in two 30-s sonication intervals with a 30-s intermittent delay. Peak-rarefactional acoustic pressures of 0.15, 0.30, 0.45 and 0.60 MPa were used in this study. For both transducers, these values were obtained experimentally in degassed water and adjusted to account for murine skull attenuation values of 18.1%. The left hippocampus was not targeted and was used as the control for MRI examination. The sonication on the right hippocampus without microbubbles could provide the baseline of acoustic emission acquired by the PCD. It was shown that the sonication without microbubbles at lower pressures (< 2 MPa, peak-rarefactional) would not induce BBB opening[41]. As a result, the net bubble response could be calculated after subtraction from the baseline.

3.2.2.2 Magnetic resonance imaging

A vertical-bore 9.4T MR system (Bruker Biospin, Billerica, MA, USA) was used to confirm the blood-brain barrier opening in the murine hippocampus. Each mouse was anesthetized using 1-2% of isoflurane gas and was positioned inside a single resonator. The respiration rate was monitored throughout the procedure using a monitoring or gating system (SA Instruments Inc., Stony Brook, New York, USA). Prior to introducing the mouse into the scanner, intraperitoneal (IP) catheterization was performed. Because the MR system underwent a software upgrade during the course of the study, two different protocols were used for MR imaging. The first protocol was a three-dimensional (3D), T1-weighted SNAP gradient echo pulse sequence, which acquired horizontal images using

TR/TE=20/4 ms, a flip angle of 25 deg, NEX of 5, a total acquisition time of 6 min and 49 s, a matrix size of 256×256×16 pixels and a field of view (FOV) of 1.92×1.92×0.5 cm^3, resulting in a resolution of 75×75×312.5 μm^3. The second protocol was a 3D T2*-weighted GEFC gradient echo pulse sequence, which acquired horizontal images using TR/TE=20/5.2 ms, a flip angle of 10 deg, NEX of 8, a total acquisition time of 8 min and 12 s, a matrix size of 256×192×16 pixels and a FOV of 2.25×1.69×0.7 cm^3, resulting in a resolution of 88×88×437.5 μm^3. Both protocols were applied approximately 30 min after IP injection of 0.30 ml of gadodiamide (Omniscan®, GE Healthcare, Princeton, NJ, USA), which allowed sufficient time for the gadodiamide to diffuse into the sonicated region.

3.2.2.3 Histological analysis

Five hours after sonication, all mice were sacrificed and transcardially perfused with 30 ml phosphate buffered saline and 60 ml 4% paraformaldehyde. After soaking the brain in paraformaldehyde for 24 hours, the skull was removed and the brain was fixed again in 4% paraformaldehyde for six days. The post-fixation processing of the brain tissue was then performed according to standard histological procedures. The paraffin-embedded specimens were sectioned horizontally at 6-μm thickness section. A 1.2-mm layer from the top of the brain was first trimmed away. A total of twelve separate levels that covered the entire hippocampus were then obtained at 80-μm intervals. At each level, six sections were acquired and the first two sections were stained with hematoxylin and eosin (H&E).

3.2.2.4 Acoustic emission signal acquisition and analysis

The acoustic emission signals acquired by the PCD were sampled at 25 MHz in the *in vivo* study to accommodate the highest memory limit of the digitizer involved in each case. A customized spectrogram function (30-cycles, i.e., 20 μs, Chebyshev window; 95% overlap; 4096-point FFT) in MATLAB® (2007b, Mathworks, Natick, MA) was used to generate a time-frequency map, which provided the spectral amplitude in time (Fig. 3.4(a)). The spectrogram can then clearly indicate how the frequency content of a signal changes over time. Therefore, the onset of the broadband response and its duration could be clearly demonstrated on the spectrogram.

In terms of the quantification of the acoustic emission signal acquisition, the filtering technique has been described in the section 3.2.1.4. Here, the root mean square (RMS) of the spectral amplitude (V_{RMS}) could be obtained from the spectrogram through filtering (Fig. 3.4). Fig. 3.4(a) depicts the spectrogram after high-pass filtering with a 4-MHz cutoff and Fig. 3.4(b) showed the corresponding V_{RMS}. To maximize the broadband response compared to the sonication without microbubbles, only the first 50 μs of sonication (from 0.095 ms to 0.145 ms, denoted by the two dash lines in Fig. 3.4 were considered in the ICD calculation, which was performed by integrating the V_{RMS} variation within an interval of 0.75 μs (i.e., calculating the area below the V_{RMS} curve between 0.095 ms and 0.145 ms). In order to remove the effect of the skull in the ICD calculation, the V_{RMS} in the case without microbubbles was also calculated and was subtracted from the results with the microbubbles to obtain the net bubble response. A Student's *t*-test was used to determine whether the ICD was statistically different between different pressure amplitudes. A P-value of $P < 0.05$ was considered to denote a significant difference in all comparisons.

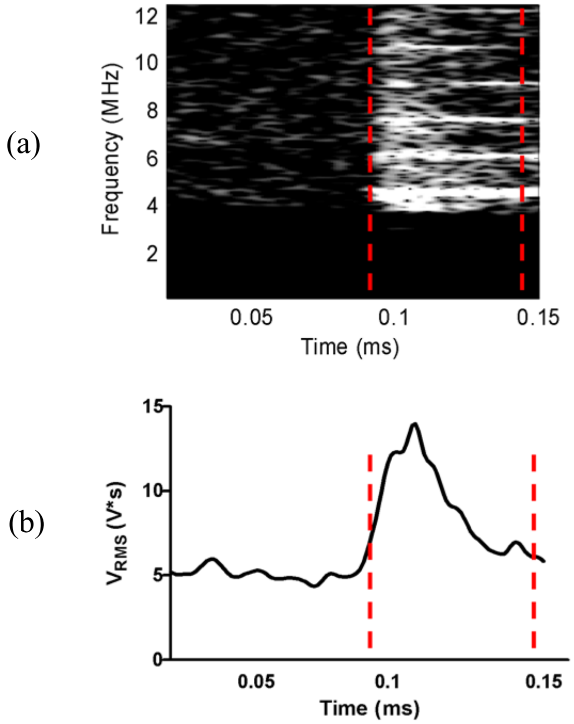

Figure 3.4 – Illustration of the inertial cavitation dose (ICD) calculation of the *in vivo* experiments. (a) The spectrogram of the first pulse from 0.02 to 0.15 ms after a 4 MHz high-pass filter (chebshev type 1) at 0.60 MPa. The harmonics and the broadband response could be observed in this figure. The corresponding V_{RMS} was depicted in (b) and the ICD was obtained using the integral of V_{RMS} curve between two dash lines.

3.3 Results

3.3.1 Phantom validation of the skull effect

The frequency response of the first pulse as recorded by the 60°-PCD and 90°-PCD configurations, with and without the presence of the skull in the wave propagation path is depicted in Fig. 3.5. Without the skull, the frequency spectra in the 60°-PCD and 90°-PCD cases are similar. As mentioned in *Chapter 2, t*he frequency response shown in this study can be classified into two types[125]. The first response is generated by stable cavitation, i.e., at harmonic, sub-harmonic and ultra-harmonic frequencies. The second response is generated by inertial cavitation, which will produce broadband acoustic emission. Here, the broadband response was detected when the pressure was at, or higher than, 0.45 MPa (Fig. 3.5(a, c)). This broadband response was used to determine the threshold of inertial cavitation for Definity® within the 610-micron-diameter vessel. The skull presence led to a decrease in the peak amplitude of all harmonics, but the characteristic broadband response was still detected (Fig. 3.5(b, d)). This indicated that the threshold of inertial cavitation of 0.45 MPa was not dependent on the skull presence. However, comparison of the results between the 60°-PCD and 90°-PCD configurations showed that the detection of acoustic emissions was influenced by the skull's presence, i.e., part of broadband response was absorbed by the skull (Fig. 3.5(b)).

The spectrogram of the first pulse as recorded by the 60°-PCD and 90°-PCD configurations in the presence of the skull in the wave propagation path is depicted in Fig. 3.6, which shows that the pressure threshold of the broadband response (or, inertial cavitation) was the same between these two PCD configurations, i.e., 0.45 MPa. This indicated that the pressure threshold of the broadband response was not affected by the skull *in vivo*. At 0.30 MPa, however, the 90°-PCD could detect the ultra-harmonics but the 60°-PCD could not, which indicated that the stable cavitation response was filtered by the skull. Also, the comparison of the results between the 60°-PCD and 90°-PCD configurations showed that the 2nd harmonic would be detected by the 60°-PCD without microbubbles at 0.30 MPa and the acoustic emission amplitude was influenced by the presence of the skull, i.e., the response was partially absorbed by the skull.

In order to assess the temporal behavior of the bubbles, the frequency response's temporal variation was studied using spectrograms of the at the two different PCD angles with and without the skull (Fig. 3.7). The spectrogram also indicated that the skull influences the signal at 60°-PCD. The amplitude around the fundamental frequency was enhanced by the skull (Fig. 3.7(b)). However, both Figs. 3.6 and 3.7 confirm the threshold of inertial cavitation to be 0.45 MPa.

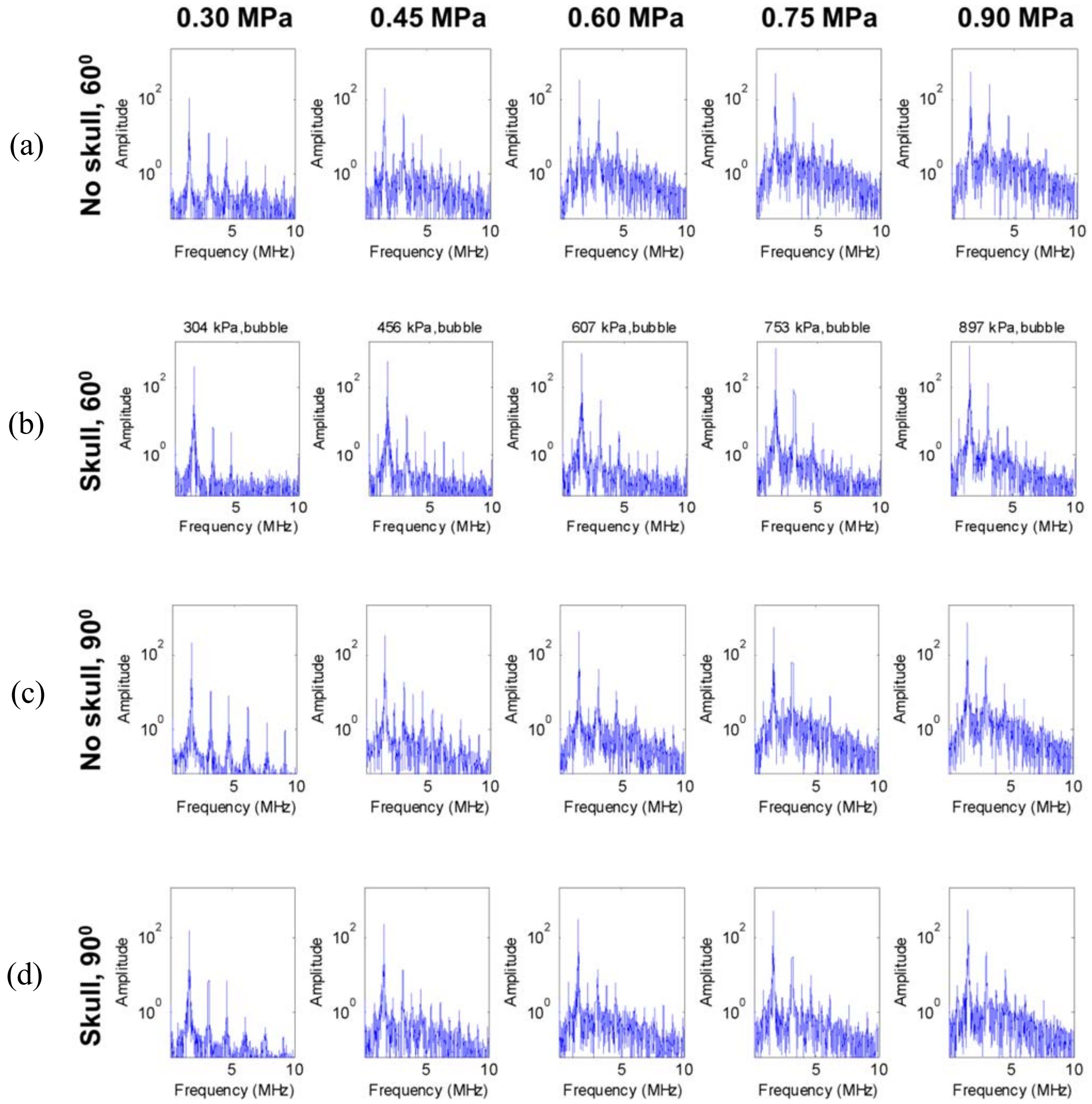

Figure 3.5 – Frequency response of the first pulse (a,c) through no skull and (b,d) through an *ex vivo* skull at 5 distinct acoustic pressures. Acoustic emissions were collected with a PCD positioned at (a,b) 60º and (c,d) 90º from the longitudinal axis of the FUS beam. Broadband acoustic emissions were detected at and higher than 0.45 MPa.

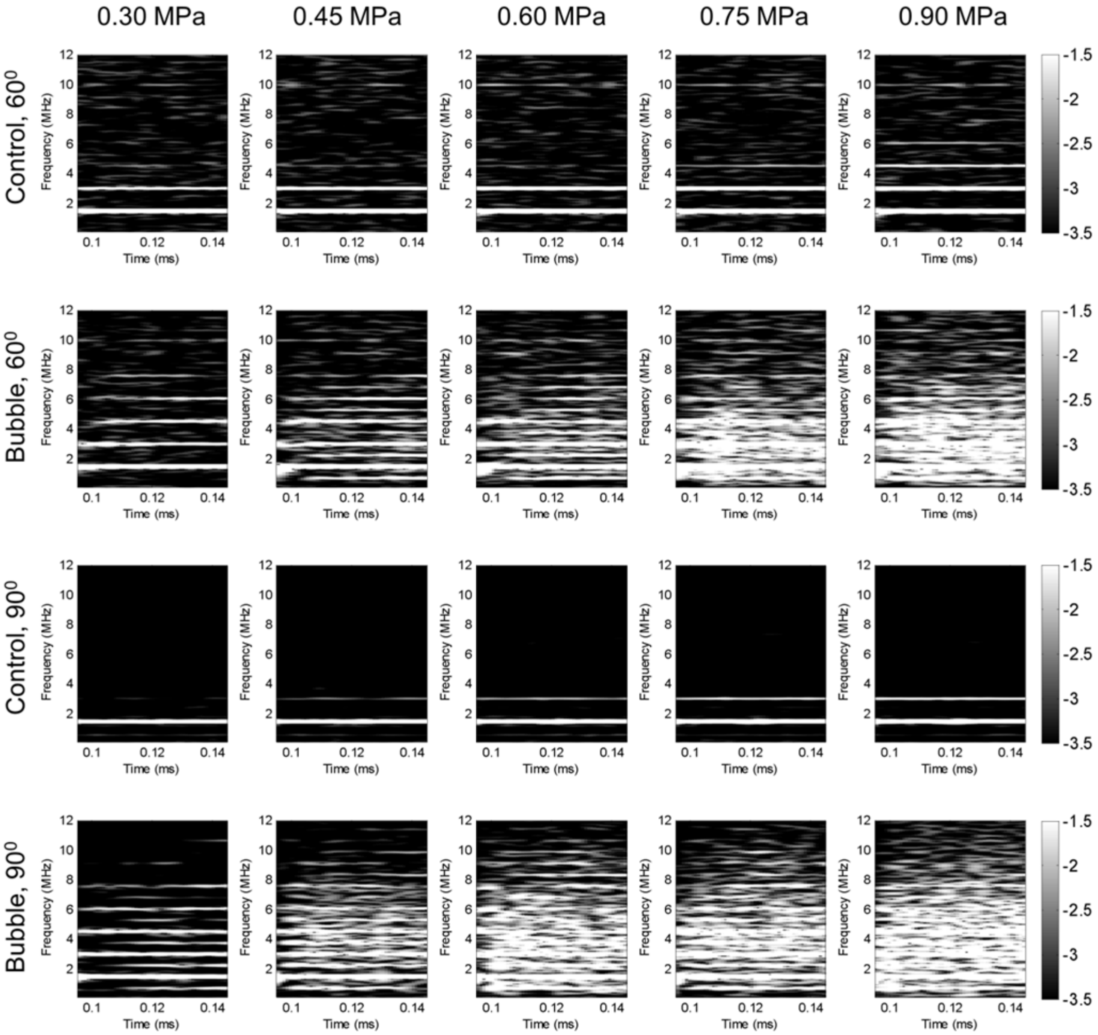

Figure 3.6 – Spectrogram of the first pulse in the phantom study without and with the microbubbles at 5 distinct acoustic pressures. Acoustic emissions were acquired with a PCD positioned at 60º and 90º from the longitudinal axis of the FUS beam. No broadband acoustic emissions were detected without the microbubbles while with the microbubbles the broadband acoustic emissions were detected at pressure at or higher than 0.45 MPa. At 0.30 MPa, the ultra-harmonics were detected at the 90º-PCD but not the 60º-PCD.

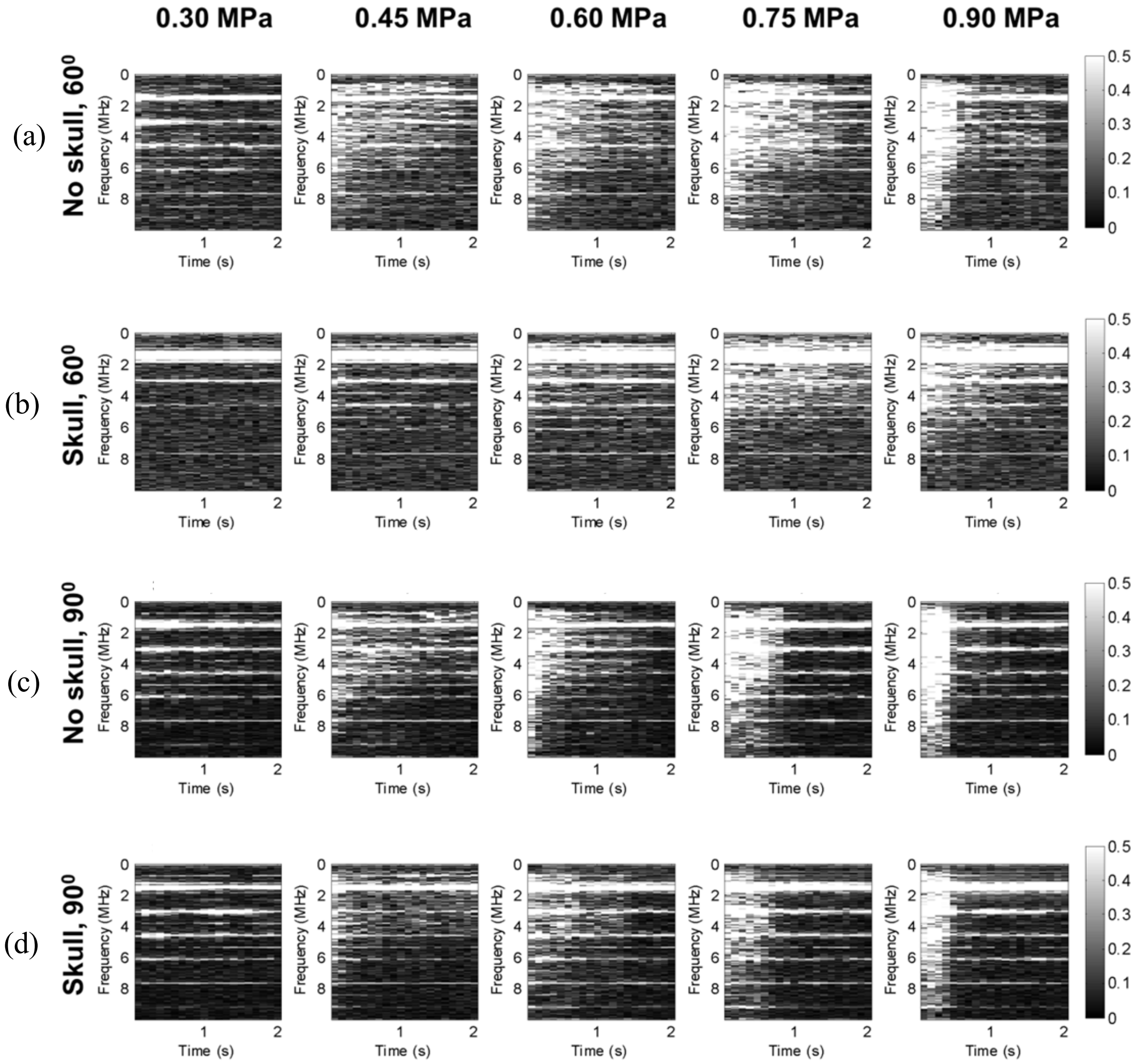

Figure 3.7 – The spectrogram (a,c) without the skull and (b,d) through an *ex vivo* skull at five distinct acoustic pressures. The duration of each sonication was 2 s, i.e., 20 pulses. Please note that the broadband acoustic emissions could only be detected at the first two pulses at 0.45 MPa in (b) and their amplitudes were much lower than at higher pressures.

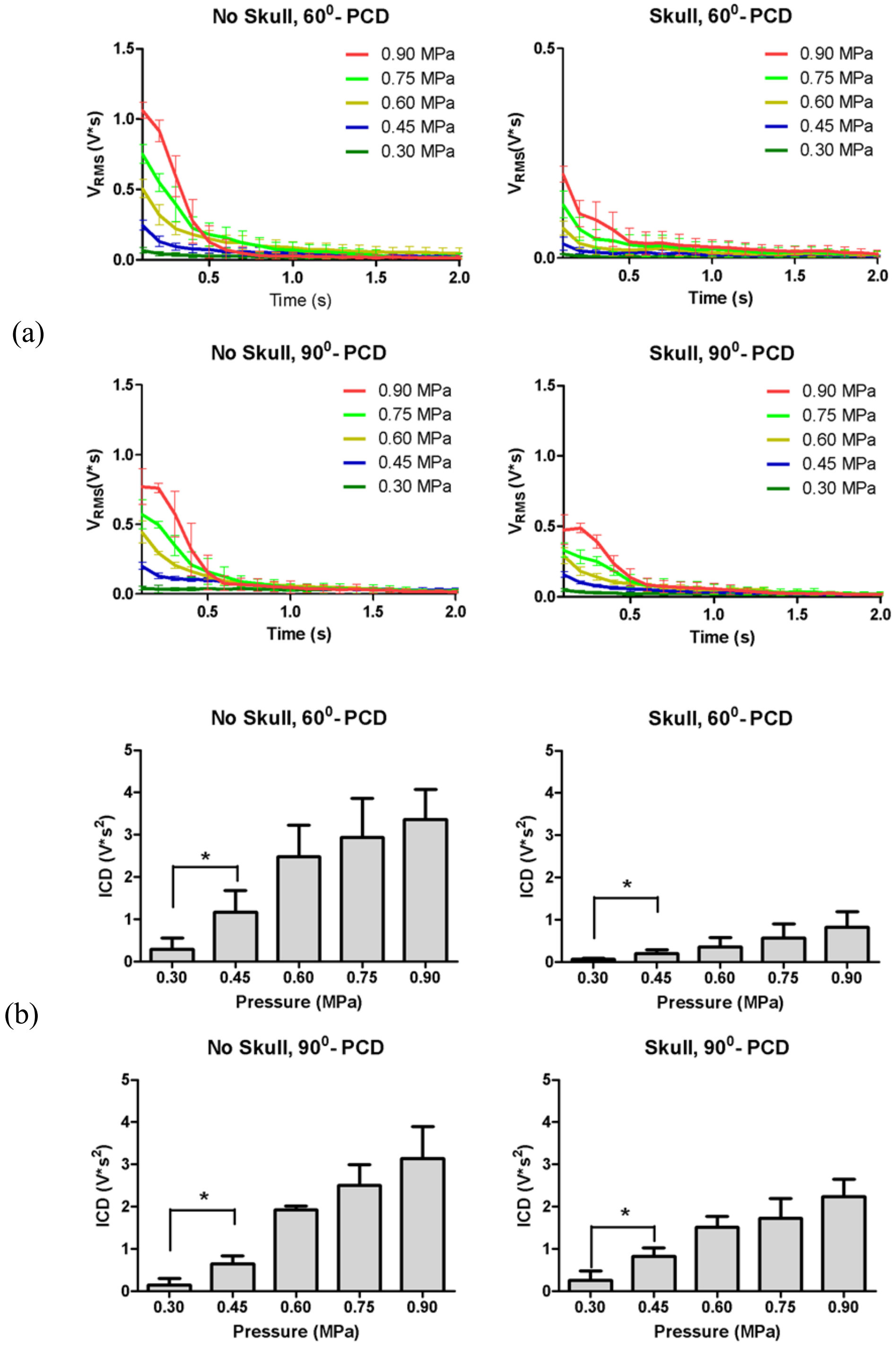

Figure 3.8 – (a) Root mean square (V_{RMS}) and (b) ICD at 5 distinct acoustic pressures are indicated here. In order to emphasize the difference between 5 distinct acoustic pressures, the limit of the y-axis is from 0 to 0.5 at 60º-PCD, with the presence of skull. ICD was quantified as the area below V_{RMS} curve, at each pressure. Twenty pulses were applied for each sonication set. The ICD at 0.45 MPa was significantly larger than 0.30 MPa (*:$P < 0.05$, indicates the threshold of inertial cavitation).

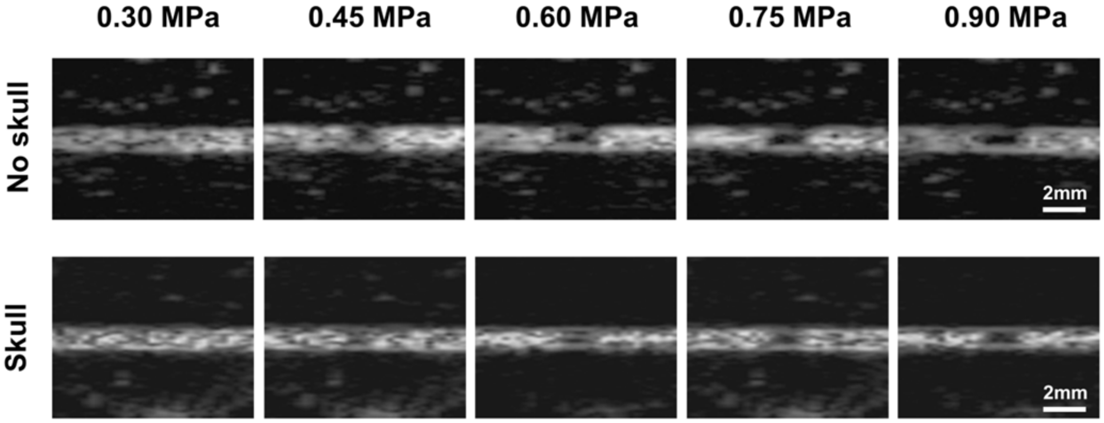

Figure 3.9 – B-mode imaging provided a means of determining whether the microbubbles were present following sonication. Images were acquired after 2 seconds of sonication at 5 distinct acoustic pressures in skull and non-skull experiments.

The broadband response as detected by the PCD was quantified by using the V_{RMS} at each pressure amplitude (Fig. 3.8(a)) and the ICD (Fig. 3.8(b)). The ICD, which is shown in Fig. 3.8(b), was calculated by taking the integral of the V_{RMS} variation. The V_{RMS} curve depicted no significant difference between different pressure amplitudes beyond 1 s. As indicated by the ICD calculations (Fig. 3.8(b)), the presence of the skull induced lower ICD and the ICD at 60°-PCD was lower than at 90°-PCD. The ICD at 0.45 MPa was statistically higher than at 0.30 MPa ($P < 0.05$), which confirmed that the threshold of inertial cavitation was around 0.45 MPa.

B-mode images acquired after two seconds of sonication were used to depict the spatial distribution of microbubbles within the vessel at five different pressure amplitudes, with or without the presence of the skull (Fig. 3.9). As the pressure amplitude increased, an increasingly dark region in the center of the B-mode image coinciding with the FUS focus (Fig. 3.10(a)), representing loss of echogenicity, was observed in the focal region.

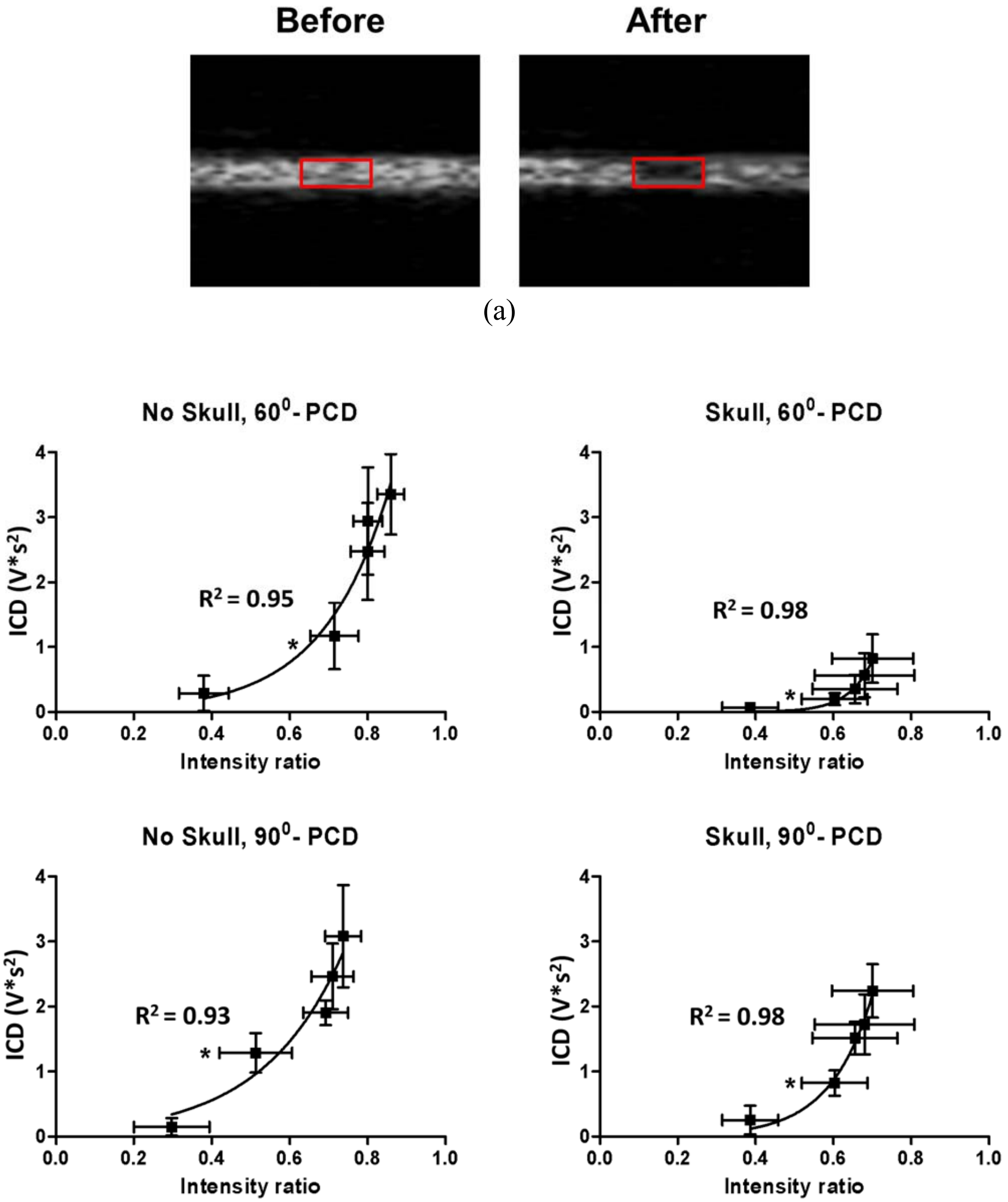

(a)

(b)

Figure 3.10 – (a) The illustration of ROI and (b) the correlation between ICD and the intensity decrease ratio of B-mode imaging at 5 distinct acoustic pressures (0.30, 0.45, 0.60, 0.75 and 0.90 MPa). The intensity decrease ratio at 0.45 MPa was significantly larger than 0.30 MPa (*: $P < 0.05$)

With the skull in place, the dark region appeared only when the pressure amplitude was at and above 0.45 MPa, which was consistent with the aforementioned threshold of inertial cavitation from the PCD (Fig. 3.8). The spatial maps were compared against the ICD measurements. The region of interest (ROI) around the focal region of FUS was traced and the intensity ratio (Eq. 3.1) decrease was calculated from the radio frequency (RF) signal corresponding to the B-mode images (Fig. 3.10(a)). The intensity ratio was found to be statistically different between 0.30 MPa and 0.45 MPa ($P < 0.05$) (Fig. 3.10 (b)). This was also consistent with the results of the ICD quantification.

3.3.2 *In vivo* transcranial cavitation detection in mice

The confirmation of BBB opening and the corresponding spectrogram are depicted in Fig. 3.11. As a result of the deposition of gadodiamide into the brain parenchyma through the BBB opening, the MRI indicated that the threshold of BBB opening was at 0.30 MPa (Fig. 3.11(a) and (c)), but the spectrogram showed that the broadband response occurred at 0.45 MPa (Fig. 3.11(b) and (d)). After bubble administration, higher harmonics could be detected, including the 3rd harmonic at 0.15 MPa without BBB opening, the 3rd to 5th harmonics at 0.30 MPa with BBB opening, and the 3rd to 8th harmonics together with the broadband response and BBB opening at 0.45 MPa and 0.60 MPa. The threshold of inertial cavitation was consistent between the two systems (Fig. 3.6(b), (d)) and the duration of the broadband response was around 5 μs at 0.45 MPa. However, the duration of the broadband response detected from the 10-MHz P/E transducer at 0.60 MPa was 0.5 ms longer than the hydrophone, especially at higher frequencies. At 0.30 MPa, not only the 3rd to 5th but also the 6th to 8th harmonics could be detected by the 10-MHz P/E transducer. An ultra-harmonic peak between the 7th (10.5 MHz) and 8th harmonics (12 MHz) was detected as indicated in Fig. 3.11(d).

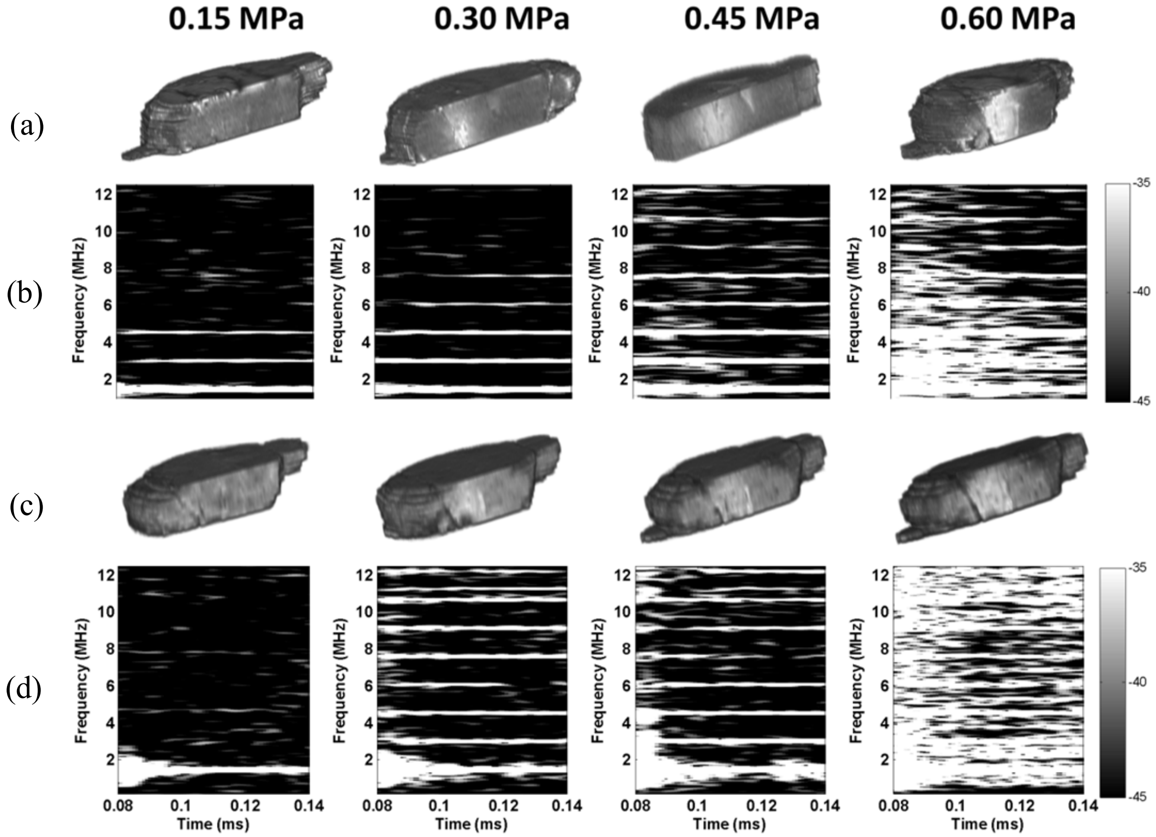

Figure 3.11 – BBB opening using confirmed by 3D-MRI images, using (a) System-A and (c) System-B. The corresponding spectrograms of the first pulse using (b) System-A and (d) System-B showed that the broadband acoustic emissions were detected at 0.45 MPa and 0.60 MPa but not at 0.15 MPa and 0.30 MPa. The 3D-MR images confirmed that the BBB could open at 0.30 MPa, i.e., without inertial cavitation.

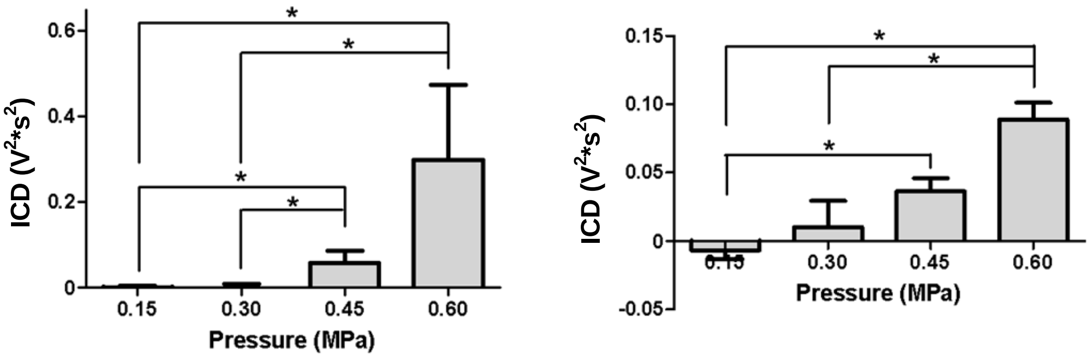

(a) (b)

Figure 3.12 – The inertial cavitation dose (ICD) at 4 distinct acoustic pressures (a) using the System-A and (b) using the System-B. ICD was quantified as the area under the V_{RMS} curve from 0.095 ms to 0.145 ms, at each pressure. The signal used for quantification was from a focused hydrophone. For the System-A, the ICD at 0.45 MPa and 0.60 MPa was significantly higher than 0.15 MPa and 0.30 MPa (*: $P < 0.05$). For the System-B, the ICD at 0.60 MPa was significantly higher than at 0.30 MPa and 0.15 MPa. The ICD at 0.45 MPa was also significantly higher than 0.15 MPa (*: $P < 0.05$).

The broadband response as detected by the PCD was quantified using the ICD (Fig. 3.12). As indicated by the ICD calculations, the ICD at 0.45 MPa and 0.60 MPa was statistically higher than at 0.30 MPa and 0.15 MPa ($P < 0.05$) (Fig. 3.12(a)), which confirmed that the threshold of inertial cavitation during the BBB opening was around 0.45 MPa. The histological findings are shown in Figs. 4.13 and 4.14. In the cases of BBB opening at 0.30 MPa and no BBB opening at 0.15 MPa confirmed by 2D-MR horizontal images, no cell damage, e.g., red blood cell (RBC) extravasations or neuronal death [91], was observed after histological examination (Fig. 3.13 and 4.14, (a-f)). In the cases of BBB opening at 0.45 MPa, no extravasations were detected in the sonicated brain regions (Fig. 3.13 and 4.14, (j-l)) even though a broadband response was detected (Fig. 3.11(b), (d)). Brain samples sonicated at 0.60 MPa showed higher incidence of microscopic damage at multiple distinct damaged sites (Fig. 3.13 and 4.14, (j-l)). The exposure pressures that resulted in RBC extravasations were those associated with the largest broadband response.

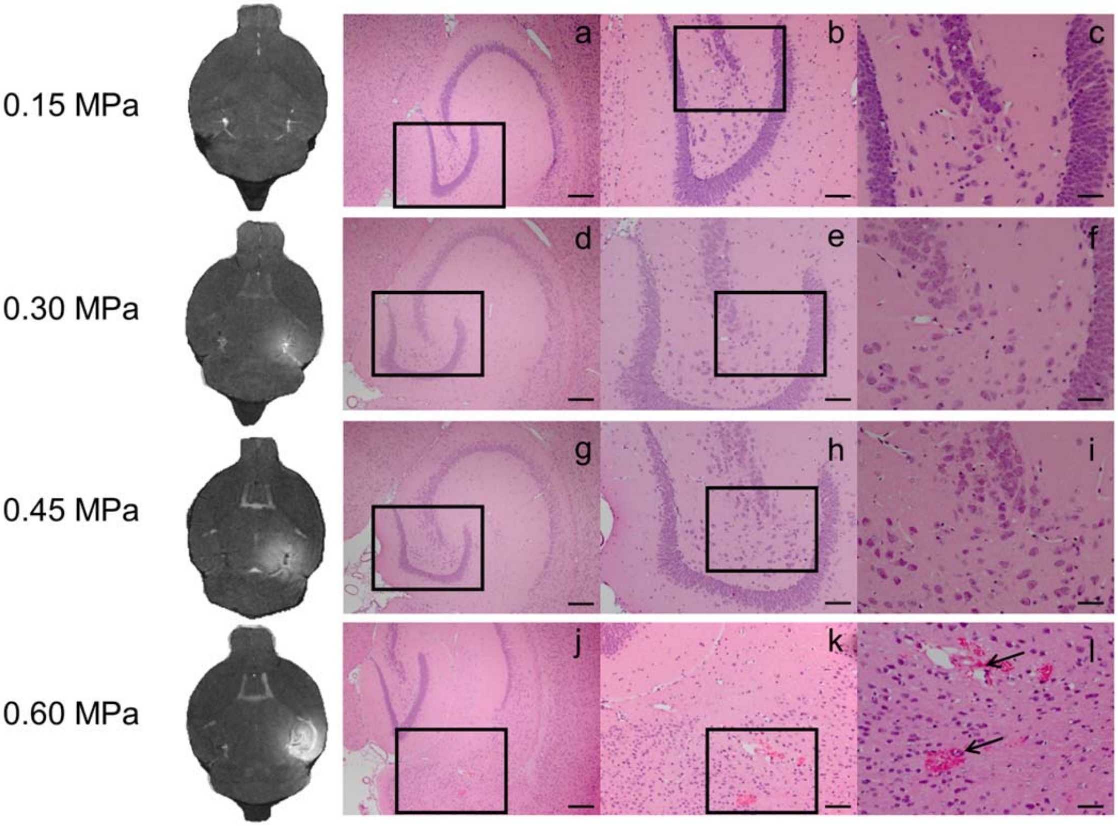

Figure 3.13 – 2D-MRI images and H&E-stained horizontal sections of the BBB-opened hippocampi at (a-c) 0.15 MPa, (d-f) 0.30 MPa, (g-i) 0.45 MPa, and (j-l) 0.60 MPa using the System-A with microbubbles administration. Sonicated brains at 0.15 MPa, 0.30 MPa and 0.45 MPa showed no histological damage. Brain samples sonicated at 0.60 MPa (j-l) showed higher incidence of microscopic damage at multiple distinct damaged sites. Black arrows point to the RBC extravasations. Black boxes in the left and middle column indicate the enlarged regions shown in the middle column and right column, respectively. Magnifications and scale bars in (a,d, g, j) were 40x and 200 μm, in (b, e, h, k) 100x and 100 μm, and in (c, f, I, l) 200x and 50 μm, respectively.

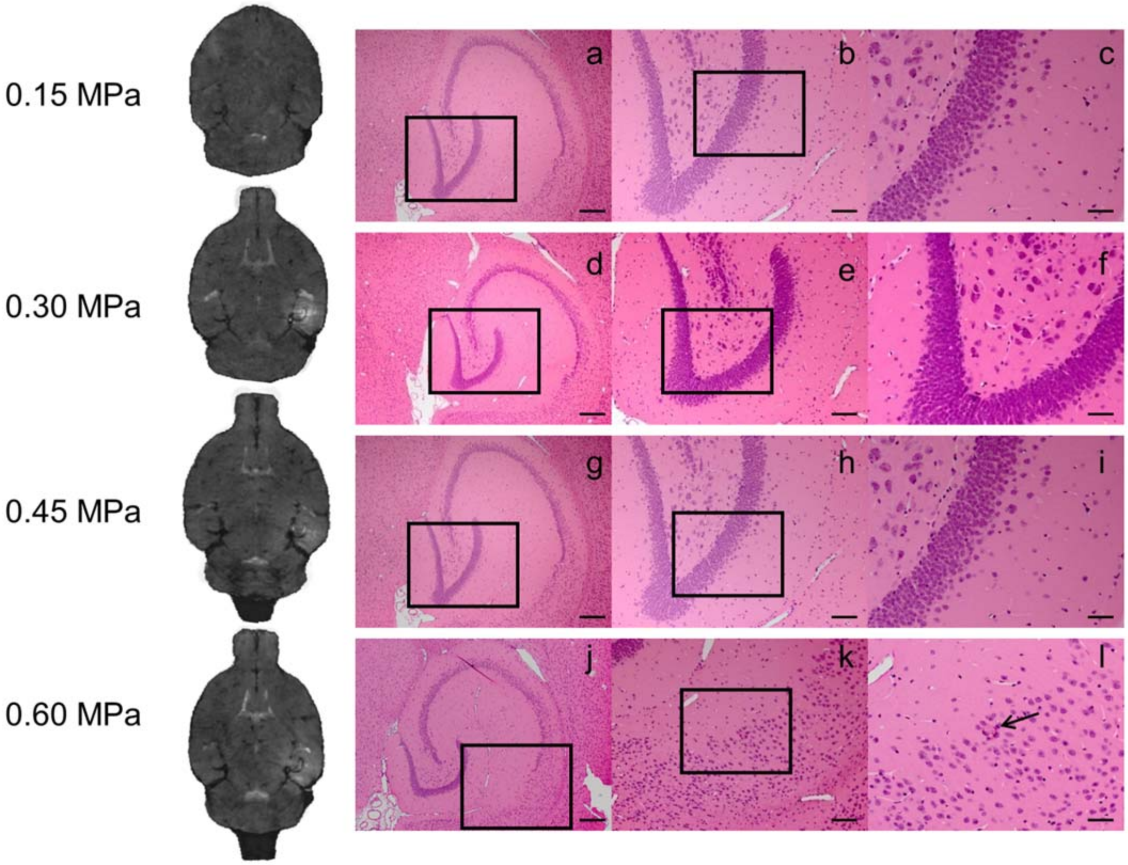

Figure 3.14 – 2D-MR images and H&E-stained horizontal sections of the BBB-opened hippocampi at (a-c) 0.15 MPa, (d-f) 0.30 MPa, (g-i) 0.45 MPa, and (j-l) 0.60 MPa using the System-B with microbubbles administration. Sonicated brains at 0.15 MPa, 0.30 MPa and 0.45 MPa showed no histological damage. Minor microscopic damage was noticeable in one location of the right hippocampus sonicated 0.60 MPa, constituting one distinct damaged site (g-i). Black arrows point to RBC extravasations. Black boxes inside the left and middle column showed enlarged regions in the middle and right columns, respectively. Magnifications and scale bars in (a,d, g, j) were 40x and 200 μm, in (b, e, h, k) 100x and 100 μm, and in (c, f, I, l) 200x and 50 μm, respectively.

3.4 Discussion

3.4.1 Phantom validation of the skull effect

The peak-rarefactional pressure threshold of inertial cavitation in the presence of preformed microbubbles in a vessel phantom by FUS in the absence or presence of a skull was investigated in this chapter. Qualitatively and quantitatively, the threshold of inertial cavitation was identified to be at the peak-rarefactional pressure of 0.45 MPa with or without an *ex vivo* skull in place (Figs. 3.4-3.10). The frequency spectrum of the first pulse showed that the broadband response appeared when the pressure was at, or higher than, 0.45 MPa (Fig. 3.5). Spatial mapping using B-mode imaging provided further evidence of bubble disruption caused by inertial cavitation (Fig. 3.9). The decrease in echogenicity was consistent with the emergence of the broadband response shown in Fig. 3.5, which demonstrated that the microbubbles were disrupted by inertial cavitation. Quantitative results of spatial maps also showed that the image intensity ratio (Eq. (3.1)) at 0.45 MPa was larger than at 0.30 MPa ($P < 0.05$). Hence, both the PCD frequency response and the spatial information from B-mode imaging could be used to determine the threshold of inertial cavitation.

This study also investigated the effect of the skull to predict feasibility in *in vivo* transcranial applications where transcranial cavitation detection is required. At the same pressure amplitude, the ICD was lower in the presence of the skull (Fig. 3.8(b)), which showed that the acoustic wave was distorted by the skull. In order to reduce skull thickness effects being responsible for the difference between the 0º and 60º cases, based on our measurements, the area of the parietal bone, which was assumed to have uniform thickness, was around 5 mm^2 which would cover the ultrasound path for both the 0° and 60° cases. When the PCD was placed at 60°, the PCD signal amplitude was the lowest because the acoustic wave propagated through the skull twice (Fig. 3.5(b), Fig. 3.8(b)). However, the quantification showed that the significant broadband response could still be detected at 60°-PCD (Fig. 3.8(b)). Hence, the PCD system used in this study might be suitable for the *in vivo* applications.

The broadband response appeared when the microbubbles were sonicated at or above 0.45 MPa. The broadband response at 0.90 MPa persisted for approximately 0.5 s, which was consistent with the V_{RMS} curves (Fig. 3.8(a)). Inertial cavitation may have caused microbubble destruction, thus hampering the likelihood of subsequent inertial cavitation. However, harmonics were still detectable during the entire sonication at each pressure amplitude (Fig. 3.7) and these harmonics appears to have been due to microbubbles (Fig. 3.15(b)), as they were absent in the degassed water filled vessel (Fig. 3.15(a)). Figure 8 showed that only the 1st and 2nd harmonics appeared when degassed water was sonicated, while distinct 1st to 6th harmonics were observed in the presence of microbubbles. There are three possible explanations for this phenomenon. First, since the focal region of the PCD was larger than the focal region of FUS (Fig. 3.1), the harmonics may be due to the oscillation of microbubbles, which were near the focal region of FUS but had not experienced the full extent of the peak pressure amplitude. Second, some microbubbles may have adhered to the vessel wall and they continued to be acoustically driven. Third, the initial microbubbles may have been disrupted into smaller bubbles, which were not detectable on the B-mode images. These smaller bubbles could then be acoustically driven to emit the characteristic harmonics.

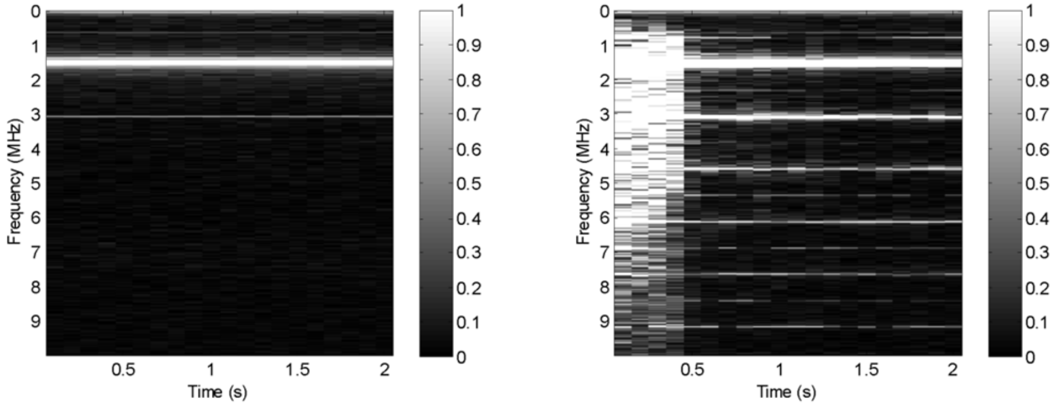

(a) (b)

Figure 3.15 – Comparison between (a) water and (b) bubble experiments without skull for spectrogram from 90º-PCD at 0.90 MPa. Broadband acoustic emissions and the amplitude of the 3rd to 6th harmonics were not obtained in the water experiments.

Quantitative results of the frequency response and spatial maps indicated the threshold of inertial cavitation (Fig. 3.10(b)). When the pressure was higher than 0.60 MPa, no significant difference was shown in the intensity ratio, since the microbubbles in the focal region might have completely disappeared after 2 s of sonication. In contrast, the ICD increased exponentially when the pressure exceeded the threshold of inertial cavitation.

Here, we provided a simplified method to show that the ICD was influenced by the skull unlike the threshold of inertial cavitation. This implied that, if the BBB is opened at 0.30 MPa[74], the mechanism involved at that pressure may be stable cavitation. However, some issues remain to be investigated further in order to understand the mechanism of BBB opening. The diameter of the vessel in this study was 610 μm, which was larger than most murine vessels. The internal carotid artery of the mouse brain has a diameter of 218±19 μm[126]. The compliance or stiffness of the vessel also influences the bubble behavior [110]. Therefore, a smaller diameter vessel phantom should be implemented to confirm the threshold of inertial cavitation of microbubbles within smaller vessels, such as 100 to 300 μm, will not be affected by the skull.

No flow effects were investigated in this study unlike in the *in vivo* case. The concentration of microbubbles may also affect the threshold of inertial cavitation, which has been shown to decrease with the concentration of microbubbles in the vessel phantom[127]. The effect of flow and concentration will be investigated in future implementations.

The PCD sensitivity also needs to be considered. The broadband response captured by the PCD is dependent on its sensitivity. The results of this study showed that the threshold of inertial cavitation was equal to 0.45 MPa. However, it might be possible that the broadband response was not captured at 0.30 MPa because the PCD sensitivity was not high enough. However, based on the complementary results of the spatial maps from the B-mode imaging, we believe that the sensitivity of the PCD used in this study is deemed sufficiently high.

Two different angles of PCD were used to understand whether the results will be influenced by the presence of the skull. At 0.30 MPa without the skull, some signal at 60º-PCD (Fig. 3.5(a)) was higher than at 90º-PCD (Fig. 3.5(c)). The signals obtained by 60º-PCD may include some reflected signals from the surface of the phantom, which may not have been captured by 90º-PCD. The PCD used in this study had a cylindrical focus, which was ideal when the hydrophone was positioned perpendicular to the focused ultrasound transducer's main axis. When positioned in this manner, the cylindrical focal region closely matches the ellipsoidal shape of the FUS focal spot (Fig. 3.1(b)). If the PCD is placed at a 60º angle to the focused ultrasound transducer's main axis, other reflected signals from the surface of the phantom and the effect of the skull will also be observed. Therefore, it may be better to place the PCD at 90 degrees for vessel phantom experiments.

3.4.2 *In vivo* transcranial cavitation detection in mice

The presented study noninvasively detected *in vivo* acoustic emissions during FUS-induced BBB opening and showed that BBB could be opened without inertial cavitation or cell damage. The reliability, sensitivity, and transcranial capability of our PCD setup to detect acoustic emissions was validated first in a phantom[119]. Broadband emission, a signature of IC, could be detected transcranially (with the 60°-PCD configuration) and the IC threshold was identical to that at 90°-PCD (non-transcranial PCD). Hence, the PCD system used in this study was deemed suitable for transcranial *in vivo* detection of inertial cavitation.

Both the phantom and *in vivo* studies indicated that the threshold of inertial cavitation during BBB opening was at the peak-negative pressure of 0.45 MPa. This was verified qualitatively and quantitatively. When the sonication was performed one minute after bubble administration, the bubble concentration in the mouse body would decrease because the increased circulation time would increase the probability of bubble disruption, dissolution, absorption and clearance. However, the threshold of the broadband response was not affected by this one-minute delay, which indicated that the variation of bubble concentration within one minute inside the capillaries of the brain does not significantly affect the threshold of inertial cavitation.

Our findings indicated that the BBB remained intact at 0.15 MPa and opened at 0.30 MPa, which was consistent with our previous work on the threshold of BBB opening as confirmed using fluorescence imaging[74,91]. In addition, a broadband response was not detected at the pressure of 0.30 MPa. Our findings were in good agreement with McDannold et al.'s findings that indicated that the BBB in the rabbit after craniotomy would be intact at 0.14 MPa and open at 0.29 MPa. The threshold of broadband response was also found to fall around 0.40 MPa in their study. On the other hand, they proposed that the second and third harmonics may be used to monitor BBB opening. However, in our study, the third harmonic could not be used to monitor BBB opening because it could still be detected at 0.15 MPa, which was shown not to induce BBB opening. Based on the results of our phantom study, at 0.30 MPa, the ultra-harmonics were effectively filtered by the skull (Fig. 3.6), which suggested that the stable cavitation might be responsible for BBB opening at 0.30 MPa *in vivo* and that the associated ultra-harmonics could not be detected by the broadband hydrophone, potentially due to sensitivity limitation and the skull presence (Fig. 3.11(b)). However, the signals from 10-MHz P/E transducer with *in vivo* implementation (Fig. 3.11(d)) showed that not only could higher harmonics be detected at 0.30 MPa but also the ultra-harmonics at 11.25 MHz. Therefore, both transcranial phantom and *in vivo* studies showed that BBB opening might be induced by stable cavitation only, at or near the opening threshold.

In the *in vivo* study, the fourth and fifth harmonics could be detected and associated with BBB opening at 0.30 MPa (Fig. 3.11(b, d)). This was also consistent with our phantom work, which indicated that the fourth and fifth harmonics were detected at 0.30 MPa by the 60°-PCD (Fig. 3.6). At 0.30 MPa, nonlinear oscillations may induce the fourth and fifth harmonics, and bubble expansions may lead to BBB opening. In simulations, the resonance frequency of 1-2 μm-diameter microbubble was about 4-8 MHz, which included the fourth and fifth harmonics of 1.5 MHz[128,129]. As a result, the fourth and fifth harmonics detected by the broadband hydrophone might serve as a reliable indicator for BBB opening.

The spectrogram used in this study could clearly elucidate the onset and duration of IC within a signal pulse. In this study, the IC occurred at the beginning of sonication and the longest duration was around 50 μs as detected by the hydrophone (Fig. 3.11(b)) and 500 μs as detected by the 10-MHz P/E transducer (Fig. 3.11(d)) at 0.60 MPa. The overlap of the focal regions of the FUS and the 10-MHz P/E transducers was larger than with the broadband hydrophone, hence the longer duration of inertial cavitation detected. Therefore, the System-B will be used in the following *in vivo* studies in mice.

At 0.45 MPa, the broadband response was detected at the first but not the second pulse. However, at 0.60 MPa, a broadband response was detected in the first three pulses. A likely explanation for this may be that the pulse repetition frequency (PRF) used in this study was not low enough to allow blood reperfusion in the capillaries between pulses. As a result, the microbubbles were disrupted after the first pulse but not a sufficient number of microbubbles replenished the vessel within the interval of 80 ms (20% duty cycle, PRF = 10 Hz). However, harmonics could be detected at each pulse. Since the focal region of the PCD was larger than the FUS focal region (Fig. 3.3), the harmonics may be due to the nonlinear oscillation of the microbubbles, which were near the FUS focal region but were not activated at the highest pressure amplitude.

In the phantom study, the sub-harmonic and ultra-harmonics were clearly detected at 0.30 MPa when the detection was performed without the skull in the PCD path, i.e., in the 90°-PCD case, but it was masked by the skull at 60°-PCD. In the *in vivo* study, sub-harmonics and ultra-harmonics could not be detected transcranially and are thus probably filtered by the skull. Since the broadband response is more commonly associated with inertial cavitation, inertial cavitation was detected and quantified through the measurement of broadband emissions at different pressures.

The histological results in this study were consistent with existent literature that investigated the relationship between tissue damage and inertial cavitation[113,130]. Some red blood cell extravasations were induced at 0.60 MPa but no extravasations could be found at 0.15, 0.30 or 0.45 MPa. Even with higher ICD estimated at 0.60 MPa, the extravasations were limited to 2-3 sections. However, in order to investigate more specific forms of cellular damage (i.e., apoptosis), more sensitive staining protocols, such as TUNEL, will be applied in future studies.

Standing waves might also be generated due to the long pulse lengths used in our *in vivo* study that may lead to peak pressure variations within the mouse brain. However, in this study, the threshold of inertial cavitation was identical between the phantom and *in vivo* studies, which indicated that the standing wave effects might not be significant *in vivo*. This is in agreement with simulation findings predicting the standing wave effects intracranially[131]. Figure 3.11 also showed that the inertial cavitation occurred at the beginning of sonication. Therefore, our results on the IC threshold may be independent of the number of cycles and thus potential standing wave effects. Of course, we might have to take into account the fact that the *in vitro* (atmospheric) and *in vivo* (i.e., capillary) pressures were not the same. However, the identical threshold of BBB opening across all mice and the phantom study strongly indicates the insignificance of the capillary pressure effect.

Since two systems and poly-dispersed microbubbles were used in this chapter, it is difficult to identify the role of stable cavitation. In order to determine the effect of stable cavitation with distinct microbubble diameter, the stable cavitation dose will be quantified in the next chapter.

Because the bubble response could be detected through the skull, more parameters should be investigated to unveil the mechanism of BBB opening. Different PRF could be applied to obtain the blood velocity, which will affect the reperfusion rate of microbubbles. The microbubbles used in this study were commercial ultrasound contrast agents, which were poly-dispersed. Because the threshold of BBB opening was shown to be higher for the 1-2 μm than the 4-5 μm bubbles[56], the size-dependent threshold of inertial cavitation will be investigated to identify the role of different bubble diameters on the inertial cavitation and BBB opening, which will be described in detail in *Chapter 4.*. Finally, a smaller pressure step size can be used to identify a more precise IC pressure threshold associated with BBB opening by using more sensitive instrumentation.

3.5 Conclusion

In summary, preliminary investigation on the *in vivo* transcranial cavitation detection and quantification of the inertial cavitation activity during BBB opening was presented. The bubble behavior was shown detectable in mice *in vivo* through the intact scalp and skull. The threshold of inertial cavitation using transcranial FUS and microbubbles in a vessel phantom was also investigated to provide complementary information to the *in vivo* findings. This novel system will allow us to investigate the role of microbubbles and differentiate the mechanism between SC- and IC-induced BBB openings.

Chapter 4

Microbubble-Dependent Mechanism of Blood-Brain Barrier Opening Using Focused Ultrasound and Microbubbles

4.1 Introduction

In *Chapter 3,* an *in vivo* transcranial cavitation detection system was successfully developed. Then deeper investigations regarding the bubble property and acoustic parameters should be performed. Since microbubbles are the necessary agents to induce a safe BBB opening, their role needs to be thoroughly investigated. In this chapter, we aim at understanding how the interaction between microbubbles and ultrasound-induced BBB opening and corresponding permeability. Following the development of *in vivo* transcranial PCD system, this system was applied to order to unveil the physical effects of different microbubble properties, including diameter and shell component, responsible for FUS-induced BBB opening,

Typically, most reported studies in FUS-BBB opening use commercially available and poly-dispersed microbubbles, such as Definity®, Optison®, or Sonovue®. Thus, it has been difficult to determine the role of the microbubble properties in those applications. The bubble diameter is inversely proportional to the resonance frequency, when every other bubble parameter remains the same. For a bubble constrained in a vessel, regardless of the shell property, the resonance frequency increases when the bubble size decreases[128,132]. For example, when the bubble is confined in a compliant, 10-μm-diameter vessel, its resonance frequency at a diameter of 2 μm, 4 μm, 6 μm and 8 μm is 3.92 MHz, 1.93 MHz, 1.41 MHz and 1.26 MHz, respectively[132]. When microbubbles are confined within a vessel, the bubble behavior changes due to the vessel wall constraints. Some numerical studies have predicted how the vessel size and stiffness affect the bubble behavior. In rigid vessels, it has been shown that the resonance frequency of microbubbles decrease as the vessel diameter decreases[128]. The resonance frequency of microbubbles also decreases as the vessel compliance decreases[132,133].

Therefore, the frequency of the FUS used in this study (1.5 MHz) is close to the resonance frequency of 4-5 μm bubbles. High-speed camera findings have also indicated that the pressure threshold of bubble fragmentation increases with bubble size[105]. Recently, mono-dispersed microbubbles were shown as an important factor in high frequency ultrasound imaging[134]. It has also been shown that the pressure threshold of BBB opening is bubble-size dependent. The threshold of 1-2-μm bubbles was higher than that of 4-5-μm microbubbles[56], which underlined the importance of the microbubble role in BBB opening. Hence, the physical mechanism of FUS-induced BBB opening may also be bubble-size dependent, so understanding the role of different microbubble sizes is very important to unveil the physical mechanism of BBB opening.

Besides the diameter, the shell has been shown to dictate bubble behavior. The main shell constituent is lipid/surfactant, albumin, and lipid for the Definity®, Optison®, and Sonovue® bubbles, respectively. The pressure threshold of inertial cavitation has been shown to differ between the aforementioned contrast agents[135]. Because the shell and diameter range distribution of commercial microbubbles are different, both factors need to be investigated. Theoretical models have shown a clear dependence of the bubble wall velocity, attenuation coefficient in a bubbly liquid, and resonance frequency on the viscosity of the surface layer[136,137]. The increase in shell stiffness and shell friction would increase the damping coefficient, and affect the oscillation[138]. Therefore, it is expected that stiffer shells may undergo smaller expansion during oscillation. Recently, Marmottant et al. have proposed a model to describe the buckling behavior of lipid-shelled microbubbles[139].

Moreover, it has been shown that the acyl-chain length (i.e., lipid hydrophobic chain) dictates the dissolution behavior of the lipid monolayer-coated microbubbles[140] and the ultrasound-induced microbubble fragmentation[141]. The surface shear viscosity of the phospholipid monolayer-coated microbubbles has also been found to be acyl-chain length dependent[142]. In addition, some studies have shown that the polyethylene glycol (PEG), an additional component of the lipid shell composition, may affect the fraction of the bubble fragmentation induced by inertial cavitation[143,144]. Therefore, shell effects are expected to affect the acoustic response from microbubbles. Until now, however, most models or experimental studies were implemented on a single free bubble, i.e., not *in vivo*. The bubble behavior may be affected due to wall constraints when the bubble is confined within a vessel. It has been shown that the microbubble resonance frequency decreases, and the pressure threshold of inertial cavitation increases, as the vessel diameter or compliance decreases[128,145]. The expansion ratio (R(t)/R(0)) of a microbubble in a 8-μm capillary is half of a free bubble[132]. The shell effect is still unknown *in vivo*, especially in the brain vasculature.

The objective of this chapter was to unveil the physical effects of microbubble diameter and shell properties responsible for FUS-induced BBB opening. First, the physical effects of different microbubble sizes were determined. Microbubbles were size-isolated into 1-2, 4-5, and 6-8-μm diameter ranges and the acoustic response of different-sized microbubbles were transcranially detected during BBB opening. Second, we proposed a method to investigate the effect of lipid shell composition on the microbubble response in the brain vasculature. In order to exclude the impact of bubble size, the diameter of microbubbles was kept constant at 4-5-μm. Several tools were used in these two investigations. First, MRI was used to determine the threshold of BBB opening and the BBB opening volume, as well as to generate the permeability maps based on the kinetic model determined from previous study (*Appendix*). Second, during BBB opening, the acoustic emission from microbubbles with three diameters or with three acyl-chain lengths was detected transcranially and noninvasively. The spectrogram, stable cavitation dose (SCD), and inertial cavitation dose (ICD) were then generated to identify the threshold of inertial cavitation and the bubble behavior of distinct bubble properties. Third, in each study, histology was used to detect any macroscopic effects of BBB opening and T_2 images were used to assess the possibility of hemorrhage in the sonicated area. In addition, in order to determine the precise PRP threshold of inertial cavitation of each microbubble diameter, simulation based on several theoretical models and phantom validation were implemented.

4.2 Theoretical models for microbubble oscillation

Microbubbles are the necessary agent to induce BBB opening within safe pressure ranges (i.e., by avoiding the thermal effects). Since the theoretical model about microbubbles can be used to explain the bubble behavior, including the radius, bubble wall velocity, and frequency response, an appropriate theoretical model will be used for the simulation to identify the behavior of lipid-shelled microbubbles under FUS. A variety of models have been developed to study bubble dynamics in liquids, Qin et al.[146] provided a detailed description regarding bubble behavior simulation, including some main models, such as the classic Rayleigh-Plesset equation about unshelled bubble in incompressible unbounded liquid[147], Keller and Miksis equation about liquid compressibility[148], and shell property derived by Church et al[136]. Specifically, bubble dynamics regarding phospholipids shell property has been proposed in 1995[139]. Since the microbubbles used in our study, Definity® and mono-dispersed microbubbles, are phospholipids shell, this model will be used to explain the bubble behavior in our studies.

4.2.1 Oscillation of a free air and a shelled microbubble

Bubblesim, an ultrasound contrast bubble simulation codes, was used for estimating the radial oscillation and scattered sound from an ultrasound contrast bubble under acoustic field. Bubblesim was developed by Dr. Hoff and was in collaboration with the Acoustics Group at the Department of Telecommunications and with the Department of Physiology and Biomedical Engineering, both at NTNU, the Norwegian University of Science and Technology, in Trondheim, Norway[149].

It was implemented as a toolbox in Matlab™ program (Math Works, Natick, MA) on a PC to solve the model of microbubbles and to plot the variation of some parameters (velocity of bubble wall, radius, etc…). Fig. 4.1 showed the basic interface of the Bubblesim. Here the R-P with radiation damping equation was the main model for the response of a bubble behavior under the ultrasound pulse. Most parameters (Pulse Amplitude, Pulse Length, Pulse Center Frequency, Sample rate and Bubble Radius) were the same as the experimental situation.

The shell model was also considered in Bubblesim. Regarding the property of the shell material, most of them were in general not known. Therefore, in this experiment, several literatures were searched to find the related parameters about the shell. An optical method was developed to measure the resonance frequency of contrast agent. Under this model, the shell might slightly influence the resonance frequency. The shell thickness was set for 3 nm and the shell viscosity was 0.19 Pa•s[150]. The shell shear modulus of microbubble was measured based on the observation of effects of ultrasound radiation force. The shear modulus of phospholipid shell was 32 MPa[150]. The aforementioned parameters will be then applied into Bubblesim to obtain the oscillation of shelled microbubbles.

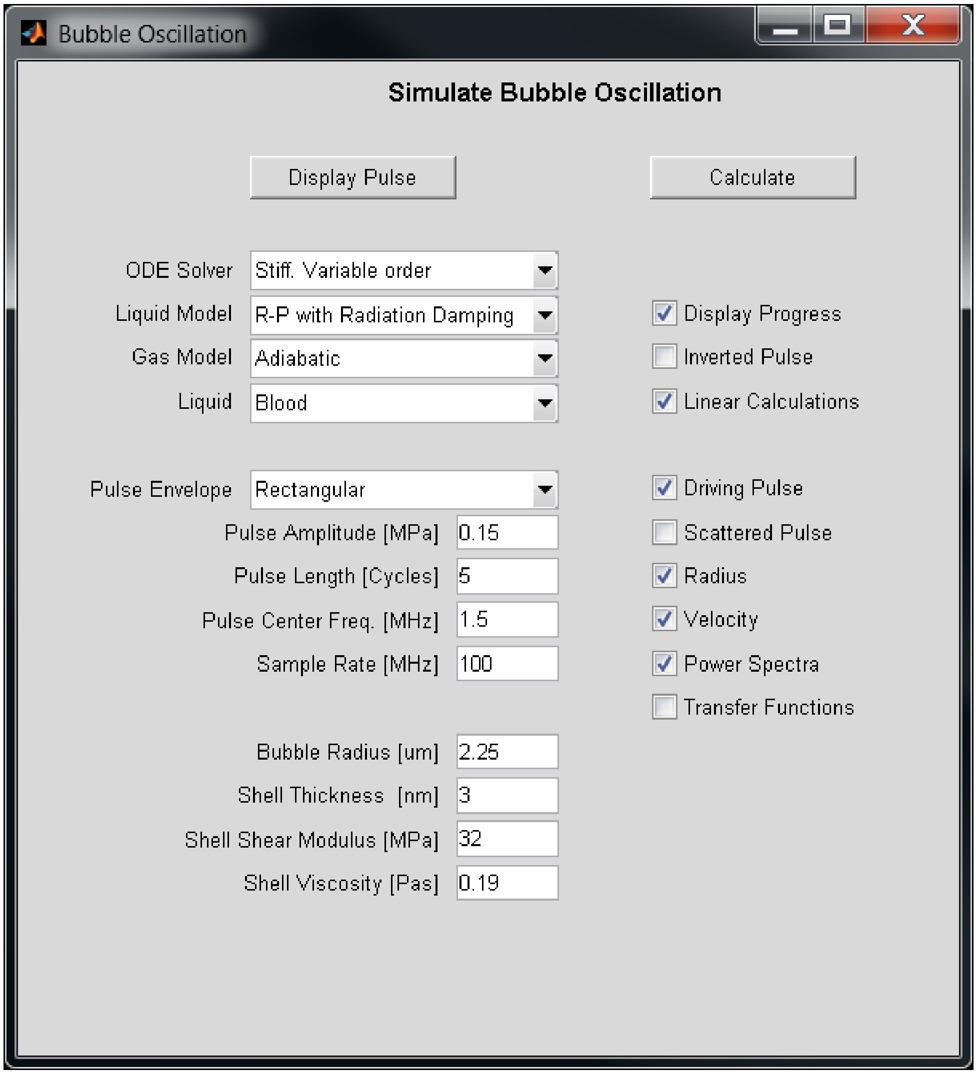

ODE Solver: Stiff. Variable order
Liquid Model: R-P with Radiation Damping
Gas Model: Adiabatic
Liquid: Blood

Pulse Envelope: Rectangular
Pulse Amplitude [MPa]: 0.15
Pulse Length [Cycles]: 5
Pulse Center Freq. [MHz]: 1.5
Sample Rate [MHz]: 100

Bubble Radius [um]: 2.25
Shell Thickness [nm]: 3
Shell Shear Modulus [MPa]: 32
Shell Viscosity [Pas]: 0.19

☑ Display Progress
☐ Inverted Pulse
☑ Linear Calculations

☑ Driving Pulse
☐ Scattered Pulse
☑ Radius
☑ Velocity
☑ Power Spectra
☐ Transfer Functions

Figure 4.1 – The graphical user interface of bubblesim used to specify bubble, pulse and calculation parameters.

4.2.2 Oscillation of a lipid-shelled microbubble

Fig. 4.2 shows three states during the oscillation of the lipid-shell bubble. When the lipid molecules are larger than the bubble surface area (i.e. bubble compression until $R \leq R_{buckling}$), the surface tension will be equal to zero. The bubble surface tension will be equal to the water surface tension when $R \geq R_{ruptured}$. The bubble will behave elastically between those two states. The main equations are as follows:

$$\rho\left(R\ddot{R}+\frac{3}{2}\dot{R}^2\right)=\left[P_0+\frac{2\sigma(R_0)}{R_0}\right]\left(\frac{R}{R_0}\right)^{-3\gamma}\left(1-\frac{3\gamma}{c}\dot{R}\right)-P_0-\frac{2\sigma(R)}{R}-\frac{4\mu\dot{R}}{R}-\frac{4k\dot{R}}{R}-P_{ac}(t) \qquad (5.1)$$

$$\sigma(R)=\begin{cases} 0 & if\ R \leq R_{buckling} \\ x\left(\frac{R^2}{R_{buckling}^2}-1\right) & if\ R_{buckling} \leq R \leq R_{break-up} \\ \sigma_{water} & if\ ruptured\ and\ R \geq R_{ruptured} \end{cases} \qquad (5.2)$$

Where

R	Bubble radius
$\dot{R}$	The velocity of bubble wall
$\ddot{R}$	The acceleration of bubble wall
P_0	The hydrostatic pressure
P_{ac}	The acoustic pressure
σ	surface tension
ρ	Liquid density, 10^3 kg/m^3
γ	Polytropic exponent,
c	Speed of sound in the liquid, 1500 m/s
μ	Liquid viscosity, 10^{-3} Pa
k	Shell viscosity 10^{-9}, 10^{-8}, and 2.5 x 10^{-8} kg/s for 1-2, 4-5, and 6-8-µm microbubbles
x	Shell elasticity 2.5 N/m

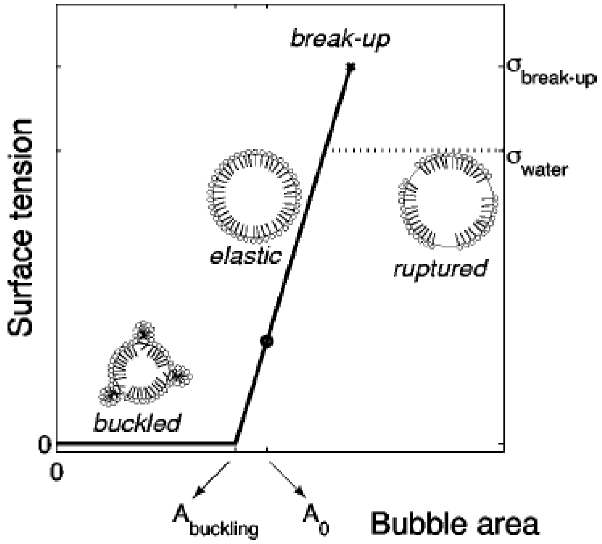

Figure 4.2 – The illustration of dynamic surface tension of a lipid-coated bubble as presented by Marmottant et al.[139]

4.3 Materials and Methods

4.3.1 Mono-dispersed microbubbles

4.3.1.1 Microbubble size distribution

In general, as shown in Fig. 4.3, the distribution of Definity® is not well centralized around a certain diameter. In this chapter, Lipid-shelled microbubbles with three different diameters (1-2, 4-5 and 6-8 μm) were in-house manufactured and size-isolated using differential centrifugation described by Feshitan et al.[151]. The concentration was diluted from a higher concentration to approximately 10^7 numbers / mL after microbubble administration and the sonication was performed immediately after microbubble administration. microbubble size distributions and concentrations were determined by laser light obscuration and scattering (Accusizer 780A; NICOMP Particle Sizing Systems, Santa Barbara, CA, USA). The number- and volume-weighted size distributions before and after

(~8h later) the experiments (those were unused bubbles obtained from the same vial at those times) are shown in Fig. 4.4, which shows that the microbubbles used for BBB opening remain stable. In the study of the size effect, two sets of 1-2-μm diameter bubbles were found not to be stable after the experiments, i.e., the peak in the number distribution was still 1-2 μm, but the peak of the volume distribution had shifted to larger diameters (around 4-8 μm). However, the results of the two vials were statistically different from the 4-5-μm and 6-8-μm diameter bubbles, which led to the conclusion that the number distribution is a more reliable measure of stability.

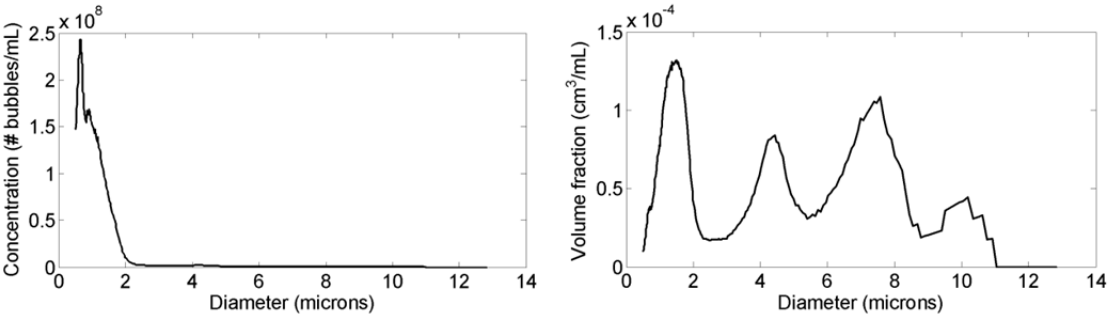

(a) (b)

Figure 4.3 – The size distribution of the Definity® microbubbles (a) according to the number concentration and (b) volume fraction was characterized. This indicated that the size distribution of Definity® microbubbles was not well centralized.

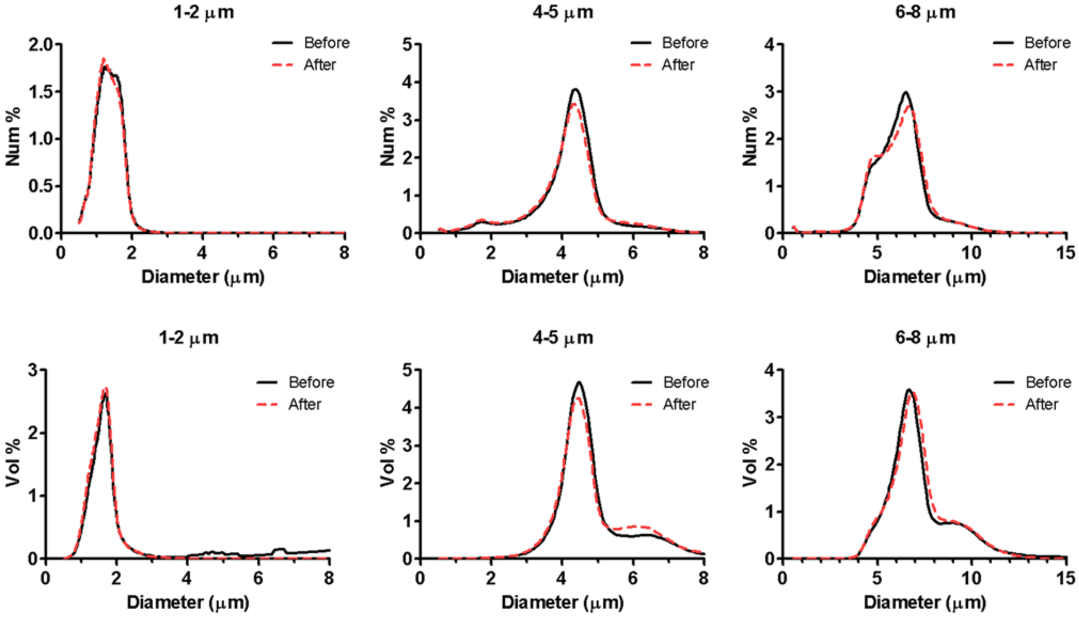

Figure 4.4 – Size distributions of 3 mono-dispersed microbubbles are depicted as number-weighted percent of the total concentration of bubbles and volume-weighted percent of the total volume of bubbles. Before *in vivo* experiment, the distribution is centralized at 1-2 μm, 4-5 μm, and 6-8 μm (solid black). Distribution analysis is performed again at the same day, after *in vivo* experiments (dashed red), depicting small decrease at the peaks.

Table 4.1 Abbreviations, molecular weight, viscosity, and gel-liquid transition temperature of each acyl-chain length

		Property		
Acyl-chain	**Abbreviations**	**M.W.**	**Viscosity (mN s/m)**[142]	**T_m(°C)**[142]
C16	DPPC	734.05	1	41
C18	DSPC	790.16	3	55
C24	DLgPC	958.48	22	80

4.3.1.2 Microbubble shell materials

In the study of the shell effect, lipid-shelled microbubbles with three different acyl-chain lengths (C16, C18, and C24) were manufactured and size-isolated in-house with a 4-5-μm diameter. The concentration was diluted from a higher concentration to approximately 8 x 10^8 bubbles / mL before microbubble administration and sonication was performed after microbubble administration. microbubble-size distributions and concentrations were determined by the electrical impedance sensing zone method (Multisizer 3, Beckman couter, Brea, CA, USA). The properties, including the molecular weight (M.W.), viscosity and get-to-liquid crystalline phase-transition temperature, of the three acyl-chain lengths are shown in Table 4.1.

4.3.2 Sonication protocol

4.3.2.1 *In vivo* study for BBB opening properties assessment

Different numbers of mice are used in three distinct studies shown in this chapter. First, in the study of the bubble-size effect, 67 mice were sonicated at 0.15, 0.30, 0.45, or 0.60 MPa. The number of mice used at each pressure and bubble size is shown in Table 4.2. Second, in the study of the shell effect, 0.15, 0.225, 0.30, 0.45, and 0.60 MPa peak-rarefactional acoustic pressures were used on 31 mice. The number of mice used at each pressure and acyl-chain length was provided in Table 4.3.

The experimental setup has been mentioned in section 3.2.2 (Fig. 3.3(b)) and the experimental timeline was shown in Fig. 4.5. The pulse length, pulse repetition frequency (PRF) and the total sonication duration were respectively 100 cycles, i.e., 67 μs, 10 Hz, and one minute. Prior to the microbubble administration, a 2-s sonication was applied in order to obtain the baseline of acoustic response used in the quantification of cavitation dose. The mice were sacrificed 3 hrs or 7 days after sonication for histological analysis. The procedure has been described in section 4.2.2.3.

Table 4.2 Number of mice studied at each pressure and each bubble size

	Pressure (MPa)				# of mice
Diameter	**0.15**	**0.30**	**0.45**	**0.60**	67
1-2 µm	3	6	6	8	23
4-5 µm	4	7	6	6	23
6-8 µm	3	6	5	7	21

Table 4.3 Number of mice studied at each pressure and each acyl-chain length

	Pressure (MPa)					# of mice
Acyl-chain	**0.15**	**0.225**	**0.30**	**0.45**	**0.60**	31
C16	1	1	2	2	3	9
C18	1	1	3	3	3	11
C24	1	1	3	3	3	11

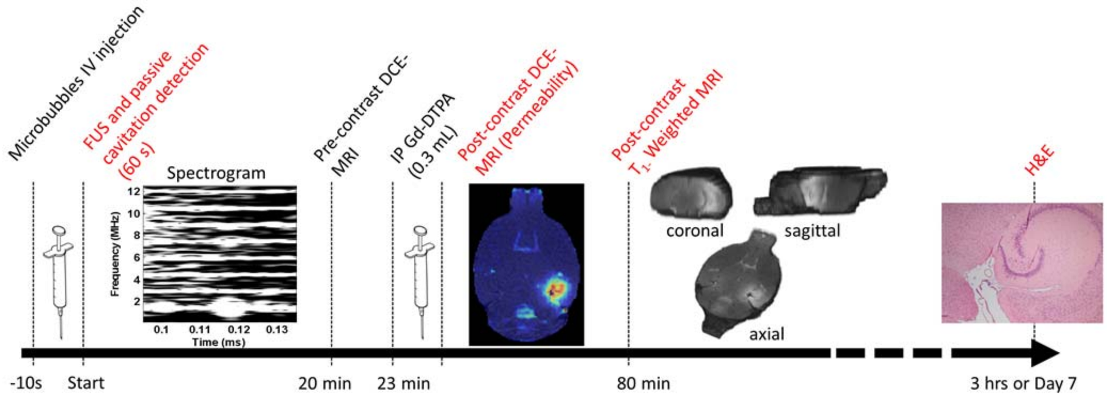

Figure 4.5 – Experimental timeline for each study in this chapter

4.3.2.2 Phantom validation for IC threshold determination

As mentioned in section 3.2.1.1, the same materials for the vessel phantom are used here for 3 different microbubble diameters. Each sonication set includes a pulse length of 100 cycles (67 μm) and a pulse repetition frequency (PRF) of 10 Hz. The total duration of a sonication set is 2 seconds (i.e. 20 pulses). Five sonications are done in a row with a space of 5 mm in between each focus, and repeated for three times with fresh microbubble administration. Acoustic signals emitted from microbubbles are obtained for each pulse. The peak rarefactional pressure amplitude ranges between 0.15 and 0.60 MPa at a 0.05 MPa step size as calibrated in previous studies[40,41]

4.3.3 MRI protocol

All the mice were imaged in a 9.4 T microimaging MRI system (DRX400, Bruker Biospin, Billerica, MA, USA). Each mouse was scanned 30-40 minutes after sonication, using a 30-mm-diameter single resonator. Isoflurane gas (1-2%) was used to keep the mouse anesthetized at 50-70 breaths/min during the entire MRI procedure. Dynamic contrast-enhanced MR imaging (DCE-MRI) was performed using a 2D FLASH T1-weighted sequence of a 192×96 matrix size (reconstructed to 256×128), a spatial resolution of 130×130 μm^2 (reconstructed to 98×130 μm^2), a slice thickness of 600 μm (no interslice gap), a flip angle of 70°, TR/TE=230/2.9 ms, NEX=4 and a scan time of 88 s. Forty dynamic acquisitions were made over a total period of 60 min. Each acquisition produced 20 horizontal slices that covered the entire mouse head. Upon completion of the second dynamic acquisition, a 0.30 mL non-diluted bolus of gadodiamide (Gd-DTPA) was injected intraperitoneally (IP) through a catheter at a rate of approximately 10μL/s. The relatively large dosage of contrast agent was preferred in order to secure the presence of a bolus peak in the vascular system, which is essential for the AIF determination, but also to have a clearer depiction of the extent of BBB opening. Gd-DTPA has been shown to reduce the longitudinal relaxation time when excreted in the extravascular extracellular space (EES), thus enhancing the T1 signal intensity, where the BBB opening has occurred. Upon completion of DCE-MRI, a 2D FLASH T1-weighted sequence (TR/TE=230/3.3 ms; flip angle: 70°; NEX=18; scan time: 9 min 56 s) with higher spatial resolution (matrix size: 256×192; spatial resolution: 86×86 μm^2; slice thickness: 500 μm with no interslice gap) and a 2D RARE T2-weighted sequence (TR/TE=3300/43.8 ms; echo train: 8; NEX=10; scan time: 9 min 54 s; matrix size: 256×192; spatial resolution: 86×86 μm^2; slice thickness: 500 μm with no interslice gap) were acquired.

The kinetic model used here to generate permeability map was developed by Vlachos et al. and is summarized in *Appendix A*. The volume of BBB opening was quantified using Medical Image Processing, Analysis, and Visualization software (MIPAV, Center for Information Technology, National Institutes of Health, Bethesda, MD, USA). In each 2D horizontal image, an intensity threshold was determined from the left hippocampal region. A levelset volume of interest (VOI) was then used to analyze the intensity values and identify the contour boundary of the BBB opening, where the intensity was higher than a pre-specified threshold. After defining the area and the thickness of each slice, the BBB opening volume was calculated.

4.3.4 Acoustic emission signal processing

The acoustic emission detected by the PCD was sampled at 100 MHz and a customized spectrogram function (24-cycles, i.e., 16 μs, Chebyshev window; 98% overlap; 4096-point FFT) in MATLAB® (2007b, Mathworks, Natick, MA) was used to generate a time-frequency map, which provided the spectral amplitude in time and frequency. The spectrogram can then clearly indicate how the frequency content of a signal changes over time. Therefore, the duration of the broadband response can be demonstrated using the spectrogram. In order to obtain the stable cavitation dose, the root-mean-square (RMS) spectral amplitude with a 100-kHz bandwidth of each ultra-harmonic frequency (2.5f to 7.5f) was calculated. The quantification of ICD has been shown in section 3.2.1.4. In general, the cavitation dose was defined as the area under the time-amplitude curve of the ultra-harmonics (SCD) or broadband response (ICD) over the entire sonication duration (*Chapter 2)*.

4.4 Results

4.4.1 Bubble size dependent BBB opening properties

4.4.1.1 *In vivo* BBB opening investigation

The qualitative results, including 3D T1-weighted MR images, spectrogram of the first pulse permeability maps, and histological analysis of each pressure and microbubble diameter are depicted in Fig. 4.6. Here, only the second harmonic is present at 0.60 MPa in the spectrogram without microbubble administration, which has been shown in *chapter 3*. Therefore, harmonics higher than the 3rd and any broadband response are due to microbubble effects (Fig. 4.6). 3D coronal, sagittal and horizontal T1-MR images were used to identify the location of BBB opening. As a result of the deposition of the MRI contrast agent induced by BBB opening, the MR images indicate that the threshold of BBB opening is at 0.45 MPa for the 1-2-μm diameter bubbles and at 0.30 MPa for the 4-5-μm and 6-8-μm diameter bubbles. The corresponding spectrogram shows that only lower harmonics (1st to 4th) are detected at 0.15 MPa and higher harmonics (up to 8th) can be detected at 0.30 MPa and beyond at each bubble size. However, the broadband response, i.e., the inertial cavitation, occurs at 0.45 MPa and 0.60 MPa for all microbubbles used in this study. Therefore, the BBB opening can be induced by nonlinear oscillation (i.e., with harmonics but without broadband emissions) at 4-5-μm and 6-8-μm diameter but not 1-2 μm diameter bubbles. The permeability maps assessed both the efficacy of the targeting and the spatial extent of the opening. The corresponding histological analysis (methods is shown in section 3.2.2.3) shows indicates that no damage was detected in any of these cases shown in Fig. 4. 6 (damaged cases are shown in Fig. 4.11).

The quantitative results, including the SCD, ICD, BBB opening volume, and permeability are shown in Figs. 4.7-4.9. Stable cavitation based on the 2nd to 7th ultra-harmonic (3.75 – 11.25 MHz) with three distinct diameters is quantified as the SCD and depicted in Fig. 4.7. The SCD at the 6-8-μm diameter was significantly higher than at the 1-2-μm diameter (*: $P < 0.05$, compared to 1-2-μm diameter) in most cases, and at the 4-5-μm diameter in two cases (#: $P < 0.05$, compared to 4-5-μm diameter). At 0.30 MPa, the SCD at the 4-5-μm or 6-8-μm diameter was significantly higher than at the 1-2-μm diameter in 7 cases, which provides the evidence that the BBB is opened via the stable cavitation.

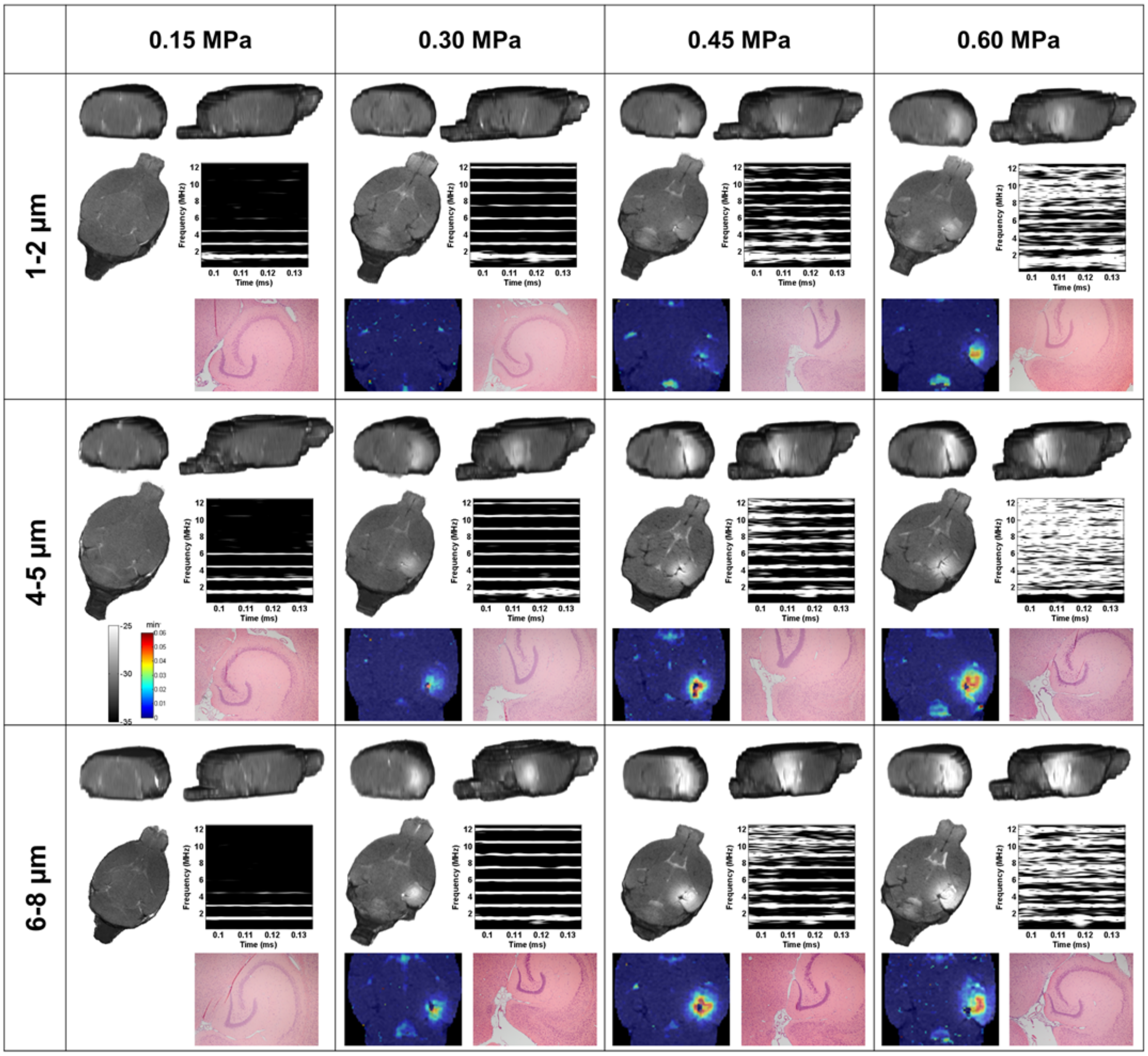

Figure 4.6 – The BBB opening with 3 bubble diameters confirmed by 3D-MRI images with coronal (top left), sagittal (top right), and horizontal (middle left) views. The corresponding spectrogram (middle right) of the first pulse from 95 to 135 μs with microbubbles administration shows the acoustic response from microbubbles. The corresponding H&E sections (40x magnifications, bottom left) and permeability maps (bottom right) are also provided. In the case of 1-2 μm bubbles, the broadband acoustic emissions are detected at 0.45 and 0.60 MPa but not at 0.15 and 0.3 MPa. The 3D-MR images confirmed that the BBB is opened at 0.45 and 0.60 MPa, with inertial cavitation. In the case of 4-5 and 6-8 μm bubbles, the broadband acoustic emissions are detected at 0.45 and 0.60 MPa but not at 0.15 and 0.3 MPa. The 3D-MR images confirmed that the BBB is opened at 0.30 MPa without inertial cavitation or 0.45 MPa and 0.60 MPa with inertial cavitation. In each H&E image, its center indicated the focus as viewed on the MRI. No damage was detected in any of these cases (see Fig. 4.11 for cases with damage).

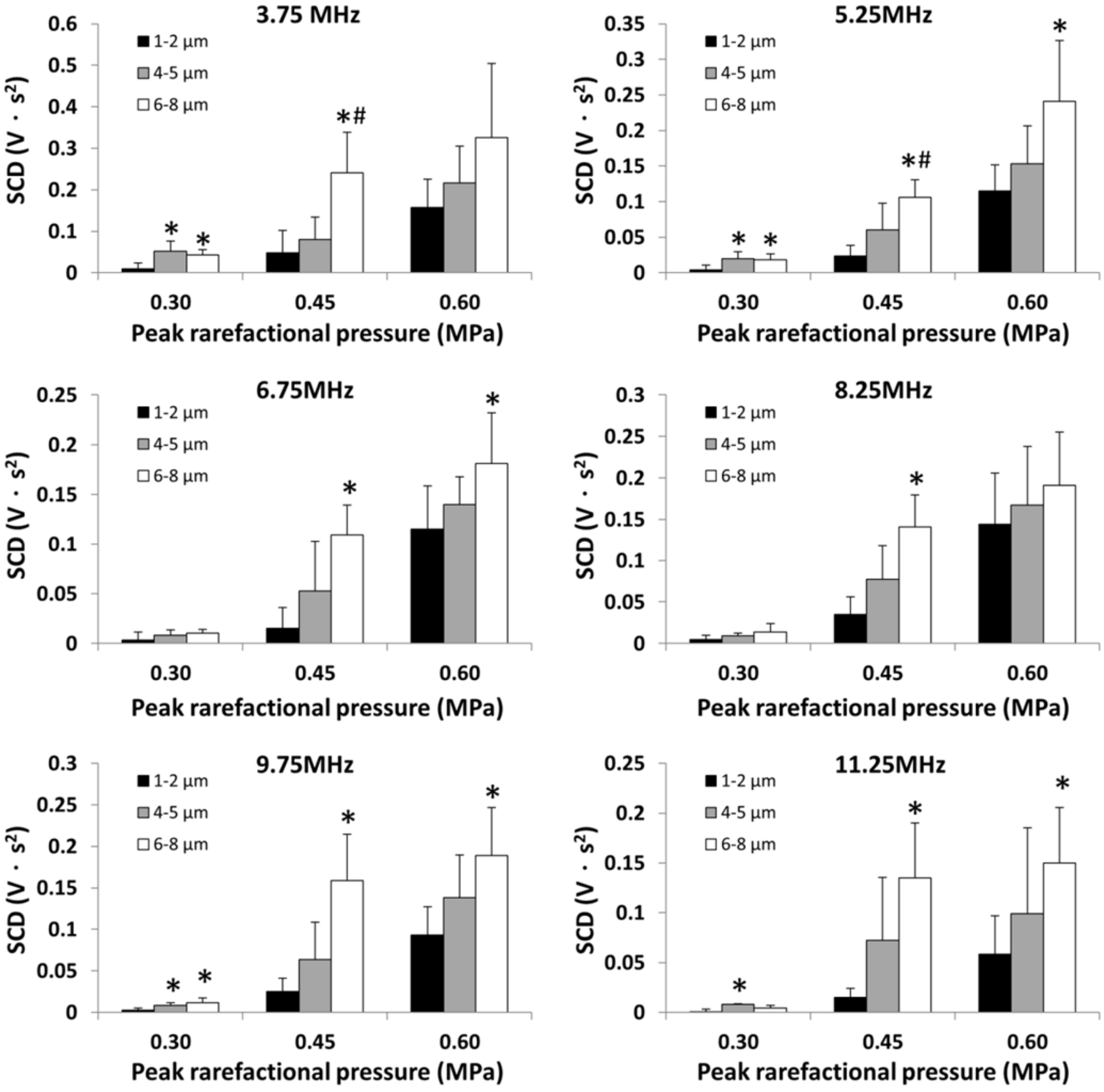

Figure 4.7 – Statistical analysis of the stable cavitation dose (SCD) at the ultra-harmonics 3.75 MHz (2.5f), 5.25 MHz (3.5f), 6.75 MHz (4.5f), 8.25 MHz (5.5f), 9.75 MHz (6.5f), and 11.25 MHz (7.5f) against three distinct pressures at three microbubble diameters. The SCD at the 6-8-μm diameter was significantly higher than at the 1-2-μm diameter (*: $P < 0.05$, compared to 1-2-μm diameter) in most cases, and at the 4-5-μm diameter in two cases (#: $P < 0.05$, compared to 4-5-μm diameter). At 0.30 MPa, i.e., no inertial cavitation occurrence, the SCD at the 4-5-μm or 6-8-μm diameter was significantly higher than at the 1-2-μm diameter in 7 cases, which provides the evidence that the BBB is opened via the stable cavitation.

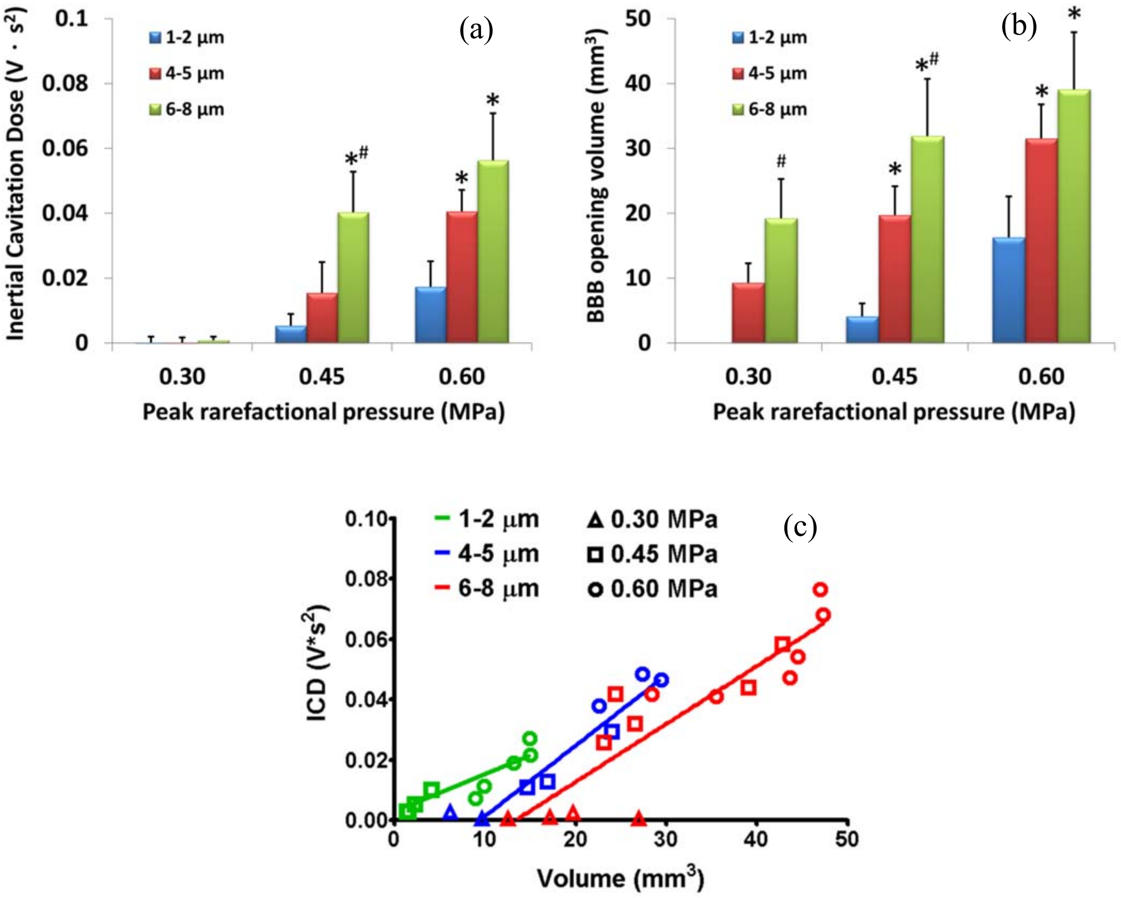

Figure 4.8 – The quantification of (a) the inertial cavitation dose (ICD), (b) BBB opening volume and (c) the correlation in between. Statistical analysis indicates that the ICDs and BBB opening volume are both pressure and bubble-size dependent. [*: $P < 0.05$, compared to 1-2-µm diameter, #: $P < 0.05$, compared to 4-5-µm diameter]. Regression analysis shows a linear correlation between the ICD and the BBB opening volume with three bubble diameters. It also shows that inertial cavitation is necessary for 1-2 µm bubbles to induce BBB opening. The intercept indicates that the BBB can be opened without inertial cavitation in the case of 4-5 and 6-8-µm diameter bubbles.

The ICD, BBB opening volume of different bubble diameters, and their relationship are shown in Fig. 4.8. The ICD 6-8-µm is larger than at 1-2-µm-diameter bubbles (*: $P < 0.05$) at 0.45 and 0.60 MPa, as well as larger than at 4-5-µm-diameter bubbles at 0.45 MPa (#: $P < 0.05$), which shows that the ICD is also bubble-size dependent [Fig. 4.8(a)]. The statistical analysis results of the BBB opening volume at different bubble diameters are shown in Fig. 4.8(b). The volume with 4-5- and 6-8-μm-diameter bubbles is larger than with 1-2-μm-diameter bubbles (*: $P < 0.05$) at 0.45 and 0.60 MPa. In the cases of 0.30 and 0.45 MPa, the BBB opening volume with 6-8 μm is statistically larger than with 4-5-μm-diameter bubbles (#: $P < 0.05$). The correlation between the BBB opening volume and ICD is shown in Fig. 4.8(c), which a linear correlation with all bubble diameters. The intercept indicates that the BBB can be opened without inertial cavitation in the case of 4-5 and 6-8-μm diameter bubbles as configured by Fig. 4.7.

The 1-2 μm bubbles exhibited no uptake of Gd-DTPA at 0.30 MPa and a small uptake at 0.45 MPa. At 0.60 MPa a K_{trans} was found higher than 0.005 min^{-1}. Similar K_{trans} distributions were found between the 4-5 μm/0.30 MPa and 6-8 μm/0.30 MPa cases, resulting in mildly permeable BBB openings. The quantitative measurements provided numerical permeability values of the BBB opening (Fig. 4.9). The opening threshold for the 1-2 μm bubbles was found to be at 0.45 MPa, yielding a K_{trans} value of 0.011 ± 0.004 min^{-1}, while at 0.60 MPa K_{trans} reached a value of 0.039 ± 0.008 min^{-1}. The 4-5 μm bubbles exhibited higher K_{trans} values, i.e. 0.028 ± 0.013 min^{-1}, 0.044 ± 0.011 min^{-1} and 0.052 ± 0.007 min^{-1}, for the pressures of 0.30, 0.45 and 0.60 MPa, respectively. Similar results with the 4-5 μm bubbles were found for the 6-8 μm, where the estimated K_{trans} was 0.033 ± 0.007 min^{-1}, 0.049 ± 0.001 min^{-1} and 0.049 ± 0.006 min^{-1} for the pressures of 0.30, 0.45 and 0.60 MPa, respectively. The statistically significant p-values for each acoustic pressure and microbubble size using a two-tailed Student's t-test with unequal variances are depicted on the corresponding graphs (Fig. 4.9). The permeability of the epicranial muscle was also measured in every mouse and the mean K_{trans} value throughout the entire group of mice was found to be equal to 0.047 ± 0.007 min^{-1}.

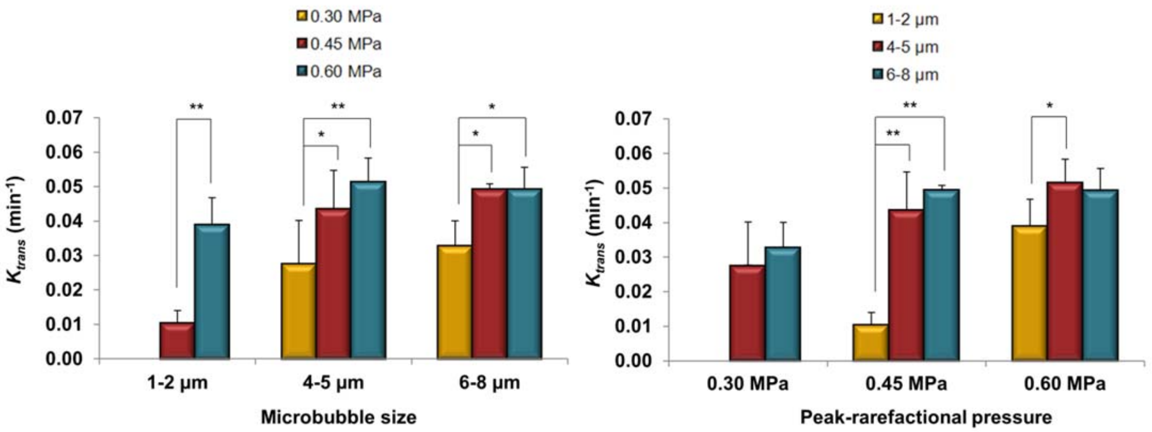

Figure 4.9 – Mean quantitative K_{trans} measurements. The results are presented in two different ways in order to demonstrate the dependence of the BBB opening K_{trans} on both the acoustic pressure and the microbubble size. The mean K_{trans} in the epicranial muscle (no barrier) is also presented for comparison. One asterisk (*) refers to a statistical significance of $P < 0.05$ and two asterisks (**) refer to a statistical significance of $P<0.01$.

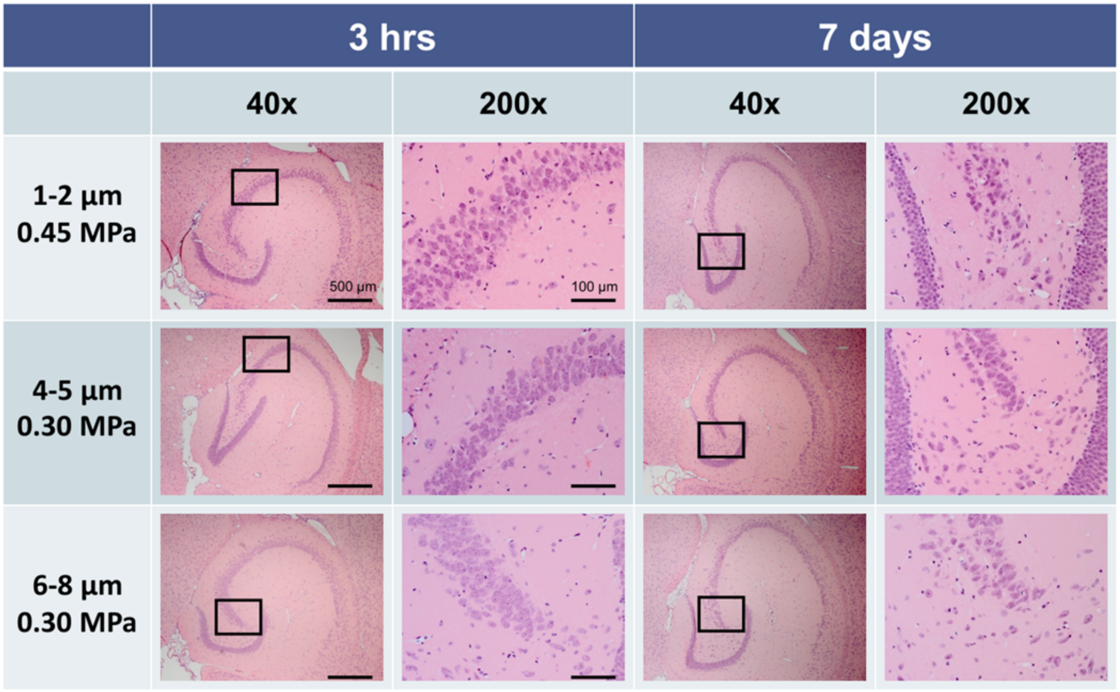

Figure 4.10 – Histology at the BBB opening threshold. The mouse was sacrificed either 3 hrs or 7 days after sonication. In both cases, no red blood cell extravasations and dark neurons were found with H&E staining, which means that safe BBB opening can be achieved at adequate pressure with all bubble diameters.

Two histological analyses were performed. First, the histological analysis at the BBB opening threshold at both the 3-hours and 7-day time points was shown in Fig. 4.10. In both cases, no cell damage, e.g., red blood cell (RBC) extravasations or dark neurons[91], was detected after histological examination, which signifies that safe BBB opening can be achieved at all bubble diameters. Second, the damaged cases were inspected and shown in Fig. 4.11. The histological findings showed that only three out of all mice used in this study revealed some structural neuronal damage and cell loss in the sonicated hippocampal area. In two of these mice, which were sonicated at 0.45 and 0.60 MPa, using 4-5 μm microbubbles (Fig. 4.11(c-h) and (k-p), respectively), cell loss was detected in the granule cell layer of the right dentate gyrus (GrDG). Moreover, the presence of dark neurons in the layer could be an indication of apoptosis. More serious damage was found in the 6-8μm/0.60 MPa case (Fig. 4.11(v-x)), which underwent a major deformation of the structure of the CA3 field of the right hippocampus, followed by cell loss and multiple dark neurons. However, the H&E slices of all the mice showed no red blood cell extravasations that could indicate hemorrhage. The regular T_1 images (Fig. 4.11(a, i, q)) and the permeability maps (Fig. 4.11(b, j, r)) of the corresponding mice, acquired approximately 1.5 h after sonication are presented along with the histological findings, but no direct correlation could be found between the two imaging techniques.

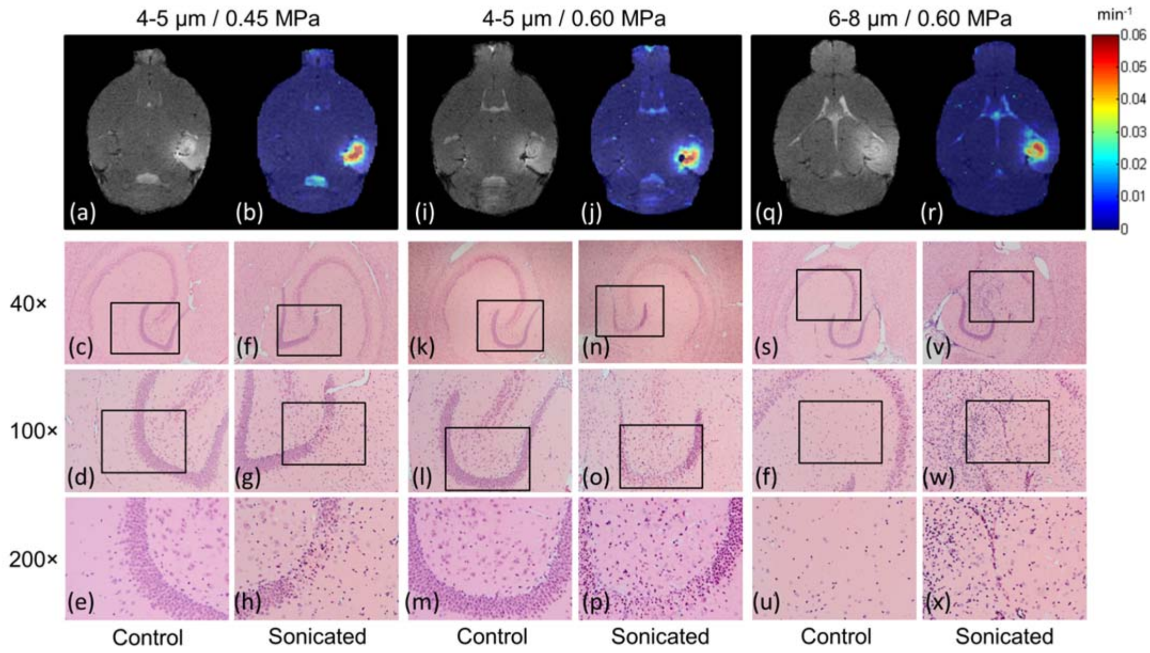

Figure 4.11 – Permeability and histological findings of the only three mice that exhibited neuronal damage and cell loss. (a) T1 image, (b) corresponding permeability map and (c-h) H&E sections of the first mouse, sonicated at 0.45 MPa using 4-5 µm bubbles. (i) T1 image, (j) corresponding permeability map and (k-p) H&E sections of the second mouse, sonicated at 0.60 MPa using 4-5 µm bubbles. (q) T1 image, (r) corresponding permeability map and (s-x) H&E sections of the third mouse, sonicated at 0.60 MPa using 6-8 µm bubbles. The black boxes in (c, f, k, n, s, v) refer to the regions of interest depicted in (d, g, l, o, t, w), respectively. The black boxes in (d, g, l, o, t, w) refer to the regions of interest depicted in (e, h, m, p, u, x), respectively.

T_2 imaging was used as a complementary tool for the assessment of any physiological changes in the sonicated region. Dark regions were detected in the sonicated region in most of the cases of higher pressures and larger microbubbles (Fig. 4.12), but a distinct correlation with the histological findings could not be established, since H&E staining showed no signs of erythrocyte extravasations. This led to the conclusion that the dark regions in T_2 imaging were the result of susceptibility artifacts from the excessive Gd-DTPA excreted in the EES, rather caused by hemorrhage.

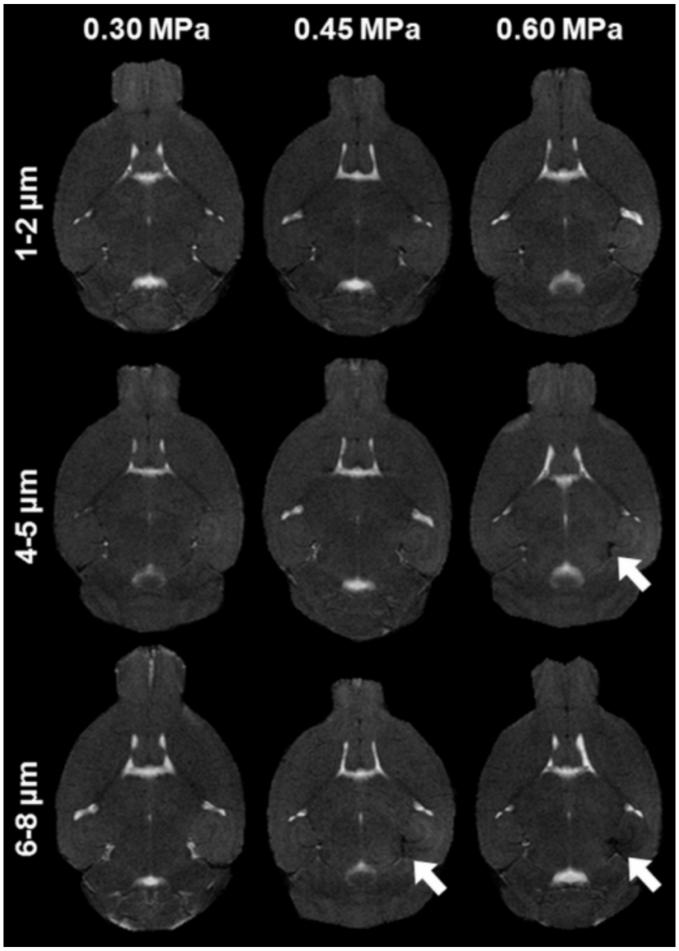

Figure 4.12 – Transverse T2 images of the brain from each mouse cohort. Dark areas in the sonicated regions (indicated by white arrows) were detected at higher pressures for the larger bubbles as a result of susceptibility artifacts from the excessive Gd-DTPA presence in the extravascular extracellular space.

4.4.1.2 IC threshold determination of mono-dispersed microbubbles

In 4.4.2.1, we have found that the BBB opening properties, including the pressure threshold, permeability, and volume are bubble size dependent. However, the pressure threshold of IC lay between 0.30 and 0.45 MPa within all bubble sizes, which was different from theoretical interpretation[105] and optical observation[104]. Therefore, a channel phantom was used to determine the pressure threshold of IC for mono-dispersed microbubbles used in our *in vivo* studies. The SC was also quantified to compare the *in vivo* results. Figures 4.13-4.15 showed the spectrum and the ICD at pressures from 0.15 to 0.60 MPa, as well as the SCD at pressures from 0.15 to 0.35 MPa, of 1-2, 4-5, and 6-8 μm diameter bubbles, respectively. The IC threshold lay between 0.30 and 0.35 MPa for 1-2 and 4-5 μm diameter bubbles, and it lay between 0.35 and 0.40 MPa for 6-8 μm diameter bubbles. This confirmed our *in vivo* results which showed that the IC threshold lay between 0.30 and 0.45 MPa for all microbubbles used in this chapter. The SC did not occur at pressures of 0.15 - 0.35 MPa for 1-2-μm diameter bubbles (Fig. 4.13), but occur at 0.30 MPa for 4-5- and 6-8-μm diameter bubbles (Figs. 4.14, 4.15).

The oscillation of a 1.5-μm diameter bubble simulated by three bubble conditions, an unshelled and a shelled bubble using Bubblesim, as well as a shelled bubble using the Marmottant model, was shown in Fig. 4.16. The result of the Marmottant model was implemented on Matlab. Here, the "compression-only" behavior, i.e. the bubble only compresses and hardly expands beyond its initial diameter, observed by DeJong[152] was successfully simulated. The expansion ratio (R_{max}/R_0), which can be used to determine the IC threshold, at 0.30, 0.35, and 0.40 MPa for each diameter and each theoretical model was shown in Table 4.4.

Table 4.4 Expansion ratio (R_{max}/R_0) for each diameter and each theoretical model

Diameter	**1-2 μm**			**4-5 μm**			**6-8 μm**		
Bubble\PRP	**0.30**	**0.35**	**0.40**	**0.30**	**0.35**	**0.40**	**0.30**	**0.35**	**0.40**
Unshelled	4.48	5.11	5.78	2.69	2.99	3.34	2.60	2.69	2.84
Shelled	1.51	1.83	2.24	2.35	2.70	3.01	1.91	2.12	2.29
Marmottant	1.67	2.40	3.51	3.22	4.48	5.75	3.06	4.01	5.52

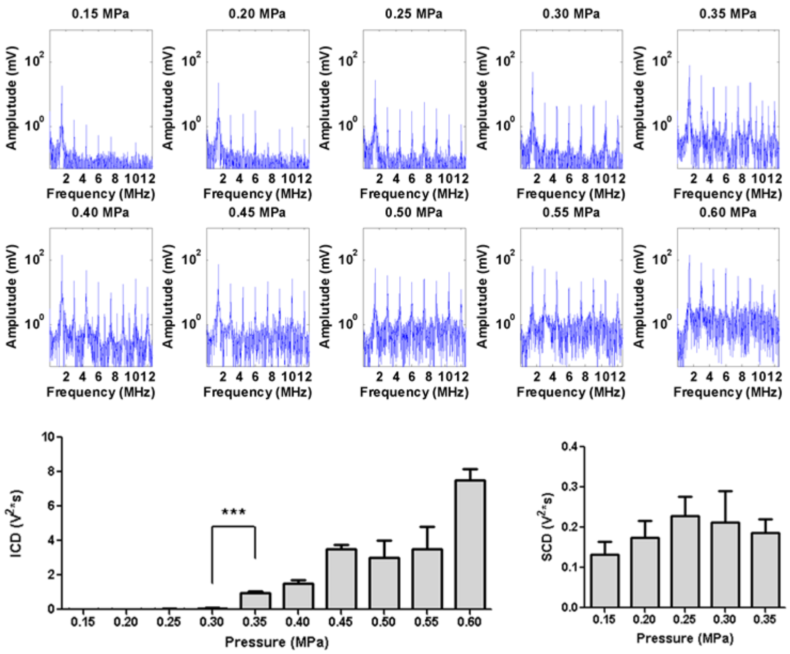

Figure 4.13 – The frequency spectrum and ICD of the 1-2-μm diameter bubbles. The IC threshold is determined to lie between 0.30 and 0.35 MPa (***: *P < 0.001)*. The SC does not occur between 0.15 and 0.35 MPa.

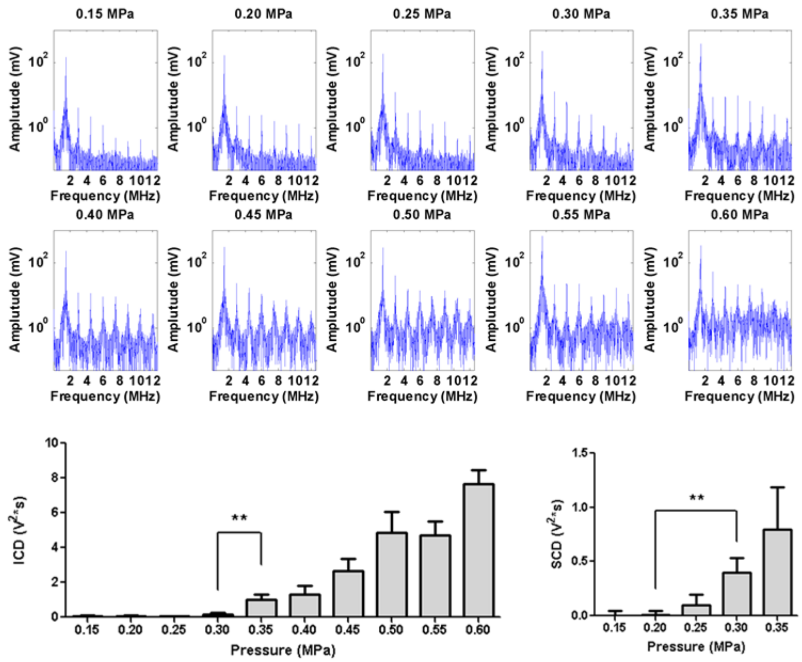

Figure 4.14 – The frequency spectrum and ICD of the 4-5-μm diameter bubbles. The IC threshold is determined to lie between 0.30 and 0.35 MPa (**: *P<0.01*), but the SC occurs at 0.30 MPa.

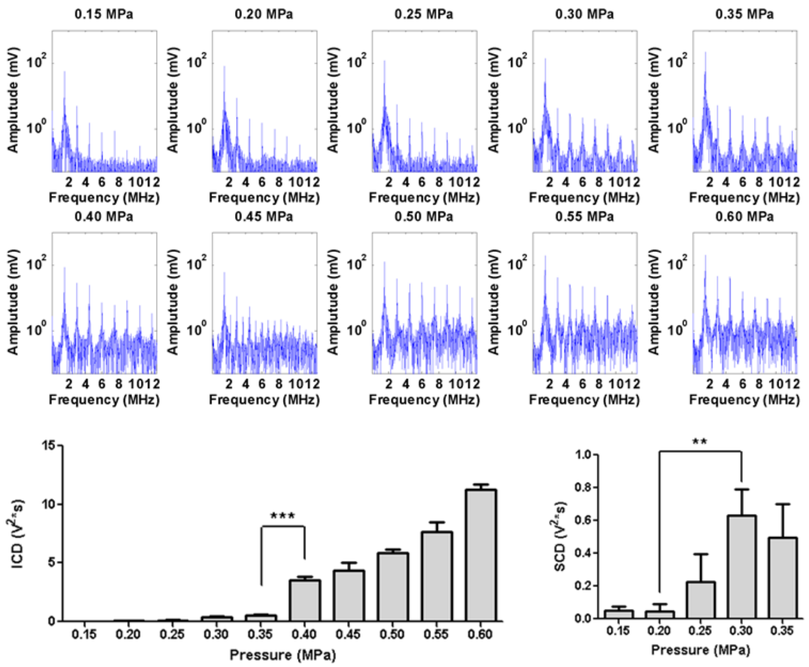

Figure 4.15 – The frequency spectrum and ICD of the 6-8-μm diameter bubbles. The IC threshold is determined to lie between 0.35 and 0.40 MPa (***: *P<0.001*), but the SC occurs at 0.30 MPa.

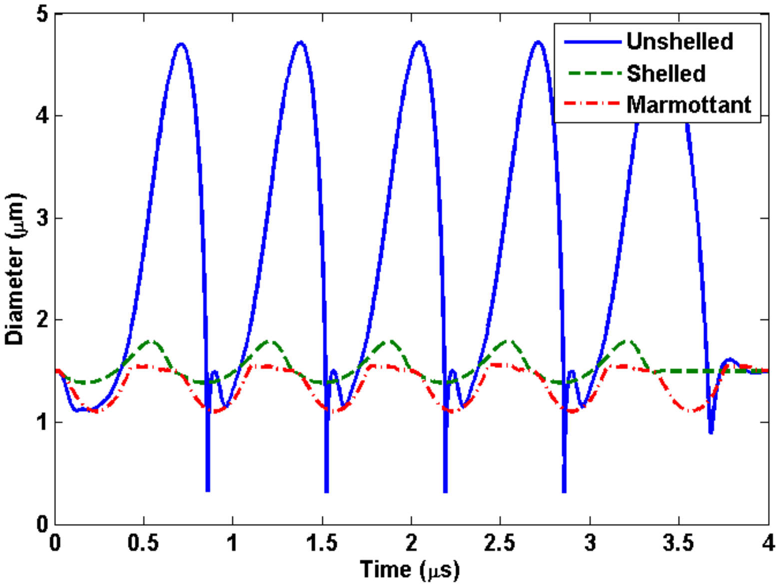

Figure 4.16 – Simulation of the oscillation of a 1.5 μm diameter bubble at 0.20 MPa PRP using Bubblesim (unshelled, shelled), and Marmottant model. The "compress-only" behavior of a lipid shelled microbubble is observed here.

4.4.2 Shell effect on bubble behavior during BBB opening

Since no BBB opening was induced at 0.15 or 0.225 MPa, the results at these two pressures are not shown here. The T1-weighted MR images, permeability maps, histological sections and corresponding spectrograms of the first pulse of each acyl-chain length case are depicted in Fig. 4.17 and four main observations can be made: 1) the BBB opening pressure threshold is 0.30 MPa at all acyl-chain lengths, which means that the BBB opening pressure threshold is not affected by the acyl-chain length; 2) the corresponding permeability map clearly shows that the BBB opening region at high K_{trans} (> 0.03 min^{-1}) increases with the pressure amplitude, but no difference is observed across all acyl-chain lengths; 3) the spectrogram shows that the threshold of inertial cavitation with the 4-5-μm bubbles lies between 0.30 and 0.45 MPa for all acyl-chain lengths, which is the same as what was shown in our previous study on the effect of microbubble diameter; 4) histological findings showed that some dark neurons or red blood cell (RBC) extravasations are generated at 0.45 and 0.60 MPa (Fig. 4. 17). The number of damaged cases at each acyl-chain length and applied pressure are shown in Table 4.5. Despite the fact that a high damaged rate (6/9) at 0.60 MPa or with C24 microbubbles were obtained, no significant damage difference between acyl-chain lengths was noted.

Table 4.5 Safety assessment (damaged / BBB-opened mice) at each pressure and each acyl-chain length

	Pressure (MPa)				
Acyl-chain	**0.15**	**0.225**	**0.30**	**0.45**	**0.60**
C16	0/0	0/0	0/2	1/2	1/3
C18	0/0	0/0	0/3	1/3	2/3
C24	0/0	0/0	1/3	2/3	3/3
Total	0/0	0/0	1/8	4/8	6/9

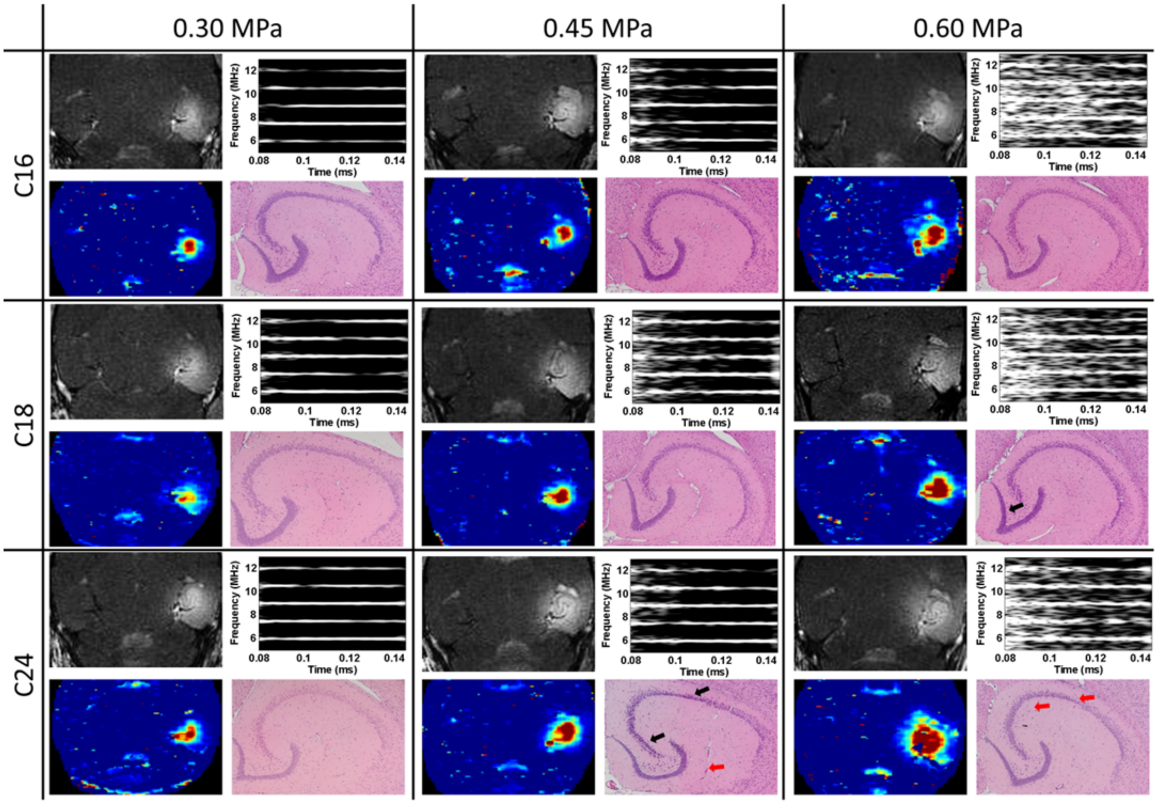

Figure 4.17 – The 2D horizontal T1-weighted MR image (top left), corresponding spectrogram of the first pulse (top right), 2D horizontal permeability map (bottom left), and H&E sections of the hippocampus (bottom right) in each table entry at 3 bubble diameters and 3 peak-rarefactional pressures. Few histological damage cases were noted and shown here (black arrow: dark neuron, red arrow: red blood cell extravasations) were observed with inertial cavitation occurrence (see Table 3 for summary of damage cases).

As used in the investigation on the effect of microbubble diameter, T_2 imaging was also used as a complementary tool for the assessment of any physiological changes in the sonicated region here. Dark regions were detected in the sonicated region in most of the cases of higher pressures and larger microbubbles (Fig. 4.18), including one case at 0.30 MPa with the C24 microbubbles. This is the only case with corresponding hemorrhage in the absence of inertial cavitation.

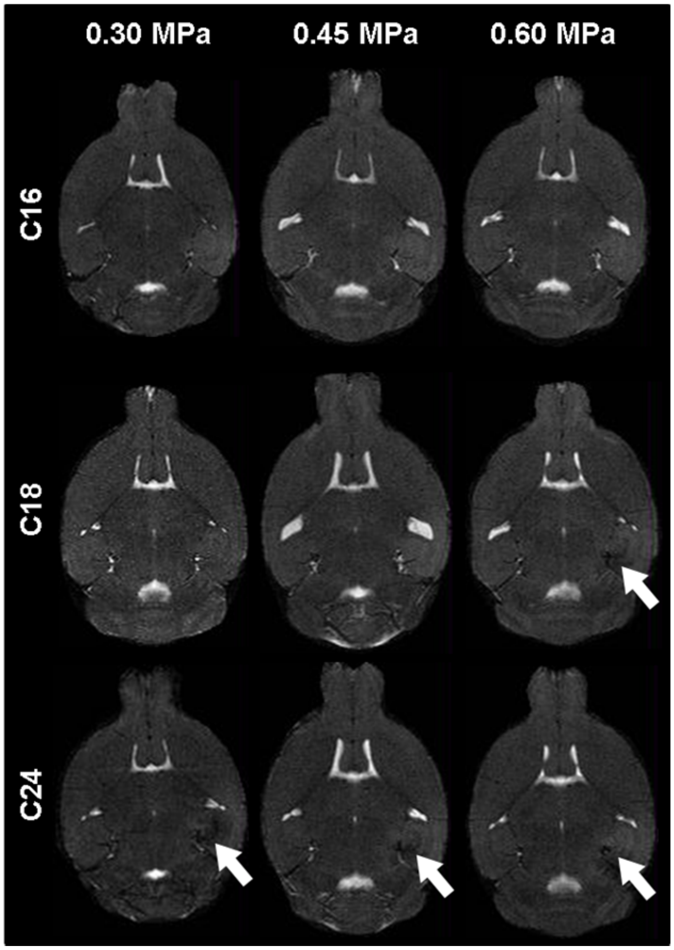

Figure 4.18 – Transverse T2 images of the brain from each mouse cohort. Dark areas in the sonicated regions (indicated by white arrows) were detected at all pressures for the C24 bubbles, which indicated that C24 may not be an appropriate shell material for BBB opening application.

Stable cavitation based on the 2nd to 7th ultra-harmonic (3.75 – 11.25 MHz) with three applied pressures is quantified as SCD and depicted in Fig. 4.18. In most cases, no difference was observed among the three acyl-chain lengths studied. As a result, the acyl-chain length does not seem to have an effect on the ultra-harmonic response emitted by the microbubbles during BBB opening. At 0.30 MPa and above, however, all SCDs were statistically higher than zero (i.e., more ultramonics were generated in the presence of microbubbles than with the skull alone), which confirms the results shown in Fig. 4.7.

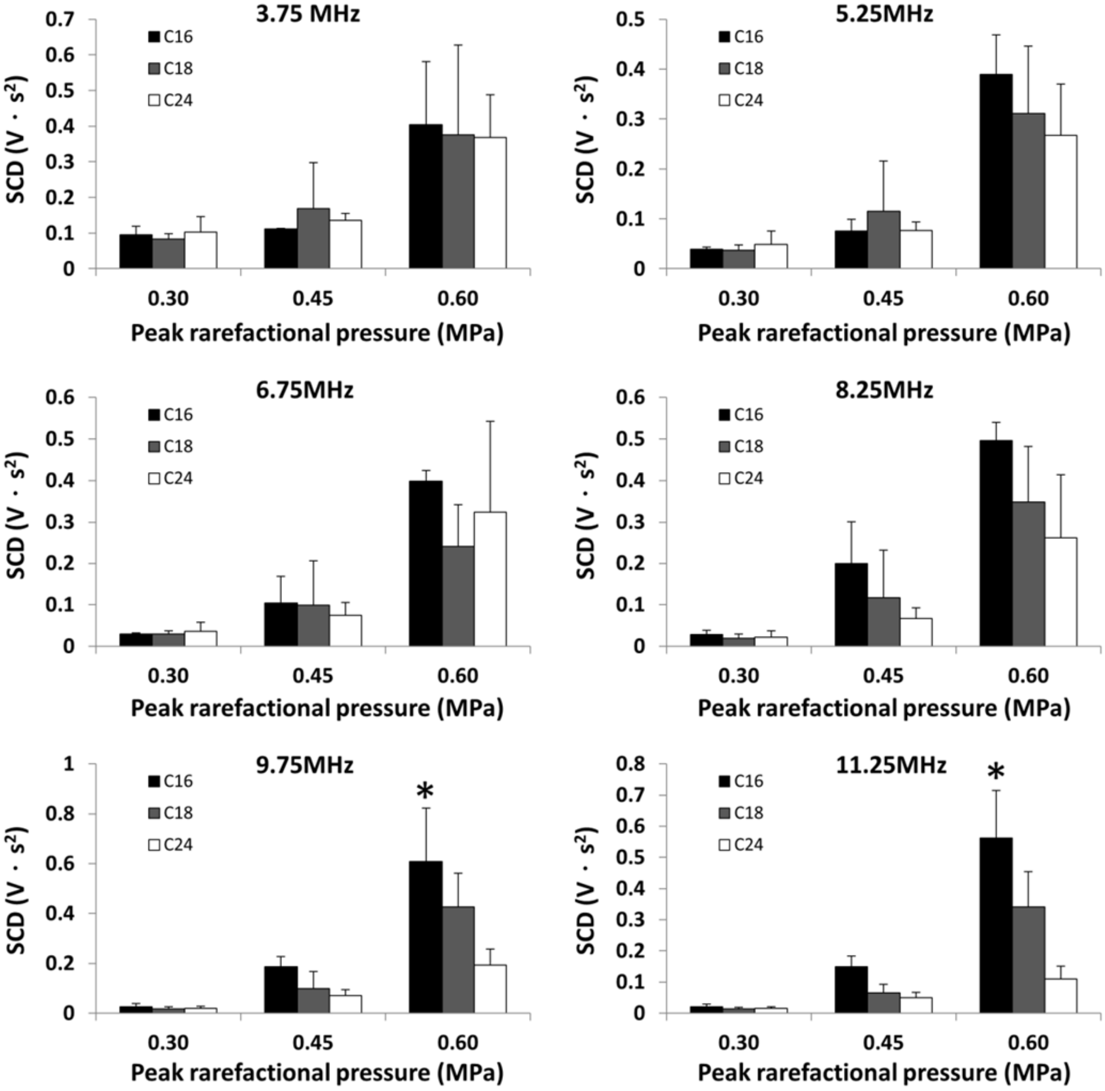

Figure 4.19 – Statistical analysis of the stable cavitation dose (SCD) at the ultra-harmonics 3.75 MHz (2.5f), 5.25 MHz (3.5f), 6.75 MHz (4.5f), 8.25 MHz (5.5f), 9.75 MHz (6.5f), and 11.25 MHz (7.5f) with three acyl-chain lengths at three distinct pressures. No significant difference was observed across the different acyl-chain lengths in most cases. However, at 9.75 MHz and 11.25 MHz, the SCD of the C16 microbubbles was significantly higher than the C24 microbubbles (*: $P < 0.05$). Since the center frequency of the PCD is 10 MHz, the sensitivity may be higher when the ultra-harmonic is close the 10 MHz. At 0.30 MPa, i.e., no inertial cavitation occurrence, the SCD was statistically higher than the background noise, which indicated that the BBB was opened through stable cavitation.

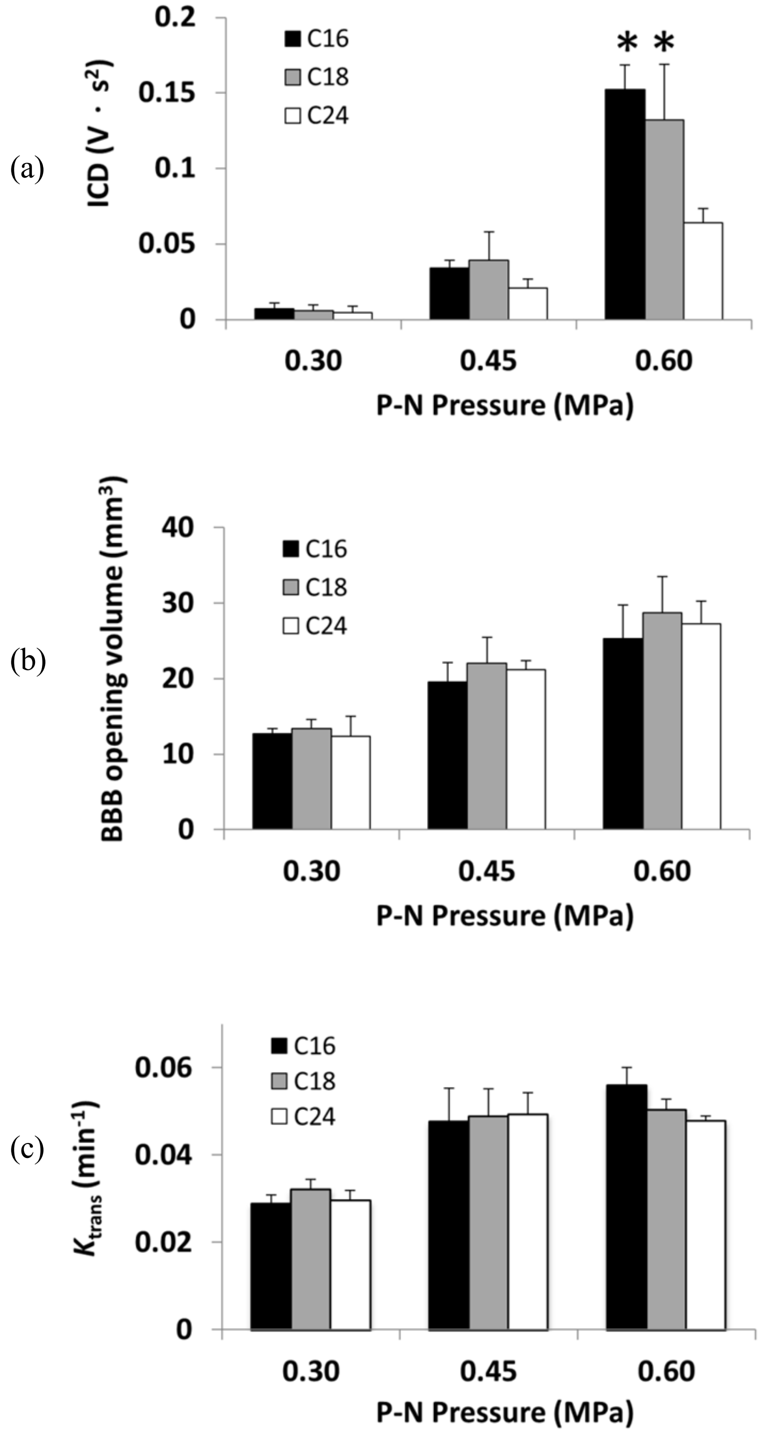

Figure 4.20 – Statistical analysis of the (a) inertial cavitation dose (ICD), (b) BBB opening volume, and (c) permeability between three acyl-chain lengths at three distinct pressures. The ICD of C24 microbubbles was significantly lower than the C16 and C18 microbubbles at 0.60 MPa (*: $P < 0.05$). In the rest cases, however, no statistically difference was observed.

The inertial cavitation dose (ICD), BBB opening volume, and K_{trans} are shown in Fig. 4.20. The threshold of inertial cavitation is identified to lie between 0.30 and 0.45 MPa for all acyl-chain lengths but, at 0.60 MPa, the ICD with the C24 microbubbles is statistically lower than with the C16 and C18 microbubbles ($P < 0.05$, Fig. 4.9(a)). The quantification of BBB opening volume and permeability are shown in Fig. 4.9(b) and (c), and no significant difference is observed between the three acyl-chain lengths at all pressures, although the ICD is lower with the C24 microbubbles. Similar to our previous studies, however, the ICD and BBB opening increase with pressure, and the permeability reaches an upper limit around 0.05 min^{-1} at 0.45 and 0.60 MPa.

4.5 Discussion

4.5.1 Bubble size dependent BBB opening properties

4.5.1.1 *In vivo* BBB opening investigation

The objective of this study was to investigate the physical effects of the systematically circulating microbubbles on the FUS-induced BBB opening and corresponding permeability. The pressure threshold of BBB opening, determined by the MRI contrast enhancement, was 0.45 MPa for the 1-2-µm and 0.30 MPa for both the 4-5-µm and 6-8-µm bubbles. However, the spectrogram showed that the broadband response occurred at 0.45 MPa for all microbubbles. The uncorrelated threshold between BBB opening and inertial cavitation implied that the physical effects responsible for the BBB opening may be bubble size dependent. The inertial cavitation may be necessary for BBB opening with smaller diameter (1-2 µm) but not with larger diameter (4-5 and 6-8 µm) microbubbles.

For larger diameter (4-5 and 6-8 μm) microbubbles, at 0.45 and 0.60 MPa, with the occurrence of inertial cavitation, both the volume and the shape of the contrast enhancement region was different from the case at 0.30 MPa. In the sagittal images, the shape of the contrast enhancement region at 0.45 MPa and 0.60 MPa with 4-5 μm and 6-8 μm bubbles indicated enhanced shielding effects induced by the bubbles and potential inertial cavitation occurrence (Fig. 4.6). However, at 0.30 MPa without inertial cavitation occurrence, the contrast enhancement region, which covered the hippocampal formation (Fig. 4.21(a)), was more homogeneous and was similar in shape and geometry to the -6 dB focal spot of the FUS beam (Fig. 4.21(b)).

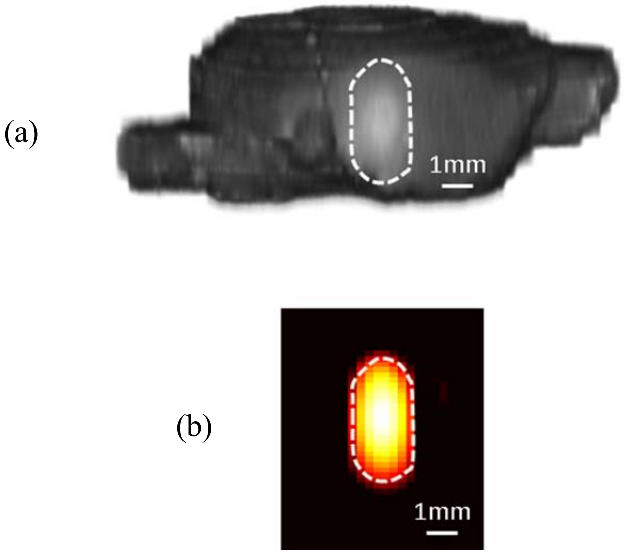

Figure 4.21 – Comparison between (a) sagittal section of 3D-T1-MR images and (b) -6dB focal region of the FUS transducer in the case of 6-8 μm bubbles at 0.30 MPa. The consistence between the contrast enhancement region and focal region of the FUS transducer indicates that IC is not necessary to induce BBB opening.

The capillary diameter in the murine brain ranges between 4-8 μm[153], which is 2-8 times larger than the 1-2-μm diameter bubbles. It has been shown that the microbubble will be fragmented when the radius expands to higher than three times the initial radius at rest (i.e., $R_{max} / R_{rest} > 3$)[104]. However, the ratio of expansion of the 4-5-μm and 6-8-μm diameter bubbles needed not to be as high as for the 1-2-μm diameter bubbles to enter into contact with the capillary wall. BBB opening may thus be induced through nonlinear oscillation only in the case of larger bubbles. In addition, the bubbles of 6-8-μm in diameter are even closer in size to the diameter of the capillary, increasing the probability of opening in a larger number of locations.

The spectrogram used in this study clearly elucidated the onset and duration of inertial cavitation within the first pulse. Here, the inertial cavitation occurred at the beginning of sonication (Fig. 4.6). At the highest pressure (0.60 MPa), the broadband response corresponding to the first pulse, lasted throughout the entire duration of the pulse length at all bubble sizes (Fig. 4.6), which indicated that the highest pressure may fragment the microbubbles to smaller bubbles that serve as cavitation nuclei. In the case at 0.15 and 0.30 MPa at all bubble sizes, only harmonics without broadband emissions, were detected. However, the BBB opened at 0.30 MPa only in the 4-5 and 6-8 μm cases. Despite the fact that up to the 8th harmonic could be detected by our PCD, no BBB opening was induced at 0.30 MPa with the 1-2 μm bubbles. Therefore, the nonlinear oscillation of smaller bubbles would not induce BBB opening. The harmonics which corresponded to the nonlinear oscillation of microbubbles thus may not be used as an indicator of BBB opening in the case of the smaller diameter bubbles.

In *chapter 3*, we showed that the BBB was opened at 0.30 MPa using FUS and Definity® [120]. Despite the fact that the mean bubble diameter was within 1.1-3.3 μm, close to 1-2 μm, they were not considered as mono-dispersed because the maximum diameter was 20 μm and 98% was under 10 μm. It has also been shown that Definity® are poly-dispersed microbubbles based on the size distribution[119]. Therefore, the BBB opening may be induced by the larger (4-10 μm) bubbles rather than the smaller (1-3 μm) Definity® bubbles at 0.30 MPa.

According to previous reports on Definity® and Optison®, Optison® appeared to produce larger effects than Definity® when applied at the same pressure amplitude with respect to the magnitude of the BBB opening[63]. Here, our findings using both ICD and BBB opening volume confirmed this conclusion. The mean diameter range of Optison® and Definity® was 2.0-4.5 μm and 1.1-3.3 μm, respectively. Both the effects to the vasculature and the acoustic emission detection were different at distinct microbubble sizes.

It has been shown that the active vesicular transport is more pronounced in arterioles than in capillaries and venules after BBB opening[5], which provided evidence that opening is not restricted to the capillaries. Since the size of the arterioles was around 10 – 20 μm[99], bubble expansion may not be the factor inducing BBB opening in arterioles. According to multiphoton imaging findings, a vasoconstriction induced after microbubble administration was previously reported[99]. Vasoconstriction may be induced by bubble aggregation caused by a secondary radiation force[154]. Therefore, larger bubbles may induce vasoconstriction with higher probability than smaller bubbles. After vasoconstriction is induced by bubble aggregation, the shear stress surrounding the microbubble may be high enough to enhance the permeability of endothelial cells, or to rupture tight junctions. Therefore, the tensile strength of the tight junctions and the shear stress amplitude will be considered in future investigations to unveil the mechanical effect onset of FUS-induced BBB opening.

Similar to the threshold of BBB opening, the SCD, ICD and BBB opening volume were also bubble size dependent (Figs. 4.7 and 8). At 0.30 MPa, the SCDs at the 4-5- or 6-8-μm diameter bubbles were significantly higher than at the 1-2-μm diameter bubbles at frequencies of 3.75, 5.25, 9.75, and 11.25 MHz (Fig. 4.7). Also, at the same pressure, mean ICD was almost zero for all microbubble diameters (Fig. 4.8(a)). As a result, both SCD and ICD indicated that the BBB was opened via stable cavitation in the cases of larger bubbles. A good linear correlation between the ICD and BBB opening volume was also observed (Fig. 4.8(c)), thus the PCD may serve as a good indicator to estimate the BBB opening volume based on the ICD calculation.

According the histological analysis at the BBB opening threshold, the BBB opening can be induced without RBC extravasations or neuronal damage (Fig. 4.10). Despite the fact that the inertial cavitation occurred at 0.45 MPa with the 1-2-μm diameter bubbles, a small opening volume was induced without any damage. In this case, inertial cavitation did not induce cell death but was sufficient to change the permeability of endothelial cell or ruptured the tight junctions.

The histological findings of this study revealed that no significant damage was induced in the majority of the sonicated mice, proving that the permeability can increase, but not at the expense of safety. Three out of forty mice (7.5%) showed signs of neuronal damage under histological examination or cell loss in the sonicated hippocampus seven days after sonication at pressures higher than 0.45 MPa and microbubble sizes larger than 4-5 μm (Fig. 4.11). The damage was represented by the presence of necrotic or apoptotic cells. In one particular case a significant deformation of the right hippocampal anatomical structure was observed. The presence of dark regions in T_2 imaging (Fig. 4.12) in the cases of sonications with higher pressures using larger-sized bubbles was found not to correlate with hemorrhage, since no red blood cell extravasations were found in the H&E sections of any of the mice that underwent the FUS procedure. Thus, the dark regions were assumed to be directly related to the field inhomogeneities as a result of the excessive Gd-DTPA presence in the EES. Liu *et al*[42] have suggested that susceptibility-weighted imaging (SWI) can detect massive hemorrhagic regions after FUS at the acoustic pressure of 3.47 MPa, but the detection of a few erythrocyte extravasations that low acoustic pressure sonications may induce is limited by the spatial resolution that MRI can offer.

As mentioned in the Materials and Methods section, the stability of the 1-2-μm bubbles is being improved in ongoing investigations. During our experiments, mono-dispersed microbubbles were generated on the same day or one day before our experiments. The number-weighted distribution was always centered around 1-2 μm. In every case of the 1-2-μm diameter bubbles, the BBB was not opened at 0.30 MPa. Therefore, it would also be expected that the threshold of BBB opening might be higher than 0.45 MPa, if the 1-2 μm bubbles are still stable after our experiments.

Based on a quantitative summary of findings of this study, the BBB opening pressure threshold, BBB opening volume, inertial cavitation dose, and the percentage of mice with dark neurons are all bubble size dependent but the inertial cavitation threshold is not. In this study, the pressure interval was 0.15 MPa which may not be small enough to determine the real pressure threshold of inertial cavitation. Regarding the neuronal damage, the inertial cavitation with 1-2 μm bubbles can open the BBB without dark neurons, which implies that the mechanism of BBB opening may also be bubble size dependent. The highest percentage of mice with dark neurons is in the case of 4-5 μm bubbles. Since the resonance frequency of 4-5 μm bubbles embedded in a compliant vessel is close to 1.5 MHz, i.e., the FUS frequency used in this study, the inertial cavitation at this bubble size may induce more damage.

4.5.1.2 IC threshold of lipid-shelled mono-dispersed microbubble

Since the IC threshold of mono-dispersed microbubbles with three distinct diameters was observed within the same range from our *in vivo* investigation, which is different from previous reports about the relationship between the IC and bubble diameter[104,105], a phantom validation, together with theoretical models implementation, was performed to identify the IC threshold of the microbubbles used in this chapter. As shown in Figs. 4.19-21, the IC threshold was determined as 0.35, 0.35, and 0.40 MPa for the 1-2, 4-5, and 6-8-μm diameter bubbles, respectively. The largest microbubbles (6-8-μm diameter) were shown having higher threshold than the other two microbubbles, which is similar as previous report[105]. The IC threshold, however, was identical between 1-2 and 4-5-μm diameter bubbles. This may be resulted from the effect of the resonance frequency. Since the resonance frequency of 4-5-μm bubbles lies between 1.25 MHz and 1.61 MHz, where our insonation frequency lies in, the IC threshold may hence be lower than expected. However, the results of our phantom validation confirmed our *in vivo* investigation, which indicated that the IC will not occur below 0.30 MPa using 1.5-MHz insonation.

A theoretical model can be used to estimate the microbubble oscillation. From previous reports, the IC threshold for the microbubble “relative expansion ratio (R_{max}/R_{rest})” is defined as 3[104]. The ratio of each diameter microbubble at 0.30, 0.35, and 0.45 MPa with three bubble conditions was shown in Table 4.4. In the case of the 1-2-µm microbubbles, the estimation of an unshelled bubble was considered not proper since the ratios (4.48-5.78) were twice than the threshold, which can be clearly observed from Fig. 4.16. Compared with the unshelled bubble, the other two conditions, Shelled and Marmottant, provided more accurate ratio corresponding to our phantom validation. Furthermore, the Marmottant model not only estimated the correct ratio (2.40 at 0.35 MPa), but also described the "compression-only" behavior which has been observed in previous reports[152,155]. Therefore, in the case of 1-2-µm microbubbles, the Marmottant model was concluded to be more appropriate.

However, the ratio estimated by the Marmottant model became inaccurate (> 5 at 0.40 MPa) compared to the other two models. Till now, the oscillation of larger microbubbles at the pressure higher than 0.3 MPa using Marmottant model has not been reported. In this model, the fitting of experimental radius-time curves for lipid-shelled microbubbles reveals that the shell material parameters are found to be dependent on the initial bubble radius[137]. In our simulation, the shell viscosity and elasticity were determined based on previous reports at much lower pressure (40 kPa), which may not be applicable at higher pressure up to megaPascal level. Also, "compression-only" behavior was only observed in the case of small microbubbles (< 2-µm diameter), which can be explained by this model mainly based on the "buckling behavior" within narrow range of radii change[137]. If, during expansion, the bubble radius exceeds the threshold value $R_{\text{break-up}}$, the shell ruptures, which will affect the estimation of the next bubble expansion. Therefore, larger microbubbles with the insonation higher than 0.3 MPa may not be simulated by the Marmottant model.

In comparison with the theoretical model and phantom validation, the simulation of a shelled bubble using Bubblesim may hence be suitable for the case of 4-5 and 6-8-μm diameter bubbles. Therefore, this model and corresponding shell parameters will be implemented to estimate the bubble oscillation in *Chapter* 5, which will use 4-5-μm diameter bubbles and relative low pressure (0.18 MPa) to determine the BBB opening mechanism triggered by the stable cavitation. However, this is an approximate simulation in order to estimate possible bubble oscillation *in vivo*. More accurate models, such as taking into account red blood cells[156], should be investigated to provide more accurate estimation in the future.

4.5.2 Shell effect on bubble behavior during BBB opening

In this study, the effect of the acyl-chain on the BBB opening characteristics and corresponding microbubble behavior was investigated. The threshold of BBB opening was found to be identical across all acyl-chain lengths. According to the qualitative and quantitative analysis, four cases of microbubble oscillation can be determined in this study. First, at 0.15 and 0.225 MPa, the microbubble expansion or the shear stress induced by microbubble oscillation did not induce BBB opening. Second, at 0.30 MPa, when no inertial cavitation was detected, the BBB could be opened through stable cavitation (Fig. 4.19), at a lower permeability ($K_{\text{trans}} \sim 0.03$ min^{-1}). The microbubble expansion, at this stage, may thus not be affected by the capillaries. Third, at 0.45 MPa, i.e., the threshold of inertial cavitation, the bubble expansion ratio may reach the threshold of inertial cavitation, which would lead to larger BBB opening volume and higher permeability than at 0.30 MPa. At this stage, however, no significant difference between the three acyl-chains was observed in the ICD, most likely because the capillary wall may have a larger effect on the bubble expansion. Finally, at 0.60 MPa, i.e., the pressure at which a 66% damage rate was noted, the ICD of the C24 microbubbles was statistically lower than with the C16 and C18 microbubbles, but no difference in the BBB opening volume and permeability was noted. The bubble expansion may exceed the wall strength at this stage, which induced similar BBB opening volume and permeability. The permeability at 0.60 MPa did not exceed the value at 0.45 MPa, since the well-known upper limit had been reached ($K_{\text{trans}} \sim 0.05 \text{ min}^{-}$)[64].

The plateau in the permeability (Fig. 4.20) was reached at 0.45 and 0.60 MPa, which was the same as our previous studies[64]. The permeability reached the upper limit when the inertial cavitation occurred, even if the ICD with the C24 acyl-chain was significantly lower than with the C16 and C18 acyl-chains. Therefore, it was expected that, since different acyl-chain lengths have no effect on the threshold of the inertial cavitation, the permeability will not be affected. However, because of the upper limit, the permeability may not be used to estimate the BBB opening volume. According to the findings of our previous study regarding the physical mechanism of the BBB opening with three microbubble diameters, the ICD can be used towards the estimation of the BBB opening volume. The shell, however, was shown to have an effect on the ICD but not on the BBB opening volume. Thus, the correlation between the ICD and the BBB opening volume changes both pressure and shell types.

In terms of the acoustic response from microbubbles, a previous study has shown that shell composition influences microbubble response in ultrasonic imaging[157]. Larger molecular-weight shell was shown to have lower imaging intensity since the elasticity of the shell was lower. Here, our investigation confirmed these results with respect to the ICD *in vivo*. The ICD from the C24 microbubbles was significantly lower than from the C16 and C18 microbubbles at 0.60 MPa. As shown in Table 4.1, the molecular weight, viscosity, and phase transition temperature were comparable between the C16 and C18 microbubbles. In the case of the C24 microbubbles, the molecular weight was 170 Da higher than the C18 microbubbles, and the viscosity was 22 times higher than the C16 microbubbles. Thus, as previously mentioned, since the bubble expansion was not affected by wall strength at 0.60 MPa, the expansion ratio of the C24 microbubbles may be lower, thereby inducing lower ICD. Regarding the BBB opening characteristics, however, the shell composition did not have any effects on the BBB opening volume, BBB opening threshold, or permeability. Since the microbubble diameter in this study was 4-5 μm, which was similar to the diameter of a capillary, a stable oscillation at 0.30 MPa was sufficient to open the BBB regardless of the acyl-chain lengths. Therefore, the bubble size effect may override the bubble shell effect on the BBB opening.

Histological findings (Table 4.5) revealed that the damage ratio was 1/8, 4/8, and 6/9 at 0.30, 0.45, and 0.60 MPa, respectively, which means that the probability of inducing damage increased with pressure, especially correlated with the occurrence of inertial cavitation. T2 images also showed dark region in the damage cases (fig. 4.18). This finding was different from previous studies using 4-5-μm microbubbles. Only few damaged cases were observed in that study because the mice were sacrificed 7 days as opposed to 3 hours. Because certain damage may be reversible after 7 days, more damage cases were observed in this study.

Interestingly, In the case of the C24 microbubbles, five out of six brains were observed having RBC extravasations or dark neurons at 0.45 and 0.60 MPa (Table 4.5), even if the

ICD was the lowest at 0.60 MPa. It was expected that the ICD was lower with the C24 microbubbles due to the moderate expansion. However, most studies reported that the damage was correlated with the ICD[107,113,114]. This study therefore provided another insight into the shell effect. Borden et al. have shown that buds and strings build up to form large lipid particles several microns in diameter after few pulses insonification in the case of DBPC (i.e., C22 acyl-chain length) microbubbles[141]. Compared with the C24 microbubbles, the C16 and C18 microbubbles mostly experienced acoustic dissolution, which resulted in diameter decrease. Thus, larger contact area between the aforementioned large lipid particles and endothelial cells may be reached in the case of the C24 microbubbles, which may increase the probability of inducing damage with inertial cavitation (i.e. at 0.45 and 0.60 MPa). The effect of buds or strings formed due to the ultrasonic pulses may not be sufficiently reflected by the ICD. However, since this is a preliminary study regarding the effects of the acyl-chain length, we cannot safely conclude that the acyl-chain length will have effect on the RBC extravasations or dark neurons observed. Further studies need to be performed in order to investigate the effect of the acyl-chain length on safety.

Here, three acyl-chain lengths (C16, C18 and C24) were used to identify the shell effects. In the composition of the lipid-coated microbubbles, however, polyethylene glycol (PEG) is frequently used as the emulsifier to prevent coalescence and nonspecific adsorption of blood plasma proteins[140]. PEG has been considered as a tuning parameter with respect to the cavitation events. The pressure required to yield 50% fractional destruction of the microbubble population was affected by PEG, despite the fact that the inertial cavitation was not observed at pressures lower than 0.40 MPa [143]. Compared to the

PEG-5k used in this study, PEG-40 stearate (PEG 40s) was used as the emulsifier in our previous studies on the effect of bubble size. Therefore, the effects between PEG-40s and PEG-5k could now be studied here with identical acyl-chain length and the bubble size (C18 and 4-5-μm diameter, respectively). The threshold of inertial cavitation and BBB opening lied between 0.30 and 0.45 MPa for PEG-40s and PEG-5k microbubbles. In terms of quantitative parameters, such as the ICD, BBB opening volume and permeability, no statistical difference was noted between the PEG-40s and PEG-5k. Hence, following the findings on the acyl-chain length reported here, the threshold of inertial cavitation, threshold of BBB opening, BBB opening volume, and permeability were concluded not to be affected by the microbubble shell (PEG and acyl-chain length) in the brain vasculature.

In addition, in the brain vasculature, the acoustic emission was found to be affected by the acyl-chain length, but the BBB opening characteristics were not. In terms of BBB opening, combined with our previous studies, the microbubble size was concluded to be the most important parameter compared to the shell properties. In order to adequately control the contact area between the microbubbles and the endothelial cells, smaller acyl-chain length would be preferable. For example, C18 microbubbles will be recommended as the agent to induce BBB opening. On the other hand, since the vibration of microbubbles in the brain will still be affected, shell properties should be considered in the optimization for drug delivery.

4.6 Conclusion

This chapter has revealed the microbubble-dependent effect on FUS-induced BBB opening, based on the analysis of permeability, volume, and cavitation response of distinct microbubble size and shell properties. First, we have investigated the relationship between permeability, cavitation response, the diameter of the administered microbubbles and the peak rarefactional pressure of the focused ultrasound-induced blood-brain barrier opening. The volumetric, quantitative permeability measurements and inertial cavitation dose showed that K_{trans}, SCD, and ICD in the sonicated region are increasing with the bubble size and the acoustic pressure. Inertial cavitation was observed to be required for smaller bubbles to induce BBB opening. Based on our findings on the SCD and ICD, however, the interaction between larger bubbles (4-5-μm and 6-8-μm) and the FUS beam could induce the BBB opening through nonlinear oscillation, without inertial cavitation. No significant damage was detected at the BBB opening threshold, at all bubble sizes. Therefore, larger diameter bubbles and lower pressure amplitudes (0.20 – 0.30 MPa) were determined to be safe and consistent in BBB opening. Second, in order to characterize the microbubble behavior during BBB opening, three distinct acyl-chain lengths were used in the fabrication of mono-dispersed microbubbles (4-5-μm diameter). Our findings indicated that the BBB opening characteristics, such as the pressure threshold of BBB opening, the BBB opening volume, and permeability were not affected by the acyl-chain lengths. In addition, the BBB was opened through stable cavitation at 0.30 MPa at all acyl-chain lengths. The quantification of SCD in both studies on microbubble size and shell properties provided the evidence that the stable cavitation, i.e., ultra-harmonics, occurred in the absence of inertial cavitation at 0.30 MPa. The microbubble behavior, however, was affected by the acyl-chain length at 0.60 MPa. The C24 microbubbles might also have higher probability to induce RBC extravasations and dark neurons. Further studies need to be performed to investigate the effect of acyl-chain length on the safety profile.

Chapter 5

The Cavitation-Dependent Tight-Junction Integrity of Blood-Brain Barrier Opening Using Focused Ultrasound and Microbubbles

5.1 Introduction

In *Chapter 4,* the role of microbubbles in FUS-induced BBB opening has been determined. Also, based on our findings in *Chapter 3,* the cavitation type can be monitored and controlled for the BBB opening. As mentioned in *Chapter 2,* several physiological responses to the FUS-induced BBB opening have been studied. The corresponding physical mechanism, however, has not been investigated. Therefore, in this chapter, we will focus on the cavitation dependent mechanism of the FUS-induced BBB opening. Meanwhile, the conditions for BBB opening induced by different cavitation types will also be investigated.

In *Chapter 2,* two types of cavitation have been defined for the microbubbles activated in the acoustic field: inertial cavitation (IC) and stable cavitation (SC). Under IC, the collapse of microbubbles, in association with microjets and shockwaves, was shown responsible for the perforation of cell membranes[158] or hemolysis[107]. Under SC, microbubbles expand and contract in the negative and positive acoustic fields, respectively[103]. The mechanical index (MI), defined as the peak rarefactional pressure (PRP, negative pressure) divided by the square root of the center frequency, was used for the determination of IC likelihood. It has been shown that the IC is not required to induce BBB opening and MI = 0.37 was able to induce the IC during BBB opening[120]. Therefore, real-time modulation of treatment pressures on the basis of acoustic emissions from the exposed microbubbles is capable of monitoring and controlling the cavitation during BBB opening[159].

As shown in Fig. 2.4, tight junction (TJ) plays an important role in the formation of the BBB. Therefore, understanding the TJs response to the specific cavitation type can be helpful to unveil the mystery of delivery for larger compound across the BBB via the microbubble oscillation in the acoustic fields. The MI, however, used in the studies shown in *Chapter 2* about the TJs integrity of BBB opening was above the IC threshold (0.37), and the microbubbles were poly-dispersed. Since the pressure threshold of BBB opening is bubble size-dependent[56,57], using poly-dispersed microbubbles at high MI would raise the difficulty of unveiling the physics of FUS-induced BBB opening.

To date, the physical mechanism of causing the disruption of the TJ proteins after FUS-induced BBB opening is unclear. Therefore, the purpose of this study is to investigate the TJ response and corresponding cavitation during BBB opening. In order to exclude the bubble size effect, 4-5-μm diameter bubbles are used in each sonication and the concentration remained the same. SC-induced BBB opening is generated at a PRP of 0.18 MPa using various pulse lengths (PLs). In contrast, IC-induced BBB opening is generated at a PRP of 0.45 MPa using a burst sequence based on our previous study[53]. Although, as mentioned in *Chapter 2,* IC occurs along with SC occurrence, the IC dominates BBB opening while the PRP is higher than the IC threshold. In both cases, the TJ integrity is studied with respect to SC- and IC-induced BBB opening.

5.2 Materials and Methods

5.2.1 Sonication protocol

The system of focus ultrasound and cavitation detection was shown in Fig. 3.3(b). A total of thirty-three (n=33) adult male mice (strain: C57BL/6, weight: 23.35 ± 1.93 g, Harlan Sprague Dawley, Indianapolis, IN, USA) were sonicated in this chapter. The right hippocampus was targeted and the left hippocampus served as the control following a precise grid-targeting procedure[40]. The focus was placed 3 mm beneath the skull so that the focal region overlapped with the right hippocampus as in previous studies[41].

In the study of SC-induced BBB opening, a PRP of 0.18 MPa accounting for tissue attenuation was used[40]. The pulse repetition frequency (PRF) was 5 Hz. Six sets of acoustic parameters were used to investigate the effect of pulse length (PL), exposure energy, and duty cycle. The number of mice used at each set of acoustic parameters is provided in Table 5.1. A PRP of 0.45 MPa was used in the study of the IC-induced BBB opening. As employed in our previous study[160], a burst of 100 short-cycle pulses (3 cycles, PRF = 5, 25, or 100 kHz) was applied at 5-Hz burst repetition frequency. The method of the quantification for the ICD has been proposed in section 4.3.4.

Lipid-shelled microbubbles of 4-5-μm in diameter were manufactured and size-isolated in-house using differential centrifugation as described in Feshitan et al.[151]. The concentration was diluted from a higher concentration to approximately 8 x 10^8 bubbles / mL before microbubble administration and sonication was performed 5 s after microbubble administration. Microbubble-size distributions and concentrations were determined by the electrical impedance sensing zone method (Multisizer 3, Beckman couter, Brea, CA, USA).

Table 5.1 Acoustic parameters for SC-induced BBB opening

Protocol	(a)	(b)	(c)	(d)	(e)	(f)
PL (cycles)	150	750	3000	7500	30000	150
PL (ms)	0.1	0.5	2	5	20	0.1
PRF	5	5	5	5	5	100
Duty cycle (%)	0.05	0.25	1	2.5	10	1
Duration (s)	300	300	300	300	30	300
Exposure time (s)	0.15	0.75	3	7.5	3	3
Opening	1/3	4/4	3/3	4/4	3/3	0/3

5.2.2 BBB opening confirmation

In this study, MRI and fluorescence microscopic examination of dextran delivery was used to confirm the BBB opening. A vertical-bore 9.4T MR system (Bruker Biospin, Billerica, MA, USA) was used to confirm and quantify the BBB opening in the murine hippocampus. The procedure and volume quantification method were then used as previously described in *Chapter 4*[57]. The average MR intensity within the opening volume was also measured simultaneously.

Lysine-fixable dextran at a molecular weight of 3 kDa and fluorescently tagged with Texas Red® (Invitrogen, Carlsbad, CA, USA, excited wavelength: 568±24 nm.) were used as the model drug. Dextran was dissolved (concentration: 40 μg/g) in phosphate-buffered saline (PBS). A 100 μl volume was injected into the tail vein during 30 s after sonication. Brains were prepared for fluorescence microscopy and image analysis by serial dilution of 10%, 20%, and then 30% sucrose at 30 min, 1 h, and overnight time increments, respectively. They were then embedded in a formulation of water-soluble glycols and resins (Sakura Tissue-Tek O.C.T. Compound; Torrance, CA, USA), frozen in a square mold, and then sectioned using a cryostat into 80-μm and 10-μm slices in the horizontal orientation. Images of all frozen sections were then acquired using an upright fluorescence microscope (BX61; Olympus, Melville, NY, USA).

5.2.3 Immunofluorescence Staining

Immunofluorescence staining of the frozen brain sections was performed according to the manufacturers' instructions. Briefly, sections were prewashed once in PBS for 3 min, and then permeabilized using PBS/0.2% Triton-X-100 solution for 1 hr at room temperature. The antigens were unmasked by incubating the sections in 10 mM sodium citrate buffer (pH 6.0) and heating them just below the boiling temperature (95-99 ºC) for 20 min. The slides were then cooled down at room temperature for 30 min, rinsed in PBS for 3 min and then followed by immunofluorescence staining. Sections were blocked with blocking buffer (PBS/0.3% Triton-X-100/5% goat serum) for 1 hr at room temperature and then incubated with rabbit anti-ZO-1 antibody (Invitrogen) diluted with antibody dilution buffer (PBS/0.3% Triton-X-100/1% BSA) overnight at 4 ºC. After washing sections with PBS 3 times, they were incubated with Alexa Fluor 488 conjugated goat anti-rabbit IgG (Invitrogen) for 1 hr in the dark at room temperature. Sections were then washed and covered with vectashield mounting medium containing DAPI (Vector Lab; Burlingame, CA) and cover slips. The final fluorescence images were captured with an Olympus DP30BW camera mounted on an Olympus BX61 inverted microscope using a 100x objective.

5.3 Results

5.3.1 SC- and IC-induced BBB opening

The BBB opening confirmed by MRI of each parametric set is depicted in Fig. 5.1. In the case of low PRP (0.15 MPa), three main observations can be concluded. First, at 5-Hz PRF, the BBB is not opened with a 0.1-ms PL, but is opened at PLs of 0.5, 2, 5, and 20 ms (Figs. 5.1(a-e)). Second, BBB opening is not observed at 0.1-ms PL and 100-Hz PRF (Fig. 5.1(f)). Third, the histological analysis shown in Figs. 5.1(g-i) depicts that no damage is observed at the longest exposure time (corresponding to Fig. 5.1(d), 5-ms PL and 5 min duration). The quantitative analysis depicted in Fig. 5.2 shows that both the BBB opening volume and the normalized MR intensity reach a plateau when the PL surpassed 2 ms (Fig. 5.2(a)). In the investigation on the effect of exposure time (2-ms PL and 5 min duration as well as 20-ms PL and 0.5 min duration), no significant difference was observed in the BBB opening volume (Fig. 5.2(b), left axis), but the normalized MR intensity is significantly higher at longer sonication durations (*: $P < 0.05$, Fig. 5.2(b), right axis).

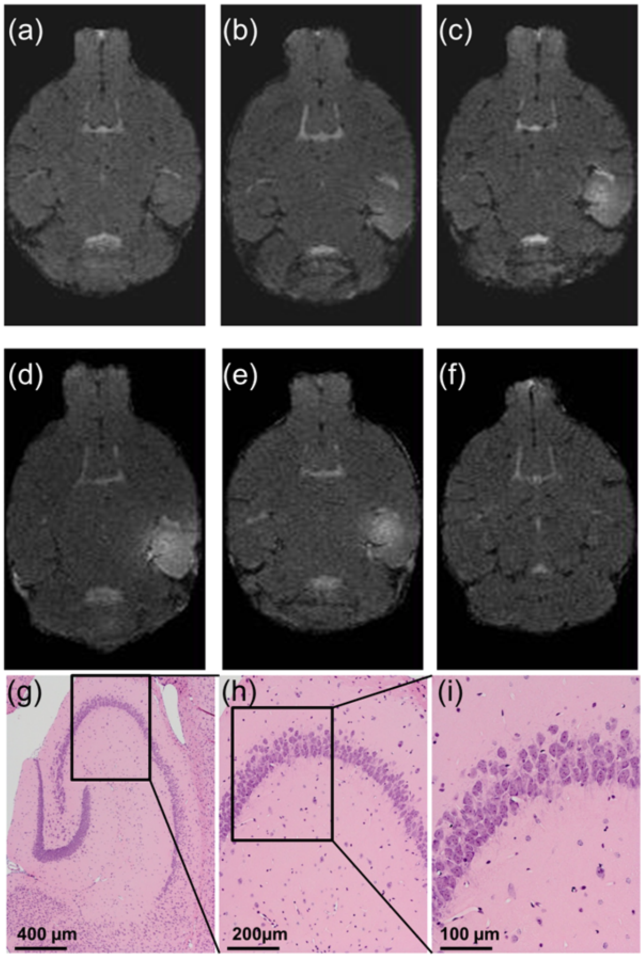

Figure 5.1 – The 2D T1-weighted MR image of each acoustic parameter set shown in Table 1. At 5-Hz PRF, sonications were (a-d) at PLs of 0.1, 0.5, 2, and 5 ms at 300-s duration, or (e) at 20-ms PL and 30-s duration. In addition, identical duty cycle as set (c), sonication was at (f) 0.1-ms PL and 100-Hz PRF. The BBB was not opened in protocol (a) and (f), but was opened in protocol (b-e). Histological analysis (g-i) showed that no red blood cell extravasations were observed in protocol (d), i.e., the longest exposure time. The magnification in (g), (h), and (i) are 40x, 100x, and 200x, respectively.

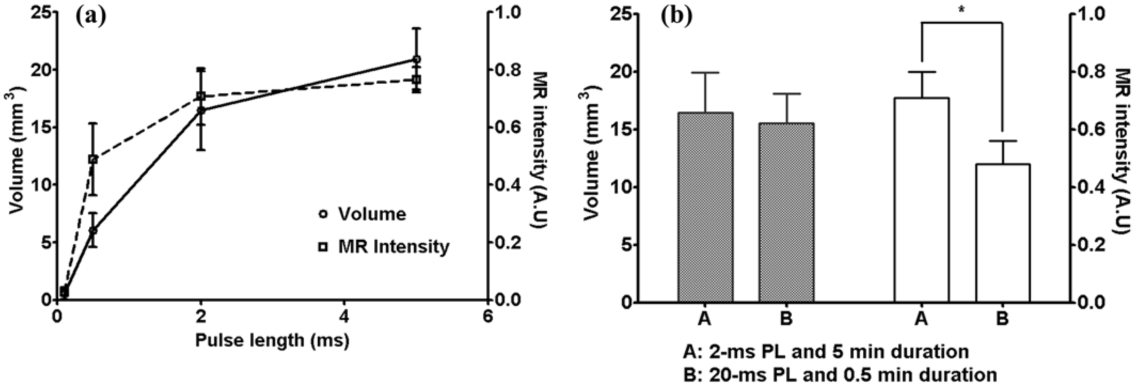

Figure 5.2 – Statistical analysis of the BBB opening volume and normalized MR intensity on the effects of (a) 4 different PLs, and (b) exposure time.

Emission of the burst sequence at the PRFs of 5, 25, and 100 kHz is capable of opening the BBB (Fig. 5.3(a-c)). No significant difference was observed between the three different PRFs in the BBB opening volume and normalized MR intensity. The inertial cavitation dose (ICD) at 100-kHz PRF is significantly higher than 5- and 25-kHz PRF (Fig. 5.3(d), *: $P<0.05$).

5.3.2 Fluorescence imaging and Tight Junction integrity

Fluorescence images (Fig. 5.4) and the corresponding frequency response show that, in the case of the longest exposure time (5-ms PL and 5-min duration) of the SC-induced BBB opening, fluorescently tagged 3-kDa dextran was contained in the vessel (Fig. 5.4(b)) and only the harmonics were observed (Fig. 5.4(f)), while the dextran is diffuse into the hippocampus region in the case of IC-induced BBB opening at 100-kHz PRF (Fig. 5.4(d)) together with the presence of the broadband response (Fig. 5.4(h)).

The immunofluorescence staining of ZO-1 protein for SC- and IC-induced opening is shown in Fig. 5.5. However, no difference is observed on the expression of ZO-1 between the unsonicated (Figs. 5.5(a,c,e,g)) and sonicated sites (Figs 5.5(b,d,f,h)), neither between the opening induced by SC (Figs. 5.5(b,d)) and IC (Figs. 5.5(f,h)).

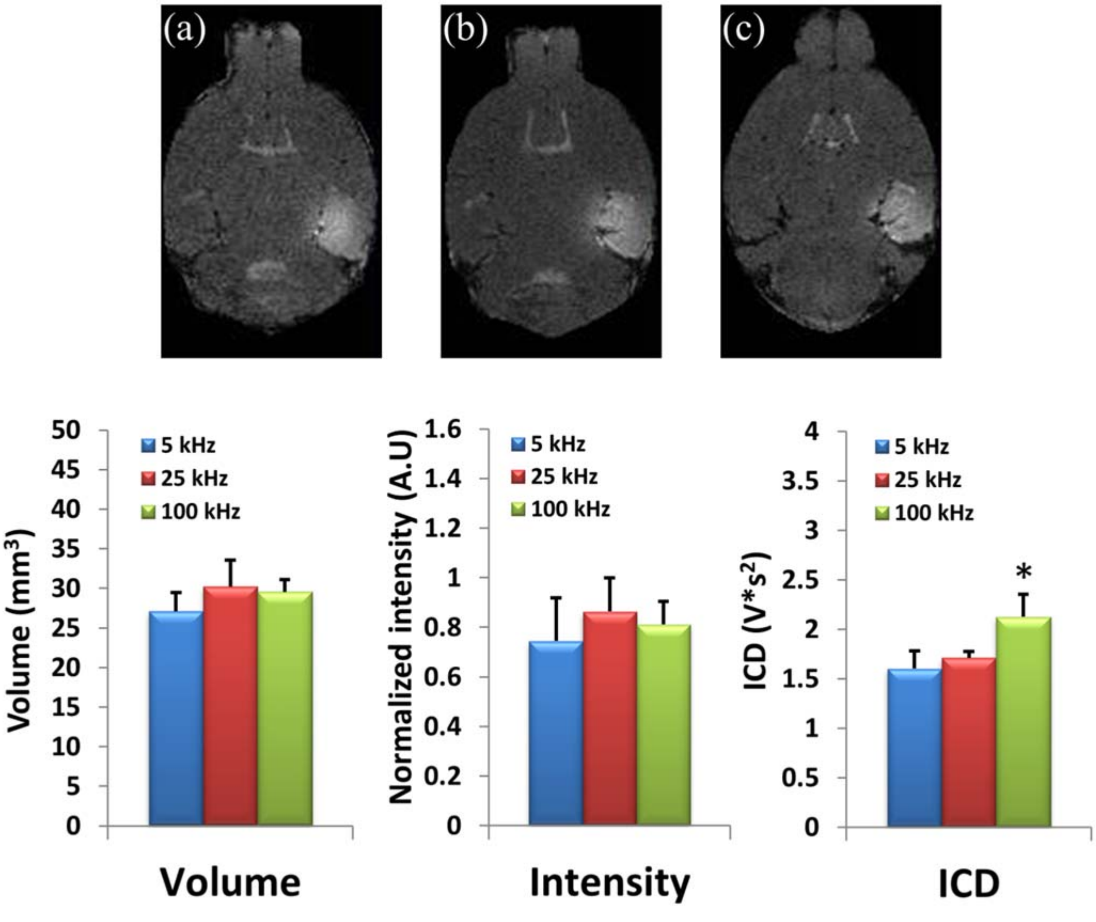

(d)

Figure 5.3 – The 2D T1-weighted MR image of IC-induced BBB opening sonicated at PRFs of (a) 5 kHz, (b) 25 kHz, and (c) 100 kHz. The BBB opening volume, normalized MRI contrast enhancement, and inertial cavitation dose of 3 PRFs were measured (d). No significant difference was observed between all cases in terms of volume and intensity. The ICD of 100 kHz was significantly higher than the other cases.

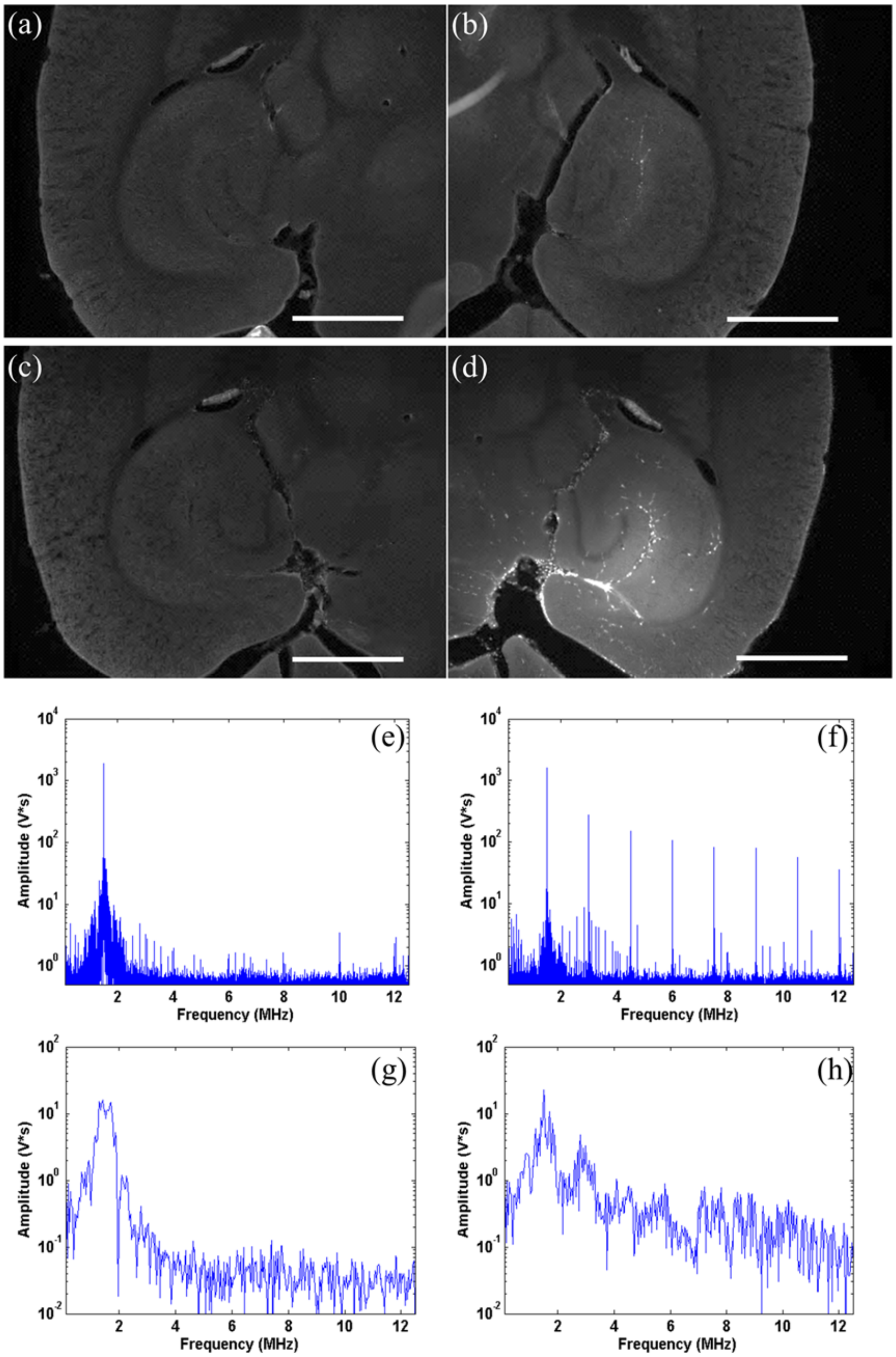

Figure 5.4 – Fluorescence images and the corresponding frequency spectrum in the case of (a,b,e,f) SC- and (c,d,g,h) IC-induced BBB opening. The right hippocampus (b,d,f,h) was sonicated in the presence of microbubbles and fluorescently tagged 3-kDa dextran, whereas the left side was the control (a,c,e,g). The dextran molecules were restricted in the vessel in the case of SC-induced BBB opening (b), together with the occurrence of harmonics, while they were diffused to the hippocampus in the case of IC-induced BBB opening (d), together with the broadband response. The scale bar depicts 1 mm.

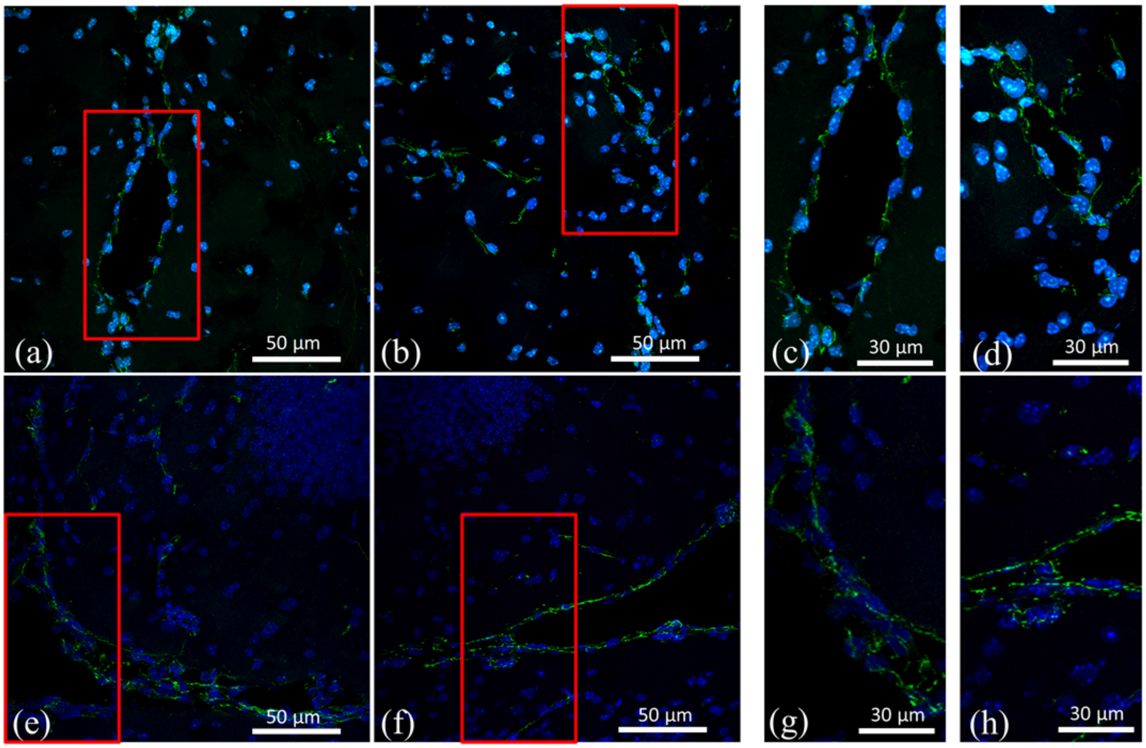

Figure 5.5 – Immunofluorescence staining in the cases of (a-d) SC- and (e-h) IC-induced BBB opening. The ZO-1 expression was indicated in green. No significant difference can be observed between the left (a,c,e,g) and the right (b,d,f,h) hippocampus, in both SC- and IC-induced BBB opening.

5.4 Discussion

Here, the cavitation-dependent TJ integrity in the presence of the FUS-induced BBB opening was investigated. The TJ protein ZO-1 was examined to evaluate the relation between TJ and cavitation. In the SC-induced BBB opening, to our knowledge, a PRP of 0.18 MPa has not been used in transcranial BBB opening using FUS and microbubbles. This study also investigated the effect of pulse length, duty cycle, and total exposure energy to explore the conditions required for SC-induced BBB opening at low PRP. In IC-induced BBB opening, the effect of PRF in the burst sequence was also determined based on the cavitation response recorded by our trascranial PCD.

5.4.1 Cavitation-dependent mechanism of BBB opening

The TJs were found not to be disrupted by either SC or IC under the FUS and microbubble pore formation used in this study (Fig. 5.5). This is different from the findings reported by Sheikov et. al [6], where ZO-1 was disassembled, leading to the loss of junctional barrier functions in brain microvessels, inspected by the immunoelectron microscopy, after sonication. The variations could be linked to the different PRPs applied in that study (1.1 MPa) comparing to ours (0.45 MPa for IC and 0.18 MPa for SC), suggesting that the TJs may not be disrupted until a sufficiently high pressure is reached. For the delivery of macromolecules (3-kDa dextran) across the BBB in our study, it is possible that transcellular transport was preferred over the paracellular at the pressures used (Fig. 5.4). Similar results have previously been reported using other lipid-coated microbubbles[161,162]. Juffermans et al. showed that the uptake of fluorescent di-4-aminonaphtylethenylpyridinium (di-4-ANEPPS, ~500 Da) was facilitated through endocytosis and macropinocytosis after rat cardiomyoglast cells were sonicated using 1 MHz at 0.25 MPa PRP with Sonovue® microbubbles[161]. Using fluorescence microscopy, Meijering et al. also showed homogeneous distribution of 4.4- and 70-kDa dextrans through the cytosol, using 1 MHz at 0.22 MPa PRP with Sonovue® microbubbles, which was linked to ultrasound and microbubble-mediated delivery of macromolecules through endocytosis *in vitro*[162]. Although the type of cavitation was not determined in the aforementioned two studies, the MIs were calculated to be 0.25 and 0.22, respectively, which was lower than the IC threshold (0.37, *Chapters 3, 4*)[120]. Therefore, it is concluded that the transcellular path may be the possible molecular uptake route of SC-induced BBB opening.

Furthermore, we observed that a sufficient PL (0.5 ms) was required for SC to induce BBB opening (Fig. 1). It has been shown that an increases in intracellular calcium occurs when subjected to mechanical stretching on keratocytes[163]. Also, the opening of stretch-activated ion channels in response to repeated mechanical deformation may lead to an increase in calcium concentration in visceral sensory neurons[164]. The vessel invagination has also been observed due to the ultrasound-driven microbubble[165]. A longer PL may thus increase probability and number of interactions between the microbubbles and the endothelial cells or surrounding neurons. Therefore, the duration of the repeated deformation of the endothelial cells, dictated by the pulse length (PL), may play an important role in the SC-induced endocytosis.

As mentioned in *Chapter 4,* the theoretical model can be a tool for estimation of microbubble oscillation. In this chapter, compared with our previous studies[56,57], the BBB was opened at 0.18 MPa but was not opened at 0.15 MPa, even at a PL of 20 ms. In order to have the possible explanation, Bubblesim was used to estimate the microbubble oscillation. As shown in Fig. 5.6, the maximum diameter of microbubble is over 9 μm at 0.18 MPa, but is less than 7 μm at 0.15 MPa based on the parameters decided in *Chapter 4.* As a result, 0.15 MPa may not be sufficient for microbubbles to have enough contacts on the endothelial cells. Using 0.18 MPa, the expansion of 4-5-μm diameter bubbles may be able to reach the capillary wall of the endothelial cells, and then induce BBB opening via sufficient PL, i.e. repeated deformation.

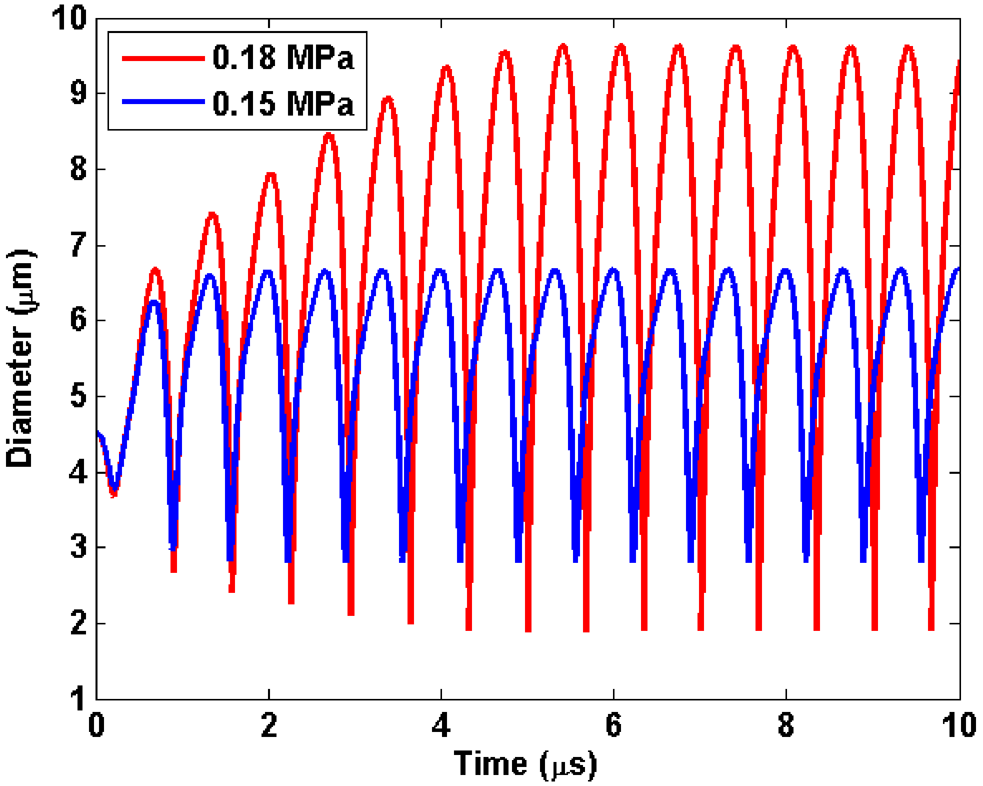

Figure 5.6 – Simulation of the oscillation of a 4.5-μm-diameter bubble at PRPs of 0.18 MPa and 0.15 MPa using Bubblesim. The shell viscosity was 0.19 Pa.s and the shear modulus was 32 MPa. The maximum diameter lies in 8-10 μm at 0.18 MPa, but in 5-7 μm at 0.15 MPa.

In *Chapter 4*, the stable cavitation dose quantified *in vivo* (Fig. 4.7) and in phantom (Fig. 4.14) showed that the SC occurred at 0.30 MPa. Here, we also quantified the SCD at 0.18 MPa PRP, but no significance was observed between the peaks at ultra-harmonics and the background noise. Despite the fact that the skull may mask the detection of ultra-harmonics, the phantom results in *Chapter 4* also showed that SC did not occur at 0.18 MPa. Therefore, using 4-5-μm diameter bubbles, the BBB may be opened via short PL (67 μs, *Chapter 4*) in the presence of ultra-harmonics, or long PL (5 ms) in the absence of ultra-harmonics.

The mechanism of IC-induced BBB opening was also investigated in this study. Our results indicate that observable BBB opening was induced using 3-cycle PL and 4-5-μm diameter bubbles(Fig. 5.3(a-c)), which confirmed the previous works using short cycles and Definity® bubbles[53,62]. Also, the ICD at 100-kHz PRF was significantly higher than at 5-kHz and 25-kHz PRF (Fig. 5.3(d)). Because of lower microbubble depletion through uninterrupted pulsed sonication in short pulse interval durations, 100-kHz PRF may increase the probability of disrupting a larger number of microbubbles, thereby causing higher ICD. However, no significant difference was observed in terms of the BBB opening volume and normalized intensity. Since the permeability plateau is reached at 0.45 MPa using 4-5-μm diameter bubbles[64], the PRF may not affect the BBB opening properties with identical conditions.

Interestingly, in the case of SC-induced BBB opening at the longest exposure time, detectable BBB opening was observed in the MR images (Fig. 5.1(d)), but not in the fluorescence images (Fig. 5.5(b,d)). Since the molecular weight of MRI contrast agent, Omniscan®, is 573 Da, while the fluorescently-tagged dextran is 3 kDa, this finding could imply that the size of SC-induced BBB opening is between 573 Da and 3 kDa. However, the uptake mechanism between them may be distinct. In addition, comparing with the IV injection for the dextran, the administration of Omniscan® was IP. It is difficult to compare the uptake of different molecules with distinct administration routes. Future studies will be carried out to investigate the maximum BBB opening size cause by SC.

5.4.2 Safe BBB opening using low mechanical index

The thresholds of MI used in previous studies (0.46 or 0.37) were determined not to be necessary and sufficient for BBB opening[12,51]. The results of this study indicate that low MI (0.15) is capable of inducing detectable BBB opening at PLs of 0.5 ms or above. The PL threshold of inducing BBB opening has been previously identified at 10 ms using Optison® at MI = 0.6[52] and 2 ms using Definity® at MI = 0.3[12]. In this study, however, it was identified between 0.1 and 0.5 ms. Compared with other studies of the PL effect, 4-5-μm mono-dispersed microbubbles were used in this study. The effect of bubble size has been investigated in our previous studies[56,57]. The BBB opening was induced without IC using larger microbubbles at 0.067-ms PL. Therefore, the PL-threshold may be also bubble-size dependent. The histological analysis showed that no RBC extravasation was observed using the longest exposure time, i.e., 5-ms PL and 5-min duration (Fig. 5.1(g-i). Also, compared with our previous study, comparable BBB opening volume (20.92 ± 2.65 mm^3) could be reached using long PL (5 ms) at relatively low pressures (0.18 MPa) instead of 100 cycles at 0.45 MPa. Therefore, equivalent therapeutic effects may be induced at low pressures and sufficient PL, which will effectively reduce the probability of damage caused by the IC.

In this study, sonication duration was observed having effects on the MR intensity. As shown in Fig. 5.2, the BBB opening volume was similar but the normalized MR intensity of the 300-s duration was found significantly higher than that of the 30-s duration. As shown in Fig. 5.1(g), since the BBB opening volume reached the plateau at 2-ms PL, longer PL may not increase the opening volume. However, longer durations may increase the likelihood of opening the BBB of different endothelial cells, i.e. the BBB opening sites, due to the reperfusion of microbubbles; thereby increasing the amount of gadolinium diffusion to the brain tissue.

The effect of the duty cycle was also investigated in this study. In order to keep the duty cycle identical, 100-Hz PRF and 0.1-ms PL was applied to compare with the results of 5-Hz PRF and 20-ms PL. Even if the duty cycle is fixed at 1%, no BBB opening was induced using 100-Hz PRF and 0.1-ms PL. Therefore, the duty cycle does not play a role in the FUS-induced BBB opening.

5.5 Conclusion

In this chapter, for the first time, MI = 0.15 was shown to be capable of transcranially opening the BBB. A sufficient PL was required to induce BBB opening at this MI, and higher MRI contrast enhancement was induced at longer sonication durations. The TJ was not disrupted at PRPs lower than 0.45 MPa, therefore longer PLs (2 ms) at lower acoustic pressure (0.18 MPa), in combination with larger (4-5-µm diameter) microbubbles, may be sufficient to deliver therapeutic molecules by changing the permeability of endothelial cells without IC occurrence or any damage.

Chapter 6

Translation of the Focused Ultrasound Induced Blood-Brain Barrier Opening System to Non-Human Primates

6.1 Introduction

In previous chapters, we have shown that a passive cavitation detector (PCD) can be used to transcranially acquire the acoustic emissions stemming from the interaction between the microbubble and the brain tissue during BBB opening in mice. During sonication, the cavitation response, which was found to be pressure- and bubble-dependent, provided real-time feedback regarding the opening occurrence and its properties, thereby determining the physical mechanism of FUS-induced BBB opening. As a result, the passive cavitation detection can serve as a useful tool for monitoring the microbubble response to predict the occurrence and volume of BBB opening, as well as the possibility of inducing damages. However, to test the potential of this technique to be applied in humans, it is very important to first translate this system of the FUS in combination with cavitation monitoring from mice to larger animals and preferable non-human primates. Contrary to rodents, the primate brain consists of sulci (fissures) and gyri (lobes). In addition, due to the thicker skull, discrepancies in sound velocity and density combined with high absorption can lead to poor focusing quality and high energy loss, especially at higher frequencies[166]. Therefore, in non-human primates, the pressure threshold of BBB opening and inertial cavitation as well as the safety window and the physical mechanism of FUS-induced BBB opening may be distinct from that in mice.

In this chapter, we aim at establishing a cavitation-guided BBB opening system in non-human primates. This study will be a major step towards the clinical translation of this emerging technology that can be combined with any type of pharmacological treatment to the brain. Based on our previous studies on the capabilities and limitations of this technique tested in *ex* vivo non-human primates (*Appendix B*), we will first determine the appropriate microbubble size and acoustic pressure for BBB opening. Second, different parameters will be applied to determine the reproducibility and reversibility of BBB opening. Finally, the correlation between the cavitation response, the BBB opening volume and targeted brain structure will be established to achieve the real-time cavitation-guided BBB opening in monkeys.

6.2 Materials and Methods

6.2.1 Sonication protocol

Initial feasibility studies were performed on five male rhesus macaques over the course of 12 sessions (a total of 25 sonications). Either the mono-dispersed 4-5-µm bubbles were manufactured in-house and size-isolated using differential centrifugation, as used in *Chapter 4 and 5,*[151] or the Definity® microbubbles, as used in *Chapter 3,* were used in this study. The PRP, PL, PRF, microbubble types, and targeting region were described in Table 6.1. The experimental setup was shown in Fig. 6.1. The single-element transducer used in our previous *ex vivo* study was mounted on a standard monkey stereotaxic frame for accurate positioning (Fig. 6.2), and the corresponding targeting region was shown in Fig. 6.3. The global attenuation (absorption, reflexion and scattering) of the skull and the skin was assumed to be -5.7 dB and -4.5 dB at 500 kHz, respectively[167]. The attenuation in the monkey brain tissue was assumed to be around -0.5 $dB.cm^{-1}$ and the thickness of this layer was estimated to be equal to 2 cm. Therefore, the emission amplitude was raised by 7.15 dB (approximately a factor of 2.28) compared to the calibration measurements obtained in water to compensate for the energy loss along the path.

Table 6.1 Acoustic parameters and corresponding targeting region # denotes the number of sonications. N is the number of monkeys. VC: Visual Cortex. HC: Hippocampus Ca: Caudate Pu: Putamen.

Protocol	PL	PRF (Hz)	microbubble	PNP (MPa)	Targeting (#)	N
A	100 cycles	10	Definity®	0.20	VC (1)	1
				0.25	VC (1)	1
				0.30	VC (1)	1
B	5000 cycles	2	Definity®	0.30	HC (3)	2
				0.45	HC (3)	2
				0.60	HC (1)	1
			4-5 µm	0.30	VC (2), Ca (2), Pu (1)	4
				0.45	VC (4), Ca (1), HC (1)	4
				0.60	VC (2), HC (2)	1

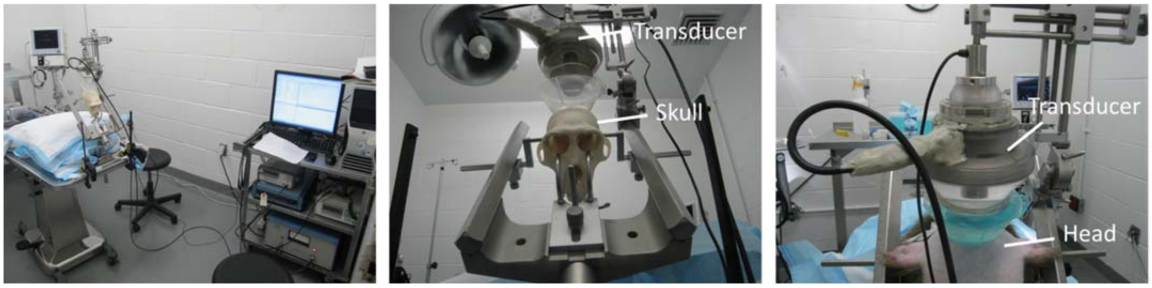

(a) (b) (c)

Figure 6.1 – Experimental setup for *in vivo* FUS-induced BBB opening in the operating room. (a) A single-element, circular focused ultrasound transducer with a hole in the center was driven by a function generator (Agilent Technologies, Palo Alto, CA, USA) through a 50-dB power amplifier (ENI Inc., Rochester, NY, USA). The center frequency, focal depth, outer radius and inner radius of FUS were 500 kHz, 90 mm, 30 mm and 11.2 mm, respectively. (b) *In vivo* of the transducer mounted on the stereotactic frame with a manipulator allowing precise positioning of the transducer in the stereotactic referential. (c) Monkey placed in the stereotactic frame. The monkey is shaved and a degassed echographic gel container is placed on the top of its head to insure maximal acoustic transmission.


(a) (b) (c)

Figure 6.2 – Targeting procedure for *in vivo* FUS-induced BBB opening. (a) A positioning rod (black arrow), indicating the position of the focus (5 cm away from the edge of the transducer), was used to target. (b) This positioning rod was mounted on the manipulator in order to locate the origin of the stereotactic coordinates. (c) The origin of the stereotactic coordinates indicated by the engraved cross on the metal piece between the ear-bars is targeted with the tip of the positioning rod.

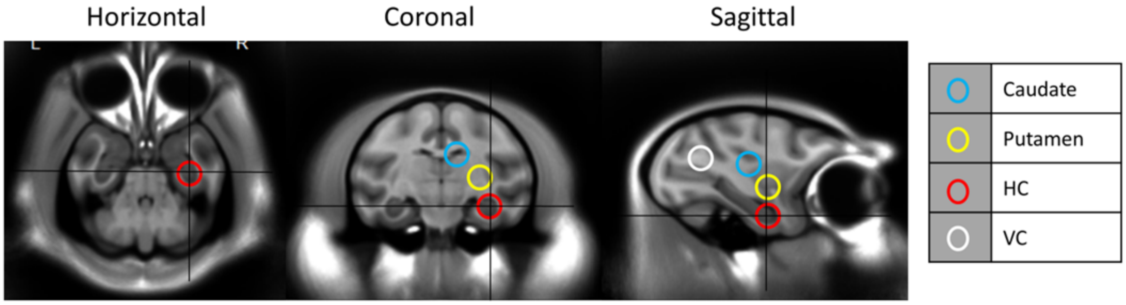

Figure 6.3 – Targeting region and corresponding view from three dimensional views, adapted from a web-based brain atlas[168].

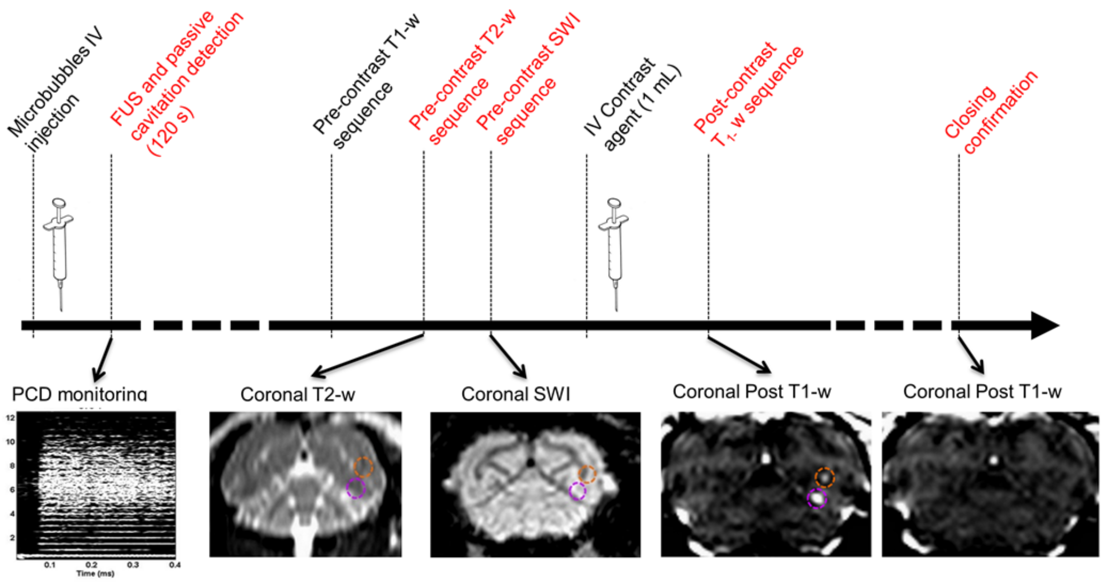

Figure 6.4 – Experimental timeline of *in vivo* BBB opening in NHPs. Two targets at 0.30 MPa (purple circle) and 0.45 MPa (orange circle) are also illustrated.

The experimental timeline is shown in Fig. 6.4. For the application of the FUS, all animals were anesthetized with 2% isoflurane (carrier gas: oxygen). The heart rate was held at approximately 120 beats per minute and the respiratory rate at around 60 breaths per minute. Prior to sonication, the scalp hair was removed with a depilatory cream to ensure maximal acoustic transmission. The animal's head was then placed in a stereotactic frame to enable careful targeting of the ultrasound. The sonication was performed immediately after intravenous (IV) injection of a 500-μL microbubble bolus in all experiments ($5\text{x}10^9$ numbers/mL for customized microbubbles and $1.2\text{x}10^{10}$ numbers/mL for Definity®). Targeting was ensured using a manipulator and a positioning rod indicating the position of the focus relatively to the stereotaxic coordinates (Fig. 6.2).

6.2.2 MRI and acoustic emission detection

MRI was used to confirm BBB opening using gadiodiamide contrast agent. 3D Spoiled Gradient-Echo (SPGR) T1-weighted sequences (TR/TE=20/1.4 ms; flip angle: 30°; NEX=2; spatial resolution: 500×500 μm^2; slice thickness: 1 mm with no interslice gap) were applied after intravenous (IV) injection of gadodiamide (Omniscan®, molecular weight 573.66 Da, GE Healthcare, Princeton, NJ, USA) 1 h after sonication. The dose applied was 0.2 mL/kg and the IV injection was performed 2 minutes before the SPGR T1-weigthed scan (scan duration: 18 minutes). Gadodiamide presence in the brain parenchyma was induced by BBB opening, similar to the mice shown in *Chapters 3-5*. 3D T2-weighted sequence (TR/TE=3000/80; flip angle: 90°; NEX=3; spatial resolution: 400×400 μm^2; slice thickness: 2 mm with no interslice gap) and 3D Susceptibility-Weighted Image (SWI) sequence were applied (TR/TE=19/27 ms; flip angle: 15°; NEX=1; spatial resolution: 400×400 μm^2; slice thickness: 1 mm with no interslice gap) and were used to assess brain damage. In the session of closing timeline and accuracy, FSL, a comprehensive library of analysis tools for MRI brain imaging data, was used to perform the image registration to keep the brain orientation at identical location for the closing timeline determination, and the focal shift identification[169,170].

A single-element passive cavitation detector (center frequency: 7.5 MHz, focal length: 60 mm, Olympus NDT, Waltham, MA, USA) was positioned through the center hole of the FUS transducer. The two transducers were aligned so that their focal regions fully overlapped within the confocal volume. The PCD and spectrogram method were mentioned in *Chapter 4*.

6.3 Results

6.3.1 BBB opening and corresponding cavitation response

Two protocols were implemented in this study. First, in the protocol A (Table 6.1), we used Definity® microbubbles and short PL (100 cycles) at 0.20 – 0.30 MPa. The results were shown in Fig. 6.5, which showed that no BBB opening was induced in any case of protocol A (Table 6.1), although inertial cavitation, i.e., broadband response, occurred in each case. However, microbubble response was detected through the monkey skull for the first time[36].

Second, in the protocol B (Table 6.1), Long PL (5000 cycles) and higher pressure (0.30 – 0.60 MPa) were applied with Definity® or 4-5-µm diameter bubbles. Figure 6.6 shows that no BBB opening was induced at 0.45 MPa using Definity® but a broadband response was detected. In the case of 4-5-µm microbubbles, however, the BBB was successfully opened at 0.30 and 0.45 MPa. The MR images and the corresponding spectrogram of the first pulse are depicted in Fig. 6.7. As a result of the deposition of the MRI contrast agent in the brain tissue after ultrasound exposure, the MR images indicated that the BBB was opened at 0.30 MPa (Fig. 6.7(d,e,g)) and 0.45 MPa (Fig. 6.7 (f,h)) using the 4-5-µm bubbles. The white matter, compared with the gray matter, was observed easier to be opened (Fig. 6.7). The peak MR intensity enhancement at the BBB-opened region relative to the average value in the parenchyma was increased by 119% and 48% at 0.3 MPa and 0.45 MPa, respectively. The volume of the BBB disruption was equal to 24.6 mm^3 and 30.5 mm^3, respectively. The two distinct opened sites were separated by a distance of 4.74 mm.

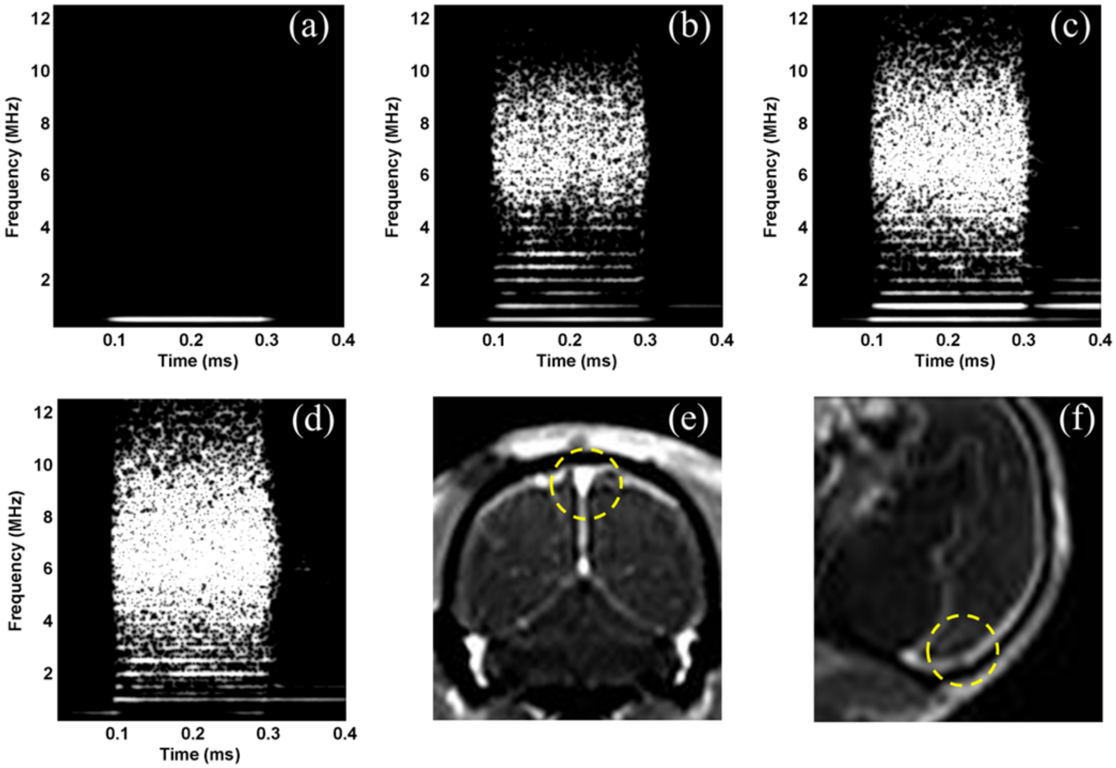

Figure 6.5 – (a) The spectrogram without microbubbles administration show that all the harmonics and broadband response are from microbubbles. Spectrograms during FUS sonication with monkey 2 at (b) 0.20 MPa, (c) 0.25 MPa, (d) 0.30 MPa, and MR images with (e) coronal and (f) sagittal planes show that the broadband response occur with all pressures, but no BBB opening is induced (dashed circle).

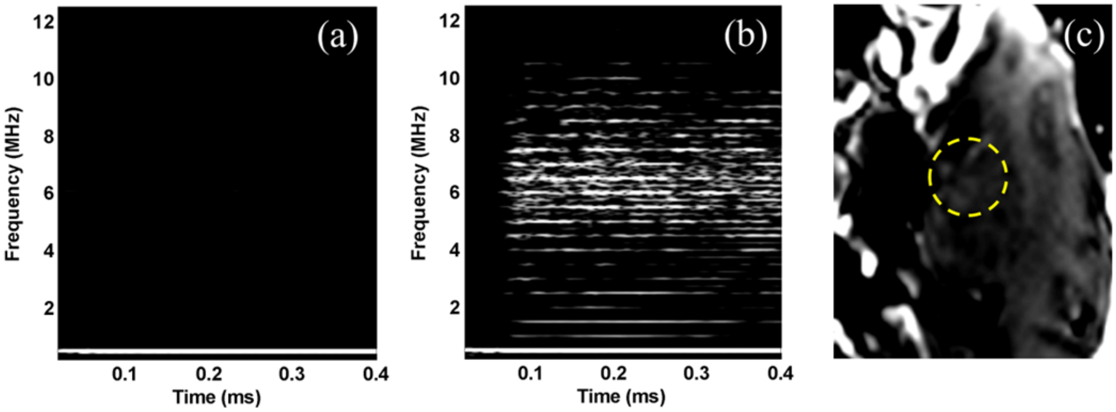

Figure 6.6 – (a) The spectrogram without microbubbles administration show that all the harmonics and broadband response are from microbubbles. The spectrogram during FUS sonication with monkey (b) 0.45 MPa shows that the broadband response takes place. The MR image with (c) sagittal plane, however, shows that no BBB opening is induced (dashed circle).

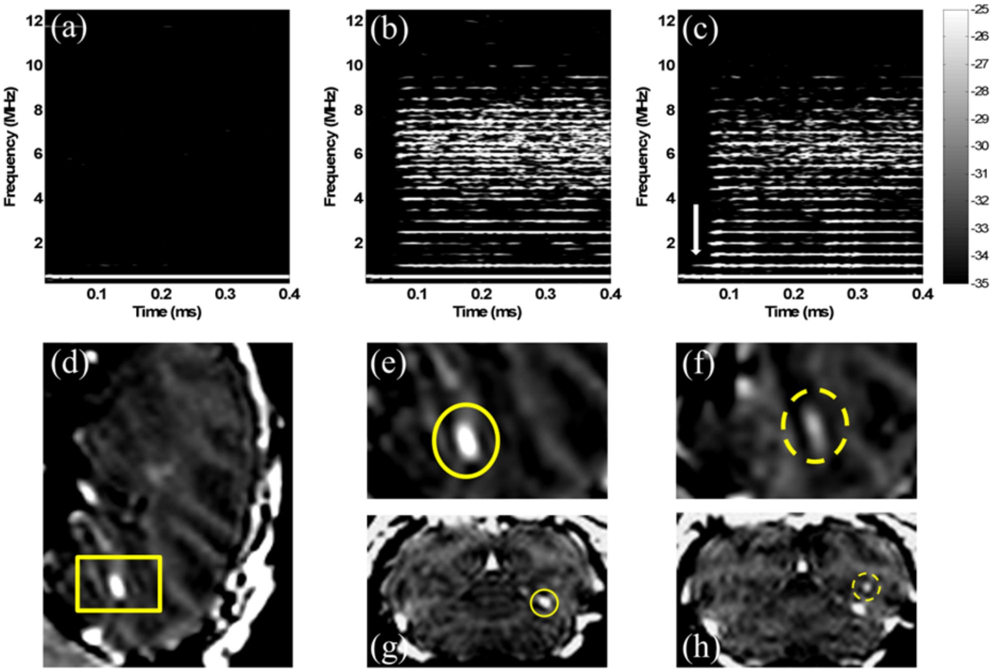

Figure 6.7 – The BBB opening confirmed by 3D-MRI images. No higher harmonics and broadband response are present at 0.30 MPa in (a) the spectrogram without microbubbles administration. The corresponding spectrogram of the first pulse with microbubbles administration shows that the broadband acoustic emissions are detected at (b) 0.30 MPa and (c) 0.45 MPa. The 3D-MR images confirm that the BBB is opened at (d, e, g) 0.30 MPa and (f, h) 0.45 MPa with inertial cavitation. The yellow box in the sagittal plane in (d) defines a region of interest from which images in (e) and (f) were acquired. The coronal plane with BBB opening is provided at (g) 0.30 MPa and (h) 0.45 MPa. The white arrow in (c) indicates that the time-point of occurrence of the second harmonic coincides with the travel distance to the skull.

The corresponding spectrogram (Figs. 6.7 (b) and (c)) showed that the broadband response, i.e., the inertial cavitation, occurred at 0.30 MPa and 0.45 MPa. No harmonics were present at 0.30 MPa in the spectrogram without microbubble administration (Fig. 6.7 (a)), which confirms our findings in mice (*Chapter 3*)[120]. The spectrogram can also be used to determine the position of the focus. The white arrow in Fig. 6.7 (c) indicates that the time-point of occurrence of the second harmonic coincides with the travel distance to the skull. Therefore, harmonics higher than the 3rd harmonic and any broadband response are due to microbubble effects (Fig. 6.7 (b,c)).

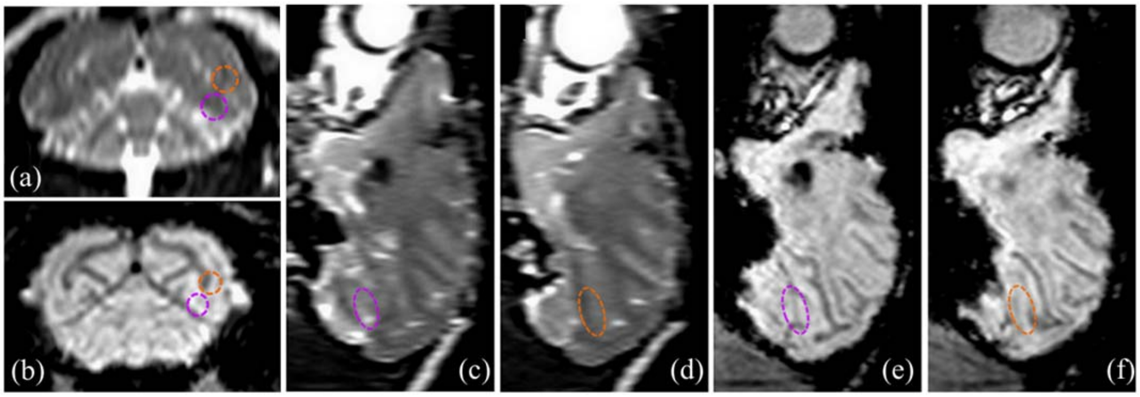

Figure 6.8 – Damage assessment. (a,c,d) 3D T2-weighted sequence. Edemas should appear brighter in these images. (b,e,f) 3D Susceptibility-Weighted Image (SWI) sequence was applied. Hemorrhages, as well as large vessels should appear in black in these images. (a,b) Same reconstructed coronal slice as shown in Fig. 6.7. The two opening sites are circled with the corresponding colors. There is no difference between the two hemispheres. (c,d,e,f) Corresponding reconstructed sagittal slices for the two opening sites. No edemas or hemorrhages are visible in the sonicated regions (dashed contour).

The same MRI sequence and IV contrast agent injection were repeated six days after BBB opening. No intensity enhancement was observed indicating that the BBB was closed or reinstated. Two other MRI sequences (T2-weighted and susceptibility-weighted) were used to assess potential brain damage after ME-FUS and both of them indicated absence of detectable damage such as edema or hemorrhage (Fig. 6.8). The same protocol was repeated for the two following sessions applying 0.6 MPa and two different kinds of microbubbles. The results are shown in Fig. 6.9 and 6.10. T1-weighted MR sequences were used to track the diffusion of gadodiamide. The peak MR intensity enhancement at the BBB-opened region relative to the average value in the parenchyma was increased by 68% and 41% using customized and Definity® microbubbles, respectively. The volume of the BBB disruption was equal to 285.5 mm^3 and 116.3 mm^3, respectively. The BBB opening regions at the caudate and the hippocampus were shifted from the targeted location by respectively 0.6 mm and 0.9 mm laterally and 6.5 mm and 7.2 mm axially. T2-weighted

MR sequences were also used to assess potential damages in the brain. An edematous region was detected on the T2-weighted MRI in one case using custom made microbubbles while no damage was detected using Definity® with all acoustic parameters being the same. All the animals have been survived and therefore histological findings are not available at this time. Even though no in-depth cognitive tests have been performed thus far, qualitative assessment of basic the animal behavior has been monitored. Normal cognitive behavior has been noted following ME-FUS procedures at moderate pressures and using Definity®. In the case of 0.6 MPa and customized microbubbles, the animal with the edema exhibited a weakness in the contra-lateral arm over four days after treatment, but then fully recovered after that four-day period. The corresponding spectrogram showed that a large broadband signal was recorded for both customized and Definity® microbubbles.

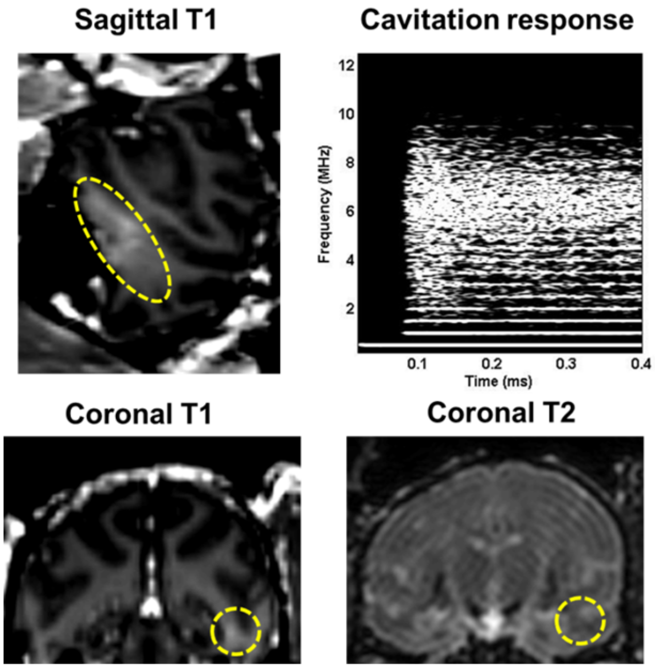

Figure 6.9 – BBB opening experiment targeting hippocampus using Definity® microbubbles and applying 0.6 MPa (yellow dashed line shows region of interest). 3D Spoiled Gradient-Echo (SPGR) T1-weighted sequence was applied after intravenous (IV) injection of gadodiamide 1 h after sonication. No damage was detected using Definity® microbubbles from T2-weighted sequence.

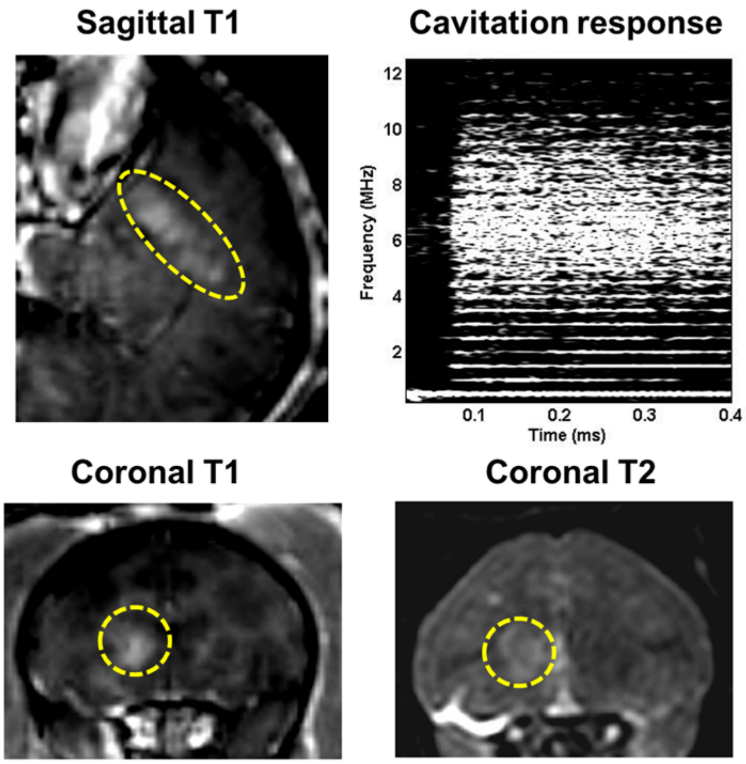

Figure 6.10 – BBB opening experiment targeting hippocampus using custimized microbubbles and applying 0.6 MPa (yellow dashed line shows region of interest). 3D Spoiled Gradient-Echo (SPGR) T1-weighted sequence was applied after intravenous (IV) injection of gadodiamide 1 h after sonication. An edema was visible using Definity® microbubbles from T2-weighted sequence.

Here, a total of 11 BBB openings were induced at 0.30 and 0.45 MPa (Table 6.1) using 4-5-μm diameter bubbles. The correlation between the ICD and the BBB opening volume was shown in Fig. 6.11. At 0.60 MPa, because the BBB opening volume was the combination of four sonications (two in the visual cortex and two in the hippocampus), this opening volume (285.5 mm^3) is not including the Fig. 6.11. The SCD at all ultra-harmonics of difference regions at 0.30 and 0.45 MPa is shown in Fig. 6.12. At 0.30 MPa, the amplitude at ultra-harmonics was the largest in the putamen and the lowest in the visual cortex. At 0.45 MPa, the amplitude in the visual cortex was higher than in the caudate and the hippocampus.

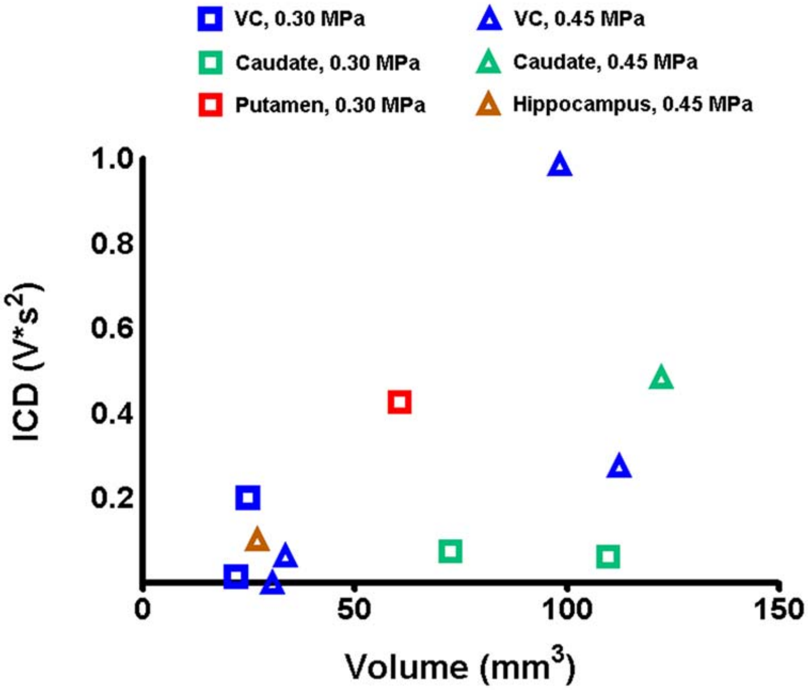

Figure 6.11 – The correlation between the ICD and the BBB opening volume at 0.30 and 0.45 MPa at 4-5-μm diameter bubbles (a total of 11 openings). The volume at 0.60 MPa is not shown because only one big opening is induced by 4 sonications (Fig. 6.10).

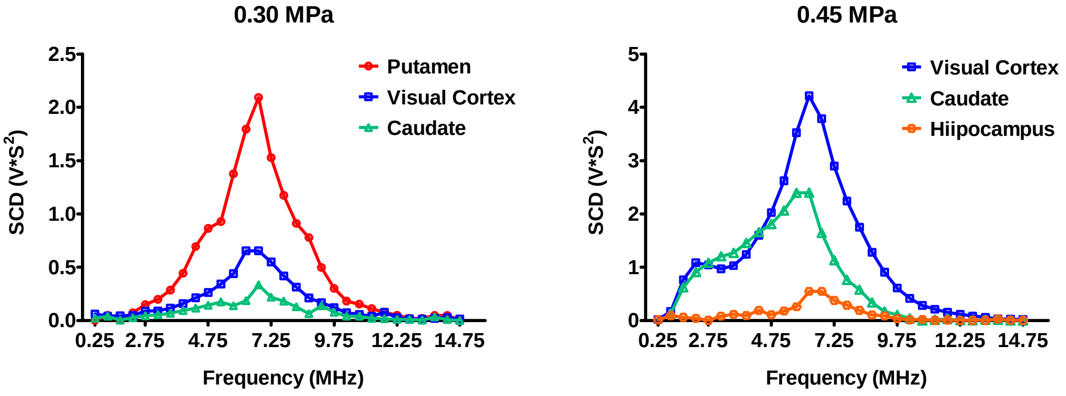

(a) (b)

Figure 6.12 – The region dependent SCD at 0.30 and 0.45 MPa. The amplitude level is putamen > caudate > visual cortex at 0.30 MPa, as well as visual cortex > caudate > hippocampus at 0.45 MPa.

6.3.2 Closing timeline and accuracy

The duration of BBB opening and the corresponding opening volume of each scan were shown in Fig. 6.13. At 0.30 MPa, the BBB was opened in the caudate and lasted two days. On day 4, the opened BBB was completely recovered. The targeting precision was also investigated. Figures 6.14 and 6.15 show the estimated focal region (yellow area) and the BBB opening region (blue area) from the coronal, sagittal, and horizontal plane. The axial shift of the focus was found to vary in 6.9 mm. The corresponding spectrogram for all duration (120s) is also presented. The focal shift, BBB opening volume, and MRI contrast enhancement of the visual cortex and caudate are quantified in Table 6.2.

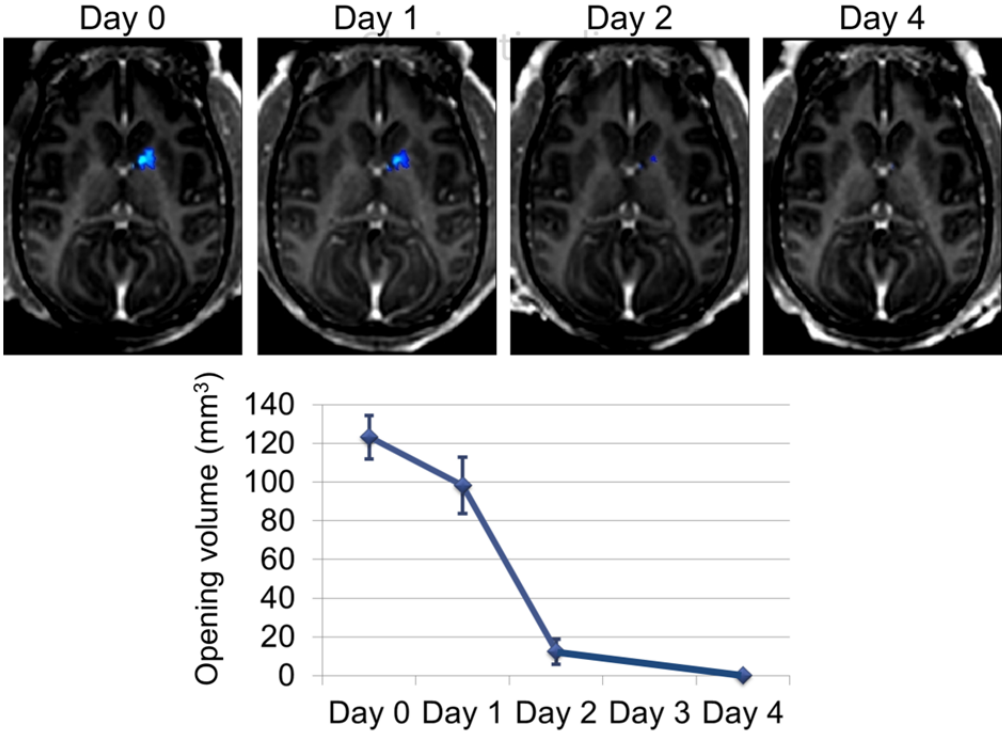

Figure 6.13 – An example of BBB closing in the NHP caudate using 0.30 MPa and 4-5-µm microbubbles. The blue region indicates the opening region and it is no longer visible in day 4. The corresponding quantification of BBB opening volume indicates that the BBB is nearly closed on day 2. The error bar denotes the stander deviation of the MR intensity of the BBB opening area.

Table 6.2 The axial focal shift, BBB opening volume, and MRI contrast enhancement of two opening regions. The focal shift is as our expectation shown in *Appendix B*.

Region	Caudate	Visual cortex
Pressure (MPa)	0.30	0.45
Axial focal shift (mm)	3.4	6.9
Volume (mm^3)	72.5	112.3
MR Enhancement	52%	63%

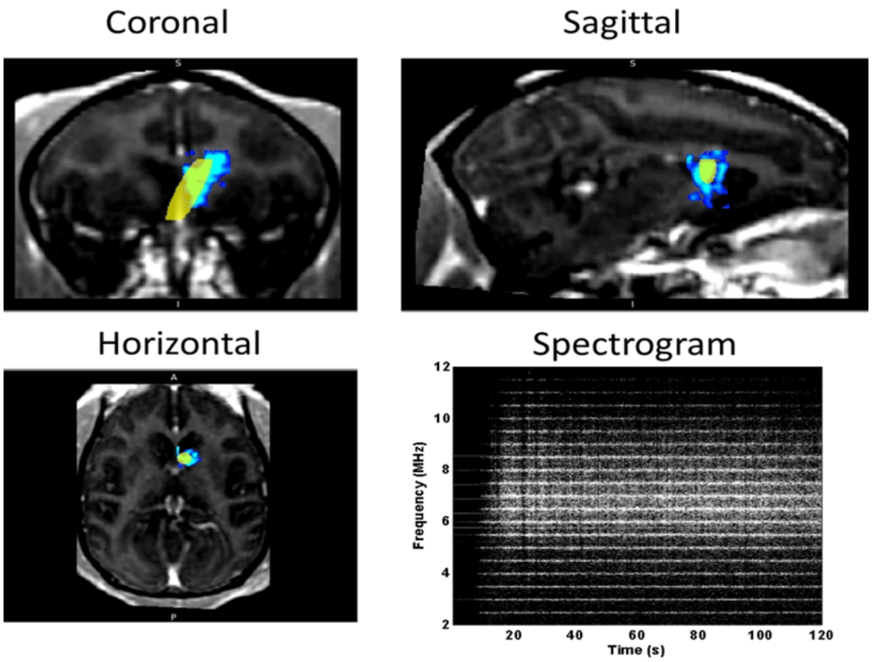

Figure 6.14 – The discrepancy between focal region (yellow area) and BBB opening region (blue area) at the caudate at 0.30 MPa. Corresponding spectrogram shows the cavitation response along 2 min duration.

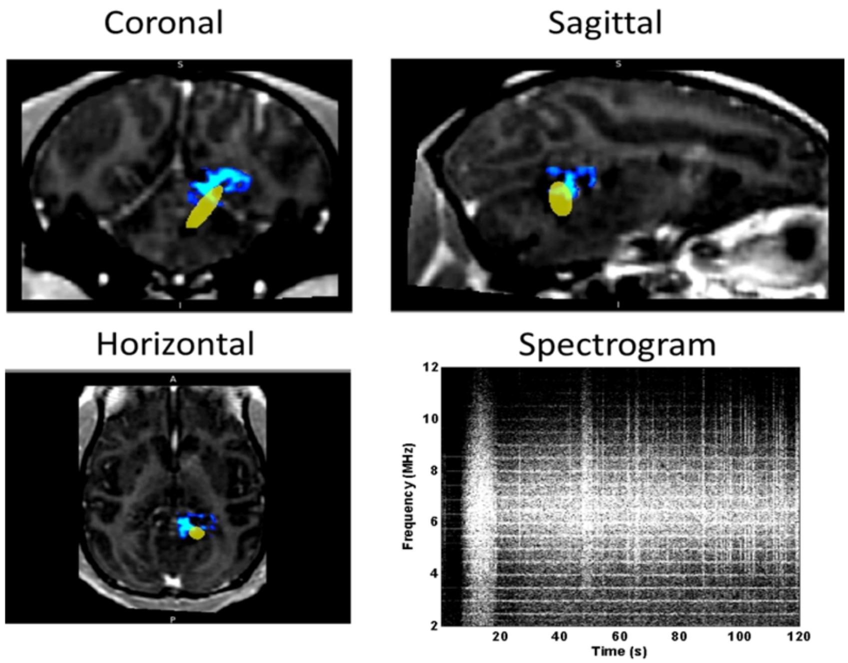

Figure 6.15 – The discrepancy between the focal region (yellow area) and the BBB opening region (blue area) at the visual cortex at 0.45 MPa. Corresponding spectrogram shows the cavitation response along 2 min duration.

6.4 Discussion

In this chapter, the FUS-induced BBB opening, combined with the transcranial cavitation detection, in non-human primates is reported for the first time. A total of four locations were disrupted in five animals (Table 6.1). Pressures ranging from 0.3 MPa to 0.6 MPa were investigated. Previous studies have shown that a pressure increase results in a larger BBB opening extent and higher BBB permeability while a safety window exists within the pressure range of 0.30 MPa and 0.60 MPa[91,120]. For all experiments, T1-weighted MRI at 3.0 T was used to confirm the BBB disruption, tracking the diffusion of IV-injected gadodiamide in the brain. Since this cavitation response was capable of being used to estimate the BBB opening volume and predict the occurrence of BBB opening[57], further information could be obtained in this study to investigate the cavitation-guided BBB opening in NHP.

Understanding the discrepancy of physical mechanism between mice and monkeys is helpful for clinical translation. Here, except for one case sonicated at 0.60 MPa, no BBB opening was induced using Definity® microbubbles and 10-ms pulse length, despite the occurrence of inertial cavitation (Figs. 6.5 and 6.6). Therefore, lower pressures (0.20 - 0.30 MPa) and shorter pulse length (0.2 ms) shown in protocol A (Table 6.1) may not be sufficient to induce BBB opening. However, in our previous studies, the BBB was opened at 0.45 MPa and PLs of 0.1, 0.2, 1, 2, and 10 ms, using the same microbubbles in mice. Therefore, higher pressures may be required to open the BBB in monkeys using Definity®.

Also, given that the medial areas were targeted (Fig. 6.5), the focus included the superior sagittal sinus that, due to the large volume of microbubbles circulating, resulted in larger amplitude of the cavitation spectrum. Measuring the cavitation spectrum may, therefore, be helpful to determine whether a large vessel is in the path of the FUS beam and thus predict or avoid its effects on inducing BBB opening. This is important as this likelihood may be hard to exclude otherwise: 1) due to the interference from the skull, the exact location of the focus in the brain is difficult to predict; 2) the exact location of large vessels in the brain relative to the beam is not known a priori. Hence, the relationship between the amplitude of the cavitation spectrum, the area of BBB opening, and the BBB opening threshold will provide valuable additional information regarding the presence of large vessels close to the focus. This information can thus be used to predict whether opening of the BBB was obstructed due to the focal spot proximity to a large vessel and subsequent shielding and adjust the targeting accordingly to achieve BBB opening, i.e. avoid shielding by large vessels.

Those preliminary results have also indicated the dependence of the BBB opening on the microbubble types. In protocol B (Table 6.1), at 0.30 and 0.45 MPa, BBB opening was only observed with the 4-5-μm bubbles (Figs. 6.7 and 6.8). At 0.60 MPa, larger BBB opening area was obtained with the 4-5-μm bubbles (Figs. 6.9 and 6.10). This is mainly because by increasing the peak pressure, a larger portion of the brain reaches the disruption threshold. We have shown that the 4-5-μm bubbles result in a larger BBB opening region in mice. Based on this finding, which complements our previously reported studies on the bubble size in mice[57], it is believed that the bubble size also plays an important role in the BBB opening in primates.

In *Chapter 4*, we showed that the BBB was opened at 0.3 MPa and the inertial cavitation occurred at 0.45 MPa using 1.5-MHz FUS and 4-5-μm diameter bubbles. Here, the BBB was also opened at 0.30, 0.45, and 0.60 MPa with the presence of inertial cavitation. The mechanical index was 0.25, 0.37, and 0.49 at 1.5 MHz, as well as 0.42, 0.64 and 1.02 at 500 kHz for 0.3 MPa, 0.45 MPa and 0.6 MPa, respectively. Since the MI threshold of the broadband response was close to 0.4[51] and the broadband response was observed in most cases of BBB opening, lower pressures will be applied and the stable cavitation dose will be quantified to determine whether the BBB can be opened without inertial cavitation using 4-5-μm diameter bubbles.

In our previous studies, the cavitation response was shown capable of estimating the BBB opening volume (*Chapter 4*)[57]. By taking into account 11 openings performed with the 4-5-μm bubbles, preliminary feasibility of volume prediction using the ICD was shown in Fig. 6.11. More openings will be performed in the future to determine the relation between the ICD and the BBB opening volume. If successful BBB opening and the corresponding opening volume can be predicted using the PCD system, MRI is not required for monitoring BBB opening during sonication, thereby expanding the application of FUS while maintaining its low cost and real-time capability for the clinical application.

In the cavitation response, not only the ICD, but also the spectrogram can provide very useful information on the microbubble behavior in real-time. Figure 6.16 shows three spectrograms. First, the spectrogram of total duration (120s) (Fig. 6.16(a)) indicated the duration for microbubbles to reach the brain after the IV-injection. For instance, it takes 10 seconds for Definity® microbubbles to reach the brain (Fig. 6.16(a)). In clinical application, the patient may have a circulation problem, which may be indicated by the spectrogram of total duration. The microbubble persistence can also be identified. Compared with the response of 4-5-μm bubbles shown in in Fig. 6.15, the 4-5-μm bubbles is shown more robust during 120s. Second, the spectrogram of one pulse (red line in Fig. 6.16(a)), showing a pulse length of 10 ms (Fig. 6.16(b)), can determine the duration of inertial cavitation. This duration may be microbubble dependent and correlated to the ICD. If insufficient microbubbles are sonicated at each pulse, the duration of inertial cavitation may be shorter, thereby inducing lower ICD and BBB opening volume.Third, the first few hundred microseconds of one pulse (Fig. 6.16(c), 0-0.4 ms of the Fig. 6.16(b)), can indicate the location of the focus based on the starting point of harmonics and broadband response. This might be useful to estimate the actual focus, thereby determining the axial shift between the actual focus and the desired targeting region.

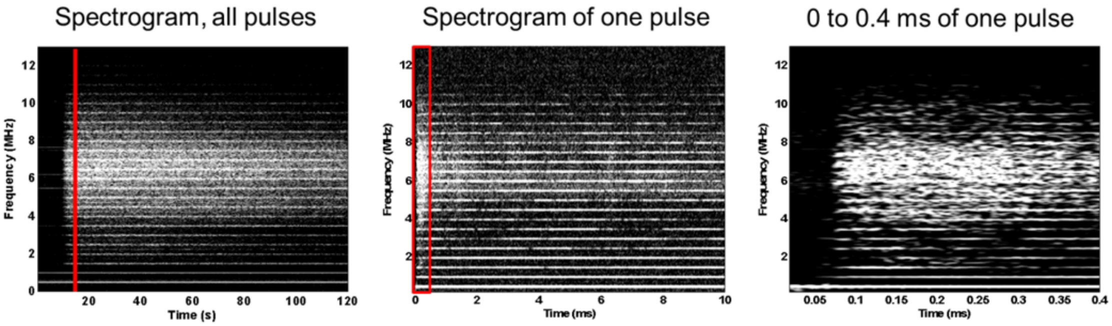

(a) (b) (c)

Figure 6.16 – Three spectrograms of the cavitation response. (a) The spectrogram of all pulses provides the information about the microbubble persistence and the duration for them to reach the brain after the IV-injection. (b) The spectrogram of one pulse (red line in (a)) indicates the duration of inertial cavitation. (c) The actual location of the focus may be determined by the first 0.4 ms of one pulse, i.e., the red square in (b).

Since the primate brain is inhomogeneous, the BBB opening properties may be distinct between different areas. As shown in Fig. 6.7, the intensities of MRI contrast enhancement in the BBB opening region at 0.30 MPa was 2.3 times higher than at 0.45 MPa. These differences may be due to a higher concentration of microbubbles in the sonicated region during the 0.30 MPa stimulation. This would explain both, the enhanced MRI contrast and the stronger broadband response.

In addition, the cavitation response may also be region dependent. The SCD at distinct regions at 0.30 and 0.45 MPa was depicted in Fig. 6.11. The higher sensitivity lied near the center frequency of the PCD (7.5 MHz). Four different locations were shown having distinct cavitation response. In Fig. 6.11, at 0.30 MPa, the amplitude level in the putamen is the largest and the visual cortex is the lowest. In comparison between the caudate (Fig.6.12) and the virtual cortex (Fig. 6.13), the visual cortex is deeper than the caudate. This might be one of the reasons why lower amplitudes are detected in the visual cortex. The comparison between the caudate and putamen can be seen in Fig. 6.3. The putamen is deeper than caudate in the sagittal view, but is roughly the same depth in the coronal view. Also, because of only one sonication in the putamen, more sonications will be implemented to determine the region dependent cavitation response. In the comparison between the visual cortex and hippocampus, the hippocampus is deeper than visual cortex from the sagittal and coronal view (Fig. 6.3). Therefore, the amplitude was lower in the hippocampus. Although the depth of the targeting regions would have an effect on PCD amplitude, the region dependent cavitation response might be used to characterize the BBB opening properties in different location in NHP.

6.5 Conclusion

In this chapter, we successfully translated the *in vivo* transcranial BBB opening system together with real-time passive cavitation detection from mice to NHPs. First, initial feasibility of noninvasive, highly selective, drug-independent and reversible BBB opening was demonstrated in non-human primates *in vivo*. High spatial selectivity of this technique was also shown. Compared to the mouse application (*Chapters 3-5*), the BBB in monkeys was considered more difficult to be opened, and the larger microbubbles facilitated BBB opening. Ongoing investigations entail optimization of the procedure including safety and efficacy of the trans-BBB drug delivery. Second, the noninvasive and transcranial cavitation detection during BBB opening in non-human primates was achieved. The ICD can be used to estimate the BBB opening and corresponding opening volume. In addition, the MRI contrast enhancement and cavitation response were shown to be region and/ or microbubble-size dependent. Therefore, this technique might be used for a cavitation-guided BBB opening to better monitor the target of sonication without requiring real-time

MRI. Further studies will be performed to optimize the application in primates and determine the correlation between the location of BBB opening and the cavitation spectrum. This study is a major step toward clinical translation of this emerging technology that can be combined with any type of pharmacological treatment to the brain.

Chapter 7

Conclusion and future directions

7.1 Conclusion

In this dissertation, the physical mechanism and corresponding safety assessment have been fully investigated. The safety window, including the threshold of the inertial cavitation and the damage (here is red blood cell extravasations), in terms of microbubble types and peak rarefactional pressure, was determined in mice and shown in Fig. 7.1. First, the BBB was opened in the absence of inertial cavitation and damage using Definity® microbubbles at 0.30 MPa (*Chapter 3*) as well as using 4-5-μm diameter bubbles at 0.18 and 0.30 MPa (*Chapters 4 and 5*), considered as the safest window (green rectangular). Second, using Definity® or 1-2-μm diameter bubbles, although the inertial cavitation occurred at 0.45 MPa, no damage was observed. As a result, another safety window (orange rectangular) lies between 0.45 and 0.60 MPa using Definity® (*Chapter 3*) or 1-2-μm diameter bubbles (*Chapter 4*).

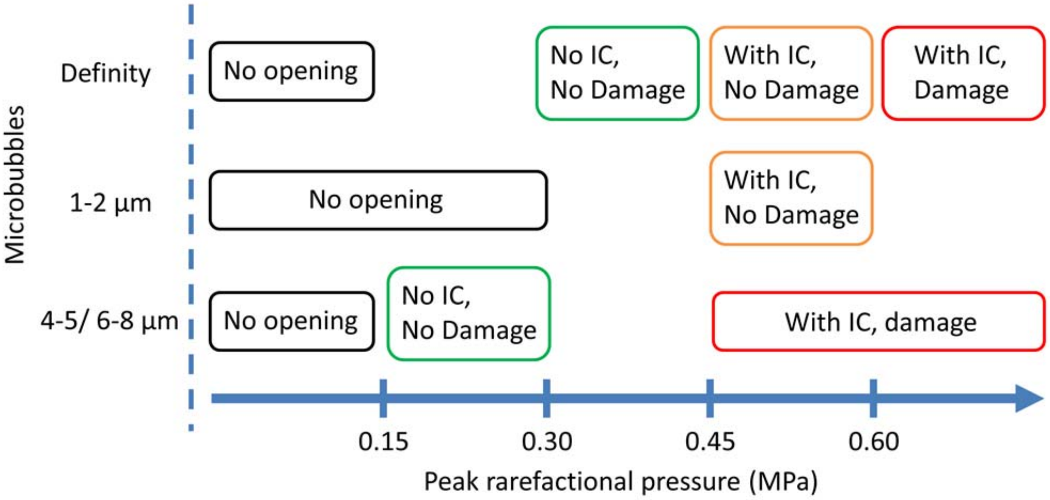

Figure 7.1 – Safety windows in terms of peak rarefactional pressure and microbubble types in mice. The safest window (green rectangular), in the absence of inertial cavitation (IC) and damage, lies between 0.15 and 0.30 MPa using 4-5- or 6-8-μm diameter bubbles, as well as between 0.30 and 0.45 MPa using Definity®. Another safety window, in the absence of damage with the IC occurrence (orange rectangular), lies between 0.30 and 0.45 MPa using 1-2-μm diameter bubbles or Definity®. However, the pressure threshold of the damage occurrence at 1-2-μm diameter bubbles has not been determined.

A major step toward the clinical application was the successful BBB opening in monkeys using our noninvasive and transcranial cavitation-guided BBB opening system. The probability of opening the BBB in monkeys was 100% using 4-5-µm diameters bubbles at 0.5 MHz and at pressures of 0.30 – 0.60 MPa (*Chapter 6*). Therefore, microbubbles in diameters of 4-5-µm or 6-8-µm were suggested for future application in monkeys or human.

In this dissertation, the physical mechanism was determined based on the cavitation response, combined with theoretical model simulation and the phantom validation. In mice, harmonics at 0.18 MPa (*Chapter 5*), ultra-harmonics, i.e. SCD, at 0.30 MPa (*Chapter 4*), and broadband response, i.e. ICD, at 0.45 and 0.60 MPa (*Chapters 3,4*) were detected and the corresponding BBB opening properties was obtained. Therefore, the conclusions of our main findings were as follows:

1) The transcranial cavitation response, including the SCD and ICD, during BBB opening was successfully detected and calculated for the first time (*Chapters 3-6*).
2) The BBB can be opened in the absence of inertial cavitation or any cellular damage in mice (*Chapters 3-5*).
3) A sufficiently long pulse length was required to induce BBB opening in mice via stable cavitation, without disrupting the tight junction (*Chapter 5*).
4) The physical mechanism may be distinct between mice and monkeys (*Chapter 6*).
5) Cavitation response can serve as a decent indicator to estimate the BBB opening occurrence (SCD, *Chapter 4*), the BBB opening volume (ICD, *Chapter 4*), microbubble persistence (Spectrogram, *Chapter 6*), and the location of focus (Spectrogram, *Chapter 6*).

7.2 Future directions

This dissertation has revealed the physical mechanism of FUS-induced BBB opening and achieved the feasibility of cavitation-guided BBB opening in non-human primates. However, in order to achieve the goal of safe delivery of therapeutic drugs, several studies are recommended.

Successful delivery of therapeutic agents (BDNF) in mice has been reported by our group[4]. The acoustic pressure, however, was at 0.46 or 0.60 MPa along with the IC occurrence. Although the IC in conjunction with Definity® microbubbles at 0.45 MPa was still within the safety window, until now, the capability of brain drug delivery using the SC has not been investigated. As shown in *Chapter 5,* fluorescently tagged 3-kDa dextran was contained in the vessel in the case of SC-induced BBB opening at 0.18 MPa. Thus, the BDNF, with a total molecular mass of 27 kDa, may not be delivered at 0.18 MPa. Choi et al. have shown that the FUS combined with microbubbles opened the BBB sufficiently to allow passage of compounds of at least 70 kDa, but not greater than 2000 kDa into the brain parenchyma, using 0.46-MPa sonication, i.e. the inertial cavitation threshold of Definity®. Therefore, identifying the range of molecular mass of the agents across the SC- or the IC-induced BBB opening will be important to assess the efficacy of this approach. Based on the findings in *Chapter 3*, microbubbles in the diameter of 4-5- or 6-8-μm were able to induce sufficient BBB opening in the absence of the inertial cavitation. Also, at relative low pressure (0.18 MPa), a sufficiently long PL (5 ms) was capable of enhancing the MR contrast in the BBB opening region. On this ground, we suggest using those microbubbles in combination with sufficient pressure and PL to determine the maximum size of the SC-opened BBB.

A long term study, in combined with the cognitive monitoring, is obligated to be investigated in order to determine the effect of repeated sonication with intervals of few days to few weeks. If any injury was induced by the repeated sonication, the corresponding behavior may be different from the normal mice. This study will provide useful information for the clinical application in the future.

In *Chapter 6*, the feasibility of BBB opening using FUS and microbubbles, along with transcranial cavitation detection, was achieved. More aspects should be investigated:

1) Safety windows determination, including the wide investigates on pressures, pulse length, microbubble sizes, and behavior monitoring after BBB opening.
2) Delivery of pharmacological compounds in monkeys.
3) Successful prediction of BBB opening occurrence and the BBB opening volume at different region by real-time monitoring the cavitation response.

List of Publications Related to the Thesis

Chapter 4

Y.-S. Tung, J. J. Choi, B. Baseri, E. E. Konofagou., “Identifying the Inertial Cavitation Threshold and Skull Effects in a Vessel Phantom Using Focused Ultrasound and microbubbles,” *Ultrasound Med Biol* 36 840-52, Apr 2010

Y.-S. Tung, F. Vlachos, J. J. Choi, T. Deffieux, K. Selert, E. E. Konofagou., “*In vivo* Transcranial Cavitation Threshold Detection During Ultrasound-Induced Blood-Brain Barrier Opening in Mice” *Phys Med Biol* 55 6141-55, Oct 2010.

Chapter 5

J. J. Choi, J. A. Feshitan, B. Baseri, S. Wang, **Y.-S. Tung**, M. A. Borden, E. E. Konofagou., "microbubble-size Dependence of Focused Ultrasound-Induced Blood-Brain Barrier Opening in Mice I*n vivo*," *IEEE Trans Biomed Eng*., vol. 57, no. 1, pp. 145-54, Jan 2010.

F. Vlachos, **Y.-S. Tung**, E. E. Konofagou., "Permeability Assessment of the Focused Ultrasound-Induced Blood–Brain Barrier Opening Using Dynamic Contrast-Enhanced MRI" *Phys Med Biol* 55 5451-66, Aug 2010.

F. Vlachos, **Y.-S. Tung**, E. E. Konofagou., "Permeability Dependence Study of the Focused Ultrasound-Induced Blood–Brain Barrier Opening at Distinct Pressures and microbubble Diameters Using DCE-MRI" *Magn Reson Med* 66 821-830, Apr 2011

Y.-S. Tung, F. Vlachos, J. Feshitan, M. Borden, E. E. Konofagou., "The Mechanism of the Interaction between FUS and microbubbles in Blood-Brain Barrier Opening in Mice" *J. Acous. Soc. Am.* 130(5) 3059-3067, Nov 2011

G. Samiotaki, F. Vlachos, **Y.-S. Tung**, E. E. Konofagou., “Quantitative Pressure and microbubble-Size Dependence Study of Focused Ultrasound-Induced Blood-Brain Barrier Opening Reversibility *In vivo* Using MRI” *Magn Reson Med* Aug 19. doi: 10.1002/mrm.23063. [Epub ahead of print] 2011

Y.-S. Tung, J. Feshitan, O. Olumolade, S.-Y. Wu, M. Borden, E. E. Konofagou., “microbubble Shell Effect on the Bubble Behavior during FUS-induced Blood-Brain Barrier Opening *In vivo*” *IEEE UFFC* (in review)

Chapter 6

Y.-S. Tung, O. Olumolade, C. C. Chen, J. Feshitan, S. Wang, S.-Y. Wu, M. Borden, E. E. Konofagou., "Cavitation-Dependent mechanism BBB opening using FUS and microbubbles" (in submission)

J. J. Choi, S. Wang, **Y.-S. Tung**, B. Morrison 3rd, E. E. Konofagou., "Molecules of Various Pharmacologically-relevant Sizes can Cross the Ultrasound-Induced Blood-Brain Barrier Opening *In vivo*," *Ultrasound Med Biol.*, vol. 36, no. 1, pp.58-67, Jan 2010.

B. Baseri, J. J. Choi, **Y.-S. Tung**, E. E. Konofagou., "Multi-modality Safety Assessment of Blood-Brain Barrier Opening Using Focused Ultrasound and Definity Microbubbles: A Short-term Study." *Ultrasound Med Biol* 36 1445-59, Sep 2010

Chapter 7

Y.-S. Tung, F. Marquet, T. Teichert, F. Ferrera, E. E. Konofagou., "The Feasibility of Cavitation-Guided Blood-Brain Barrier opening using FUS and microbubbles in Non-Human Primate" *Appl Phys Lett* 98(16):163704. 2011

F. Marquet, **Y.-S. Tung**, T. Teichert, F. Ferrera, E. E. Konofagou., " Noninvasive, Transient and Selective Blood-Brain Barrier Opening in Non-Human Primates *In vivo*" *PLoS one* 6(7) e22598, Jul 2011

F. Marquet, **Y.-S. Tung**, E. E. Konofagou., "Feasibility Study of a Clinical Blood-Brain Opening System" *NanoLife* (in press) [invited] 2012

F. Marquet, **Y.-S. Tung**, T. Teichert, F. Ferrera, E. E. Konofagou., "Targeting Accuracy and Closing Timeline of the microbubble-Enhanced Focused Ultrasound Blood-Brain Barrier Opening in Non-Human Primates" (in preparation) 2012

Y.-S. Tung, F. Marquet, T. Teichert, F. Ferrera, E. E. Konofagou., "Region dependent Cavitation-Guided Blood-Brain Barrier opening using FUS and microbubbles in Non-Human Primate" (in preparation) 2012

Chapter 8

E. E. Konofagou, **Y.-S. Tung**, J. J Choi, T. Deffieux , J. Feshitan, M. Borden, B. Baseri, F. Vlachos, "Ultrasound-Induced Blood-Brain Barrier Opening" *Curr. Pharm.Biotech. Rev.*, (in press). [Invited] 2011.

B. Baseri, J. J. Choi, G. Samiotaki, **Y.-S. Tung**, S. A. Small, B. Morrison, E. E. Konofagou., "Activation of Signaling Pathways Following Localized Delivery of Systemically-Administered BDNF across the Blood-Brain Barrier Using Focused Ultrasound and microbubbles." *Phys Med Biol* 57 N1-17, 2012

Reference

1. W. M. Pardridge, "The blood-brain barrier: bottleneck in brain drug development," *NeuroRx* **2** (1), 3-14 (2005).

2. M. D. Habgood, D. J. Begley and N. J. Abbott, "Determinants of passive drug entry into the central nervous system," *Cell Mol Neurobiol* **20** (2), 231-253 (2000).

3. K. Hynynen, N. McDannold, N. Vykhodtseva and F. A. Jolesz, "Noninvasive MR imaging-guided focal opening of the blood-brain barrier in rabbits," *Radiology* **220** (3), 640-646 (2001).

4. B. Baseri, J. J. Choi, T. Deffieux, G. Samiotaki, Y. S. Tung, O. Olumolade, S. A. Small, B. Morrison and E. E. Konofagou, "Activation of signaling pathways following localized delivery of systemically administered neurotrophic factors across the blood-brain barrier using focused ultrasound and microbubbles," *Phys Med Biol* **57** (7), N65-81 (2012).

5. N. Sheikov, N. McDannold, F. Jolesz, Y. Z. Zhang, K. Tam and K. Hynynen, "Brain arterioles show more active vesicular transport of blood-borne tracer molecules than capillaries and venules after focused ultrasound-evoked opening of the blood-brain barrier," *Ultrasound Med Biol* **32** (9), 1399-1409 (2006).

6. N. Sheikov, N. McDannold, S. Sharma and K. Hynynen, "Effect of focused ultrasound applied with an ultrasound contrast agent on the tight junctional integrity of the brain microvascular endothelium," *Ultrasound Med Biol* **34** (7), 1093-1104 (2008).

7. N. Sheikov, N. McDannold, N. Vykhodtseva, F. Jolesz and K. Hynynen, "Cellular mechanisms of the blood-brain barrier opening induced by ultrasound in presence of microbubbles," *Ultrasound Med Biol* **30** (7), 979-989 (2004).

8. A. van Wamel, A. Bouakaz, M. Versluis and N. de Jong, "Micromanipulation of endothelial cells: ultrasound-microbubble-cell interaction," *Ultrasound Med Biol* **30** (9), 1255-1258 (2004).

9. M. W. Miller, D. L. Miller and A. A. Brayman, "A review of in vitro bioeffects of inertial ultrasonic cavitation from a mechanistic perspective," *Ultrasound Med Biol* **22** (9), 1131-1154 (1996).

10. L. A. Crum, "Cavitation microjets as a contributory mechanism for renal calculi disintegration in ESWL," *J Urol* **140** (6), 1587-1590 (1988).

11. W. L. Nyborg, "Biological effects of ultrasound: development of safety guidelines. Part II: general review," *Ultrasound Med Biol* **27** (3), 301-333 (2001).

12. J. J. Choi, K. Selert, Z. Gao, G. Samiotaki, B. Baseri and E. E. Konofagou, "Noninvasive and localized blood-brain barrier disruption using focused ultrasound can be achieved at short pulse lengths and low pulse repetition frequencies," *J Cereb Blood Flow Metab* (2010).

13. Z. Fan, R. E. Kumon, J. Park and C. X. Deng, "Intracellular delivery and calcium transients generated in sonoporation facilitated by microbubbles," *J Control Release* **142** (1), 31-39 (2010).

14. M. Daffertshofer and M. Hennerici, "Sonothrombolysis: experimental evidence," *Front Neurol Neurosci* **21**, 140-149 (2006).

15. K. C. Tsai, S. Y. Fang, S. J. Yang, M. J. Shieh, W. L. Lin and W. S. Chen, "Time dependency of ultrasound-facilitated gene transfection," *J Gene Med* **11** (8), 729-736 (2009).

16. Y. S. Tung, H. L. Liu, C. C. Wu, K. C. Ju, W. S. Chen and W. L. Lin, "Contrast-agent-enhanced ultrasound thermal ablation," *Ultrasound Med Biol* **32** (7), 1103-1110 (2006).

17. T. Y. Wang, Z. Xu, T. L. Hall, J. B. Fowlkes and C. A. Cain, "An Efficient Treatment Strategy for Histotripsy by Removing Cavitation Memory," *Ultrasound Med Biol* (2012).

18. N. R. Owen, M. R. Bailey, L. A. Crum, O. A. Sapozhnikov and L. A. Trusov, "The use of resonant scattering to identify stone fracture in shock wave lithotripsy," *J Acoust Soc Am* **121** (1), EL41-47 (2007).

19. A. Dove, "Breaching the barrier," *Nat Biotechnol* **26** (11), 1213-1215 (2008).

20. W. M. Pardridge, "Blood-brain barrier delivery," *Drug Discov Today* **12** (1-2), 54-61 (2007).

21. A. H. Nagahara, D. A. Merrill, G. Coppola, S. Tsukada, B. E. Schroeder, G. M. Shaked, L. Wang, A. Blesch, A. Kim, J. M. Conner, E. Rockenstein, M. V. Chao, E. H. Koo, D. Geschwind, E. Masliah, A. A. Chiba and M. H. Tuszynski, "Neuroprotective effects of brain-derived neurotrophic factor in rodent and primate models of Alzheimer's disease," *Nat Med* **15** (3), 331-337 (2009).

22. N. K. Patel and S. S. Gill, "GDNF delivery for Parkinson's disease," *Acta Neurochir Suppl* **97** (Pt 2), 135-154 (2007).

23. B. K. Fiske, M. A. Frasier and T. B. Sherer, "Special focus section: gene therapy for Parkinson's disease," *Exp Neurol* **209** (1), 28-29 (2008).

24. P. A. LeWitt, A. R. Rezai, M. A. Leehey, S. G. Ojemann, A. W. Flaherty, E. N. Eskandar, S. K. Kostyk, K. Thomas, A. Sarkar, M. S. Siddiqui, S. B. Tatter, J. M. Schwalb, K. L. Poston, J. M. Henderson, R. M. Kurlan, I. H. Richard, L. Van Meter, C. V. Sapan, M. J. During, M. G. Kaplitt and A. Feigin, "AAV2-GAD gene therapy for advanced Parkinson's disease: a double-blind, sham-surgery controlled, randomised trial," *Lancet Neurol* **10** (4), 309-319 (2011).

25. A. G. de Boer and P. J. Gaillard, "Drug targeting to the brain," *Annu Rev Pharmacol Toxicol* **47**, 323-355 (2007).

26. R. Deane and B. V. Zlokovic, "Role of the blood-brain barrier in the pathogenesis of Alzheimer's disease," *Curr Alzheimer Res* **4** (2), 191-197 (2007).

27. P. S. Churchland and P. Winkielman, "Modulating social behavior with oxytocin: How does it work? What does it mean?," *Horm Behav* **61** (3), 392-399 (2012).

28. K. D. Foust, E. Nurre, C. L. Montgomery, A. Hernandez, C. M. Chan and B. K. Kaspar, "Intravascular AAV9 preferentially targets neonatal neurons and adult astrocytes," *Nat Biotechnol* **27** (1), 59-65 (2009).

29. N. D. Doolittle, M. E. Miner, W. A. Hall, T. Siegal, E. Jerome, E. Osztie, L. D. McAllister, J. S. Bubalo, D. F. Kraemer, D. Fortin, R. Nixon, L. L. Muldoon and E. A. Neuwelt, "Safety and efficacy of a multicenter study using intraarterial chemotherapy in conjunction with osmotic opening of the blood-brain barrier for the treatment of patients with malignant brain tumors," *Cancer* **88** (3), 637-647 (2000).

30. D. Fortin, C. Gendron, M. Boudrias and M. P. Garant, "Enhanced chemotherapy delivery by intraarterial infusion and blood-brain barrier disruption in the treatment of cerebral metastasis," *Cancer* **109** (4), 751-760 (2007).

31. C. J. Harvey and T. Albrecht, "Ultrasound of focal liver lesions," *Eur Radiol* **11** (9), 1578-1593 (2001).

32. J. Y. Chapelon, M. Ribault, F. Vernier, R. Souchon and A. Gelet, "Treatment of localised prostate cancer with transrectal high intensity focused ultrasound," *Eur J Ultrasound* **9** (1), 31-38 (1999).

33. Y. S. Kim, B. Keserci, A. Partanen, H. Rhim, H. K. Lim, M. J. Park and M. O. Kohler, "Volumetric MR-HIFU ablation of uterine fibroids: Role of treatment cell size in the improvement of energy efficiency," *Eur J Radiol* (2011).

34. S. Sirsi and M. Borden, "Microbubble Compositions, Properties and Biomedical Applications," *Bubble Sci Eng Technol* **1** (1-2), 3-17 (2009).

35. W. C. Culp, R. Flores, A. T. Brown, J. D. Lowery, P. K. Roberson, L. J. Hennings, S. D. Woods, J. H. Hatton, B. C. Culp, R. D. Skinner and M. J. Borrelli, "Successful microbubble sonothrombolysis without tissue-type plasminogen activator in a rabbit model of acute ischemic stroke," *Stroke* **42** (8), 2280-2285 (2011).

36. Y. S. Tung, F. Marquet, T. Teichert, V. Ferrera and E. E. Konofagou, "Feasibility of noninvasive cavitation-guided blood-brain barrier opening using focused ultrasound and microbubbles in nonhuman primates," *Appl Phys Lett* **98** (16), 163704 (2011).

37. T. Nishioka, H. Luo, M. C. Fishbein, B. Cercek, J. S. Forrester, C. J. Kim, H. Berglund and R. J. Siegel, "Dissolution of thrombotic arterial occlusion by high intensity, low frequency ultrasound and dodecafluoropentane emulsion: an in vitro and in vivo study," *J Am Coll Cardiol* **30** (2), 561-568 (1997).

38. L. Bakay, H. T. Ballantine, Jr., T. F. Hueter and D. Sosa, "Ultrasonically produced changes in the blood-brain barrier," *AMA Arch Neurol Psychiatry* **76** (5), 457-467 (1956).

39. M. Reinhard, A. Hetzel, S. Kruger, S. Kretzer, J. Talazko, S. Ziyeh, J. Weber and T. Els, "Blood-brain barrier disruption by low-frequency ultrasound," *Stroke* **37** (6), 1546-1548 (2006).

40. J. J. Choi, M. Pernot, S. A. Small and E. E. Konofagou, "Noninvasive, transcranial and localized opening of the blood-brain barrier using focused ultrasound in mice," *Ultrasound Med Biol* **33** (1), 95-104 (2007).

41. J. J. Choi, M. Pernot, T. R. Brown, S. A. Small and E. E. Konofagou, "Spatio-temporal analysis of molecular delivery through the blood-brain barrier using focused ultrasound," *Phys Med Biol* **52** (18), 5509-5530 (2007).

42. H. L. Liu, Y. Y. Wai, W. S. Chen, J. C. Chen, P. H. Hsu, X. Y. Wu, W. C. Huang, T. C. Yen and J. J. Wang, "Hemorrhage detection during focused-ultrasound induced blood-brain-barrier opening by using susceptibility-weighted magnetic resonance imaging," *Ultrasound Med Biol* **34** (4), 598-606 (2008).

43. F. Xie, M. D. Boska, J. Lof, M. G. Uberti, J. M. Tsutsui and T. R. Porter, "Effects of Transcranial Ultrasound and Intravenous Microbubbles on Blood Brain Barrier Permeability in a Large Animal Model," *Ultrasound Med Biol* (2008).

44. K. Hynynen, N. McDannold, N. A. Sheikov, F. A. Jolesz and N. Vykhodtseva, "Local and reversible blood-brain barrier disruption by noninvasive focused ultrasound at frequencies suitable for trans-skull sonications," *Neuroimage* **24** (1), 12-20 (2005).

45. K. Hynynen, N. McDannold, N. Vykhodtseva, S. Raymond, R. Weissleder, F. A. Jolesz and N. Sheikov, "Focal disruption of the blood-brain barrier due to 260-kHz ultrasound bursts: a method for molecular imaging and targeted drug delivery," *J Neurosurg* **105** (3), 445-454 (2006).

46. D. Games, D. Adams, R. Alessandrini, R. Barbour, P. Berthelette, C. Blackwell, T. Carr, J. Clemens, T. Donaldson, F. Gillespie and et al., "Alzheimer-type neuropathology in transgenic mice overexpressing V717F beta-amyloid precursor protein," *Nature* **373** (6514), 523-527 (1995).

47. J. J. Choi, S. Wang, T. R. Brown, S. A. Small, K. E. Duff and E. E. Konofagou, "Noninvasive and transient blood-brain barrier opening in the hippocampus of Alzheimer's double transgenic mice using focused ultrasound," *Ultrason Imaging* **30** (3), 189-200 (2008).

48. F. Marquet, Y. S. Tung, T. Teichert, V. P. Ferrera and E. E. Konofagou, "Noninvasive, transient and selective blood-brain barrier opening in non-human primates in vivo," *PLoS ONE* **6** (7), e22598 (2011).

49. H. L. Liu, C. H. Pan, C. Y. Ting and M. J. Hsiao, "Opening of the blood-brain barrier by low-frequency (28-kHz) ultrasound: a novel pinhole-assisted mechanical scanning device," *Ultrasound Med Biol* **36** (2), 325-335 (2010).

50. F. Y. Yang, Y. S. Lin, K. H. Kang and T. K. Chao, "Reversible blood-brain barrier disruption by repeated transcranial focused ultrasound allows enhanced extravasation," *J Control Release* **150** (1), 111-116 (2011).

51. N. McDannold, N. Vykhodtseva and K. Hynynen, "Blood-brain barrier disruption induced by focused ultrasound and circulating preformed microbubbles appears to be characterized by the mechanical index," *Ultrasound Med Biol* **34** (5), 834-840 (2008).

52. N. McDannold, N. Vykhodtseva and K. Hynynen, "Effects of acoustic parameters and ultrasound contrast agent dose on focused-ultrasound induced blood-brain barrier disruption," *Ultrasound Med Biol* **34** (6), 930-937 (2008).

53. M. Choi, T. Ku, K. Chong, J. Yoon and C. Choi, "Minimally invasive molecular delivery into the brain using optical modulation of vascular permeability," *Proc Natl Acad Sci U S A* **108** (22), 9256-9261 (2011).

54. R. Chopra, N. Vykhodtseva and K. Hynynen, "Influence of exposure time and pressure amplitude on blood-brain-barrier opening using transcranial ultrasound exposures," *ACS Chem Neurosci* **1** (5), 391-398 (2010).

55. F. Y. Yang, W. M. Fu, R. S. Yang, H. C. Liou, K. H. Kang and W. L. Lin, "Quantitative evaluation of focused ultrasound with a contrast agent on blood-brain barrier disruption," *Ultrasound Med Biol* **33** (9), 1421-1427 (2007).

56. J. J. Choi, J. A. Feshitan, B. Baseri, S. Wang, Y. S. Tung, M. A. Borden and E. E. Konofagou, "Microbubble-size dependence of focused ultrasound-induced blood-brain barrier opening in mice in vivo," *IEEE Trans Biomed Eng* **57** (1), 145-154 (2010).

57. Y. S. Tung, F. Vlachos, J. A. Feshitan, M. A. Borden and E. E. Konofagou, "The mechanism of interaction between focused ultrasound and microbubbles in blood-brain barrier opening in mice," *J Acoust Soc Am* **130** (5), 3059-3067 (2011).

58. J. C. Weng, S. K. Wu, W. L. Lin and W. Y. Tseng, "Detecting blood-brain barrier disruption within minimal hemorrhage following transcranial focused ultrasound: a correlation study with contrast-enhanced MRI," *Magn Reson Med* **65** (3), 802-811 (2011).

59. J. C. Weng, S. K. Wu, F. Y. Yang, W. L. Lin and W. Y. Tseng, "Pulse sequence and timing of contrast-enhanced MRI for assessing blood-brain barrier disruption after transcranial focused ultrasound in the presence of hemorrhage," *J Magn Reson Imaging* **31** (6), 1323-1330 (2010).

60. F. Y. Yang, S. C. Horng, Y. S. Lin and Y. H. Kao, "Association between contrast-enhanced MR images and blood-brain barrier disruption following transcranial focused ultrasound," *J Magn Reson Imaging* **32** (3), 593-599 (2010).

61. G. Samiotaki, F. Vlachos, Y. S. Tung and E. E. Konofagou, "A quantitative pressure and microbubble-size dependence study of focused ultrasound-induced blood-brain barrier opening reversibility in vivo using MRI," *Magn Reson Med* **67** (3), 769-777 (2012).

62. M. A. O'Reilly, A. C. Waspe, M. Ganguly and K. Hynynen, "Focused-ultrasound disruption of the blood-brain barrier using closely-timed short pulses: influence of sonication parameters and injection rate," *Ultrasound Med Biol* **37** (4), 587-594 (2011).

63. N. McDannold, N. Vykhodtseva and K. Hynynen, "Use of ultrasound pulses combined with Definity for targeted blood-brain barrier disruption: a feasibility study," *Ultrasound Med Biol* **33** (4), 584-590 (2007).

64. F. Vlachos, Y. S. Tung and E. Konofagou, "Permeability dependence study of the focused ultrasound-induced blood-brain barrier opening at distinct pressures and microbubble diameters using DCE-MRI," *Magn Reson Med* **66** (3), 821-830 (2011).

65. F. Y. Yang, S. H. Liu, F. M. Ho and C. H. Chang, "Effect of ultrasound contrast agent dose on the duration of focused-ultrasound-induced blood-brain barrier disruption," *J Acoust Soc Am* **126** (6), 3344-3349 (2009).

66. F. Vlachos, Y. S. Tung and E. E. Konofagou, "Permeability assessment of the focused ultrasound-induced blood-brain barrier opening using dynamic contrast-enhanced MRI," *Phys Med Biol* **55** (18), 5451-5466 (2010).

67. G. P. Howles, Y. Qi and G. A. Johnson, "Ultrasonic disruption of the blood-brain barrier enables in vivo functional mapping of the mouse barrel field cortex with manganese-enhanced MRI," *Neuroimage* **50** (4), 1464-1471 (2010).

68. F. Wang, Y. Cheng, J. Mei, Y. Song, Y. Q. Yang, Y. Liu and Z. Wang, "Focused ultrasound microbubble destruction-mediated changes in blood-brain barrier permeability assessed by contrast-enhanced magnetic resonance imaging," *J Ultrasound Med* **28** (11), 1501-1509 (2009).

69. K. F. Bing, G. P. Howles, Y. Qi, M. L. Palmeri and K. R. Nightingale, "Blood-brain barrier (BBB) disruption using a diagnostic ultrasound scanner and Definity in Mice," *Ultrasound Med Biol* **35** (8), 1298-1308 (2009).

70. H. L. Liu, P. H. Hsu, P. C. Chu, Y. Y. Wai, J. C. Chen, C. R. Shen, T. C. Yen and J. J. Wang, "Magnetic resonance imaging enhanced by superparamagnetic iron oxide particles: usefulness for distinguishing between focused ultrasound-induced blood-brain barrier disruption and brain hemorrhage," *J Magn Reson Imaging* **29** (1), 31-38 (2009).

71. K. J. Lin, H. L. Liu, P. H. Hsu, Y. H. Chung, W. C. Huang, J. C. Chen, S. P. Wey, T. C. Yen and I. T. Hsiao, "Quantitative micro-SPECT/CT for detecting focused ultrasound-induced blood-brain barrier opening in the rat," *Nucl Med Biol* **36** (7), 853-861 (2009).

72. F. Y. Yang, W. M. Fu, W. S. Chen, W. L. Yeh and W. L. Lin, "Quantitative evaluation of the use of microbubbles with transcranial focused ultrasound on blood-brain-barrier disruption," *Ultrason Sonochem* **15** (4), 636-643 (2008).

73. S. B. Raymond, L. H. Treat, J. D. Dewey, N. J. McDannold, K. Hynynen and B. J. Bacskai, "Ultrasound enhanced delivery of molecular imaging and therapeutic agents in Alzheimer's disease mouse models," *PLoS ONE* **3** (5), e2175 (2008).

74. J. J. Choi, S. Wang, Y. S. Tung, B. Morrison, 3rd and E. E. Konofagou, "Molecules of various pharmacologically-relevant sizes can cross the ultrasound-induced blood-brain barrier opening in vivo," *Ultrasound Med Biol* **36** (1), 58-67 (2010).

75. L. H. Treat, N. McDannold, N. Vykhodtseva, Y. Zhang, K. Tam and K. Hynynen, "Targeted delivery of doxorubicin to the rat brain at therapeutic levels using MRI-guided focused ultrasound," *Int J Cancer* **121** (4), 901-907 (2007).

76. F. Y. Yang, H. E. Wang, G. L. Lin, H. H. Lin and T. T. Wong, "Evaluation of the increase in permeability of the blood-brain barrier during tumor progression after pulsed focused ultrasound," *Int J Nanomedicine* **7**, 723-730 (2012).

77. P. Y. Chen, H. L. Liu, M. Y. Hua, H. W. Yang, C. Y. Huang, P. C. Chu, L. A. Lyu, I. C. Tseng, L. Y. Feng, H. C. Tsai, S. M. Chen, Y. J. Lu, J. J. Wang, T. C. Yen, Y. H. Ma, T. Wu, J. P. Chen, J. I. Chuang, J. W. Shin, C. Hsueh and K. C. Wei, "Novel magnetic/ultrasound focusing system enhances nanoparticle drug delivery for glioma treatment," *Neuro Oncol* **12** (10), 1050-1060 (2010).

78. H. L. Liu, M. Y. Hua, P. Y. Chen, P. C. Chu, C. H. Pan, H. W. Yang, C. Y. Huang, J. J. Wang, T. C. Yen and K. C. Wei, "Blood-brain barrier disruption with focused ultrasound enhances delivery of chemotherapeutic drugs for glioblastoma treatment," *Radiology* **255** (2), 415-425 (2010).

79. C. Y. Ting, C. H. Fan, H. L. Liu, C. Y. Huang, H. Y. Hsieh, T. C. Yen, K. C. Wei and C. K. Yeh, "Concurrent blood-brain barrier opening and local drug delivery using drug-carrying microbubbles and focused ultrasound for brain glioma treatment," *Biomaterials* **33** (2), 704-712 (2012).

80. A. Burgess, C. A. Ayala-Grosso, M. Ganguly, J. F. Jordao, I. Aubert and K. Hynynen, "Targeted delivery of neural stem cells to the brain using MRI-guided focused ultrasound to disrupt the blood-brain barrier," *PLoS ONE* **6** (11), e27877 (2011).

81. M. Kinoshita, N. McDannold, F. A. Jolesz and K. Hynynen, "Noninvasive localized delivery of Herceptin to the mouse brain by MRI-guided focused ultrasound-induced blood-brain barrier disruption," *Proc Natl Acad Sci U S A* **103** (31), 11719-11723 (2006).

82. J. F. Jordao, C. A. Ayala-Grosso, K. Markham, Y. Huang, R. Chopra, J. McLaurin, K. Hynynen and I. Aubert, "Antibodies targeted to the brain with image-guided focused ultrasound reduces amyloid-beta plaque load in the TgCRND8 mouse model of Alzheimer's disease," *PLoS One* **5** (5), e10549 (2010).

83. M. Kinoshita, N. McDannold, F. A. Jolesz and K. Hynynen, "Targeted delivery of antibodies through the blood-brain barrier by MRI-guided focused ultrasound," *Biochem Biophys Res Commun* **340** (4), 1085-1090 (2006).

84. Q. Huang, J. Deng, F. Wang, S. Chen, Y. Liu, Z. Wang and Y. Cheng, "Targeted gene delivery to the mouse brain by MRI-guided focused ultrasound-induced blood-brain barrier disruption," *Exp Neurol* **233** (1), 350-356 (2012).

85. H. L. Liu, P. Y. Chen, H. W. Yang, J. S. Wu, I. C. Tseng, Y. J. Ma, C. Y. Huang, H. C. Tsai, S. M. Chen, Y. J. Lu, M. Y. Hua, Y. H. Ma, T. C. Yen and K. C. Wei, "In vivo MR quantification of superparamagnetic iron oxide nanoparticle leakage during low-frequency-ultrasound-induced blood-brain barrier opening in swine," *J Magn Reson Imaging* **34** (6), 1313-1324 (2011).

86. A. B. Etame, R. J. Diaz, M. A. O'Reilly, C. A. Smith, T. G. Mainprize, K. Hynynen and J. T. Rutka, "Enhanced delivery of gold nanoparticles with therapeutic potential into the brain using MRI-guided focused ultrasound," *Nanomedicine* (2012).

87. Y. Gavrieli, Y. Sherman and S. A. Ben-Sasson, "Identification of programmed cell death in situ via specific labeling of nuclear DNA fragmentation," *J Cell Biol* **119** (3), 493-501 (1992).

88. I. V. Victorov, K. Prass and U. Dirnagl, "Improved selective, simple, and contrast staining of acidophilic neurons with vanadium acid fuchsin," *Brain Res Brain Res Protoc* **5** (2), 135-139 (2000).

89. K. Hynynen, N. McDannold, H. Martin, F. A. Jolesz and N. Vykhodtseva, "The threshold for brain damage in rabbits induced by bursts of ultrasound in the presence of an ultrasound contrast agent (Optison)," *Ultrasound Med Biol* **29** (3), 473-481 (2003).

90. Y. Ishihara, A. Calderon, H. Watanabe, K. Okamoto, Y. Suzuki and K. Kuroda, "A precise and fast temperature mapping using water proton chemical shift," *Magn Reson Med* **34** (6), 814-823 (1995).

91. B. Baseri, J. J. Choi, Y. S. Tung and E. E. Konofagou, "Multi-Modality Safety Assessment of Blood-Brain Barrier Opening Using Focused Ultrasound and Definity Microbubbles: A Short-Term Study," *Ultrasound Med Biol* **36** (9), 1445-1459 (2010).

92. N. McDannold, N. Vykhodtseva, S. Raymond, F. A. Jolesz and K. Hynynen, "MRI-guided targeted blood-brain barrier disruption with focused ultrasound: histological findings in rabbits," *Ultrasound Med Biol* **31** (11), 1527-1537 (2005).

93. H. L. Liu, Y. Y. Wai, P. H. Hsu, L. A. Lyu, J. S. Wu, C. R. Shen, J. C. Chen, T. C. Yen and J. J. Wang, "In vivo assessment of macrophage CNS infiltration during disruption of the blood-brain barrier with focused ultrasound: a magnetic resonance imaging study," *J Cereb Blood Flow Metab* **30** (1), 177-186 (2010).

94. N. McDannold, Y. Zhang and N. Vykhodtseva, "Blood-brain barrier disruption and vascular damage induced by ultrasound bursts combined with microbubbles can be influenced by choice of anesthesia protocol," *Ultrasound Med Biol* **37** (8), 1259-1270 (2011).

95. N. J. Abbott, L. Ronnback and E. Hansson, "Astrocyte-endothelial interactions at the blood-brain barrier," *Nat Rev Neurosci* **7** (1), 41-53 (2006).

96. S. Jalali, Y. Huang, D. J. Dumont and K. Hynynen, "Focused ultrasound-mediated bbb disruption is associated with an increase in activation of AKT: experimental study in rats," *BMC Neurol* **10**, 114 (2010).

97. A. Alonso, E. Reinz, J. W. Jenne, M. Fatar, H. Schmidt-Glenewinkel, M. G. Hennerici and S. Meairs, "Reorganization of gap junctions after focused ultrasound blood-brain barrier opening in the rat brain," *J Cereb Blood Flow Metab* **30** (7), 1394-1402 (2010).

98. J. Deng, Q. Huang, F. Wang, Y. Liu, Z. Wang, Q. Zhang, B. Lei and Y. Cheng, "The role of caveolin-1 in blood-brain barrier disruption induced by focused ultrasound combined with microbubbles," *J Mol Neurosci* **46** (3), 677-687 (2012).

99. S. B. Raymond, J. Skoch, K. Hynynen and B. J. Bacskai, "Multiphoton imaging of ultrasound/Optison mediated cerebrovascular effects in vivo," *J Cereb Blood Flow Metab* **27** (2), 393-403 (2007).

100. E. E. Cho, J. Drazic, M. Ganguly, B. Stefanovic and K. Hynynen, "Two-photon fluorescence microscopy study of cerebrovascular dynamics in ultrasound-induced blood-brain barrier opening," *J Cereb Blood Flow Metab* **31** (9), 1852-1862 (2011).

101. W. H. Chou and R. O. Messing, "Hypertensive encephalopathy and the blood-brain barrier: is deltaPKC a gatekeeper?," *J Clin Invest* **118** (1), 17-20 (2008).

102. R. E. Apfel, "Sonic effervescence: A tutorial on acoustic cavitation," *Journal of the Acoustical Society of America* **101** (3), 1227-1237 (1997).

103. R. E. Apfel and C. K. Holland, "Gauging the likelihood of cavitation from short-pulse, low-duty cycle diagnostic ultrasound," *Ultrasound Med Biol* **17** (2), 179-185 (1991).

104. J. E. Chomas, P. Dayton, J. Allen, K. Morgan and K. W. Ferrara, "Mechanisms of contrast agent destruction," *IEEE Trans Ultrason Ferroelectr Freq Control* **48** (1), 232-248 (2001).

105. J. E. Chomas, P. Dayton, D. May and K. Ferrara, "Threshold of fragmentation for ultrasonic contrast agents," *J Biomed Opt* **6** (2), 141-150 (2001).

106. T. Giesecke and K. Hynynen, "Ultrasound-mediated cavitation thresholds of liquid perfluorocarbon droplets in vitro," *Ultrasound Med Biol* **29** (9), 1359-1365 (2003).

107. W. S. Chen, A. A. Brayman, T. J. Matula and L. A. Crum, "Inertial cavitation dose and hemolysis produced in vitro with or without Optison," *Ultrasound Med Biol* **29** (5), 725-737 (2003).

108. W. S. Chen, A. A. Brayman, T. J. Matula, L. A. Crum and M. W. Miller, "The pulse length-dependence of inertial cavitation dose and hemolysis," *Ultrasound Med Biol* **29** (5), 739-748 (2003).

109. A. Y. Ammi, R. O. Cleveland, J. Mamou, G. I. Wang, S. L. Bridal and W. D. O'Brien, Jr., "Ultrasonic contrast agent shell rupture detected by inertial cavitation and rebound signals," *IEEE Trans Ultrason Ferroelectr Freq Control* **53** (1), 126-136 (2006).

110. S. Qin and K. W. Ferrara, "Acoustic response of compliable microvessels containing ultrasound contrast agents," *Phys Med Biol* **51** (20), 5065-5088 (2006).

111. H. Zheng, P. A. Dayton, C. Caskey, S. Zhao, S. Qin and K. W. Ferrara, "Ultrasound-driven microbubble oscillation and translation within small phantom vessels," *Ultrasound Med Biol* **33** (12), 1978-1987 (2007).

112. C. F. Caskey, S. M. Stieger, S. Qin, P. A. Dayton and K. W. Ferrara, "Direct observations of ultrasound microbubble contrast agent interaction with the microvessel wall," *J Acoust Soc Am* **122** (2), 1191-1200 (2007).

113. J. H. Hwang, J. Tu, A. A. Brayman, T. J. Matula and L. A. Crum, "Correlation between inertial cavitation dose and endothelial cell damage in vivo," *Ultrasound Med Biol* **32** (10), 1611-1619 (2006).

114. J. Tu, T. J. Matula, A. A. Brayman and L. A. Crum, "Inertial cavitation dose produced in ex vivo rabbit ear arteries with Optison by 1-MHz pulsed ultrasound," *Ultrasound Med Biol* **32** (2), 281-288 (2006).

115. K. Kooiman, M. Emmer, M. Foppen-Harteveld, A. van Wamel and N. de Jong, "Increasing the endothelial layer permeability through ultrasound-activated microbubbles," *IEEE Trans Biomed Eng* **57** (1), 29-32 (2010).

116. R. A. Roy, A. A. Atchley, L. A. Crum, J. B. Fowlkes and J. J. Reidy, "A Precise Technique for the Measurement of Acoustic Cavitation Thresholds and Some Preliminary-Results," *Journal of the Acoustical Society of America* **78** (5), 1799-1805 (1985).

117. A. Tsukamoto, S. Higashiyama, K. Yoshida, Y. Watanabe, K. S. Furukawa and T. Ushida, "Stable cavitation induces increased cytoplasmic calcium in L929 fibroblasts exposed to 1-MHz pulsed ultrasound," *Ultrasonics* **51** (8), 982-990 (2011).

118. S. Datta, C. C. Coussios, A. Y. Ammi, T. D. Mast, G. M. de Courten-Myers and C. K. Holland, "Ultrasound-enhanced thrombolysis using Definity as a cavitation nucleation agent," *Ultrasound Med Biol* **34** (9), 1421-1433 (2008).

119. Y. S. Tung, J. J. Choi, B. Baseri and E. E. Konofagou, "Identifying the inertial cavitation threshold and skull effects in a vessel phantom using focused ultrasound and microbubbles," *Ultrasound Med Biol* **36** (5), 840-852 (2010).

120. Y. S. Tung, F. Vlachos, J. J. Choi, T. Deffieux, K. Selert and E. E. Konofagou, "In vivo transcranial cavitation threshold detection during ultrasound-induced blood-brain barrier opening in mice," *Phys Med Biol* **55** (20), 6141-6155 (2010).

121. N. McDannold, N. Vykhodtseva and K. Hynynen, "Targeted disruption of the blood-brain barrier with focused ultrasound: association with cavitation activity," *Phys Med Biol* **51** (4), 793-807 (2006).

122. K. Takegami, Y. Kaneko, T. Watanabe, T. Maruyama, Y. Matsumoto and H. Nagawa, "Polyacrylamide gel containing egg white as new model for irradiation experiments using focused ultrasound," *Ultrasound Med Biol* **30** (10), 1419-1422 (2004).

123. E. Talu, R. L. Powell, M. L. Longo and P. A. Dayton, "Needle size and injection rate impact microbubble contrast agent population," *Ultrasound Med Biol* **34** (7), 1182-1185 (2008).

124. C. H. Farny, R. G. Holt and R. A. Roy, "Temporal and spatial detection of HIFU-induced inertial and hot-vapor cavitation with a diagnostic ultrasound system," *Ultrasound Med Biol* **35** (4), 603-615 (2009).

125. T. G. Leighton, *The Acoustic Bubble*. (1994).

126. J. Woitzik, N. Hecht, U. C. Schneider, P. G. Pena-Tapia and P. Vajkoczy, "Increased vessel diameter of leptomeningeal anastomoses after hypoxic preconditioning," *Brain Res* **1115** (1), 209-212 (2006).

127. E. Sassaroli and K. Hynynen, "Cavitation threshold of microbubbles in gel tunnels by focused ultrasound," *Ultrasound Med Biol* **33** (10), 1651-1660 (2007).

128. E. Sassaroli and K. Hynynen, "Resonance frequency of microbubbles in small blood vessels: a numerical study," *Phys Med Biol* **50** (22), 5293-5305 (2005).

129. Y. Sun, D. E. Kruse, P. A. Dayton and K. W. Ferrara, "High-frequency dynamics of ultrasound contrast agents," *IEEE Trans Ultrason Ferroelectr Freq Control* **52** (11), 1981-1991 (2005).

130. S. Samuel, J. B. Fowlkes and D. L. Miller, "An in vitro study of the correlation between bubble distribution, acoustic emission, and cell damage by contrast ultrasound," *IEEE Trans Ultrason Ferroelectr Freq Control* **56** (3), 589-599 (2009).

131. T. Deffieux and E. E. Konofagou, "Numerical Study of a Simple Transcranial Focused Ultrasound System Applied to Blood-Brain Barrier Opening," *Ieee T Ultrason Ferr* **57** (12), 2637-2653 (2010).

132. S. Qin and K. W. Ferrara, "The natural frequency of nonlinear oscillation of ultrasound contrast agents in microvessels," *Ultrasound Med Biol* **33** (7), 1140-1148 (2007).

133. S. Martynov, E. Stride and N. Saffari, "The natural frequencies of microbubble oscillation in elastic vessels," *J Acoust Soc Am* **126** (6), 2963-2972 (2009).

134. S. Sirsi, J. Feshitan, J. Kwan, S. Homma and M. Borden, "Effect of microbubble size on fundamental mode high frequency ultrasound imaging in mice," *Ultrasound Med Biol* **36** (6), 935-948 (2010).

135. W. S. Chen, T. J. Matula, A. A. Brayman and L. A. Crum, "A comparison of the fragmentation thresholds and inertial cavitation doses of different ultrasound contrast agents," *J Acoust Soc Am* **113** (1), 643-651 (2003).

136. C. C. Church, "The effects of an elastic solid surface layer on the radial pulsations of gas bubbles," *J Acoust Soc Am* **97** (3), 12 (1995).

137. A. A. Doinikov and A. Bouakaz, "Review of shell models for contrast agent microbubbles," *IEEE Trans Ultrason Ferroelectr Freq Control* **58** (5), 981-993 (2011).

138. V. Sboros, "Response of contrast agents to ultrasound," *Adv Drug Deliv Rev* **60** (10), 1117-1136 (2008).

139. P. Marmottant, S. van der Meer, M. Emmer, M. Versluis, N. de Jong, S. Hilgenfeldt and D. Lohse, "A model for large amplitude oscillations of coated bubbles accounting for buckling and rupture," *J Acoust Soc Am* **118** (6), 7 (1995).

140. M. A. Borden and M. L. Longo, "Dissolution behavior of lipid monolayer-coated, air-filled microbubbles: effect of lipid hydrophobic chain length," *Langmuir* **18** (24), 9225-9233 (2002).

141. M. A. Borden, D. E. Kruse, C. F. Caskey, S. Zhao, P. A. Dayton and K. W. Ferrara, "Influence of lipid shell physicochemical properties on ultrasound-induced microbubble destruction," *IEEE Trans Ultrason Ferroelectr Freq Control* **52** (11), 1992-2002 (2005).

142. D. H. Kim, M. J. Costello, P. B. Duncan and D. Needham, "Mechanical properties and microstructure of polycrystalline phospholipid monolayer shells: novel solid microparticles," *Langmuir* **19** (20), 8455-8466 (2003).

143. S. Dicker, M. Mleczko, G. Schmitz and S. P. Wrenn, "Determination of microbubble cavitation threshold pressure as function of shell chemistry," *Bubble Science, Engineering and Technology* **2** (2), 55-64 (2010).

144. S. P. Wrenn, M. Mleczko and G. Schmitz, "Phospholipid-stabilized microbubbles: Influence of shell chemistry on cavitation threshold and binding to giant uni-lamellar vesicles," *Appl Acoust* **70** (10), 1313-1322 (2009).

145. E. Sassaroli and K. Hynynen, "On the impact of vessel size on the threshold of bubble collapse," *Appl Phys Lett* **89** (12), - (2006).

146. S. Qin, C. F. Caskey and K. W. Ferrara, "Ultrasound contrast microbubbles in imaging and therapy: physical principles and engineering," *Phys Med Biol* **54** (6), R27-57 (2009).

147. L. Rayleigh, "On the pressure developed in a liquid during the collapse of a shperical cavity," *Phil. Mag.* **34**, 5 (1917).

148. J. B. Keller and M. Miksis, "Bubble oscillations of large amplitude," *J Acoust Soc Am* **68** (2), 6 (1980).

149. L. Hoff, "http://home.online.no/~fam.hoff/Bubblesim/Bubblesim.htm."

150. H. J. Vos, F. Guidi, E. Boni and P. Tortoli, "Method for microbubble characterization using primary radiation force," *IEEE Trans Ultrason Ferroelectr Freq Control* **54** (7), 1333-1345 (2007).

151. J. A. Feshitan, C. C. Chen, J. J. Kwan and M. A. Borden, "Microbubble size isolation by differential centrifugation," *J Colloid Interface Sci* **329** (2), 316-324 (2009).

152. N. de Jong, M. Emmer, C. T. Chin, A. Bouakaz, F. Mastik, D. Lohse and M. Versluis, ""Compression-only" behavior of phospholipid-coated contrast bubbles," *Ultrasound Med Biol* **33** (4), 653-656 (2007).

153. B. V. Zlokovic, "The blood-brain barrier in health and chronic neurodegenerative disorders," *Neuron* **57** (2), 178-201 (2008).

154. P. Dayton, A. Klibanov, G. Brandenburger and K. Ferrara, "Acoustic radiation force in vivo: a mechanism to assist targeting of microbubbles," *Ultrasound Med Biol* **25** (8), 1195-1201 (1999).

155. J. Sijl, M. Overvelde, B. Dollet, V. Garbin, N. de Jong, D. Lohse and M. Versluis, ""Compression-only" behavior: a second-order nonlinear response of ultrasound contrast agent microbubbles," *J Acoust Soc Am* **129** (4), 1729-1739 (2011).

156. W. Wiedemair, Z. Tukovic, H. Jasak, D. Poulikakos and V. Kurtcuoglu, "On ultrasound-induced microbubble oscillation in a capillary blood vessel and its implications for the blood-brain barrier," *Phys Med Biol* **57** (4), 1019-1045 (2012).

157. H. Leong-Poi, J. Song, S. J. Rim, J. Christiansen, S. Kaul and J. R. Lindner, "Influence of microbubble shell properties on ultrasound signal: Implications for low-power perfusion imaging," *Journal of the American Society of Echocardiography* **15** (10 II), 1269-1276 (2002).

158. P. Prentice, A. Cuschierp, K. Dholakia, M. Prausnitz and P. Campbell, "Membrane disruption by optically controlled microbubble cavitation," *Nat Phys* **1** (2), 107-110 (2005).

159. M. A. O'Reilly and K. Hynynen, "Blood-Brain Barrier: Real-time Feedback-controlled Focused Ultrasound Disruption by Using an Acoustic Emissions-based Controller," *Radiology* **263** (1), 96-106 (2012).

160. J. J. Choi, K. Selert, F. Vlachos, A. Wong and E. E. Konofagou, "Noninvasive and localized neuronal delivery using short ultrasonic pulses and microbubbles," *Proc Natl Acad Sci U S A* **108** (40), 16539-16544 (2011).

161. L. J. Juffermans, O. Kamp, P. A. Dijkmans, C. A. Visser and R. J. Musters, "Low-intensity ultrasound-exposed microbubbles provoke local hyperpolarization of the cell membrane via activation of BK(Ca) channels," *Ultrasound Med Biol* **34** (3), 502-508 (2008).

162. B. D. Meijering, L. J. Juffermans, A. van Wamel, R. H. Henning, I. S. Zuhorn, M. Emmer, A. M. Versteilen, W. J. Paulus, W. H. van Gilst, K. Kooiman, N. de Jong, R. J. Musters, L. E. Deelman and O. Kamp, "Ultrasound and microbubble-targeted delivery of macromolecules is regulated by induction of endocytosis and pore formation," *Circ Res* **104** (5), 679-687 (2009).

163. J. Lee, A. Ishihara, G. Oxford, B. Johnson and K. Jacobson, "Regulation of cell movement is mediated by stretch-activated calcium channels," *Nature* **400** (6742), 382-386 (1999).

164. R. V. Sharma, M. W. Chapleau, G. Hajduczok, R. E. Wachtel, L. J. Waite, R. C. Bhalla and F. M. Abboud, "Mechanical stimulation increases intracellular calcium concentration in nodose sensory neurons," *Neuroscience* **66** (2), 433-441 (1995).

165. H. Chen, W. Kreider, A. A. Brayman, M. R. Bailey and T. J. Matula, "Blood vessel deformations on microsecond time scales by ultrasonic cavitation," *Phys Rev Lett* **106** (3), 034301 (2011).

166. F. J. Fry, "Transkull transmission of an intense focused ultrasonic beam," *Ultrasound Med Biol* **3** (2-3), 179-184 (1977).

167. R. S. C. Cobbold, "Foundations of biomedical ultrasound," *Oxford University Press* (2007).

168. R. P. Woods, S. C. Fears, M. J. Jorgensen, L. A. Fairbanks, A. W. Toga and N. B. Freimer, "A web-based brain atlas of the vervet monkey, Chlorocebus aethiops," *Neuroimage* **54** (3), 1872-1880 (2011).

169. M. W. Woolrich, S. Jbabdi, B. Patenaude, M. Chappell, S. Makni, T. Behrens, C. Beckmann, M. Jenkinson and S. M. Smith, "Bayesian analysis of neuroimaging data in FSL," *Neuroimage* **45** (1 Suppl), S173-186 (2009).

170. S. M. Smith, M. Jenkinson, M. W. Woolrich, C. F. Beckmann, T. E. Behrens, H. Johansen-Berg, P. R. Bannister, M. De Luca, I. Drobnjak, D. E. Flitney, R. K. Niazy, J. Saunders, J. Vickers, Y. Zhang, N. De Stefano, J. M. Brady and P. M. Matthews, "Advances in functional and structural MR image analysis and implementation as FSL," *Neuroimage* **23 Suppl 1**, S208-219 (2004).

171. P. S. Tofts, G. Brix, D. L. Buckley, J. L. Evelhoch, E. Henderson, M. V. Knopp, H. B. Larsson, T. Y. Lee, N. A. Mayr, G. J. Parker, R. E. Port, J. Taylor and R. M. Weisskoff, "Estimating kinetic parameters from dynamic contrast-enhanced T(1)-weighted MRI of a diffusable tracer: standardized quantities and symbols," *J Magn Reson Imaging* **10** (3), 223-232 (1999).

172. D. M. McGrath, D. P. Bradley, J. L. Tessier, T. Lacey, C. J. Taylor and G. J. Parker, "Comparison of model-based arterial input functions for dynamic contrast-enhanced MRI in tumor bearing rats," *Magn Reson Med* **61** (5), 1173-1184 (2009).

173. G. J. Parker, C. Roberts, A. Macdonald, G. A. Buonaccorsi, S. Cheung, D. L. Buckley, A. Jackson, Y. Watson, K. Davies and G. C. Jayson, "Experimentally-derived functional form for a population-averaged high-temporal-resolution arterial input function for dynamic contrast-enhanced MRI," *Magn Reson Med* **56** (5), 993-1000 (2006).

174. D. L. Thomas, M. F. Lythgoe, D. G. Gadian and R. J. Ordidge, "In vivo measurement of the longitudinal relaxation time of arterial blood (T1a) in the mouse using a pulsed arterial spin labeling approach," *Magn Reson Med* **55** (4), 943-947 (2006).

175. M. Bilgen and P. A. Narayana, "A pharmacokinetic model for quantitative evaluation of spinal cord injury with dynamic contrast-enhanced magnetic resonance imaging," *Magn Reson Med* **46** (6), 1099-1106 (2001).

176. M. Pellerin, T. E. Yankeelov and M. Lepage, "Incorporating contrast agent diffusion into the analysis of DCE-MRI data," *Magn Reson Med* **58** (6), 1124-1134 (2007).

Appendix A

Kinetic model for permeability map

The general kinetic model (GKM) was used to measure the BBB permeability in the targeted region. Previous studies[66] have validated the reliability of GKM in the FUS-induced BBB opening. GKM classifies tissues in two compartments, the blood plasma and the EES[171]:

$$\frac{dC_t}{dt} = K_{trans} C_p - K_{ep} C_t \tag{A.1}$$

where K_{trans}, K_{ep} are the transfer rate constants from the blood plasma to the EES and from the EES to the blood plasma, respectively, and C_p, C_t are the concentrations of Gd-DTPA in the blood plasma and the EES respectively. GKM assumes prior knowledge of the arterial input of the contrast agent over time, which is model fitted to a bi-exponential equation, typically referred to as the arterial input function (AIF):

$$C_p(t) = A_1 e^{-m_1 t} + A_2 e^{-m_2 t} \tag{A.2}$$

where A_i, m_i (i=1, 2) are the amplitude and decay rates of C_p respectively and t is time. The plasma concentration C_p is calculated as a fraction of the blood concentration C_b, $C_p = (1 - H_{ct}) C_b$, where H_{ct}=0.45 is the hematocrit level for wild-type mice. The difficulty in obtaining an accurate AIF from a detectable vessel in the dynamic images has been reported and assessed with various estimating models[172]. However, recent studies[172] have demonstrated that selecting a population average from a large group of the same strain of animals in order to determine the AIF can be both accurate and robust. In this study, the entire cohort of mice was used to determine the AIF, by averaging the Gd-DTPA concentration changes in the internal carotid artery (ICA), as shown in previous studies[66].

Signal intensity in T_1 images is translated to tracer concentration, using the Solomon-Bloembergen equation[173]. The equation assumes a linear relationship between the concentration of the contrast agent ([*Gd*]) and the relaxation rate difference (ΔR_1). Relating the relaxation rate to signal intensity (*S*) in the gradient echo MR images yields a linear relationship between *S* and [*Gd*]:

$$\left[\mathrm{Gd}\right] = \frac{S_{post} - S_{pre}}{T_{1,pre} \times r_1 \times S_{pre}} \tag{A.3}$$

where $T_{1,pre}$ is the longitudinal relaxation time of the corresponding tissue before the contrast agent administration, r_1 is the longitudinal relaxivity of the contrast agent and S_{pre}, S_{post} are the signal intensities before and after Gd-DTPA injection respectively. Phantom experiments in the 9.4 T MRI system have shown that the r_1 relaxivity of gadodiamide (Omniscan®, molecular weight of 530 Da) is approximately 2.6 $\mathrm{mM^{-1}s^{-1}}$, while the longitudinal relaxation times of the brain tissue (0.9 s) and the arterial blood (1.5 s) in mice have been reported in previous studies, using arterial spin labeling techniques[174].

Prior to the quantitative K_{trans} measurements, all the images were smoothed using the N-D filtering algorithm of the Image Processing Toolbox® of Matlab (MathWorks, Inc., Natick, MA, USA). In addition, since the actual Gd-DTPA injection time occurred approximately 3 min after the beginning of DCE-MRI, exclusion criteria were set for the estimated Gd-DTPA injection time (t<0 or t>30 min) in order to avoid any fitting divergences. The spatial permeability distribution was estimated by counting the voxels that exhibited a K_{trans} value over a predefined threshold (0.005 $\mathrm{min^{-1}}$). The threshold was selected in the mouse that showed the smallest BBB opening, using the quantification method described below. The estimations represented the volume area in the sonicated region where there was a clear permeability increase. The K_{trans} values were measured both pixel-by-pixel, generating transverse and reconstructed coronal permeability maps of the mouse brain, and for a circular region of interest (ROI) of 1 mm in diameter in the targeted hippocampal area and the control side. The ROI was applied on the slice with the highest T_1 signal enhancement due to BBB opening and the ROI size was selected so it matched the axial full-width-at-half-maximum intensity area dimension of the beam. If the temporal Gd-DTPA concentration profile of a pixel fitted the AIF curve (Fig. A.1), then that pixel was excluded and the remaining pixels within the ROI were averaged to extract the K_{trans} value.

The general kinetic algorithm determined both the K_{trans} and K_{ep} values, but this study emphasized only on K_{trans}, which represents the Gd-DTPA leakage from the systemic circulation and is mostly influenced by the concentration changes immediately after the Gd-DTPA injection. K_{ep} values are mostly influenced by the "steady-state" time points of the concentration curves (Fig. A.1), when equilibrium is reached between the EES and the blood plasma concentrations[175,176].

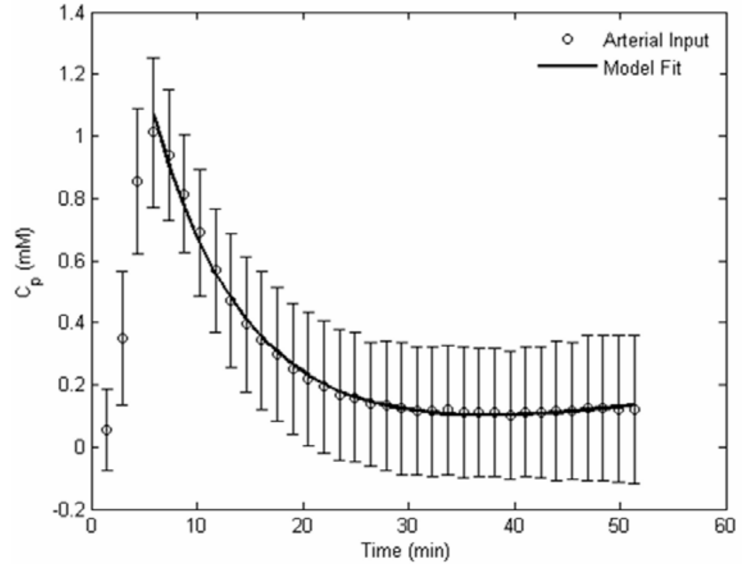

Figure A.1 – The arterial input function, averaged from a population of all 40 mice, by measuring the Gd-DTPA concentration in the internal carotid artery on the dynamic images.

Appendix B

Transcranial focusing quality quantification

Acoustic transducers

A single-element, circular focused ultrasound transducer (Riverside Institute, New York, New York, USA) with a hole in its center was driven by a function generator (Agilent Technologies, Palo Alto, CA, USA) through a 50-dB power amplifier (ENI Inc., Rochester, NY, USA). The center frequency, focal depth, outer radius and inner radius of FUS were 500 kHz, 90 mm, 30 mm and 11.2 mm, respectively. A single-element passive cavitation detector (PCD) (center frequency: 7.5 MHz, focal length: 60 mm, Olympus NDT, Waltham, MA, USA) was positioned through the center hole of the FUS transducer. The two transducers were aligned so that their focal regions fully overlapped within the confocal volume. This transducers assembly is suspended to a 3D axis positioning system (Velmex Inc., Bloomfield, NY, USA) to be able to aim the desired target through the skull. A hydrophone (HGN-0200, Onda Corp, Sunnyvale, CA, USA) is attached to a second similar 3D axis positioning system in order to scan the transcranial pressure field.

Skull preparation

Two human and two non-human primate skulls were used for this study. For these skulls, two hemispheres were used for each location. Prior to the experiment, the skulls were degassed during one day in a sealed jar. Vacuum was made using a custom made pump. For *in vitro* experiments, the transducer was connected to the first 3D positioning system and immersed in a large water tank filled with degassed water. The human or NHP skull is also immersed in water. The hydrophone was then placed inside the skull cavity at the center plane through the virtual targeted region.

Targeting

Targeting was performed using a pulse-echo transducer and utilizing the distinct landmarks on the skull. The 7.5 MHz pulse-echo transducer embedded through the central bore hole of the therapeutic transducer was used to map the surface of the targeted skull. The occipital protuberance (OP) that lines the inferior dorsal region and the lambda anatomical landmarks in both primates and humans (Fig. B.1) was identified using time-of-flight and power spectral density measurements, whose product indicates the reflectivity of the skull. To this purpose, the pulse-echo transducer was moved using the positioning system in the lateral and ventro-dorsal directions of the skull and the time of occurrence of the peak in the power spectrum of the received RF signals will be calculated in each location. The OP and lambda landmarks were then identified (Fig. 6.2) due to their distinct reflectivity and texture and then mapped onto a preexisting brain atlas. For each target, the orientation of sonication was chosen to be similar to the previous simulation study performed in our lab[131]. In this previous work, optimal orientations for the ultrasound focus to match anatomical shapes of targets were calculated. Also, as the NHP OP seemed to be hindering the ultrasonic propagation for putamen and caudate targeting, alternative orientations were defined. These alternative orientations for caudate and putamen are very similar and studying the benefit of this choice *in vitro* is relevant, therefore for NHP skulls we studied the alternative caudate and the original putamen orientations.

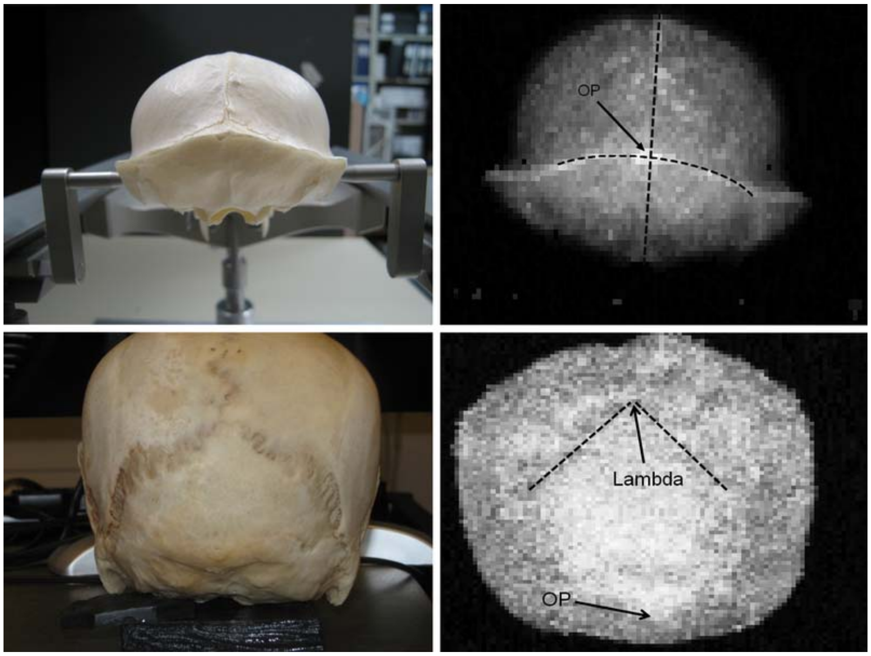

Figure B.1 – Targeting images for monkey and human skulls based on combined reflectivity and time-of-flight measurements. Anatomical landmarks are clearly identified such as the occipital protuberance or lambda.

Acoustic measurements

In order to quantify the focusing quality, pressure field measurements are realized around the geometric focus. Once the transducer is set to aim a particular region through the skull using the procedure described in the previous section, the hydrophone is set at this location using the second 3D positioning system. This second positioning system is used to move the hydrophone to scan the pressure field along one plane. The scan field of view is 2 cm along lateral dimensions and 6 cm along axial dimension, the spatial step is 0.167 mm for the lateral dimensions and 0.5 mm for the axial. For each point, the acoustic response is acquired on a PC workstation with an 80-MHz digital acquisition board (model 14200, Gage applied technologies Inc., Lachine, QC, Canada). For each location, the peak negative pressure is measured and represented in 2D matrix. For every case, transcranial pressure profiles are compared with water pressure profiles enabling quantification comparison in peak pressure amplitude, position shift and focal shape. In the previous simulation work[131], two other parameters were evaluated to quantify the quality of the target coverage by the ultrasound focus. For every case we calculated the percent-of-target-overlapped, which depicts the volume fraction of the target above half-pressure threshold, and the percent-of-beam-overlapping-target, which represents the volume fraction of the beam that falls inside the targeted region.

Results

Figures B.2 & B.3 show typical beam plots of examples the transcranial ultrasonic pressures measured in the horizontal and transverse planes of the focus of the transducer. According to previous reports[51,91,120], the ratio between the pressure threshold for damage and the pressure threshold for BBB disruption is always less than 2 or 6dB. These pressure fields have been thresholded at -6dB in order to represent the maximum extent of induced BBB opening without inducing damage. The contour of the targeted region is depicted using a blue dashed line. For each target and each skull type, these pressure profiles were acquired four times (two skulls and two hemispheres). For each acquisition, the quality of the focusing is assessed using the following parameters: attenuation compared to that of the water, lateral and axial resolution of the focus (for the lateral, small and large axis are measured to quantify the distortion of the focus), shift of the position of the focus compared to that of the water, resolution of the focus (-6 dB dimensions, roughly equivalent to half-pressure threshold) and angle tilt of the focus. Using NHP skulls, the values of these parameters were consistent from one location to the next except for the NHP putamen targeting. The overall attenuation was found to be around -6 dB (respectively -5.66 ± 0.77 dB, -6.18 ± 0.30 dB and -5.57 ± 0.47 dB for the hippocampus, caudate and vertex). The resolution of the focus was found acceptable compared to that of the water (lateral dimension 3.6 ± 0.1 mm, axial dimension 31.2 ± 1.2 mm). The difference in between the two main axis of the focus in the focal plane was also investigated in order to quantify the distortion of the focus. For the hippocampus, caudate and vertex respectively, the lateral -6 dB dimensions were 3.9 ± 0.2 mm, 4.0 ± 0.1 mm and 3.7 ± 0.1 mm for the small axis and 4.2 ± 0.2 mm, 4.2 ± 0.3 mm and 4.0 ± 0.2 mm for the large axis. Corresponding axial resolutions were found to be 38.5 ± 1.7 mm, 39.2 ± 2.3 mm and 38.9 ± 1.7 mm. The displacement of the focus compared to the geometrical focus was also quantified. The shift of the focus was found to be, respectively, 0.6 ± 0.2 mm, 0.8 ± 0.1 mm and 0.5 ± 0.3 mm in the focal plane and -4.4 ± 1.3 mm, -4.1 ± 0.7 mm and -3.9 mm ± 1.0 mm along the geometric axis of propagation. Finally the tilt of the focus induced by presence of the skull was measured, the angle between axial dimension of the focus and the principal axis of propagation. The respective measurements were 1.21 ± 0.11°, 1.43 ± 0.64° and 1.03 ± 0.18°.

For the initial orientation calculated for targeting the putamen, the effects of the skull were stronger. The total attenuation was found to be -6.91± 0.88 dB. The resolution of the focus was more altered and the difference between small axis resolution (4.3 ± 0.3 mm) and the large axis resolution (5.2 ± 0.7 mm) was increased. The axial resolution (41.2 ± 1.8 mm) was also increased but compared to the previous orientations this change was less sensitive. The shift of the focus was increase by a factor three in the lateral dimension (2.0 ± 0.7 mm) and 25% in the axial dimension (-5.0 ± 1.0 mm).

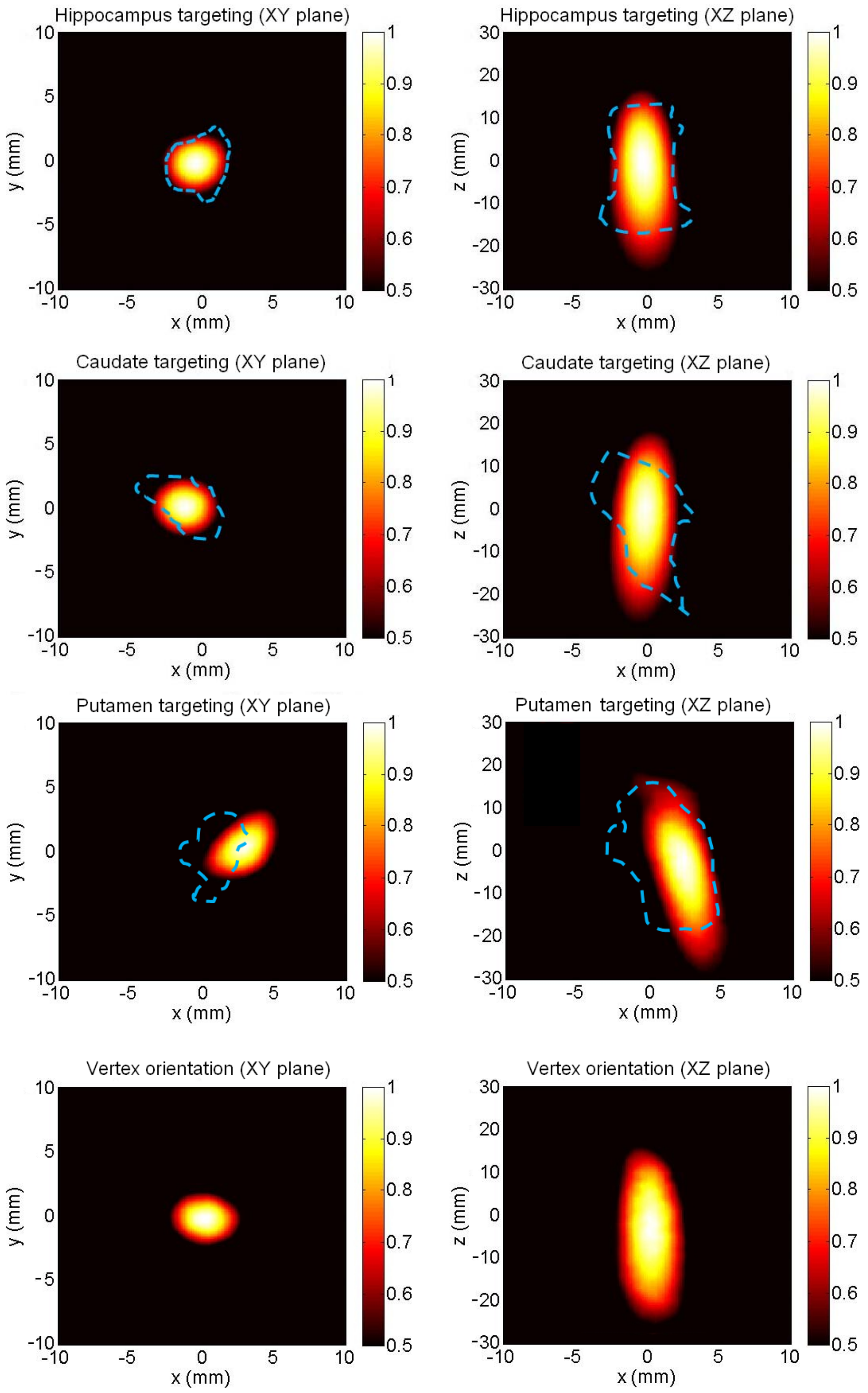

Figure B.2 – Examples of -6 dB pressure profiles obtained through a NHP skull for the four different orientations. Blue dashed lines represent the contour of the target (as indicated in the depicted plane.

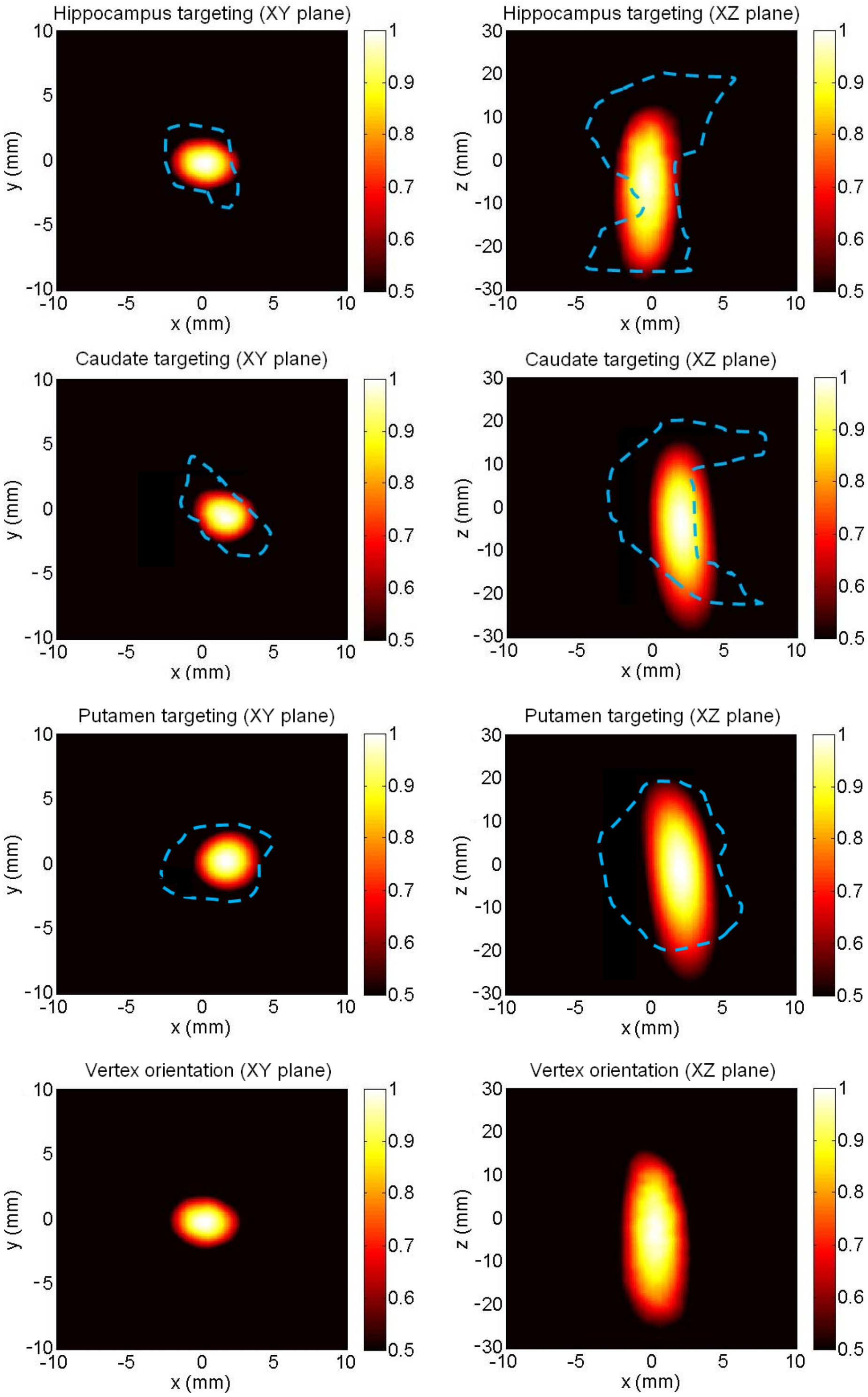

Figure B.3 – Examples of -6 dB pressure profiles obtained through a human skull for the four different orientations. Blue dashed lines represent the contour of the target as indicated in the depicted plane.

In the human skulls, the same measurements were also performed. Even though the overall effects induced by the skull are sharper, the findings were very similar. The total attenuation was measured to be -9.31 ± 0.62 dB, -9.02 ± 0.69 dB, -9.37 ± 0.65 dB and -9.05 ± 0.86 dB for the hippocampus, caudate, putamen and vertex, respectively. The lateral -6 dB resolution was found to be 4.2 ± 0.2 mm, 4.2 ± 0.2 mm, 4.1 ± 0.2 mm and 4.0 ± 0.1 mm for the small axis in the hippocampus, caudate, putamen and vertex, respectively, and 4.5 ± 0.3 mm, 4.6 ± 0.2 mm, 4.4 ± 0.2 mm and 4.3 ± 0.1 mm for the large axis in the hippocampus, caudate, putamen and vertex, respectively,. Corresponding axial resolutions were found to be 40.5 ± 1.1 mm, 42.0 ± 1.6 mm, 40.7 ± 1.3 mm and 40.3 ± 1.2 mm, respectively. The displacement of the center of the focus was found to be, respectively, 1.1 ± 0.6 mm, 1.3 ± 0.5 mm, 1.4 ± 0.3 mm and 1.2 ± 0.4 mm in the focal plane and -5.7 ± 0.6 mm, -6.5 ± 0.9 mm, -7.0 ± 0.5 mm and -6.6 mm ± 0.5 mm along the geometric axis of propagation. Tilt angles were measured to be 1.56° ± 0.64°, 2.13° ± 0.91°, 2.18° ± 0.80° and 1.39° ± 0.57°. Figure B.4 summarizes all the measurements with their means and standard deviations.

Target coverage estimations were calculated in each case. Table B.1 summarizes the findings. For NHP skulls, the percent-of-target-overlapped was found to be 42.1 ± 1.4 %, 31.0 ± 0.9 % and 21.8 ± 5.4 % for the hippocampus, caudate and putamen respectively while the percent-of-beam-overlapping-target was found to be 62.3 ± 2.4 %, 45.1 ± 2.3 % and 27.2 ± 6.7 %. For human skulls, for the hippocampus, caudate and putamen, the percent-of-target-overlapped was found to be 12.3 ± 2.1 %, 13.8 ± 2.5% and 16.6 ± 1.7 % while the percent-of-beam-overlapping-target was found to be 71.2 ± 1.7 %, 54.4 ± 3.0 % and 82.1 ± 2.8 %.

Table B.1 Targeting coverage for the different anatomical aims through NHP and human skulls.

	%-of-target-overlapped	%-of-beam-overlapping-target
NHP hippocampus	42.1 ± 1.4	62.3 ± 2.4
NHP caudate	31.0 ± 0.9	45.1 ± 2.3
NHP putamen	21.8 ± 5.4	27.2 ± 6.7
Human hippocampus	12.3 ± 2.1	71.2 ± 1.7
Human caudate	13.8 ± 2.5	54.4 ± 3.0
Human putamen	16.6 ± 1.7	82.1 ± 2.8

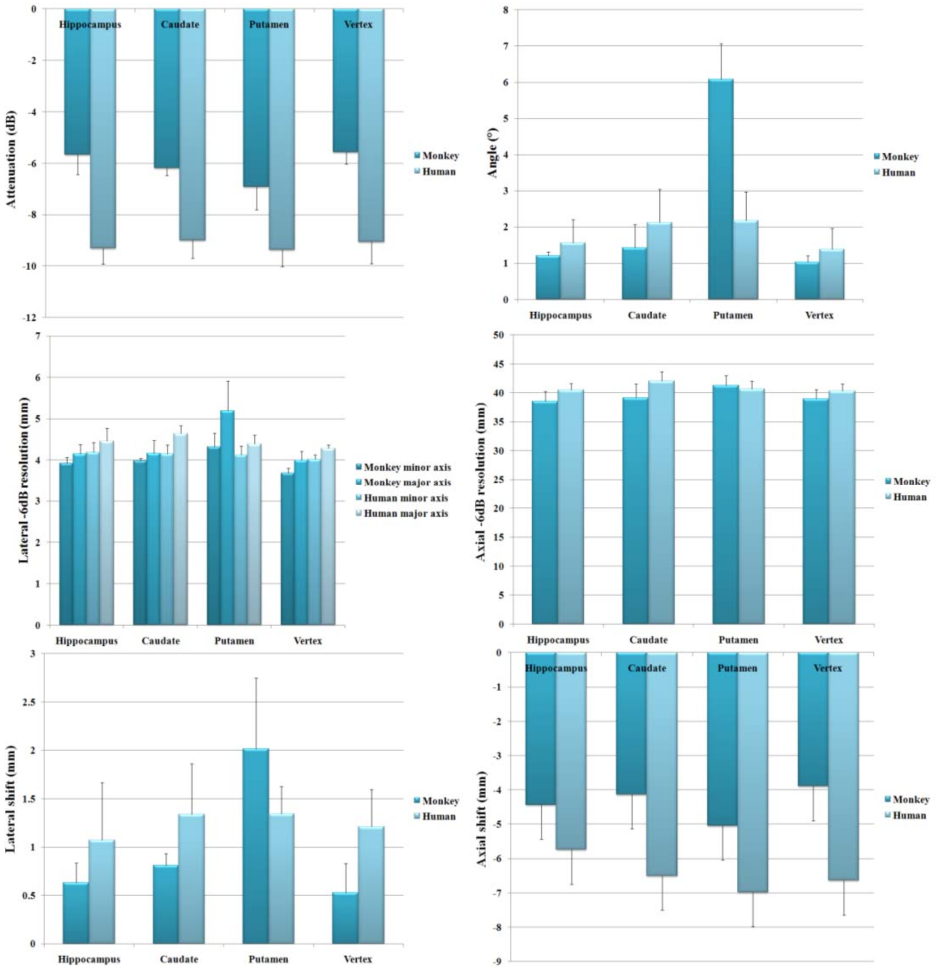

Figure B.4 – Focusing performance assessment through human and NHP skulls. Attenuation represents the energy loss crossing the skull interface compared to that of the water. Tilt represents the angle between the axial dimension of the focus and the geometric axis of propagation. Lateral resolution and axial resolution represents the dimension of the focus (-6 dB cutoff). Lateral and axial shift represents the displacement of the center of the focus.